A thesis submitted for the degree of

Doctor of Philosophy

Michaelmas Term 2020

NanoSIMS analysis of arsenic uptake and detoxification mechanisms in angiosperms

Hugh Taylor

St. Catherine's College

Supervised by Prof. C R M Grovenor

Declaration

The work reported in this thesis was carried out by the author in the Department of Materials, University of Oxford, between October 2010 and December 2020, under the supervision of Prof. C.R.M. Grovenor. No part of this thesis has been previously submitted for a degree at this or any other university. The work of other authors has been freely drawn upon and is duly acknowledged in the text. A list of references has been given at the end of the thesis and some of the work described has been presented at conferences listed below:

ICOBTE 2013: 12th International Conference on the Biogeochemistry of Trace Elements
'Using NanoSIMS Analysis to Map Trace Arsenic Distributions in Transgenic Rice Roots.' *H.M. Taylor, K.L. Moore, F.J. Zhao and C.R.M. Grovenor.*

emc2012: 15th European Microscopy Congress
'Localisation of arsenic in root cells of Asian rice (Oryza Sativa) in response to changes in transporter gene expression.' *H.M. Taylor, K.L. Moore, F.J. Zhao and C.R.M. Grovenor.*

Abstract

Rice irrigated with arsenic (As) contaminated groundwater can contain concentrations of As in the grain high enough to contribute significantly to dietary intake, leading to increased rates of adverse health effects including cancers of the liver, bladder and kidney.

The exact mechanisms by which As is transported from growth medium to grain are not fully understood. This thesis contains analyses of the distribution of As in the roots of transgenic rice and arabidopsis either defective in, or overexpressing, proteins that are thought to be involved in the transport or detoxification of As in angiosperms (flowering plants), in order to better determine their function.

The plant lines examined were rice mutants defective in Lsi3 transporter (*lsi3*), a low silicon uptake transporter believed to share transport activity with arsenite (As(III)); rice mutants overexpressing PT8 transporter (*PT8-Ov*), a PHT1 family inorganic orthophosphate (Pi) transporter believed to share transport activity with arsenate (As(V)); arabidopsis mutants defective in phytochelatin (PC) synthase (*cad1-3*), a protein responsible for forming PCs that are used to chelate and detoxify As(III); and arabidopsis mutants defective in phytochelatin transporters (*abcc1-2*), that are believed to transport As-PC complexes into vacuoles for storage. All mutants were grown alongside wild type (WT) counterparts.

Analysis of As distributions was carried out by Secondary Ion Mass Spectrometry (SIMS). The data from rice roots revealed strong co-localisation of As and sulphur (S) and high concentrations of these elements in the vacuoles of specific cells in the stele that increased with distance from the root tip and mutation on *Lsi3*, suggesting Lsi3 plays a

role in As efflux.

As concentrations increased in the stele and decreased in the epidermis in *PT8-Ov* compared to WT supplied with As(V) in the nutrient solution, this could be due to rapid transport and reduction of As(V) to As(III) for detoxification in the stele with PCs.

High concentrations of As and S were also observed in lateral root junctions, in agreement with previous research suggesting that lateral roots play in important role in As uptake.

Within arabidopsis roots high As concentrations were measured in specific cells within the stele and increased with increasing distance from root tip. A higher proportion of As to S compared to WT was observed in *cad1-3*, suggesting existence of un-chelated As, and there was a significant difference recorded in the distribution of As in *abcc1-2* compared to WT, likely due to a lack of available transport mechanisms for As-PC complexes.

Understanding the mechanisms by which As is taken up by rice plants is an important step in developing As mitigation strategies by developing the knowledge required to breed or molecularly engineer low uptake cultivars.

Acknowledgements

This thesis would not have been possible without the huge amount of support and encouragement I received over the last few years. I would especially like to thank Professor Chris Grovenor for his patience, guidance and experience. Dr Katie Moore for laying the groundwork for this project, passing on her knowledge and along with Clive Downing training me on the instruments. My collaborators at Rothamsted Research for helping design the experiments and for growing and treating all the plant lines used, including Professor Steve McGrath, Professor Fang-Jie Zhao and Dr Malcolm Hawkesford.

The team at Oxford Brookes University for providing indispensable help with their knowledge and experience. Special thanks to Professor Chris Hawes for his collaboration, and Dr Barry Martin and Dr Louise Hughes for designing and implementing the sample preparation protocols used in this thesis.

I would also like to thank my parents and siblings for their support (despite overstaying my welcome) Dr Madeleine Clarke for giving me the push that I needed, and Sonia for helping me get across the finish line.

Thanks also to David and Sara for being there for me from start to finish, and my officemates and friends in the department Dr Haibo Jiang, Dr Tayebeh Mousavi, Dr Khim Heng Lau, Dr Ele Grieveson, Dr Stella Pedrazzini and Dr Lewys Jones.

Contents

List of acronyms

HG-ICP-MS	Hydride Generation ICP-MS
HMR	High mass resolution
HPF	High pressure freezing
HPLC	High performance liquid chromatography
ICP	Inductively coupled plasma
MS	Mass spectrometry
AES	Atomic emission spectrometry
AAS	Atomic absorption spectrometry
LA-ICP-MS	Laser ablation ICP-MS
NMR	Nuclear magnetic resonance
PC	Phytochelatin
PCS	Phytochelatin synthase
RNAi	RNA interference
ROI	Region of interest
RSF	Relative sensitivity factor
SE	Secondary electrons
SEM	Secondary electron microscopy
SIMS	Secondary ion mass spectrometry
TEM	Transmission electron microscopy

Chapter 1

Literature review

1.1 Introduction

In this section I will discuss two different, but related uncertainties involving uptake and transport mechanisms in plants. Firstly, the uptake of the toxic element arsenic (As) by the rice plant (*Oryza sativa*). Commonly known as Asian rice, *Oryza sativa* is a cereal with a small genome, known to be easy to genetically modify, and is a model organism for cereal biology. Secondly the detoxification pathways of As within rice is described. These are topics of ongoing study in the field of plant biology and are the main subject of this thesis. The investigations of which arose through collaboration with Rothamstead Research, leading to a unique cross-disciplinary project using expertise from two different fields to design the experiments.

1.1.1 Contaminated ground water

It has been known since the 1980s that there are serious health risks from drinking water which contains As concentrations in the region of 0.1 parts per million (ppm) [1]. In 1958 the World Health Organisation (WHO) recommended a maximum allowable concentration of As in drinking water of $200\,\mu g\,L^{-1}$, and since then this figure has been revised to $10\,\mu g\,L^{-1}$ as the carcinogenic and long term effects of As exposure have come to light [2]. Long term exposure to low concentrations of As is known to cause hyperkeratosis, skin cancer [3], visceral lung, liver, kidney and bladder cancer [4, 5, 6].

The problem has been documented in South America and Taiwan and, in the 1990s, Bangladesh and West Bengal[1] were recognised as areas particularly affected by this problem. Tube wells dug in the area to provide clean water (as an alternative to stagnant surface water) had unknowingly tapped into underground aquifers flowing over As-rich rocks, resulting in the water containing dangerously high levels of inorganic As. According to a survey of over 3000 wells it is estimated that around 30 million people are exposed to elevated As in Bangladesh alone [7]. The distribution of As concentrations in different wells in Bangladesh is shown in figure 1.1 from which it is evident that much of the country suffers from water containing concentrations exceeding $50\,\mu g\,L^{-1}$, and large areas exist where the concentration is as high as a few thousand $\mu g\,L^{-1}$. The survey aimed to provide data on the mineral concentrations of tube well water across the country in order to better understand the distribution and extent of the As contamination. They hoped to find geographical or chemical trends that could be used to determine the source of the contamination and how best to avoid it. A more recent physical study of over 11,000 patients in the region has estimated the number of people exposed to be as high as 77 million [8]. These surveys revealed that the extent of As contamination of ground water in the area was vast, unavoidable, and dangerously high.

The mortality figure of 13 deaths per 1000 for people drinking As contaminated water at $50\,\mu g\,L^{-1}$ has been quoted in several papers as an estimate of the carcinogenicity of As; the figure first appearing in a paper published by Smith *et al.* in the Journal of Environmental Health Perspectives [9]. The figure arose from an attempt to estimate the

[1] A state in India bordering Bangladesh with a population of over 90 million

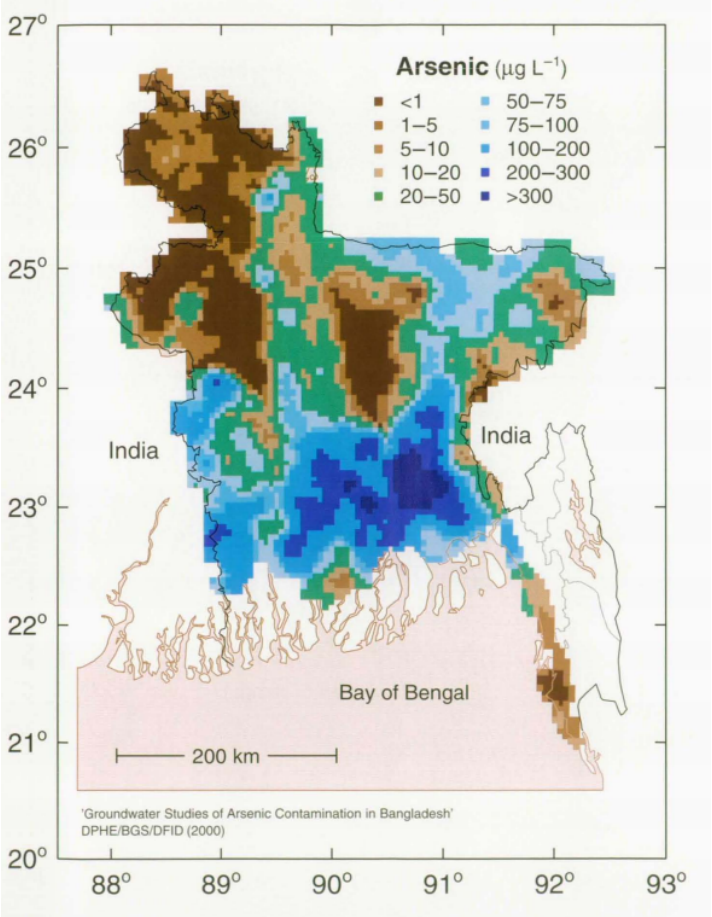

Figure 1.1: Map of the As affected areas in Bangladesh. The map was generated by taking samples from 3534 tube wells. Data and image produced by the British Geological Survey and the Department of Public Health Engineering (Bangladesh) undertaking a project funded by the UK Department for International Development (DFID) [7].

mortality rate for Americans drinking water containing As by extrapolating backwards from data collected from a carefully considered sample in Taiwan [10]. These calculations were made with reasonable consideration of the viability of such an extrapolation but did not address the differences that diet may make to the exposure and toxicity of the As. It has been suggested, for example, that a low protein diet could increase susceptibility to As toxicity [11]. More notably, as will be discussed below, rice grown using contaminated

water contains sufficiently elevated levels of As to contribute significant additional exposure. This oversight makes it difficult to quote this figure as an accurate assessment, especially when trying to apply it to different countries on different continents [12]. Nonetheless the research carried out by Smith *et al.* provides strong evidence that a linear relationship exists between As exposure and cancer mortality, later corroborated by other work [6]. A detailed review of the toxicological effects of As has been published recently in *Toxological Sciences* [13].

1.1.2 Arsenic contaminated crops

Rice farming is the largest agricultural focus in Bangladesh, accounting for approximately 75% of the total farmed land. Because of the abundance of rice, it forms the dietary staple[2], accounting for an estimated 76% of calorie intake and 66% of the protein intake of the local population. Rice production has been steadily increasing for decades and has resulted in the reallocation of farmland from other crops and vegetables to the cultivation of rice [15].

Studies have suggested that paddy fields irrigated with contaminated groundwater accumulate As in the soil. The background level of As found in soils is typically 4 to 8 $\mathrm{mg\,kg^{-1}}$, but when irrigated with contaminated water As levels can reach as high as 83 $\mathrm{mg\,kg^{-1}}$ [16]. Ali *et al.* studied the As cycle from groundwater to paddy field, noting a lack of research into contaminated irrigation due to greater emphasis being placed on its use as drinking water. Their findings indicated that hundreds of tons of As could be cycled through irrigation water each year, and at its highest, cycling of 5.5 kg of As was estimated per hectare in

[2] "A staple food is a food that is eaten regularly and in such quantities as to constitute the dominant part of the diet and supply a major proportion of energy and nutrient needs." [14]

the Laksmipur district [17]. The hypothesis of As contaminated groundwater contributing to paddy soil As has drawn a lot of interest and data suggests that a positive correlation exists [18]. Meharg *et al.* conducted a survey to establish the risk of irrigating paddy fields with the contaminated water [19]. Being careful to correctly determine the source of the As they took measurements of As concentration through different depths of the soil and sediment, and found that the As in the soil was unlikely to be "due to the geogenic origin of the soils." A correlation between tube well age and As concentration in the soil ($P = 0.048$) provided further evidence that the As was due to irrigation and was accumulating in paddy fields. It should be noted, however, that this correlation is weak and the variations are large. More data should be collected in order to better understand the cycle and severity of the contamination.

Strong correlations exist between As in the soil and As found within the rice grain [20]. Williams *et al.* studied 23 paddy fields, taking 230 soil and rice samples. The As concentrations found in the grain and straw correlated closely with the concentrations measured in the soil. Furthermore, the concentrations of nutritionally important trace elements selenium (Se), zinc (Zn) and nickel (Ni) decreased with increasing As concentration ($P < 0.001$) [21]. They concluded that As was responsible for disrupting metalloid balances, resulting in decreased crop yield in addition to decreased Se, Zn and Ni. These elements are known to be essential micronutrients [22, 23, 24] adding further concern to the health effects associated with As contaminated rice. Levels of As in the straw of rice plants were high enough to be dangerous to cattle (and possibly humans by proxy) [20].

One might assume that the As concentrations in the rice would have negligible con-

sequence in comparison to the highly elevated levels consumed from the drinking water. The work conducted by Meharg *et al.* assessed the dietary contribution of As due to rice consumption. Some of the calculations are represented in the graph shown in figure 1.2. Using this information they estimated that:

> "With a drinking water intake of $0.1\,\mathrm{mg\,L^{-1}}$ (which is considered highly elevated and a major health threat), arsenic intake from rice will account for 17.3 and 29.6% of arsenic consumption if rice contained 0.1 and $0.2\,\mathrm{\mu g\,g^{-1}}$ of arsenic, respectively. These grain values are typical of what has been observed in a range of studies in Asia, Europe, and N. America."

This work is corroborated by similar calculations by Williams *et al.* [25]. Their research also suggests that As found in rice is mostly in inorganic forms, which is considered much more toxic than the organic forms such as arsenosugars typically found in seafood [26, 27, 28].

The transformation to the organic species is considered an important step in reducing the toxicity of As [29]. The As that is found in rice grains from India and Bangladesh contains a much higher proportion of inorganic As than rice grown in the USA and Europe according to the high-performance liquid chromatography (HPLC) data provided by Williams *et al.* [25]. Due consideration was given for the possibility of extractants changing the speciation of the As and inductively coupled plasma mass spectrometry (ICP-MS) peak overlaps.

With these findings in mind, it is evident that As is present in rice grain at levels which contribute significantly to total dietary intake in areas with contaminated groundwater.

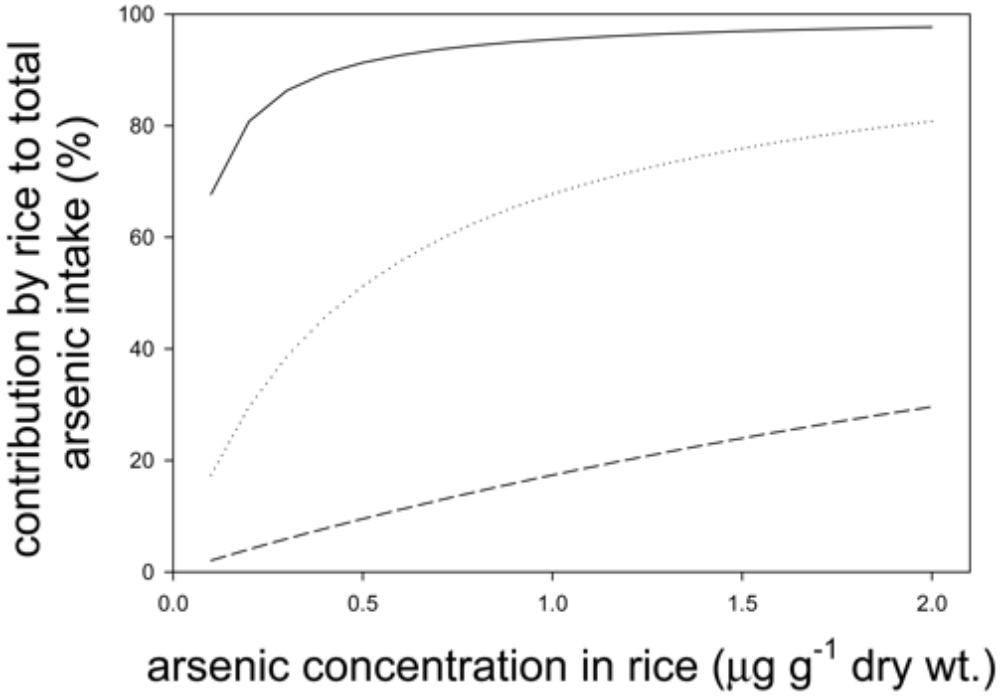

Figure 1.2: Graph showing the contribution of rice to As intake relative to drinking water. The lines represent a drinking water As concentration of $10\,\mu g\,L^{-1}$, $100\,\mu g\,L^{-1}$ and $1000\,\mu g\,L^{-1}$ for the solid, dotted, and dashed lines respectively. Reprinted with permission from *Arsenic Contamination of Bangladesh Paddy Field Soils:Implications for Rice Contribution to Arsenic Consumption*, Andrew A. Meharg, Md. Mazibur Rahman, Environmental Science & Technology. Copyright 2003 American Chemical Society.[19]

Furthermore, As contamination has been shown to decrease the nutritional value of the crop. If As concentrations in paddy fields are indeed increasing this suggests that the youngest generation will suffer not only the highest As exposure, but the most prolonged. This brings severe health concerns for the region.

1.1.3 Exposure reduction strategies

The situation is currently being addressed by the Bangladesh government's National Policy for Arsenic Mitigation, which encourages the discontinuation of contaminated wells and the

use of shallow wells. While using deeper wells is believed to provide water with lower As concentrations [7] this is not a focus of the document, due to the high cost associated with re-drilling wells to deeper depths. Decommissioning of contaminated pumps could be a viable option for private wells, where more expensive and deeper communal wells could be drilled to provide safer water within walking distance. However this approach is less viable for irrigation purposes where large volumes of water are required; and transporting it long distances could be very expensive. Alternative water sources or water treatment are other options that are likely to produce insufficient quantities of safe water or be prohibitively expensive for irrigation purposes.

Figure 1.3: Typical configuration of a shallow tubewell with powered pump used for irrigation of rice paddies in Bangladesh..

The actions being taken do not focus on the exposure of As through rice. In response to this, research has been carried out using a number of different techniques to understand the localisation and uptake of the As contamination in rice.

Williams *et al.* observed no difference in As concentration "between white (polished) and brown rice (unpolished) ($P > 0.05$)" [25]. However their sample size was small and only examined total As. Meharg *et al.*, using laser ablation ICP-MS (LA-ICP-MS), found that much of the As is concentrated in the bran. Removing the bran by milling or polishing the grain could be a practical method to reduce the total grain As concentration, however As is not exclusive to the bran and the bran also contains a number of nutritionally important trace elements, including Se and Zi [21]. Furthermore the concentration of these elements decreases with increasing As application rates [21] and studies have suggested that lower dietary Se intake can increase occurrence of arsenical skin lesions [31, 32, 33]. It should be noted that some studies found no statistical significance between As concentrations in polished and unpolished rice [34].

It has also been shown that growing rice aerobically decreases the As accumulation [35]. Growing rice in dry soils could therefore reduce grain As concentrations, but would nullify the important advantages, such as weed resistance, of growing rice under flooded conditions.

1.2 Arsenic uptake and transport in rice

Studies of As in rice began before the extent of the pollution in Bangladesh and its consequences were fully realised. The toxicity in rice of As from industrial pollution and the application of herbicides was enough justification to start studying As uptake in the early papers on this subject [36]. While the translocation of As into the grain was not the main focus of these studies, they examined the effects of As speciation in relation to its phytotoxicity. Building on the previous research into As as an industrial pollutant and in the

aquatic environment this highlighted the importance of the chemical form of the As and led to an increased interest into the study of As speciation in soils.

1.2.1 Arsenic speciation

Due to the observed importance in how As interacts with biological systems, its chemical speciation is a topic that has been approached from many different angles by many different groups in the field of plant and soil science. Here I will highlight some of the key pieces of research that are most relevant to the present study.

Speciation in soil and water

As early as 1969 it was recognised that As is present in soils almost exclusively in inorganic forms [37]. Thermodynamics based approaches revealed that the -3 and 0 oxidation states were unstable in most soils, therefore the +3 and +5 states were most common [38, 39]. More recent research has concluded that As in soil is "almost entirely" inorganic, except where organic As has been intentionally applied [40]. Studies on groundwater have also shown that As exists mostly in inorganic forms [41].

More specifically relevant to wetland grasses, a theoretical study conducted in 1983 estimated the chemical forms of As present in aqueous environments were most likely to be As(III) and As(V), with As(III) being dominant in reduced and acidic soils [39]. This was later experimentally confirmed for the case of flooded soils [42, 43] regardless of the medium applied [35]. This is contrary to the case of aerated soils where the trivalent arsenicals tend to become oxidised, therefore As(V) is the dominant species [44].

Speciation effects on uptake

The most prevalent chemical forms of As in the environment are dimethyl arsenic acid (DMAA), monomethyl arsenic acid (MMAA), arsenate (As(V)) and arsenite (As(III)). Using ICP atomic emission spectrometry (AES) Marin *et al.* [45] measured shoot and root concentrations of As in rice after applications of different chemical forms and concentrations of the element. They found that:

> "The amount of As taken up by the rice plants followed the trend: DMAA < As(V) < MMAA < As(III)."

suggesting that the inorganic form As(III) is more readily available to the plant. Analysis of the shoots revealed a similar trend, with the plant subjected to an As(III) nutrient solution presenting As concentrations in the shoot approximately twice as high as that after As(V) treatment. When comparing plants subject to different concentrations of As in solution, there was a significant increase in shoot As with increasing concentration, figure 1.4.

Having discovered that the chemical species was an important factor in uptake, the research group sought to investigate the effects of different redox-pH conditions on the uptake and speciation of As [43]. They found that, as predicted much earlier by Sadiq *et al.* [39], under reducing conditions As(III) was the dominant form found in the soil suspension, and resulted in significant translocation of As into the shoots with the majority remaining in the roots. These roots grown in reducing conditions also presented a "brownish precipitate", that when analysed was shown to contain iron (Fe) and As, suggesting the formation of an Fe plaque with adsorbed As. At the time they did not have the analytical

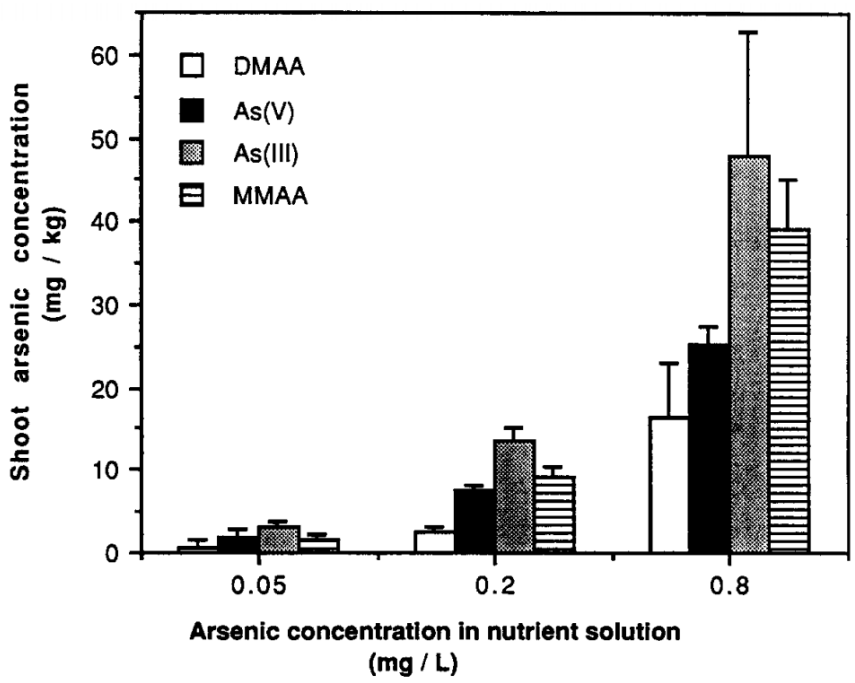

Figure 1.4: "Shoot arsenic concentration as affected by As concentration and chemical form." Reprinted by permission from Springer Nature: Plant and Soil (The influence of chemical form and concentration of arsenic on rice growth and tissue arsenic concentration, A R Marin *et al.*), Copyright 1992 [45]

techniques to determine the speciation of As in the plant.

Arsenite

Meharg and Jardine noticed that while As(III) was understood to be the dominant species in paddy fields, not much attention had been paid to studying As(III) influx in rice roots [46]. They conducted a series of experiments aimed at investigating possible As(III) transporters in rice roots, informed by previous research in yeast that showed As(III) transport was facilitated by a glycerol transporting channel [47]. These glycerol transporting channels are aquaporins known to be expressed in rice roots in high concentrations [48]. Careful to

first remove any As adsorbed onto the root surface they conducted hydride generation (HG) atomic absorption spectrometry (AAS) measurements on roots subjected to different As(III) and glycerol solution concentrations during growth. Hydride generation is commonly used in combination with AAS to detect metalloids in biological samples and increases sensitivity substantially [49].

The first notable result was that the uptake of As(III) followed saturation kinetics, meaning that with at low concentrations As influx varies linearly with As(III) in the nutrient solution. At higher concentrations the influx rate becomes independent of applied As(III), instead asymptotically approaching a maximum rate. The second observation was that As(III) uptake decreased with increasing glycerol additions in a dose dependant manner while As(V) uptake remained constant. These observations suggested that:

- As(III) transporters can become saturated
- As(III) and glycerol compete for uptake
- As(V) is influxed by a different transport mechanism to As(III)

These results indicate that transporters for As(III) are likely the same aquaporins responsible for glycerol influx and were similar to previous results by Guo *et al.* that had examined the uptake relationship between As and silicon (Si) in rice roots [50]. Guo *et al.* observed that Si limited As uptake in a dose dependant manner in a very similar fashion to glycerol, suggesting this pathway was also shared by Si uptake.

Arsenate

While we know As(III) to be the predominant species in flooded soils, As(V) is found in appreciable quantities in both the soils and the plants and therefore should not be overlooked as a possible contributor to As uptake. Increasing As(V) treatment is known to increase As concentrations in grain, decrease yield, shoot and root biomass, and plant height [20], which suggests that there exists a mechanism by which As can enter the plant and that the route through which it is metabolised results in As toxicity.

Meharg *et al.* showed that glycerol had no effect on As(V) transport, proving that As(III) and As(V) were transported into the plant via different mechanisms. Phosphorus (P) and As both have 5 electrons in their outer shells — in a $3s^2\ 3p^3$ configuration and a $4s^2\ 4p^3$ respectively. The number of electrons in the outer shell (valence electrons) determines likely oxidation states and typical reactions, therefore these two elements could form chemically very similar complexes in the nutrient solution and transporters may not be able to differentiate between them. Experimentally As(V) has long been known to take the place of inroganic phosphate (Pi) in biochemical processes [51], and early experiments had shown that As(V) uptake in barley was rate limited and strongly inhibited by Pi [52].

One of the most succinct summaries on the topic of As speciation can be found in a paper by Abedin, Feldmann and Meharg titled "Uptake kinetics of arsenic species in rice plants" [53]. They analysed a large number of papers on the topic as well as conducting their own experiments in order to better understand how uptake was affected by As speciation and determine why many of the previous results had come to contradictory conclusions.

Their work suggested that transport of both As(III) and As(V) was an active process, this would mean it requires selective binding sites and a supply of energy to drive the uptake. They observed that As(V) was "strongly suppressed" by Pi in hydroponic conditions, but that in soils "phosphate displaces the sorbed arsenate from exchange sites and therefore increases the solubility, phyto-availability, and movement down the soil profile of arsenate."

These results suggest that both the Si and the P uptake pathways, and local redox potential are all particularly relevant in the study of As, and that in order to have a better understanding of these pathways we should first try to gain a better understanding of the importance of these elements in plant nutrition, how they may be transported into the roots of rice plants under different conditions and how they are translocated from the roots to the rest of the plant.

1.2.2 Silicon uptake pathways

Evidence of competitive uptake suggests that Si could share an uptake pathway with As(III) [50] and Jones and Handreck have shown that lowland rice has unusually high Si concentrations (0.1-0.15 of the dry weight) compared to less than 0.01 for most dicotyledons (angiosperms whose seeds contain two embryonic leaves, such as legumes) [54]. Despite not being an essential nutrient silica has long been known to have beneficial effects to plant growth, particularly to monocotyledons (angiosperms whose seeds contain only one embryonic leaf, such as rice and other grasses) which contain up 10 to 20 times more silica than found in dicotyledons [55].

Additionally both Si and As exist as small molecules in flooded soils; Si exists as silicic

acid, a tetrahedron with Si at the center surrounded by four OH groups, while As forms arsenous acid, a pyramidal shape with As sounrded by three OH groups. The similar size and shape of these molecules could result in similar enough surface chemistry to allow them to pass through the same transporters. With this information in mind it is clearly very important to review Si transport and metabolism in rice in order to study it as a potential pathway for As uptake.

Silicon nutrition in plants

One of the earliest mentions of the effects of Si nutrition in plants was given by Clements [56] who noticed that addition of silicates to the soil improved plant growth, yield and P uptake in heavily weathered soils, speculating that these improvements were brought about by the presence of Si in the plant increasing the heavy metal resistance of the plants studied. Since then many similar observations have been made, showing Si to be a beneficial but 'non essential' plant nutrient capable of improving yield [57], disease resistance [58] and heavy metal tolerance [59]. The benefits have been documented specifically in rice [60] which is known to be a Si accumulator. These observations, although well tested, were made rather sporadically, garnered little attention, and did not examine the mechanisms by which the Si was transported, localised or affected the plant biochemistry.

Before Si was known to be a beneficial plant nutrient, studies had already been carried out investigating the solubility of silica in water. Notably, Alexander *et al.* proposed that amorphous silica in solution existed in the monomeric phase, $Si(OH)_4$, in equilibrium with the solid phase. Their research showing that the solubility was fairly consistent between

pH 5-8, the range within which we would expect in most soil conditions. Corroborating evidence from other research groups can be found in a review paper by Krauskopf [61] who gave a solubility figure of 100 ppm to 120 ppm for amorphous silica and 6 ppm to 14 ppm for quartz at 25 °C, with little variation in solubility below pH 9.

Silicon uptake

It could be assumed, due to the chemical form of Si in water, that the transport of Si might be passive, meaning the plant does not need to expend energy to accomplish the movement. Indeed early studies in the first half of the 20th century found that Si uptake was aided by transpiration [62]. In 1965 Jones and Handreck studied this phenomenon using oats as a model for "dryland" Poaceae (family of monocotyledonous flowering plants known as grasses, referred to in the text as Gramineae), again finding a strong correlation between Si uptake, transpiration rates, and what would be expected from non-selective transpiration mediated Si uptake [63]. These results adding weight to arguments that suggest Si uptake is taking place by passive transport.

While this evidence is corroborative in the case of dryland Poaceae, other plant species displayed contrasting Si uptake characteristics. The most convincing study was conducted by Grosse-Brauckmann [64], who grew poaceous and fabaceous species on the same soil in order to avoid complications of environmental factors. They found poaceous species contained approximately one order of magnitude more SiO_2 than the fabaceous species. Wetland, or lowland, rice (rice grown in flooded conditions) typically contained a further five times as much SiO_2 than the "dryland" grasses [65, 66]. These results suggest that it

may be possible to classify plants into three groups according to their Si uptake.

Indeed, further investigations made by Raven in 1983 noted that water and Si were taken up in a ratio equal to that present in the soil in the case of dryland grasses, in a lower ratio in the case of dicotyledons, but in a higher ratio in the case of wetland grasses [67]. The recognition of different Si uptake rates, even for plants grown in the same soil, strongly suggests that Si uptake is not always passive as discussed above but there exists a mechanism by which a plant is able to regulate the influx of Si.

A study of root hairs and lateral roots by Ma *et al.* showed that lateral roots contributed to Si uptake in rice, whereas root hairs did not [68]. Combining this information we can summarise our understanding on the topic as follows[68]:

- Rice takes up Si in higher concentrations than the solution [69]
- Si uptake is independent of transpiration
- Si uptake is suppressed by respiratory inhibitors while transpiration remains unaffected
- Rice takes up Si faster than other nutrients
- Si distribution is effected by transpiration
- Si concentration is much higher in roots than shoots
- There is no significant change to Si transport by absence of root hairs
- Si transport is significantly reduced by the absence of lateral roots

These observations imply that rice is a Si accumulator, that the Si is actively transported in a metabolic process into the roots then transported in the xylem, and that the transporters are located on roots and lateral roots but not root hairs.

Genetic identification

Because of its nutritional importance and small genome size, the International Rice Genome Sequencing Project (IRGSP) began in 1997 working towards sequencing the rice genome, making it the first monocot considered for genetic sequencing. With most of the sequence complete in 2002, the full sequence was released in 2005.

While a Si transporter had been identified in a marine diatom (*Cylindrotheca fusiformis*) for some time [70], there was no known Si transporter gene in rice even as late as 2001. At which point Ma *et al.* were able to find a rice mutant (GR1) defective in Si uptake by screening M_2 seeds of rice cv Oochikara [71]. They used germanium (Ge) resistance as a selection parameter because Ge is toxic to plants and plant roots cannot discriminate between Si and Ge, and found a mutant that was particularly resistant to Ge. Measured Si concentrations in xylem sap of this mutant were 3 times higher than in the external solution, compared to 33 times for a wild-type that was subject to methods designed to inhibit uptake. From this information it is quite reasonable to assume that this genetic mutation was responsible for disrupting active transporters of Si.

The mutant GR1 became known as 'low silicon rice 1,' *lsi1*, and presented much lower Si concentration at the top of the plant while root concentrations remained similar to the wild type. The mutant also showed significantly lower uptake in a short-term experiment

and the uptake was unaffected by metabolic inhibitors or temperature.

A detailed genetic investigation of *lsi1* revealed the form and location of the transporter, Lsi1 [72], that is encoded by the gene *Lsi1*. Green fluorescent protein (GFP) markers fused to the *Lsi1* gene showed that the transporters were located on plasma membranes on the distal side of both the exodermis and endodermis. An homologue, Lsi6, was also discovered in rice during this investigation.

This was quickly followed by the discovery of the gene 'low silicon rice 2' (*Lsi2*). This gene encodes an efflux transporter of Si which resides on the proximal side of the same exodermis and endodermis cells as the Lsi1 transporter. Fluorescence imaging of Lsi1 and Lsi2 in the exodermis is shown in figure 1.5.

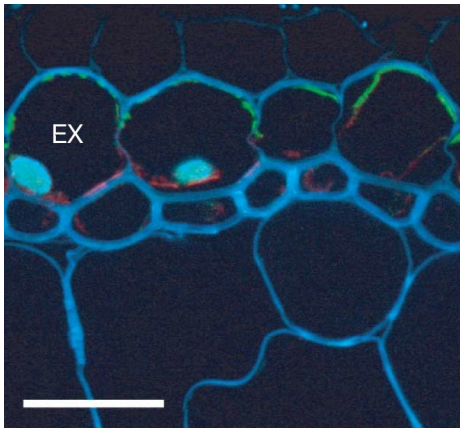

Figure 1.5: "Merged image of Lsi1 (green), Lsi2 (red) immunolocalization, nuclei stained by DAPI (cyan) and cell wall autofluorescence (blue). Scale bars, 20 µm." Reprinted by permission from Springer Nature: Nature (An efflux transporter of silicon in rice, Jian Feng Ma *et al.*), Copyright 2007 [73]

A further Si transporter in rice, Lsi3, was identified by Yamaji, Mitani and Ma in 2010. They noted it showed "efflux transport activity" similar to Lsi2, and that it was "localized at the pericycle cells of the roots." They proposed that Lsi3 could be involved "in the xylem

loading of Si" in roots and the "re-loading of Si to the diffuse vascular bundles" in the upper nodes.

1.2.3 The arsenic silicon relationship

The mechanism for As(III) transport in rice was first documented by Meharg *et al.* [19], they showed that aquaporins responsible for glycerol transport were also responsible for the transport of As(III) into the cells. In 2008 Ma *et al.* published one of the most important papers on the topic of As uptake in rice [74]. It had already been shown that the previously identified aquaporin, OsNIP2;1, a nodulin 26-like intrinsic membrane protein (NIP) [75], was the transporter "Low silicon rice 1" (Lsi1) and that suppression of the *Lsi1* gene resulted in significantly reduced Si uptake, as discussed in Section 1.2.2. Ma *et al.* recognised that arsenous acid, $As(OH)_3$, and silicic acid, H_4SiO_4, were both uncharged at pH < 8 and were both of similar physical size. Using this information they hypothesised that Lsi1 was responsible for the transport of As(III). Indeed, expressing *Lsi1* in *Xenopus* oocytes and yeast resulted in a three to five fold increase in the transport activity of As(III).

They used the genetic information on the Lsi1 influx transporter and Lsi2 efflux transporter to breed rice mutants and compare their As uptake rates with wild types. The results showed the *lsi1* mutant, defective in the Si uptake gene, exhibited a 57% lower As uptake compared to the wild type. Similarly *lsi2* had a shoot As concentration 75% lower than the wild-type.

1.2.4 Phosphate uptake pathways

As(V) had already been shown to share uptake mechanisms with Pi in a variety of bacteria and plants including the grass *Holcus lanatus* (L.) [76]. Some results have shown Pi competes more effectively than As(V) for transport sites [77] and that As(V) uptake can be inhibited by Pi [78]. Conversely Abedin *et al.* found no difference in As concentration in rice plants grown in soil when subjected to controlled Pi applications [53, 20], and Meharg *et al.* found very little difference in As uptake on the grass *Deschampsia cespitosa* grown under different Pi conditions. Abedin *et al.* speculated that the variations in results were likely to be caused by the medium in which the plants were grown, as some experiments were conducted in soil, while others were controlled hydroponically in nutrient solutions.

These contradictory results suggest that trying to investigate the relationship between Pi and As(V) transport is more complex than the seemingly analogous case of silicic acid and As(III). Variables such as changes in growth medium and redox potential can be minimised by using carefully controlled hydroponic growth of *Oryza sativa* (L.) in different concentrations of As(III), As(V) and Pi. Using this method Tsutsumi revealed no change in As toxicity for As(III) solutions mediated by Pi, but observed reduced toxicity for As(V) solutions [78].

Abedin *et al.* grew rice treated with Pi and As(V) under flooded conditions. In order to determine the speciation of As in the straw they conducted high performance liquid chromatography (HPLC)-ICP-MS. Despite As(III) treatments showing the greatest As uptake, their experiments revealed that “the predominant species present in straw was arsenate

followed by arsenite and dimethylarsinic acid (DMAA)" [79], suggesting that the chemical form could be changed in the plant either during uptake or as part of a detoxification process.

Wu *et al.* [80] demonstrated that the Pi transporter OsPht1;8 (OsPT8) had a high affinity for both Pi and As(V). And that "its overexpression increased the maximum influx by 3- to 5-fold." They observed that the proportion of As(V) in the xylem sap increased over time in flooded conditions.

Publishing that same year, Jia *et al.* [81] also produced plants overexpressing *OsPT8* and observed "excessive Pi in both roots and shoots and Pi toxic symptoms under the high-Pi supply condition." They also used flourescent protein markers to reveal *OsPT8* expression in "various tissue organs from roots to seeds independent of Pi supply."

In their investigations of Kasalath Nipponbare varieties of rice, Wang *et al.* [82] noted that "Mutation in *OsPT8* in both backgrounds decreased As(V) uptake by 33-57%." They also observed a large increase in As(V) tolerance in *ospt8* as assessed by root elongation.

A review of Pi transporters in rice was given by Młodzińska and Zboińska in 2016. They noted that in total researchers had found that "transcripts of all 13 *OsPHT1* were detected" in rice roots, and that at least six (OsPHT1;1/2/4/6/8/9/10) are "principally involved" as evidenced by "reduced Pi uptake in knockout or knockdown (RNAi) lines and enhanced uptake in overexpressing lines." They also noted that several researches had found "overexpression or mutation of one of the PHT1s may alter the expression of the others" therefore making it "very difficult to ascertain which of these transporters are crucial for Pi uptake and distribution."

Rhizosphere chemistry

Rice roots are known to oxidise the volume near the roots (the rhizosphere) which in iron rich soils can cause the formation of an iron plaque on the outside of the roots [83]. The rhizosphere chemistry is complex [84] and rice grown in low Pi nutrient solution has been shown to cause the plant to increase oxidation of the rhizosphere [85] resulting in increased iron plaque formation [53]. Liu *et al.* suggested that this was "an adaptive metabolic reaction to the condition of P deficiency" [86]. These complexities imply that it would be challenging to avoid complications when devising experiments to investigate competitive uptake between As(V) and Pi in rice. These complications include changes in redox conditions that can be caused by microbes, oxidation of the rhizosphere and redox reactions; and changes in the concentration of soluble As(V) and Pi as a result of formation of iron plaques and competition for sorption sites on soil particles.

Liu *et al.* took measurements of As concentrations on iron plaques grown on rice seedling roots in solutions either containing or lacking P. The low P treatment formed a thick iron plaque with As mainly sequestered on the surface of the roots. Conversely the high P treatment resulted in translocation of As into the plant and thus a higher concentration of As was measured in the roots [86]. These observations have been confirmed by others [87, 88, 89]

The iron hydroxides present in these plaques are known to have a very strong binding affinity to As(V) [90, 91]. Additionally the interactions of As(V) and Pi with adsorption sites on soil particles also contribute to the complexity of the system as they compete for

sorption sites [92]. Addition of Pi fertilisers can displace As(V) from sorption sites and is therefore able to increase the solubility and phyto-availability of arsenate and increase its movement down the soil profile [53, 93, 94].

These observations demonstrate that not only changes in redox-pH of the soil but also concentrations of certain nutrients can affect the uptake of As.

1.3 Arsenic detoxification mechanisms

Phytochelatins (PCs) are important in the detoxification of heavy metals in plants. They are olgiers of glutathione (GSH), a thiol containing tripeptide composed of glutamate cysteine and glycine. PCs are produced in response to the presence of heavy metals and act as chelators and are synthesised from GSH by the enzyme 'phytochelatin synthase.' In *Arabidopsis thaliana* plants the PC synthase gene *CAD1* has been identified and PC synthase deficient mutant, *cad1*, exhibits increased sensitivity to Cadmium (Cd) [95]. A decrease in glutathione was measured by Scheller *et al.* [96] in plants exposed to heavy metals, demonstrating that glutathione is likely a substrate for PC synthesis.

As is known to rapidly induce biosynthesis of phytochelatins in *Arabidopsis*. Contrary to HPLC-ICP-MS data suggesting that As was not complexed by PCs [97], Schmöger *et al.* found strong evidence to suggest that As-PC complexes did exist, including increased As sensitivity in *cad1* mutants [98]. Schmöger *et al.* found the same results as Maitani *et al.* [97] when using the same weakly alkaline buffer solution, but found that in weakly acidic solutions there was co-elution of As and PC in gel filtration experiments, demonstrating that As-PC complexes existed but were unstable in alkali solutions.

Scott *et al.* characterised GSH using ^{1}H and ^{13}C nuclear magnetic resonance (NMR). This technique provided information on the structure of GSH and the interaction between GSH and As. Their data showed "shifts in the carbon atom bonded to the sulfhydryl group", indicating binding of S to As. They also observed that As(V) solutions were reduced before complexation, in agreement with the observations made by Abedin *et al.* on rice straw [20]. This complexation of As in the roots may be the mechanism preventing root to shoot translocation of As. This can be seen when As(V) reductase synthesis in *Arabidopsis* is suppressed, resulting in an increase of the shoot to root ratio of As [99].

Sulphur (S) containing thiol compounds were experimentally confirmed by Dixit *et al.* [100] to be an important part of the detoxification process in *Oryza sativa.* They found that in high S conditions most As "was found to restricted [*sic*] in root and lesser amount [*sic*] of As was translocated in to shoot" and that this may have been due to compartmentalisation.

A transporter responsible for detoxifying and reducing the amount of As in the grain, OsABCC1, was identified by Song *et al.* [101]. ATP-binding cassette (ABC) transporters are a family of transporters that use energy supplied by adenosine triphosphate (ATP) to move solutes across a plasma membrane. The C-subfamily (ABCC) are typically involved in ion transport and toxin secretion. Song *et al.* determined that OsABCC1 sequestered As in "the vacuoles of the phloem companion cells of diffuse vascular bundles directly connected to the grain." And observed *OsABCC1* expression was "consistently up-regulated by As in roots as well as in other organs." Their research observed *OsABCC1* expression in the "exodermis and phloem region of the roots, basal nodes, and leaf blades at the vegetative

growth stage" and that knockout of *OsABCC1* results in increased sensitivity to As and increased grain As.

1.4 Arsenic uptake pathways

To summarise, inorganic As can exist as As(III) or As(V) depending on the composition and redox potential of the growth medium. In rice As(III) competes with silicic acid for uptake via aquaporin proteins. The location and genes of some of these transporters have been described and mutation of these genes results in markedly decreased As(III) influx. Lsi1 transports As(III) into the root cells, while Lsi2 mediates efflux of As(III) towards the xylem, as shown in figure 1.6. Lsi3 is understood to be another Si efflux transporter and is expressed in parenchyma of roots and diffuse vascular bundles (DVBs) [102].

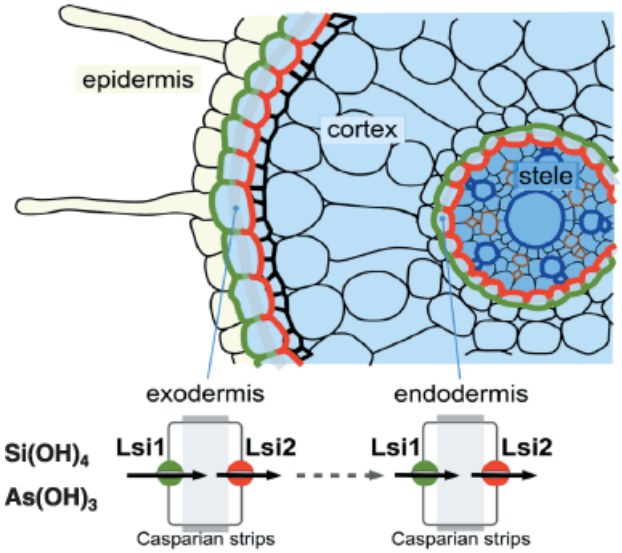

Figure 1.6: The location of the Lsi1 and Lsi2 transporters in rice roots. Modified from Ma *et al.* [73] by Zhao *et al.* [103]. Reprinted with permission John Wiley and Sons, Copyright 2009.

As(V) competes with Pi uptake via several OsPHT1 transporters. Addition of Si or

Pi to growth medium at low concentrations can desorb As from sorption sites on the soil and therefore increase bioavailability and uptake. Summaries on soil chemistry of As and strategies to reduce As uptake in rice are provided by Kumarathilaka *et al.* [104, 105].

The formation of an iron plaque decreases the short term As(V) uptake, but increases As(III) uptake. As(V) taken into the root is reduced to As(III) in the cells and effluxed by Lsi2. Genes responsible for the production of As(V) reducing enzymes have been identified in the rice genome [106]. A summary of some of the different pathways of As uptake into the root and other chemical reactions taking place near the root are illustrated in figure 1.7.

Complexation of As by PCs is considered an important step in As detoxification, with mutants lacking PC synthase are 10-20 times more sensitive to As [95]. It is speculated that As is transported into vacuoles where it can be more easily stored, and that ABC type transporters such as Heavy Metal Tolerance 1 (HMT1) can transport As-PC complexes [107].

1.5 Review of techniques

This section examines some of the different techniques that have been previously employed in this field and their strengths and weaknesses.

1.5.1 Electron microscopy

It is possible to examine biological samples using both transmission electron microscopy (TEM) and scanning electron microscopy (SEM), provided a suitable sample preparation method is used. A detailed resource on sample preparation techniques for TEM is given by

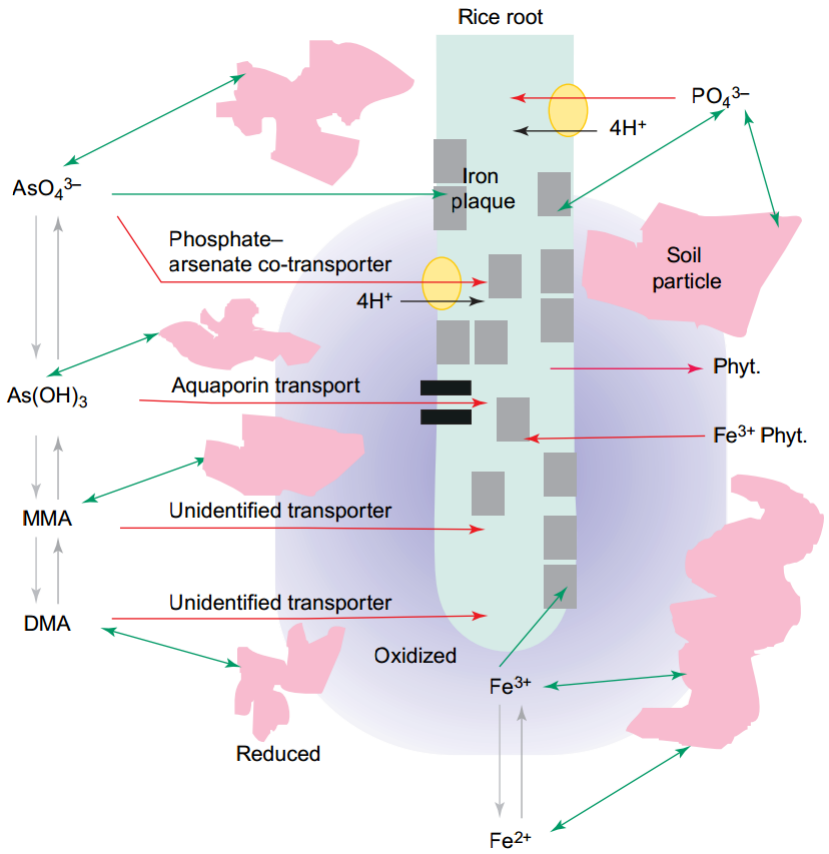

Figure 1.7: Schematic of the rice root rhizosphere illustrating the possible transport mechanisms believed to be available for As(III), As(V), Pi, and glycerol. The pink shapes represent soil particles. Green arrows represent sorption and desroption from the soil particles, grey arrows represent equilibria between different species, and the red arrows represent transport into the root. Reprinted from Trends in Plant Science, Vol 9, Andrew A Meharg, Arsenic in rice understanding a new disaster for South-East Asia, Pages 415-417, Copyright 2004, with permission from Elsevier [84].

Glauert and Lewis [108]. The main difficulties arise from the non-conducting and radiation sensitive nature of the samples, resulting in beam damage [109, 110]

Transmission electron microscopy

TEM is a popular technique in the field of materials science due to the extremely high lateral resolutions possible. A beam of electrons is focussed onto the sample, passing through the

sample and interacting with it before being focussed to form an image. This requires the sample to be very thin (less than 100 nm thick) and combined with a highly focussed electron beam this means significant energy can be imparted on a small volume of sample by the electron beam during analysis. In the case of biological samples the damage thresholds and thermal conductivities are lower than for metallic samples, consequently it is much easier to damage the sample with the electron beam.

Despite these difficulties it is possible to obtain high resolution TEM images from biological samples provided suitable sample preparation and operating conditions. Contrast is given by differences in electron density within the sample. Heavy metal compounds such as osmium tetroxide can react with biological membranes, both fixing and staining them by bonding to unsaturated carbon-carbon bonds and consequently increasing the electron density in those areas [111].

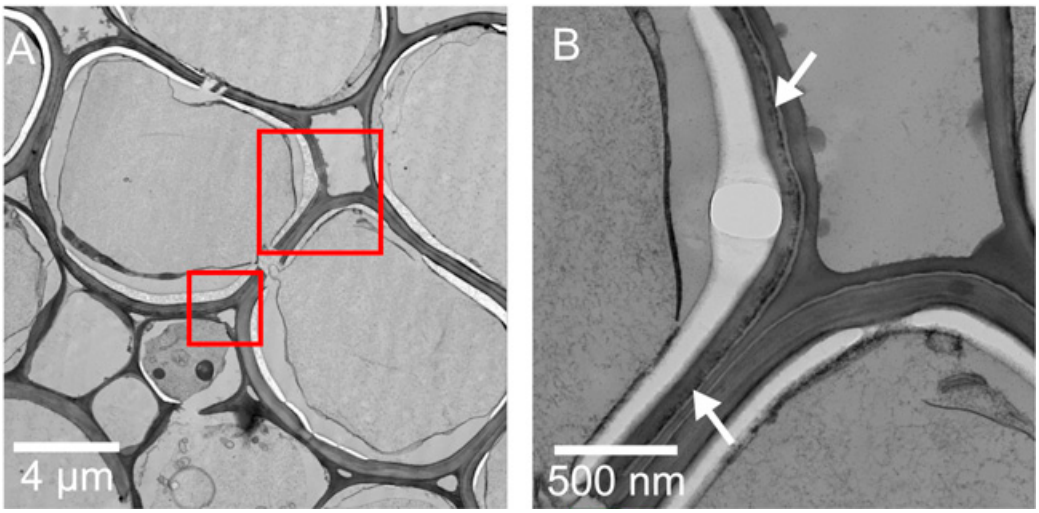

Figure 1.8: TEM images of rice roots, red squares indicate areas used for higher magnification TEM images (only one shown). Images reproduced from Moore *et al.* [112] Copyright 2011, Oxford University Press.

Biological TEM has been used previously in this specific area of interest by Moore *et al.* [112] (fig. 1.8) in combination with secondary ion mass spectrometry (SIMS) in order to image cell walls in rice roots that had been exposed to As. By imaging the same roots using both techniques they demonstrated that TEM can be used to provide much higher spatial resolution images of the roots than possible in SIMS alone. This can better resolve cellular and subcellular structure in the same regions where changes in concentration were observed by SIMS.

Scanning electron microscopy

Analysis using SEM is subject to slightly less constrictive specimen requirements than the TEM. It is possible to analyse much larger samples. In an Environmental-SEM (E-SEM) it is even possible to analyse non-conductive samples and samples with significant vapour pressures at the surface; two properties often associated with biological samples. A recent and in depth comparison of SEM and E-SEM is given by Kirk, Skepper and Donald [113].

SEMs are commonly fitted with additional detectors beside the secondary electron detector, such as backscattered electron (BSE) and energy dispersive or wavelength dispersive X-ray detectors (EDX and WDX[1] respectively). Contrast in backscattered electon signal is given by changes in average atomic mass, similar to TEM images. Using a high resolution SEM with a low current field emission gun (FEG) it is possible to obtain BSE images in an SEM of similar quality to previously demonstrated TEM images [114]. This approach has the practical advantages of simpler sample preparation and the possibility of analysing the same sample in both the SEM *and* a secondary ion mass spectrometer.

[1]WDX is sometimes also referred to as WDXRF or WDS

EDX can map chemical composition based on characteristic X-rays, and analysis on biological samples has been carried out on an As hyperaccumulator *Pteris vittata* by Lombi *et al.* [115]. The large mean free path of electrons in biological samples, along with difficulties in detecting low atomic number elements, the high accelerating voltages required to detect heavier elements and the resulting risk of beam damage during analyses make this technique largely unsuitable for high mass and spatial resolution element mapping. EDX also does not have a high enough sensitivity to accurately detect elements present in very low concentrations, typically the detection limit is approximately 0.5%.

1.5.2 ICP-MS for biological specimens

ICP-MS involves a chemical process, digesting the plant matter in a series of solutions then injecting the liquid into a plasma through a nebuliser. Ions produced in the plasma are passed into a mass spectrometer to measure their mass to charge ratio, allowing the detection of elements in concentrations as low as one part per trillion [116] and masses as small as a few femtograms [117]. It only provides an average ion count for the bulk volume being analysed and does not produce spatially resolved information.

ICP-MS can be used in conjunction with high performance liquid chromatography (HPLC), this combination of techniques allows different species of metal contaminants to be separated for analysis. This is very important in plant and soil science as the speciation of an element effects its mobility and bioavailability [118]. The technique requires a chemical extraction process followed by analysis of the solution, therefore the accuracy

of this technique to determine the oxidation state of metals present in plants and soils is considered to be low, due to both preferential extraction of different species [119] and the instability of species in the extractant [120, 20]. Despite these inherent problems, the technique is considered to be a useful analytical tool. In order to overcome the shortcomings and allow for comparable data collection from different research groups there was a drive for standardisation [121]. This has led to the publishing of standard procedures for analysis of speciation of different plant and soil contaminants [122], allowing the collected data to be compared qualitatively across different research groups, facilitated by a large amount of literature on the technique [123].

Specific regions of a bulk solid sample can be analysed by using laser ablation (LA)-ICP-MS to remove matter from the surface of the sample before passing through the plasma. The pulsed laser can liberate matter from the sample surface over an area of tens to hundreds of microns [124, 125], thus allowing some primitive mapping of the sample and much simpler sample preparation, eliminating concerns over incomplete extraction that have been used as criticisms of the solution based techniques.

1.5.3 Atomic absorption spectroscopy

Atomic absorption spectroscopy is a simple and economical way of measuring trace metal concentrations in biological samples down to the nanogram per litre level [126]. The process requires the atomisation of the species of interest followed by optical radiation absorption spectroscopy. Because the chemical process involved in atomising the sample is a bulk chemical process it is not possible to gather spatially resolved information.

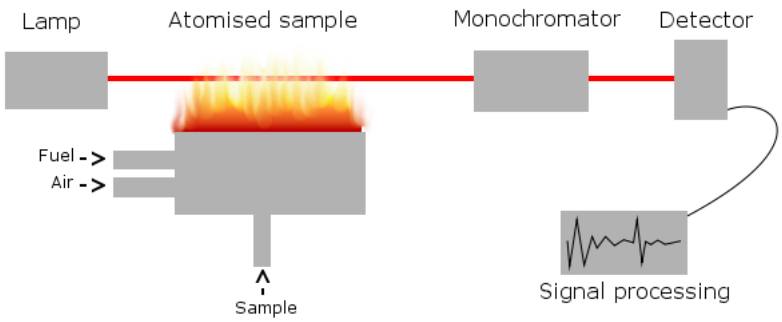

Figure 1.9: Schematic showing the basic operation of an atomic absorption spectrometer with a flame atomiser

A popular variation used in plant sciences is 'hydride generation atomic absorption spectroscopy' (HGAAS) as it allows for the atomisation of heavy metals that can be found in plants and increases the detection limits over other methods. The process involves digesting the samples to produce a solution in a fashion similar to that required for ICP-MS. Through chemical treatment the metalloids in solution form hydrides and are then reduced to their elemental form before measurement. Although it is considered more difficult to conduct speciation measurements in HGAAS compared to ICP-MS [127], a methodology for simple speciation measurements of As in groundwater has been devised [128]. Maity *et al.* tested a simple process using citric acid for selective hydride formation of As(III) against known concentration synthetic mixtures of As(III) and As(V). They found their results to be in good agreement with the true concentrations of the synthetic mixtures but did not evaluate the effectiveness of this technique for reference solutions or against other techniques.

1.5.4 X-ray based techniques

The increasing availability of synchrotron X-ray beamlines due to the construction of new facilities (more than ten worldwide in the last decade) and advances in X-ray optics and techniques has led to a growing interest in the use of synchrotron radiation (SR) as a tool in plant and soil sciences. X-ray based techniques are an area of great interest, with continuing advances in both detector technology and data analysis increasing the speed and accuracy of sample analysis [129]. The high brightness, semicoherence and polarisation of synchrotron radiation in conjunction with modern X-ray optics can generate an X-ray beam with both small lateral and energy resolutions. Devices capable of focusing X-rays below 30 nm probe size have been measured with hard X-rays [130, 131]. The greatest advantage of SR is that the versatility of the powerful X-ray beam allows for a large variety of different experimental techniques, each able to probe matter more efficiently than comparable laboratory hardware, and often many of these different techniques can be employed on the same beamline simultaneously.

Sample preparation

A very practical advantage of SR analysis is that there are very few restrictions on the physical form of the sample. Samples can be large and because there is no need for a vacuum, can be hydrated and studied in air or liquids, allowing very simple sample preparations and even *in vivo* studies. The ability to study hydrated samples leads to the possibility of conducting *in situ* studies [132, 133, 129] which greatly simplifies the sample preparation process and allows for easier interpretation and greater flexibility in experimental condi-

tions including the possibility to conduct dynamic experiments. This has already been demonstrated in the study of trace metal distributions in hydrated roots of cowpea [134].

X-ray analysis for biological specimens

Some advantages of SR in the study of biological specimens are evident in a study carried out by Betz *et al.* [135], where millimetre sized specimens of "negligible absorption" were the focus of investigation. The paper includes a brief and informative introduction to SR, and compares X-ray computed microtomography (SR-μ-CT) with conventional techniques. The nature of the radiation produced in a synchrotron meets the requirements for phase contrast tomography, which, because of the low X-ray absorption of biological specimens, they deemed more appropriate than absorption tomography where the signal to noise ratio would be low. Using this technique they were able to produce 3D reconstructions of the sample with sub-micrometer resolution, avoiding the time consuming alternative of microtoming thin sections followed by individually imaging each section. Contrast is possible even where the X-ray signals from different elements are very similar [136].

However Lombi *et al.* stated that "although very powerful in terms of resolution and sensitivity, the synchrotron techniques based on hard X-rays cannot be used to map the distribution of lighter elements such as Si, S and P which may influence the distribution and speciation of As and micronutrients." [119]

Computed tomography

While SR-µ-CT is a useful technique for imaging 3D structures [133], the X-ray doses required to produce high resolution 3D maps are known to damage biological samples. Chemical information can be collected by varying the energy of the X-rays striking the sample and measuring the relative absorption in a process known as X-ray absorption spectroscopy (XAS). Alternatively secondary X-rays can be measured when the sample is bombarded by higher energy X-rays, a process that has demonstrated successfully the ability to map metalloid distributions in 3D and in virtual cross sections [132]. Improvements in XAS are ongoing; some advancements in the theory, interpretation of the spectra and energy resolution can be found in a detailed paper by Wende [137].

Other synchrotron techniques

Synchrotron X-ray fluorescence (S-XRF) can generate element maps through thick sections of sample, requiring only some basic sample preparation. The more advanced technique of micro X-ray absorption near edge structure (µ-XANES) uses an X-ray beam less than 1 µm in diameter to generate spectra that can be used to deduce the *in situ* oxidation state of the element of interest [138]. Both of these techniques are valuable assets in the present study as they can provide element maps over relatively large areas.

1.5.5 Secondary ion mass spectrometry

SIMS is a mass spectrometry technique that analyses the secondary ions produced when a finely focussed beam of primary ions hits a sample surface. The primary ion beam is capable

of exciting secondary ions from very small areas of known position within a sample. This spatial information allows regions of the sample to be rastered to build up maps with high spatial resolution showing relative intensities of specific ions. When combined with a high mass resolution mass spectrometer and sensitive detectors this can also allow ppm or ppb detection of certain ions. Typical primary ions are generated from gallium (Ga), bismuth (Bi), caesium (Cs) or oxygen (O). The downside of this technique is the requirement for very stringent sample preparation. The CAMECA NanoSIMS 50 instrument was chosen for this study because it has sufficiently high secondary ion transmission and detection to generate elemental maps even for the trace elements present in the samples to be analysed, and has high enough spatial resolution to map the location of these elements at a cellular or subcellular level, as previously demonstrated by Moore *et al.* [112].

1.6 NanoSIMS

The basic operating principle of the CAMECA NanoSIMS involves rastering the sample surface with a 16keV Cs^+ primary ion beam. The beam can be focused down to a probe size less than one micron in size and with a current in the nano-amp range. Secondary ions produced in the resulting ion-matter interaction are then passed through a doubly focussing electro-magnetic sector mass spectrometer allowing mass detection with very high sensitivity and high mass resolution. A discussion of the use of SIMS with other complementary techniques in the analysis of trace metal detection in plants is given by Moore *et al.* [139]. A more detailed review of techniques used for studying metals and metalloids in biological specimens is given by Lombi *et al.* [140]. I have chosen NanoSIMS to

be the main instrument with which to conduct this research, therefore this section contains a more detailed introduction to the technique and the complex sample preparations required.

Discovery of secondary ion formation

SIMS has its roots in the 1930s where experiments carried out by Arnot *et al.* [141] and Sloane *et al.* [142] to study ionisation of mercury proved that it was possible to generate secondary ions from primary ion impact, and that they could be mass filtered in a magnetic sector analyser. By varying the magnetic field or accelerating voltage applied to the secondary ions they were able to generate mass spectra for these secondary ions. In these early experiments a few things became immediately clear:

1) Both research groups observed peaks in the spectra for light ions "in spite of precautions taken" [142].

2) Variations in the vacuum pressure or gas environment resulted in significant changes in secondary ion yield.

3) The secondary ions left the surface with a range of excess energies, resulting in poor mass resolution when passed through the magnetic sector.

These observations highlighted key practical difficulties with SIMS based techniques. The first observation revealed that gas atoms, molecules and light organics rapidly adsorb onto the surface of any sample and will correspond to the first elements sputtered from the surface when bombardment starts. The second observation involves a complex process that is related to how ion matter interactions vary with changes in surface chemistry; a combination of factors known as "matrix effects." The third observation simply highlights

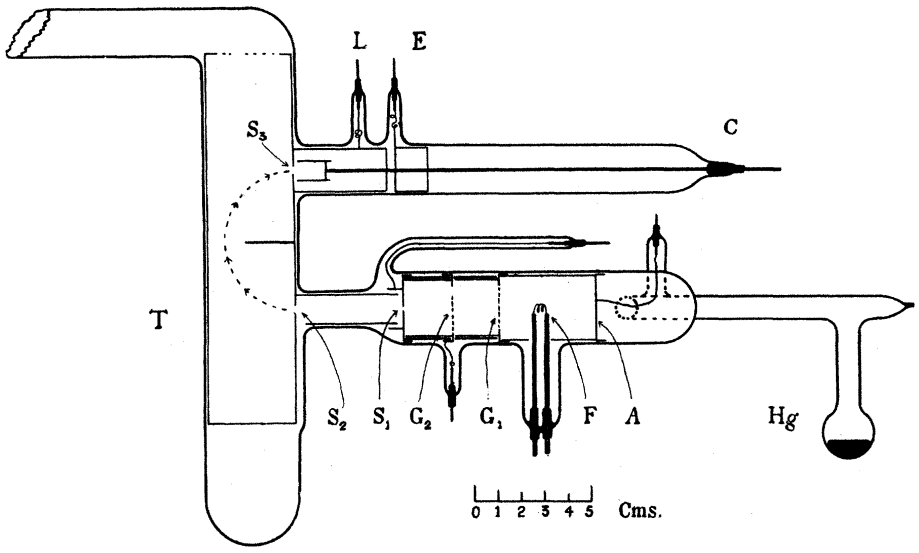

Figure 1.10: Blown pyrex tube used for generating negative ions, reproduced from Sloane *et al.* A, anode; F, filament; G, gauze; S, slit; T, magnetic deflection chamber; C, detecting cylinder. [142]

the requirement for well designed ion optics. In the case of the NanoSIMS high transmission is achieved by using the same lenses for focussing the primary and secondary ions, and high mass resolution by using a double-focussing mass spectrometer.

Ion matter interactions

After these observations made in the late 1930s a lot of interest was devoted to understanding the ion matter interactions taking place at the sample surface.

Ions impacting on the surface are known to interact with the target in a "diffusion-collision process" [143] because the velocities of the atoms are low enough that only elastic collisions need to be considered [144] and therefore neutron cooling theory can be applied [145]. A good justification on the application of this theory to the phenomenon of ion sputtering is given by Keywell *et al.* [146].

Davies *et al.* devised a series of experiments designed to measure the implantation depth profile of Cs^+ ions accelerated at an aluminium (Al) target [147]. They implanted radiocaesium (^{137}Cs) into Al foils, then measured radioactivity. By anodizing then dissolving the oxide coating of the Al foil they were able to accurately remove very uniform thin layers from the foil. Repeating the radioactivity measurement after each successive layer was removed allowed them to calculate the relative amount of ^{137}Cs in each layer. The results were double checked by comparing the radioactivity remaining in the foil to the activity of the anodizing solution. They showed good agreement and generated accurate implanted ion vs depth graphs for different conditions, data shown in figure 1.11.

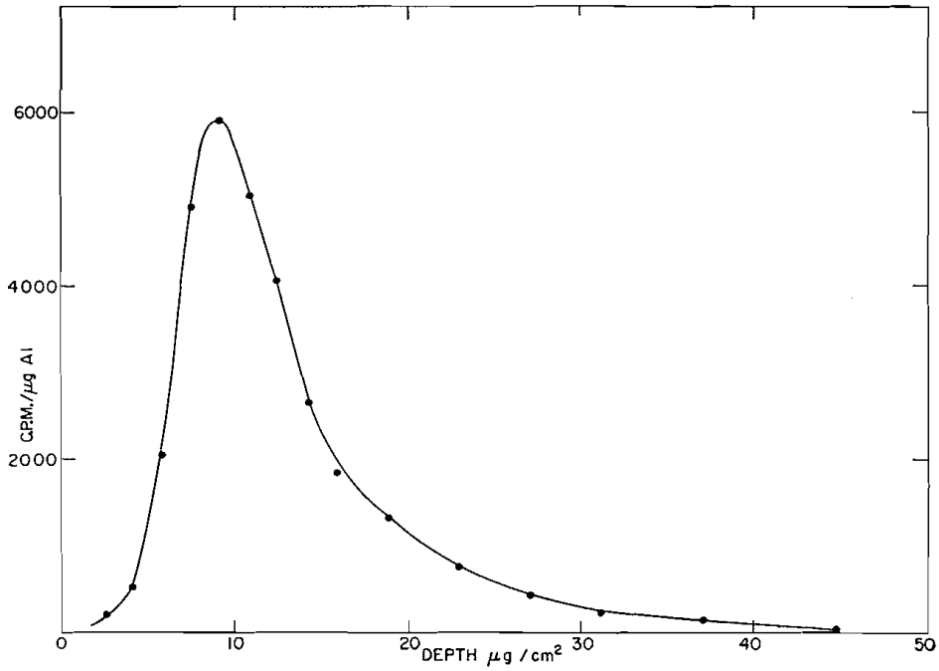

Figure 1.11: "Depth of penetration of 50 keV $^{137}Cs^-$ ions in aluminium." Image and data from Davies *et al.* [147]

The asymmetry of the ion implant depth and the exponential decrease of the Cs into the

sample beyond the modal value was demonstrated by this data. Davies *et al.* also did a two stage bombardment with ^{137}Cs followed by ^{133}Cs, and found no decrease in radioactivity after second bombardment. This suggests that the current density was too low to cause significant sputtering of the surface atoms, therefore the data gives an accurate glimpse of the the ion distribution after initial bombardment.

Almen and Bruce also used radioactive isotopes in order to determine the types of interactions taking place under ion bombardment. Writing a detailed paper on the topic [148], they found that by accelerating radioactive noble gases at targets at much higher doses than Davies *et al.* the radioactivity of the target would increase up to some saturation value. Using microbalance and a Faraday cage they confirmed that an equilibrium was reached during the sputtering process where the rate of implantation of the radioactive ions was equal to the rate of sputtering of radioactive ions that had been embedded in the target. This equilibrium is known as 'steady state' and was shown to depend on the angle of incidence, accelerating voltage and current density of the primary ion beam; as well as target material, temperature, composition, crystal structure and crystal orientation.

Implantation concentrations high enough to reach steady state are used in 'dynamic SIMS' instruments and is a feature of the CAMECA NanoSIMS 50. These instruments measure ions from regions already affected by previous ion implantation. It is possible to use implantation concentrations so low that no primary ion interaction volume overlaps with another and steady state is never reached, this is known as 'static SIMS.' Typical interaction volumes in SIMS instruments are on the order of several nm in diameter [149] and in biological samples the static limit is around $1 \times 10^{12}\,\text{primary ions}\,\text{cm}^{-2}$.

These ion matter interactions are therefore to be considered a combination or competition between implantation and sputtering. The last few observations listed above are the result of variations in sputtering rates caused by the local chemistry and local physical properties of the atoms being bombarded. Almen and Bruce noted that even targets of similar atomic mass yielded quite different results, a problem known as 'matrix effects.'

Matrix effects

The difference between the ion yield of an element when sputtered from different target materials can be very large. This is attributed to physical and chemical interactions between the element and its surrounding environment; a phenomenon more generally dubbed 'the matrix effect.'

Arnot *et al.* noticed that allowing oxygen into the apparatus between experiments completely changes the spectrum obtained [150]. They developed a series of experiments that involved bombarding a tungsten filament to produce negative secondary ions after different oxygen exposures. Repeating the experiments several times, and with different primary ions always yielded the same result; they noticed that when the filament was clean there was a peak in the mass spectrum corresponding to O_2^- ions that was not present when the filament was oxidised. Although counter-intuitive that a filament with higher surface oxygen yielded no O_2^- ions, they explained the absence of the ions by considering the higher work function of the oxidised surface relative to a clean tungsten surface. The higher work function of the oxidised tungsten reduced the probability of electrons tunnelling from the surface onto a sputtered O_2.

This alteration of the work function at the surface is an important consideration for analysis in SIMS. Andersen [151] recognised that it was compounds on the surface of Al targets that were responsible for the Al^+ yield, and that once these compounds were removed the ion yield rapidly decreased. By choosing reactive gases as the primary ions he was able to maintain an advantageous surface chemistry for the production of the Al^+ secondary ions during sputtering. The research continued to explore the surface changes during sputtering, achieving parts per billion detection and concluding that "the survival rate of the generated ions is a function of the electronic properties of the surface." Further research by Andersen covered many of the important fundamental principles involved in the effect of surface chemistry on SIMS analysis [152].

Cs implantation is found to depress the work function at the surface, promoting the formation of negative ions during sputtering [153]. This is advantageous when Cs^+ primary ions are used in the NanoSIMS for analysis of negative secondary ions. It is also possible to make Cs ion sources with small spot sizes (10 µm to 50 µm) and low energy dispersion (0.2 eV to 0.5 eV) [154, 155], making it an ideal primary ion for the detection of negative ions.

Positive second ion formation can be encouraged using more electronegative primary ions. Commonly O_2^- ions are used and are produced in a duoplasmatron, but this method suffers from higher energy dispersion (5 eV to 20 eV) and virtual source size (200 µm) compared to the surface ionisation techniques used for Cs^+ sources.

The sputtering of ions also depends on the binding affinity, relative ionisation potential, and local chemical environment of the elements of interest [156], which makes quantification

quite challenging. In order to help develop semi-quantifiable methods some researchers have produced relative sensitivity factor (RSF) values for certain elements in specific matrices, including biological matrices [157].

Ion optics

In order to achieve point analysis on a micron scale, Liebl [158] built an ion microprobe mass analyser. His research recognised that sputtering is a destructive process, therefore high sensitivity requires high transmission otherwise the sample volume will be destroyed before any trace ions arrive at the detector. Instead of separate optics for primary ion beam formation and secondary ion collection, it is possible to build co-axial optics (fig 1.12, red box) where primary ions pass through the same lenses used for extraction of the secondary ions. This allows much more favourable geometry for collection of secondary ions from a larger solid angle, improving transmission, while also providing a shorter working distance, leading to a smaller probe size.

Liebl's research also recognised that the large variations in the excess energy of sputtered secondary ions are detrimental to the spatial resolution of the instrument. Therefore in order to obtain high resolution the secondary ions need to be energy filtered — cutting all but a small fraction of the secondary ions. These issues are overcome in modern instruments such as the NanoSIMS by using a double focussing system [159]. Focusing in one direction with an electrostatic sector (fig 1.12, blue box), then the opposite with a magnetic sector (fig 1.12, green box) maintains equal dispersion factors [160], the system is energy compensated without the need for apertures, allowing the system to maintain a

high transmission.

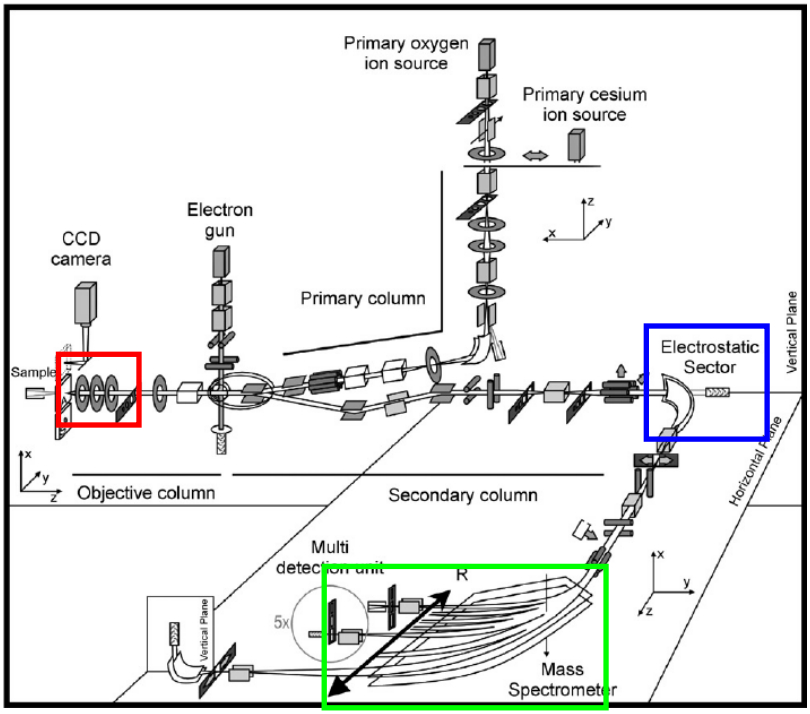

Figure 1.12: Schematics of NanoSIMS Ion Optics. Reprinted from Soil Biology and Biochemistry, 39, Anke M. Herrmann *et al.*, Nano-scale secondary ion mass spectrometry A new analytical tool in biogeochemistry and soil ecology: A review article, Page 1838, Copyright 2007, with permission from Elsevier. [161]

Biological SIMS

The use of dynamic SIMS in the field of biology is a well established science [162, 163], the main consideration is the important aspect of sample preparation. Before analysis samples must be dehydrated and sectioned ready for an ultra high vacuum (UHV) system. Different procedures on how this can be achieved and the pros and cons of techniques relevant to this project are given by Smart *et al.* [164].

The problem of high As concentrations in rice has been studied by many different

research groups, using a variety of techniques. In order to determine effective strategies for minimising the health impacts of As exposure from rice we must first have a good understanding of the biological processes involved in transporting As into the grain. The most important information to do this is the location and concentration of As within the plant. The two main methods typically used are mass spectrometry and X-ray based techniques. Most of the published work employing mass spectrometry has employed ICP-MS and variations thereof. More recently secondary ion mass spectrometry (SIMS) has been employed in the study of biological specimens; Grovenor *et al.* [164] have carried out work to assess its suitability and devise methods for sample preparation and data analysis. X-ray based techniques have been around for longer, and modern advances in X-ray based techniques are allowing increasingly complex and precise analyses, making it a popular choice for plant scientists [165, 166]. NanoSIMS as a tool for trace element analysis for biological samples has already been demonstrated [167, 112] and compares favourably to the much more costly and complex synchrotron based techniques [139].

This project aims to study the roles of *OsLSi3*, *OsPT8*, *AtABCC1,2* and *CAD1* genes in the uptake and detoxification of As. While these genes have previously been identified and studied, the methods employed were bulk methods familiar to biologists that are unable to provide detailed information on the changes on As distribution in response to mutation. NanoSIMS is a materials science method that presents an excellent opportunity to engage in a cross-disciplinary study of ppm and ppb As concentrations in biological samples at a micron scale, with the objective of measuring changes in concentration and distribution of As and other key elements in response to mutation on these genes.

Chapter 2

Experimental Methods

In this chapter I will outline the process by which samples were selected, produced and prepared for analysis. I will also give an outline of the general operating principles of the NanoSIMS and more specifically the operating conditions necessary to obtain consistent results in the experiments described.

2.1 Sample selection

The competitive uptake of Si and As(III) in *Oryza sativa* suggests that silicate transporters play an important role in the uptake of As. The functions of the previously identified Si transporters, Lsi1 and Lsi2 have already been studied by Moore *et al.*, following this research we have chosen to study the less understood Lsi3 transporter. My collaborators at Rothamsted Research were able to provide an Lsi3 transporter defective mutant of *Oryza Sativa*, *lsi3*, grown in a nutrient solution amended with Si and As(III).

OsPHT1;8 (OsPT8) is a Pi transporter in rice plants thought to be responsible for As(V) uptake. In order to investigate the function of OsPT8 we grew wild type (WT) *O. sativa* alongside a PT8 overexpressing line *PT8-Ov*. Both strains were exposed to the same growth medium and growing conditions. As(V) was added to the nutrient solution towards the end of the growth period. The plants were removed from the solution for analysis as the panicles were forming.

In order to better understand the role of phytochelatins (PCs) in the detoxification

pathways we looked at the recently identified PC synthesis and transporter genes in Arabidopsis. This offered an exciting opportunity to study the detoxification and storage of As as complexes. Mutants defective in these genes were grown in a nutrient solution amended with As(V) alongside WT. All of these plants were grown alongside WT for comparison, and are presented in Table 2.1.

Table 2.1: Biological samples used for analysis and associated additions to nutrient solution

Species	Plant line	Additions to nutrient solution
O. sativa	G1 (WT)	$Si(OH)_4$, As(III)
	G1 (*lsi3*)	$Si(OH)_4$, As(III)
	G2 (WT)	As(V)
	G2 (*PT8-Ov*)	As(V)
A. thaliana	G3 (Col-0)	As(V)
	G3 *abcc1-2*	As(V)
	G3 *cad1-3*	As(V)

2.2 Plant materials

Three rice (*O. sativa*) lines were used in this study; Nipponbare cultivar wild type, mutant defective in Lsi3 transporter gene *OsLsi3* (*lsi3*), and PT8 transporter gene *OsPT8* overexpression line (*PT8-Ov*). *lsi3* and *PT8-Ov* have been described previously [102, 80].

Three Arabidopsis lines were also used; wild type Columbia-0 (Col-0), *atabcc1 atabcc2* double knockout mutant (*abcc1-2*), and a loss-of-function mutation in the Arabidopsis *AtPCS1* gene (*cad1-3*). The *abcc1-2* mutant is a double knockout of two ABCC-type transporters that are believed to be "essential PC-metal(loid) transporters that sequester toxic metal(loid)s in plant vacuoles" and is very sensitive to As [168]. Lastly *cad1-3* is PC-

synthase deficient mutant [95, 169] that showed no detectable PCs under Cd(II) stress [170].

2.3 Hydroponic culture

O. sativa lines were prepared by surface sterilising seedlings in 0.5% NaOCl for 15 min and rinsing three times with deionised water. Seeds were arranged on a nylon net floating on a solution of 0.5 mmol L^{-1} $CaCl_2$. Once germinated the seedlings were transferred into 0.35 l pots (four seedlings per pot) in a ½ strength Kimura solution, pH adjusted to 5.5 with NaOH. The composition of the nutrient solution is listed in table 2.2 and the solution was renewed every 3 d. The plants were grown with a 16 h photoperiod, light intensity 500 µmol m^{-2} s^{-1}, day/night temperatures of 30 °C/25 °C and a 70% relative humidity.

20 d after germination Growth line 1 (G1) were transferred to a fresh nutrient solution containing ½ Kimura nutrient solution amended with 1 mmol L^{-1} silicic acid and 10 µmol L^{-1} As(III) for 3 d before harvesting. 20 d after germination Growth line 2 (G2) were transferred to a nutrient solution amended with 5 µmol L^{-1} As(V), in the form Na_2HAsO_4, for 3 d.

Arabidopsis lines were prepared by germinating seeds in vials with open bottoms containing 0.5% agar. A one-tenth-strength Hoagland nutrient solution was added to the agar medium and an additional 600 ml to an open container beneath the vials. The composition of the nutrient solution is listed in table 2.2 and the solution was renewed every 3 d. The nutrient solution was pH buffered with 2 mmol L^{-1} MES adjusted to 5.5 with KOH. The plants were grown with a 16 h photoperiod, light intensity 120 µmol m^{-2} s^{-1}, day/night temperatures of 20 °C/20 °C and a 70% relative humidity. After 21 d seedlings were transferred

to nutrient solution containing 10 µmol L^{-1} As(V) in the form Na_2HAsO_4.

Table 2.2: Composition of nutrient solutions

	one-half-strength Kimura	one-tenth-strength Hoagland
Composition	Concentration (mmol l^{-1})	Concentration (mmol l^{-1})
KNO_3	0.091	0.6
$Ca(NO_3)_2 \cdot 4\,H_2O$	0.183	0.4
$MgSO_4 \cdot 7\,H_{20}$	0.274	0.1
KH_2PO_4	0.1	-
$(NH_4)_2HPO_4$	-	0.4
$(NH_4)_2SO_4$	0.183	-
$CuSO_4$	-	0.06×10^{-3}
$MnCl_2 \cdot 4\,H_2O$	0.5×10^{-3}	0.36×10^{-3}
H_3BO_3	3×10^{-3}	2×10^{-3}
$(NH_4)_6Mo_7O_{24} \cdot 4\,H_2O$	0.1×10^{-3}	-
$NaMoO_4$	-	0.04×10^{-3}
$ZnSO_4 \cdot 7\,H_2O$	0.4×10^{-3}	0.1×10^{-3}
$CuSO_4 \cdot 5\,H_2O$	0.2×10^{-3}	0.06×10^{-3}
Fe−EDTA	40×10^{-3}	20×10^{-3}

2.4 High pressure freezing

The plant roots were rinsed with distilled water and wrapped in damp cloth once they were removed from the growth chambers and nutrient solution. They were transported in this condition to Oxford Brookes University in order to undergo the high pressure freezing (HPF) process.

Sections of root up to 2 mm long were cut from the plant at predetermined distances from the root tip. As a precaution to maintain the ion distributions as close as possible to the *in vivo* state these sections were cut under MES buffer solution. The sections were then carefully placed into planchettes (maximum diameter 2 mm, maximum thickness 0.6 mm) and surrounded by hexadecene. The planchettes were inserted into the high pressure freezer

then immediately removed and stored under liquid nitrogen.

HPF was carried out in a BAL-TEC HPM 010 machine, it exposes the planchettes to jets of liquid nitrogen under pressures of up to 210 MPa, suppressing the formation of damaging ice crystals and allowing relatively thick biological material to be cryogenically preserved with nearly complete vitrification [171].

2.5 Freeze substitution

Specimens were stored in liquid nitrogen after HPF then transferred to microporous pots (agar G3767) under liquid nitrogen and covered with frozen acetone slush and capped. A Leica AFS freeze substitution unit (FSU) was cooled to −160 °C. The pots were transferred to the FSU along with an equal number of aluminium carrier pots containing frozen 2% osmium tetroxide in acetone (HPLC Grade).

The freeze substitution protocols are outlined in table 2.3. The AFS programme was started at Protocol 1, when the acetone melted (around −85 °C) the specimen containing microporous pots were transferred into the thawed Osmium solution. The programme of the AFS was then changed to Protocol 2 and subsequently to 3. Finally the pots were transferred to a fridge as set out below.

After 24 h in a fridge at 4 °C the specimens were transferred to a fume hood for 4 h at room temperature. They were washed in 100% acetone (HPLC grade) three times, each wash lasting 20 min before being removed from the planchettes. They were then exposed to increasing concentrations of TAAB low viscosity resin (medium)[1] in acetone as detailed in

[1]ERL 4206 (7-Oxabicyclo(4.1.0)heptane, 2-(epoxyethyl)-, homopolymer)

Table 2.3: Freeze substitution protocols

FREEZE SUBSTITUTION PROTOCOL 1				
	T_{init} (°C)	T_{final} (°C)	Rate ($\mathrm{K\,h^{-1}}$)	Duration (h)
T1	−160	−160		0.5
S1	−160	−85	15	5.0
T2	−85	−85		24.0

FREEZE SUBSTITUTION PROTOCOL 2				
	T_{init} (°C)	T_{final} (°C)	Rate ($\mathrm{K\,h^{-1}}$)	Duration (h)
T1	−85	−85		26.0
S1	−85	−60	2	12.5
T2	−60	−60		8.0
S2	−60	−30	2	15.0
T3	−30	−30		24.0

FREEZE SUBSTITUTION PROTOCOL 3				
	T_{init} (°C)	T_{final} (°C)	Rate ($\mathrm{K\,h^{-1}}$)	Duration (h)
T1	−30	−30		0.5
S1	−30	−20	1	10.0
T2	−20	−20		24.0

table 2.4. They remained in 100% TAAB low viscosity resin for a further 4 days, changing to fresh resin every morning and evening before being polymerised at 70 °C for 24 h.

2.6 Microtomy

Once the preserved roots were removed from the resin moulds they were carefully prepared for microtomy by shaping the resin blocks as to expose a cross section of the root towards

Table 2.4: Concentrations of TAAB low viscosity resin in acetone used for sample preservation.

TAAB conc. (%)	Duration (h)
10	2
25	2
50	2
75	2
100	16
100	8

the cutting surface. Most of the microtomy was conducted on an RMC products PT-PC PowerTome Ultramicrotome, with a regularly replaced glass knife as the cutting surface. Some of the later sections were prepared using a Leica Reichert Jung UltraCut E microtome with a 4mm dEYEmond diamond knife.

The microtomes were operated at a cutting speed of approximately $1.3\,\mathrm{mm\,s^{-1}}$ at a section thickness of 1 µm. Sections were either dried onto aluminium stubs or onto thermanox coverslips cut to 10 mm diameter discs that had been coated with 5 nm of platinum (Pt). Dried samples were then coated with a further 5 nm of Pt and optically mapped with a light microscope before being loaded into the NanoSIMS.

2.7 SIMS

SIMS analysis was conducted with a CAMECA NanoSIMS 50. This section will describe the practical operation of the NanoSIMS used to collect data for this project. For a description of the principles of SIMS techniques refer to Section 1.6 on page 39.

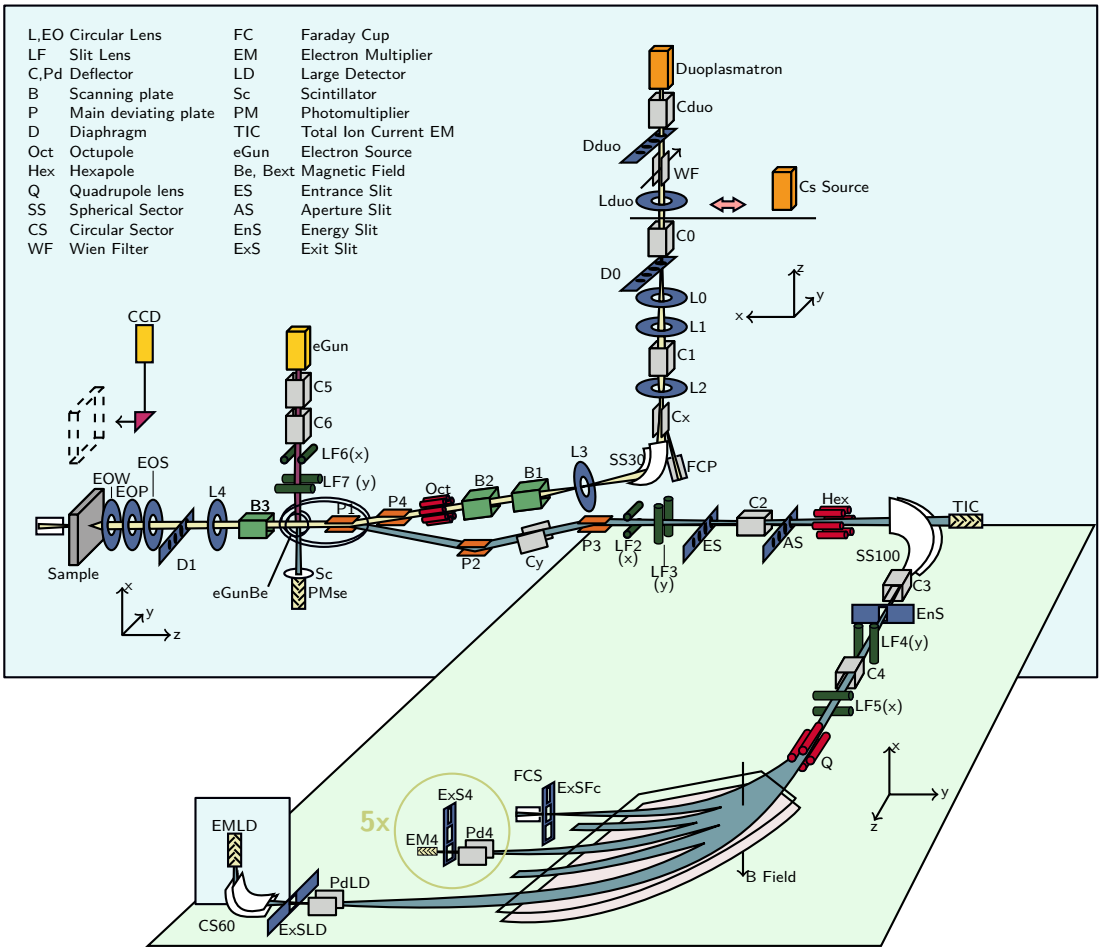

Figure 2.1: NanoSIMS schematic

2.7.1 Primary ions

The CAMECA NanoSIMS 50 was operated using the CAMECA Microbeam Caesium Source to produce a beam of Cs^+. The source heats a pellet of caesium chromate or caesium carbonate to 400 °C to produce a Cs vapour. The vapour diffuses through a reservoir towards a tungsten plate heated to 1100 °C, contact with this plate ionises to the vapour to form Cs^+ ions. The ioniser and reservoir are charged to high voltages of 6 kV to 10 kV and the Cs^+ ions are accelerated by an extraction plate at 0 V.

Source temperature is maintained by electron bombardment from annular rings. During the lifetime of the source a decrease in current density is typical [172] and can be compensated for by an increase in reservoir current. Ageing is not always uniform and may necessitate a later decrease in reservoir current.

The primary ion beam is directed down a vertical column, figure 2.1, that contains a series of lenses and apertures. This section can used to vary the demagnification of the source image, adjust primary source current and centre the beam. The beam is rotated 78° by an electrostatic sector (SS30) into the central column. The central column aligns the beam for the coaxial section, and contains deflector plates for rastering the beam on the sample surface and an octopole for correcting astigmatism. The maximum practical raster size is $200\,\mu m^2 \times 200\,\mu m^2$, but rasters over $50\,\mu m$ suffer from defocussing effects of the primary beam.

Deviating plates (P4 and P1) are used to rotate the beam a further 6° each to align with the coaxial column. The coaxial column is a feature of the CAMECA NanoSIMS that allows primary ions to be focussed and secondary ions to be collected by the same set of lenses. This has advantages of smaller probe size, and higher yield and lower angular distribution of secondary ions compared to other SIMS instruments where the primary ion beam is focussed at an oblique angle to the sample surface. It consists of an immersion lens consisting of several electrodes (EOW, EOP, EOS and L4) and an aperture (D1). EOP is mainly used for focussing the primary ion beam, which should be defocussed to match the beam size to the pixel size in order to avoid drilling small holes in the sample, such as those imaged in figure 2.6. D1 limits the angular aperture of the primary ion beam,

a smaller aperture allows a more focussed primary beam at the expense of beam current. This can be seen in figure 2.2, where $^{12}C^{14}N^-$ data for the same region was recorded four times under identical conditions except with D1 set to different sizes of aperture; the mean $^{12}C^{14}N^-$ counts decrease from 862 to 15 as the aperture is reduced from 750 µm to 150 µm. The focus is improved but for my experiments a higher secondary ion signal is typically more important than sub micron resolution as the experiments involve the detection of very low concentrations of $^{75}As^-$. D1 is near an image conjugate plane of the secondary ion beam and acts as a field diaphragm, this can be seen in figure 2.2 (A) where a slight misalignment caused D1 to limit the field of view in the bottom corners.

D1 = 1 (750 µm)	D1 = 2 (300 µm)	D1 = 3 (250 µm)	D1 = 5 (150 µm)
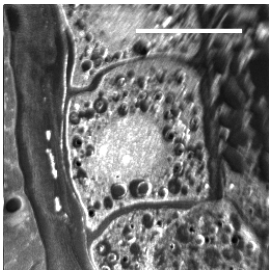	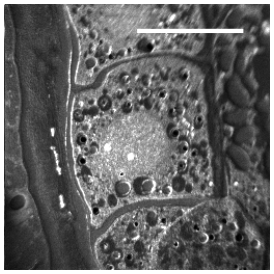	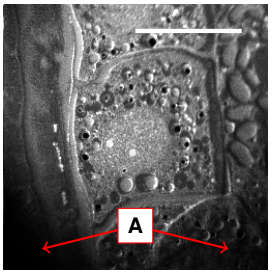	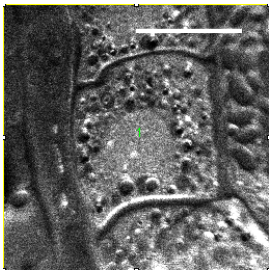
mean = 862	*mean* = 359	*mean* = 131	*mean* = 15
median = 775	*median* = 313	*median* = 118	*median* = 13

Figure 2.2: The effect of different sized D1 apertures on $^{12}C^{14}N^-$ counts recorded from a wheat cell. Scale bar 24 µm.

2.7.2 Ion matter interactions

The secondary ion yield depends on the chemistry near the sample surface. Since this chemistry is altered by the implantation of primary ions, the most consistent results are obtained after reaching steady state. Steady state was derived experimentally for these

samples at the start of each week of analysis by depth profiling over a small area. An example depth profile, figure 2.3, shows how some of the ion counts change quite dramatically at low implantation doses, before becoming more stable. This stable region is marked by a vertical line in figure 2.3, it can be considered to be the steady state region where the Cs^+ is removed by sputtering at the same rate that it is implanted, and the surface chemistry and matrix effects are relatively constant. The $^{75}As^-$ signal is a real signal even though it looks like noise, it has very few counts because the concentration is very low, but NanoSIMS has enough sensitivity to accurately measure extremely low concentrations of some elements.

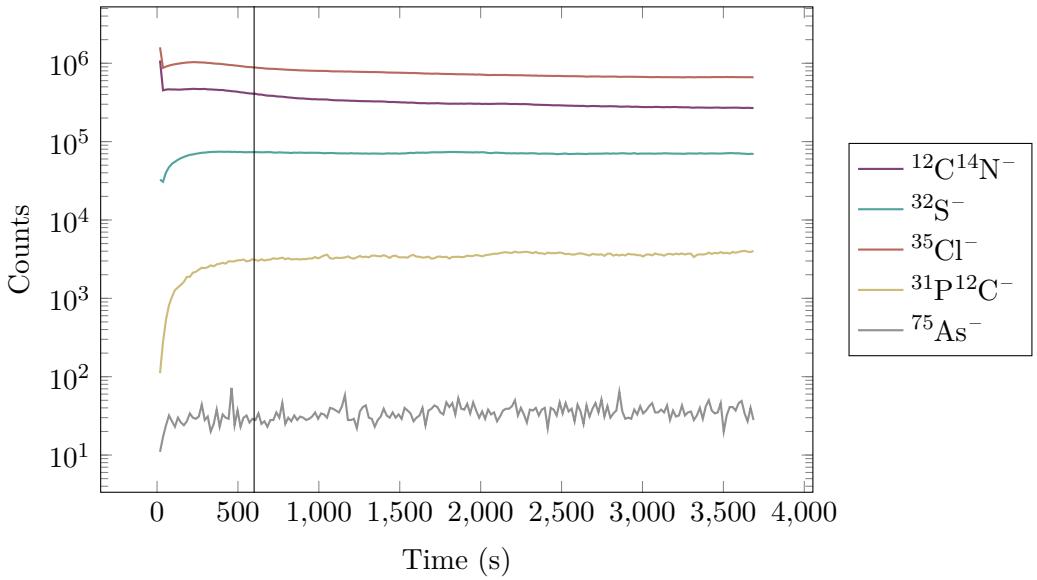

Figure 2.3: Depth profile of an arabidopsis section showing the transition from transient to steady state after approximately 600 s.

Results from a depth profile can be used to estimate the amount of ion implantation required to reach steady state under different conditions, such as when implanting a larger area or using a higher incident beam current. The ion dose is defined as the number of ions implanted per square centimetre of sample surface, equation 2.1, and can be calculated

from experimental results using equation 2.3. Beam current is determined by measuring with Fc0 (fig. 2.1), the size of the depth profile is user defined, and the time in seconds to reach steady state can be determined from the depth profile graph.

$$Dose = ions \cdot cm^{-2} \tag{2.1}$$

$$= I \cdot q \cdot t \cdot area \tag{2.2}$$

$$= pA \cdot s \cdot \mu m^{-2} \cdot 6.24 \times 10^{22} \tag{2.3}$$

An area to be used for analysis was then chosen, and implanted with enough primary ions to reach the calculated steady state dose. To speed up the process D1 was set to 0 to allow maximum primary ion current to reach the sample, and a 64×64 pixel region was rastered several times until required dose was achieved. The implantation also removes material from the sample surface, to avoid drilling holes in the sample the beam was defocussed by changing EOP, and to avoid damaging the detectors with high secondary ion and secondary electron currents ES was closed and the SE detector voltage was decreased. A crater is formed during implantation, Jones *et al.* implanted approximately 2.6×10^{15} primary ions cm^{-2} 40 keV $^{12}C_{60}{}^{+}$ into rat brain, creating a crater that was measured by atomic force microscopy at a depth of approximately 4 µm [173]. Therefore the area for analysis smaller than the size of the crater was chosen from within the crater. This is to avoid 'crater edge effects' that result from imaging the crater walls as they have different geometry and chemistry to the bottom of the crater, and can adversely affect mass

resolution [174].

An example of ion implantation without defocussing EOP or adjusting the the raster size to avoid crater edges is shown in figure 2.4. A crater edge at the extreme left edge of the image caused a much higher than expected $^{35}Cl^-$ signal as shown in the line profile (B). Holes drilled into the sample surface by the primary ion beam created a grid of high and low signal visible in both the false colour image (A) and the line profile.

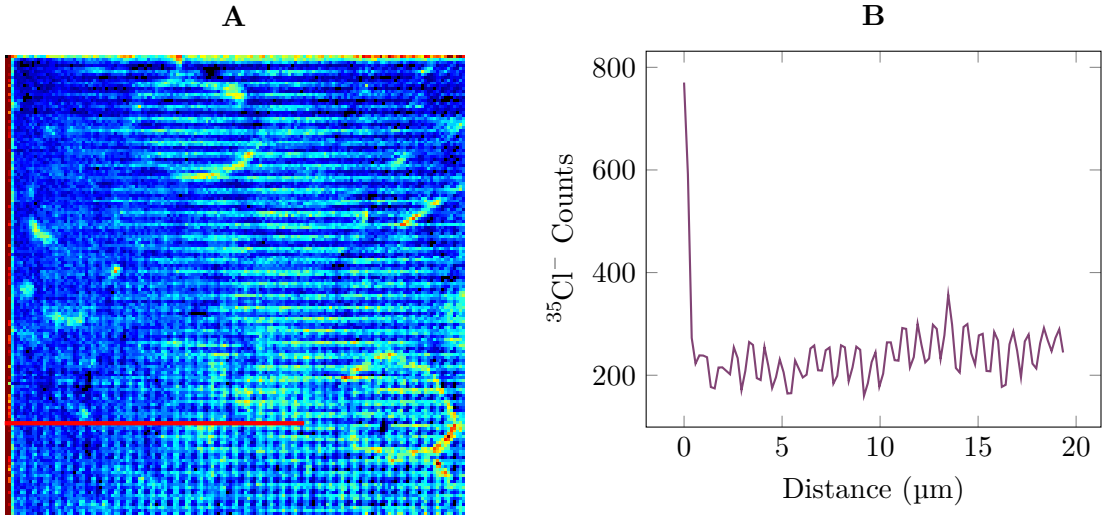

Figure 2.4: Crater in a section of arabidopsis root created by a 64×64 pixel raster over a 50 µm area using a too tightly focussed primary ion beam. (A) part of a false colour image of $^{35}Cl^-$ counts recorded over the same 50 µm area but using a 256×256 pixel raster. Grid pattern created by implantation clearly visible. Red line denotes location of 20 µm line profile. (B) line profile of $^{35}Cl^-$ counts showing grid pattern created by $64x64$ pixel raster

2.7.3 Secondary ions

Secondary ions produced in the NanoSIMS are collected by EOW (fig. 2.1) and pass back through the coaxial lens system. They are deviated towards the mass spectrometer section by a series of parallel plates (P1, P2, P3) and aligned by a deflector plate (Cy) and slit lenses (LF2, LF3).

At the entrance to the mass spectrometer is a rectangular slit assembly (ES) that limits the width and lateral energy of the secondary ion beam, followed by a second slit assembly (AS) that the limits angular extension of the beam. The effects of ES on the mass resolution and transmission of secondary ions is demonstrated in figure 2.5.

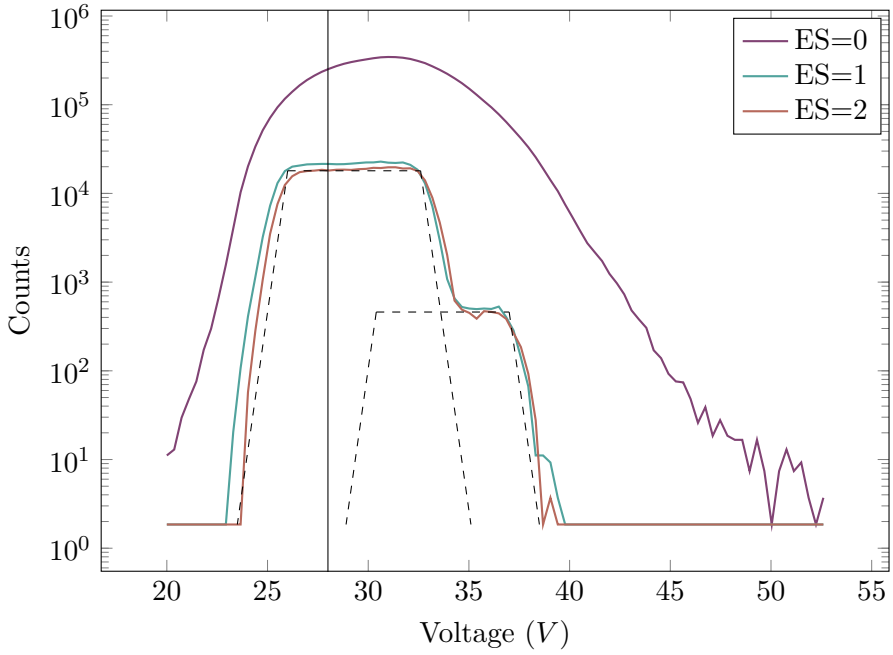

Figure 2.5: HMR scans with different entrance slit (ES) sizes. Detector tuned to 26.009 amu with the primary ion beam focussed on a wheat cell. Left peak $^{12}C^{14}N^-$ (26.003074 amu), right peak $^{12}C_2{}^1H_2{}^-$ (26.015650 amu), dashed lines approximate shape of peaks, vertical line best tuning position to avoid mass interference. Mass difference between peaks 0.012576 amu.

The mass spectrometer is a double focussing system with a spherical electrostatic sector (SS100) and a magnetic sector separated by a series of lenses, deflectors and a quadrupole that maintain focus and alignment of the beam. The effects of changing deflector voltages in the horizontal plane can be seen in figure 2.6, under ideal conditions the peak count rates from each detector will all be aligned. This secondary ion beam alignment was repeated frequently in both vertical and horizontal planes to ensure good transmission.

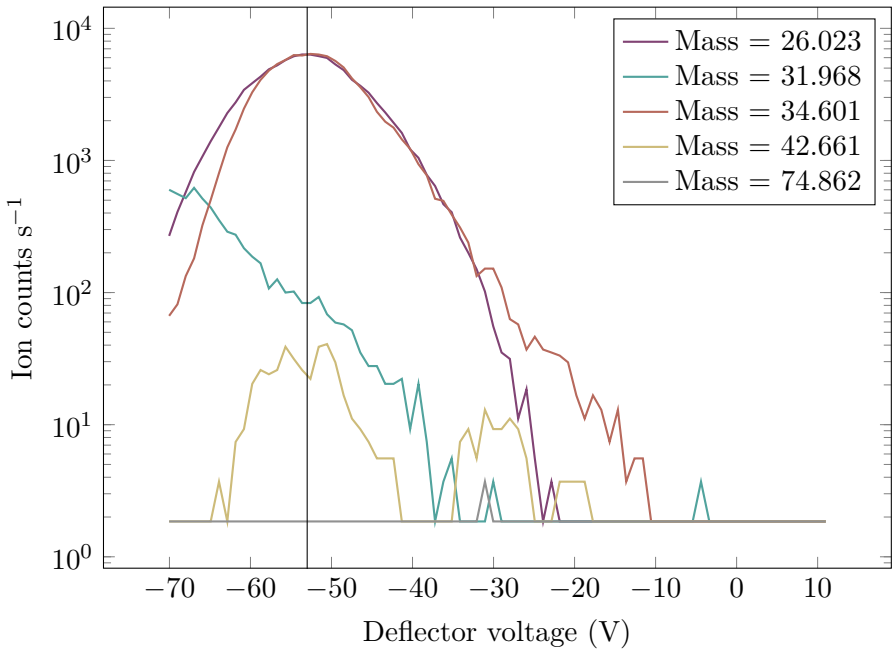

Figure 2.6: Data collected from an SIB scan in the horizontal plane on a section of Arabidopsis root. Note the asymmetry of the 'Mass = 31.968' series (turquoise line), this is caused by the $^{32}S^-$ and $^{16}O_2{}^-$ mass interference. Optimal tuning shown by vertical line.

The CAMECA NanoSIMS uses electron multipliers (EMs) to detect the secondary ions, they have a gain of around 1×10^8 and are capable of detecting single ions. The instrument has five detectors, one fixed and four on mobile trolleys. The B field of the magnetic sector is first tuned to focus the heaviest ion of interest into the fixed detector (detector five), then the four other detectors are moved along rails using stepper motors to the correct radius to collect other ions of interest.

The ion detectors are fitted with deflector plates, across which the voltage can be scanned. This changes the effective radius of the detector without physically moving it allowing high mass resolution (HMR) scans to be produced that can be used for fine tuning of the detector. An example of an HMR scan is shown in figure 2.5 and contains a mass interference between $^{12}C^{14}N^-$ and $^{12}C_2{}^1H_2{}^-$. The approximate shapes of the peaks are

drawn in dashed lines, in order to record only $^{12}C^{14}N^-$ ions a deflector voltage of 28V was selected. Note also that with the entrance slit adjusted so ES=0 it is not possible to resolve this mass interference, at ES=1 the peaks are easily resolved but the ion count rate is decreased by a factor of 15. Drift in the B field and thermal fluctuations can affect this fine tuning of the detectors, therefore it was repeated frequently to ensure optimum tuning.

Each sample holder is able to hold eight 8 mm diameter samples. One of these positions was always taken by a collection of standards that were mounted in resin, polished and loaded onto the holder. These standards included electronic grade Si, electronic grade gallium arsenide, stainless steel and gallium phosphide. Since As was the heaviest element of interest the magnet was adjusted such that detector 5 was tuned to detect $^{75}As^-$ ions.

2.7.4 Analytical parameters

Typical data acquisition therefore involved pre-implanting an area until it reached steady state, then analysing an area slightly smaller than the implanted region in order to avoid crater edge effects.

The five detectors of the mass spectrometer were fine tuned using standards by adjusting deflector positions and voltages. Tuning was repeated on the sample to ensure optimum transmission of the secondary ions. Some of the secondary ions that were tuned for are as follows:

$^{12}C^{14}N^-$ found in amino acids and proteins, these compounds are well preserved by cryofixation and cryosubstitution. Detection of these ions can be used to provide histological [175] and morphological information of biological materials [176].

$^{28}Si^-$ believed to share a transport pathway with As(III), added to nutrient solution in *O. Sativa* G1. This pathway was previously studied by Moore *et al.* [112] and that work is continued here with the study of *lsi3* mutants in chapter 4.

$^{31}P^-$ believed to share a transport pathway with As(V) [53] that includes the PT8 transporters studied in chapter 6.

$^{32}S^-$ present in PCs that are understood to be an important part of the detoxification pathway of heavy metals in plants [95].

$^{35}Cl^-$ present in the resin, detecting this element is useful for determining the condition of the section and quality of preservation as well as providing useful data for histological examination.

$^{31}P^{12}C^-$ mostly analogous to $^{31}P^-$ but also has a mass interference with $^{27}Al^{16}O$. On sections that were mounted on Al stubs the mass interference allows the detection of holes or tears in the section.

$^{75}As^-$ the main element of interest in this thesis on account of its toxicity, and the heaviest element of interest. Detector 5 was tuned to $^{75}As^-$ for all samples.

Through experimentation a combination of beam current, focus and ion yield that produced a good compromise between spatial resolution and trace element detection was found to be a 50 µm raster with D1 aperture set to position 2 and the ES and AS apertures left open. An example of data acquired with these conditions is shown in figure 2.7, each image represents data recorded from the different detectors, the black and white image

showing the information recorded by the secondary electron (SE) detector.

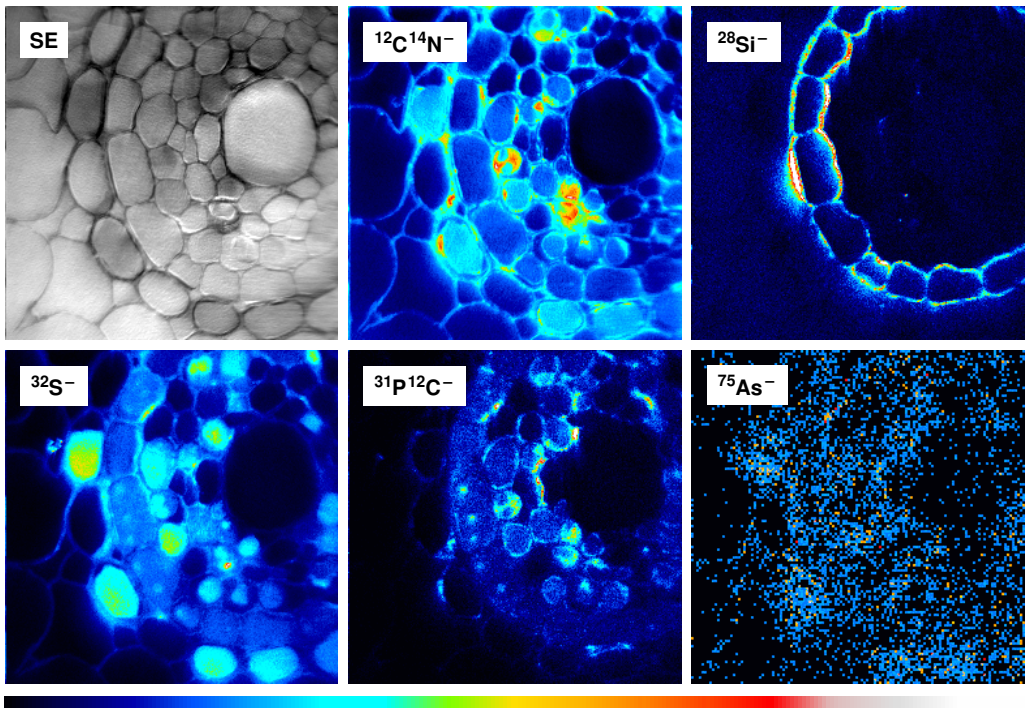

Figure 2.7: Example of a set of typical NanoSIMS maps from *O. sativa* collected over a 50 µm area. SE image in black and white, ion detectors using false colour scale (bottom) where black represents low number of counts from that detector and white a high number.

These maps show the cross section through a section of *O. Sativa* root at 1 cm from the root tip. Individual cells are clearly visible in the images produced by the SE detector and some of the ion detectors. Cell walls and some cell interiors appear bright in the $^{12}C^{14}N^-$ image because carbon nitrogen bonds are found in many biological molecules including proteins, and therefore indicate biological activity. The $^{75}As^-$ map looks like noise but is a real signal with very few counts — most pixels in the $^{75}As^-$ map contain only 0 or 1 counts despite the image taking over 1 h to acquire. Repeated experiments have shown that despite the very low concentration of As in these samples, it can be accurately mapped if time and care is used to set up the NanoSIMS.

I wrote a Scheme script for GNU image manipulation program (GIMP) to improve the contrast of $^{75}As^-$ maps printed in this thesis. The script copies the pixels with more than 0 counts, blurs them, and layers them so that they appear bigger and brighter than the original exported map. This was only done for the visual representation of the data to make it easier to see in print, and did not affect the data used for data analysis. A portion of the code is given below[2].

```
(define (script-fu-sims-enhance inImage inLayer inBlurRadius)
  (let*
    (
      ; define local variables
      (theImage inImage)
      (botLayer inLayer)
      (topLayer)
      (topLayer
              (car (gimp-layer-copy botLayer 1))
      )
      (midALayer
              (car (gimp-layer-copy botLayer 1))
      )
      (midBLayer
              (car (gimp-layer-copy botLayer 1))
      )
    ) ;end of local variables
    ;functions go here()
    (gimp-image-add-layer theImage midBLayer 0)
    (gimp-image-add-layer theImage midALayer 0)
    (gimp-image-add-layer theImage topLayer 0)
    (gimp-image-select-color theImage 0 topLayer '(0 0 0))
    (gimp-edit-fill topLayer 3)
    (gimp-edit-fill midALayer 3)
    (gimp-edit-fill midBLayer 3)
    (gimp-selection-all theImage)
    (plug-in-pixelize 0 theImage midALayer inBlurRadius)
    (plug-in-pixelize 0 theImage midBLayer inBlurRadius)
  )
)
```

[2]full script can be found at https://gitlab.com/HughTaylor/nanosims-scripts

2.8 Software

The data was analysed using the OpenMIMS plugin for ImageJ. OpenMIMS is free open source software produced by the National Resource for Imaging Mass Spectrometry (NRIMS)[3]. The software allows the data recorded from the NanoSIMS to be presented graphically, exported as raw data, or analysed with a selection of mathematical functions.

This tool allows a stack of images to be automatically corrected for beam drift, compiled into one image for analysis, or exported as a table that can be used to generate a depth profile.

I used this software to generate intensity maps from the different detectors to see relative distributions of the elements in each sample. As described in more detail in each experimental chapter I then highlighted regions of interest from within each sample and extracted the average counts from that area so that the data could be normalised and statistical analysis could be carried out.

[3]http://www.nrims.hms.harvard.edu

Chapter 3

Data Validation

Analysis of different regions within a cell could have a significant effect on the concentrations of different elements measured by the NanoSIMS as a result of the unique chemistry of different biological structures. Since my analysis will take place on 1 µm thick cross sections through the root, I was concerned that it might be possible to cut a cross section through a very specific feature that was not representative of the whole root. Such variations could create outlier information that would make it difficult to make qualitative comparisons between different roots. Testing this hypothesis is important in order to determine the repeatability of the results.

The rate at which secondary ions are produced from a sample during SIMS analysis is proportional to the primary ion beam current. The primary ions are produced by heating a caesium chromate or carbonate pellet to produce a Cs vapour that is then ionised by a heated tungsten plate. These pellets typically have a lifetime of around 18 months and the rate at which they produce Cs vapour gradually decreases over this time. Although the gradual fall in primary ion current can be compensated for by increasing the temperature of the source reservoir, the source may not age uniformly and the ion current may exhibit some instability. These instabilities can lead to systematic variations in the secondary ion signal, therefore measurements made on different days could have uniformly higher or lower signal and if not normalised correctly could incorrectly imply changes in concentration.

The NanoSIMS detectors are tuned to a very small mass range, therefore small changes

in magnetic field can result in a significant change to the transmission of secondary ions through the mass spectrometer. Changes in magnetic field may arise due to magnetic creep and temperature fluctuations. This became an important consideration as a source of systematic error during my experiments, as problems with the laboratory air conditioning resulted in temperature variations over a 24 hour period.

NanoSIMS data is produced from a raster of the sample surface. It is typically presented as false colour images of the sample where the colour of each pixel is determined by a lookup table (LUT) scaled to best include all the values. This means that even if the analytical parameters were identical different images cannot be directly compared because the colour scale could have been shifted to higher or lower minimum and maximum values. For this reason it is best to select regions on the image and the numerical values of ion counts from the raw data representing that region.

Lastly the large number of cells with similar appearance in the root and small number of very prominent features means that it can be difficult to compare the distribution of elements between samples just from the images. It is better to extract numerical values for the number of counts from specific parts of the root using regions of interest (ROIs), these values can then be compared between samples. This way comparisons can be made with much greater confidence that the same region (ie endodermis) is being compared across two different samples, but requires regions of the root to be reproducibly identified, and the data to be normalised.

Therefore finding a useful method of normalisation will be important because daily variations in temperature and weekly or monthly changes in the Cs ion source can result in

large systematic variations that should be accounted for before attempting any qualitative analysis.

3.1 Aims

My first aim is to try to determine how representative one section of root is of the rest of the surrounding root. Understanding how much biological variation might occur between samples cut along the same length of a sample will help to determine the reliability of the results.

Secondly, I wish to establish the consistency and repeatability of NanoSIMS analysis and to propose a normalisation method that could be used for semi-quantitative analysis in later experiments.

3.2 Method

For determining the repeatability of my results I devised an experiment with the primary purpose being to understand how cross sections of the root varied over distances on the order of several microns. In this experiment the preserved root would be microtomed in such a way that consecutive 1 µm sections could be placed in the same order that they were cut onto substrates for NanoSIMS analysis.

The consecutive sections were prepared from the resin embedded roots by microtoming 1 µm thick sections until sections of good quality (no obvious tears or folds) with well preserved root were consistently produced. Then individual sections were cut one by one

from the resin block, as illustrated schematically in figure 3.1, and transferred to a small droplet of water on prepared substrates. Figure 3.2 shows a micrograph of one of these sections on the substrate after it had been dried. Each consecutive section was placed in one carefully placed droplet, a total of three to a substrate, arranging them in a clockwise pattern to preserve the order in which they were cut from the resin block. After optical mapping the substrates could then be arranged on the NanoSIMS sample holder again being careful to preserve their order. Producing nine 1 µm sections allowed me to record any differences along a total distance of 9 µm along the root between the first and last section, in steps of 1 µm, effectively forming a stack of cross sections.

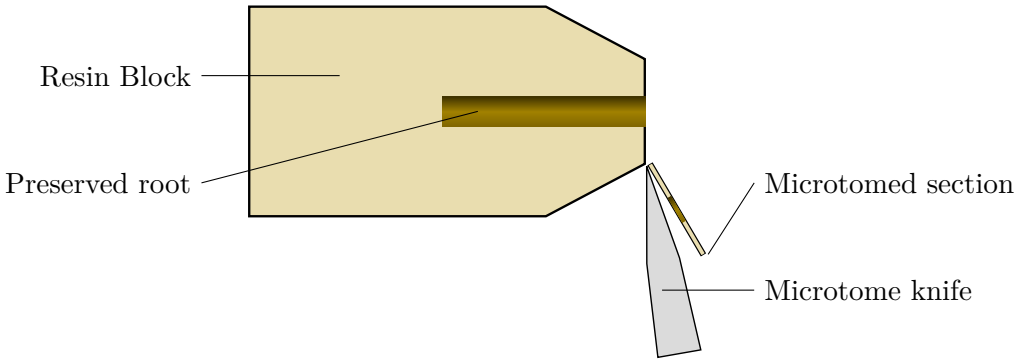

Figure 3.1: Schematic demonstrating the microtomy of preserved root cross-sections

The NanoSIMS was tuned to the signals $^{12}C^{14}N^-$, $^{32}S^-$, $^{35}Cl^-$, $^{31}P^{12}C^-$, and $^{75}As^-$, because these are elements of interest that will be used in later experiments. The importance of this choice of signals is described in section 2.7.4. Data was gathered over a 50 µm area, centred on the central xylem of the root, such that the same area would be analysed for each of the sections. The NanoSIMS analysis took place over the course of approximately one week and produced SE images and element maps of the stele of all nine sections.

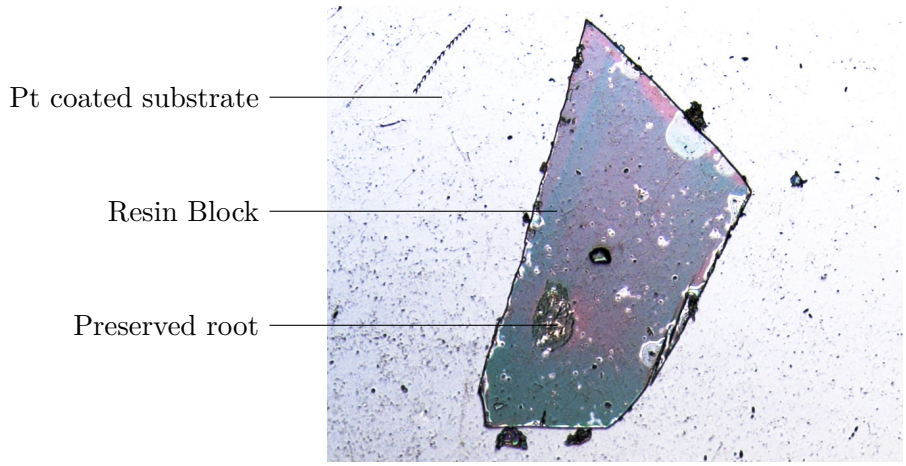

Figure 3.2: A microtomed section (HPF 742 1c) on a platinum coated substrate

3.3 Results

Data from the SE detector showed that root preservation was good and that NanoSIMS was able to produce clear images of the cells under these conditions. It is not possible to rotate the NanoSIMS stage, nor the sample holder, therefore although the same area of root could be analysed for each section it was not possible to maintain the same physical orientation for each of the samples. To better compare the samples I rotated all of the images such that they shared the same orientation. This helps to realise the first aim of determining biological variation of the root over short distances. The cropped and rotated data for the secondary electron signal is presented in figure 3.3.

From these images we can see a large cell with thick cell walls at the centre right of each section that is likely a xylem vessel (A). There are also some thick black lines in the upper left corner of most images (B). These are probably areas where the cells have become slightly separated from each other along the cells walls during the rapid changes in

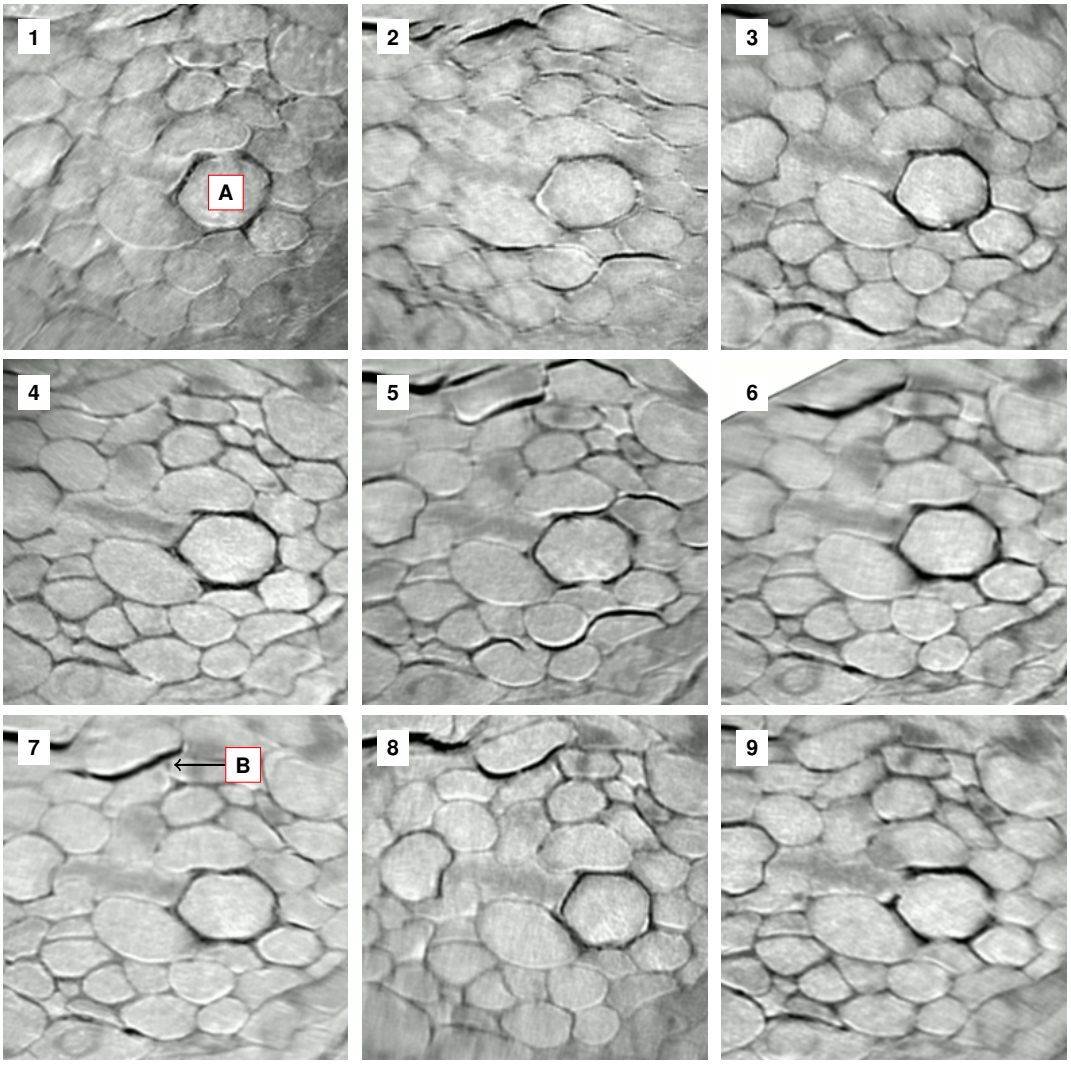

Figure 3.3: SE images from each of the nine consecutive images obtained during NanoSIMS analysis numbered in ther order in which they were produced. (*a*) Central xylem, large cell with thick cell walls, visible on all sections. (*b*) Black line indicating possible damage to structure of root during preservation, visible on most sections.

temperature and pressure required for HPF.

Visual comparisons between the SIMS data for these sections sections suggests very little variation in cell shapes or root structure over the 9 µm of root covered between the first and last image. The size and shape of the cells can be compared between sections by taking measurements on the image. Signal strength can be compared between samples by extracting SIMS data for individual cells and comparing the number of counts betweem sections.

In addition to the SE detector are the five ion detectors. These produce intensity maps of the ions they are tuned to. The colour of each pixel in the intensity map represents the number of counts of the respective ion and is determined by comparing this value to a list of colours in a lookup table. The LUT used in this thesis was "royal.lut" provided by fiji[1]. The minimum and maximum values used for the LUTs were adjusted individually for each detector to give the clearest images.

The full set of data for section 3 is shown in figure 3.4. The LUT is represented as a colour bar to the right of the data with the minimum value at the bottom (black) and maximum at the top (white). Some of the analytical conditions are listed underneath the image.

The same xylem vessel (A) and crack in the sample (B) observed in the SE images can be easily identified. The $^{35}Cl^-$ counts are very uniform across the sample, including the area where the crack was observed. Since the resin contains Cl this suggests that the gap between cells was formed before resin embedding and that the microtomed section does not

[1]https://github.com/fiji/fiji/tree/master/luts

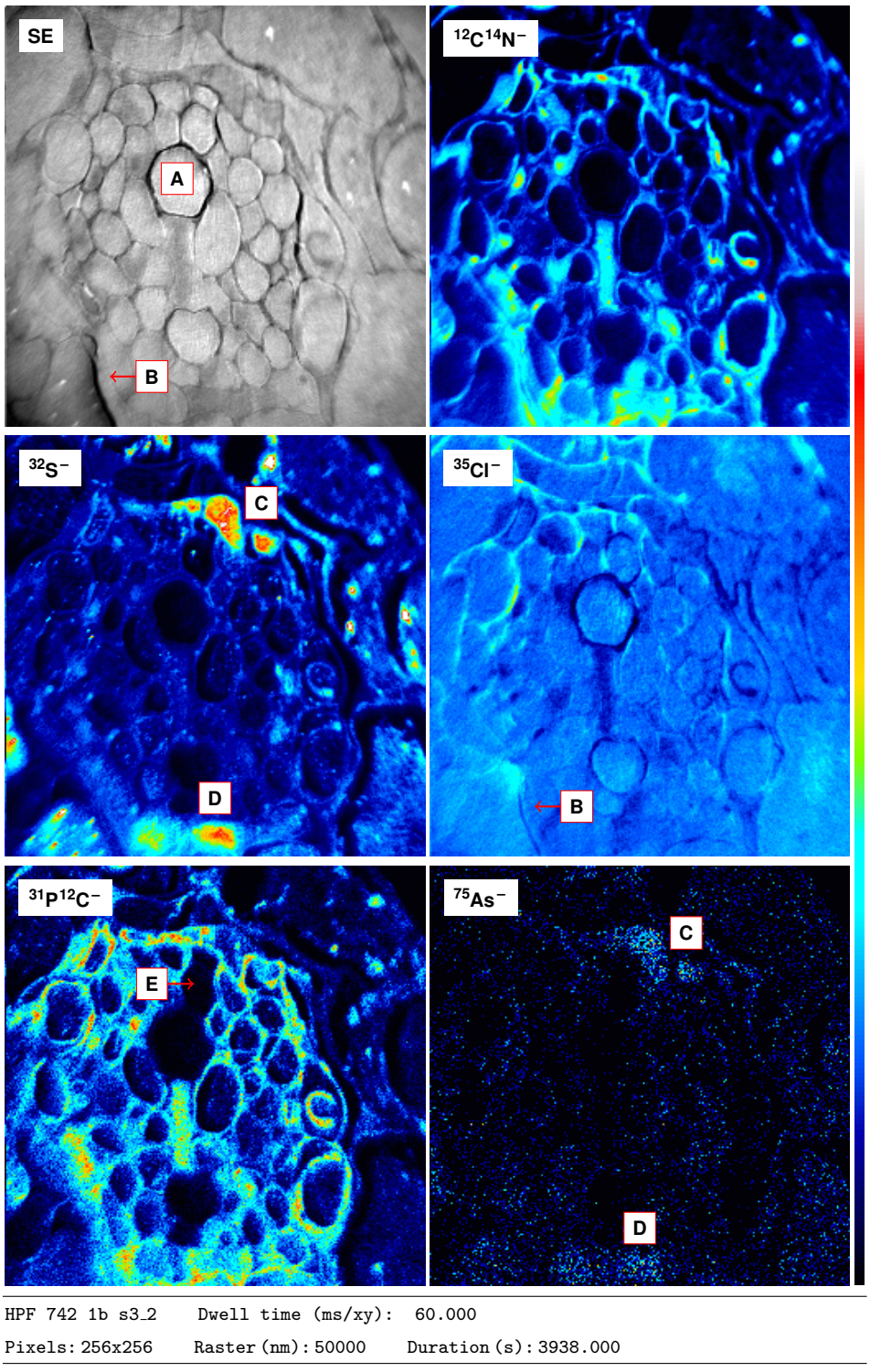

Figure 3.4: Example NanoSIMS data from section number 4 cut for this experiment. Signals presented from all five ion detectors and the SE detector. (*a*) Central xylem. (*b*) Possible damage to root structure. (*c,d*) cells that produced high $^{32}S^-$ and $^{75}As^-$ signals. (*e*) Metaxylem or protoxylem vessel.

contain holes or tears, indicating good preservation of the sample.

The $^{75}As^-$ data is dark and grainy because the concentration of As in the sample was so low that under the conditions used to record this data most of the pixels contained 0 counts of As, and the maximum was typically between 10 and 20.

Most of the cells in the stele contained $^{31}P^{12}C^-$ with the exception of the xylem vessel (A) and some of the cells adjacent to it (E). These are likely metaxylem or protoxylem, and the lack of $^{31}P^{12}C^-$ signal could be a characteristic of xylem that could be used to identify them in other experiments.

Certain cells appear bright in some detectors, suggesting that those cells have a particular biological function that differs from the surrounding cells. A clear example is the strong $^{32}S^-$ and $^{75}As^-$ signal near the top centre (C) and bottom centre (D) of the respective images in figure 3.4.

To determine that this data was accurate I re-analysed this area at a higher resolution. It is evident from the higher resolution data (fig. 3.5) that these regions do indeed contain a high concentration of S and As within the root, and that this is likely feature of the biology of the root.

There was little variation between the ion intensities recorded from the different sections. For example the $^{32}S^-$ data from sections 3 and 7 clearly show an almost identical distribution of S (fig. 3.6). The repeatability of these results demonstrate that the NanoSIMS is capable of accurately and reliably mapping element distributions in these samples despite the low concentration of some of the elements.

This also shows that the shape and chemistry of the cells over the 9 µm distance observed

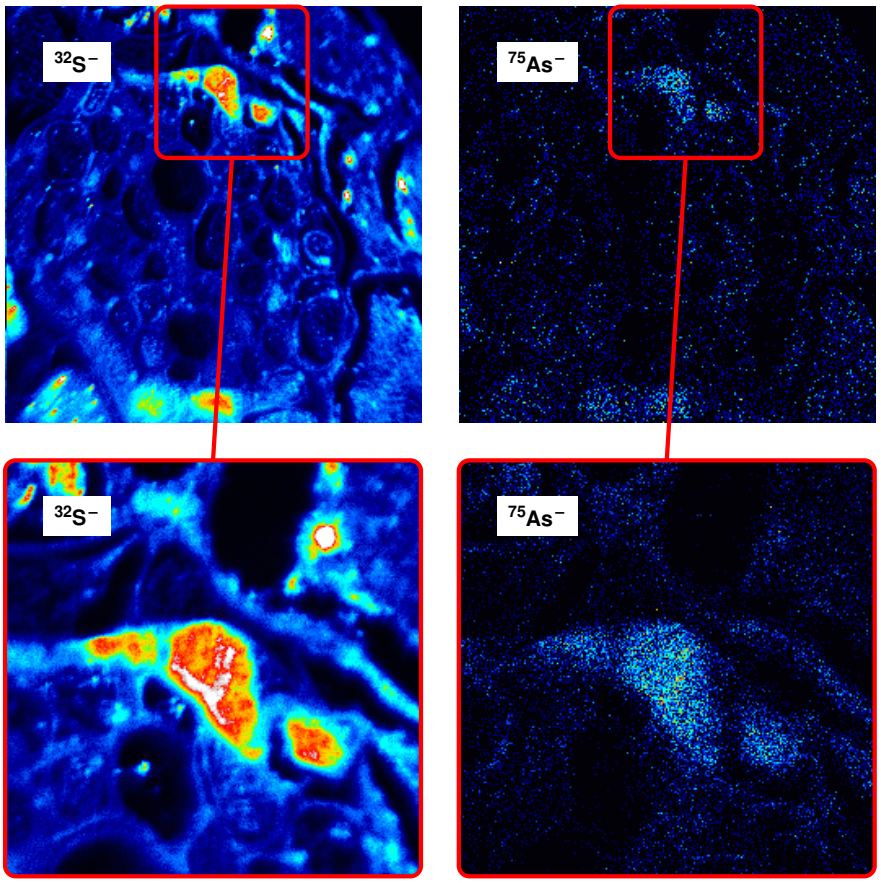

Figure 3.5: Detail of $^{32}S^-$ and $^{75}As^-$ signals showing region of high concentration. Top: 50µm rastor, 60ms/pixel dwell time. Bottom: 20µm rastor, 60ms/pixel dwell time

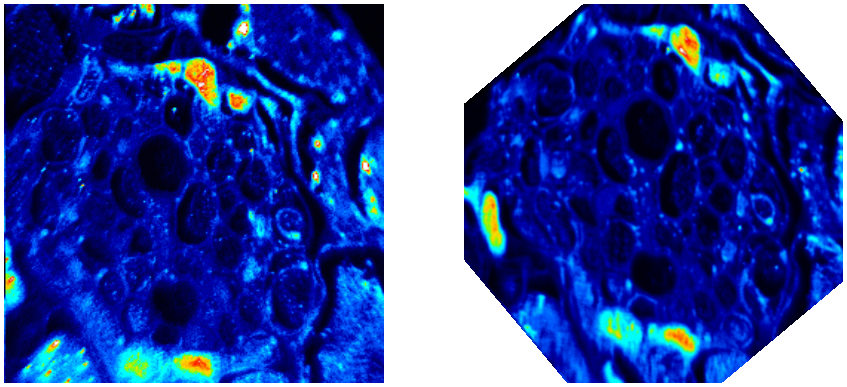

Figure 3.6: Comparison between the $^{32}S^-$ signal from section 3 (left) and section 7 (right)

in this experiment varies very little. We can be confident that on these scales we are unlikely to microtome by chance a particularly unusual feature that is unrepresentative of the rest of the sample.

The data was sufficiently clear that it is possible to compare it to diagrams of the root structure and identify the type and function of some of the cells observed. The low $^{31}P^{12}C^-$ signal from protoxylem and metaxylem made identifying them trivial. Other cells were deduced from their shapes and location relative to the xylem. An example of this process, figure 3.7, shows the SE image from section 4 (a) a diagram of an *A. Thaliana* root adapted from Miyashima *et al.* [177] (b), and the SE image again but this time colour coded to match the diagram (c).

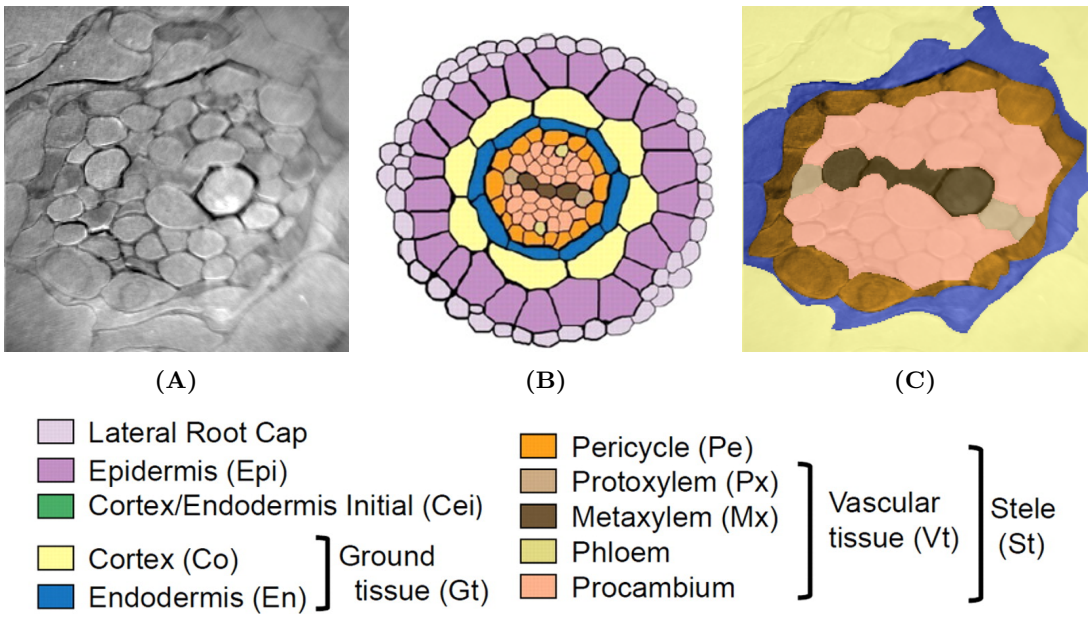

Figure 3.7: (*a*), SE signal from same arabidopsis root shown in figure 3.3; (*b*), diagram of cell types in arabidopsis thaliana roots Reprinted with permission from *Non-cell-autonomous microRNA165 acts in a dose-dependent manner to regulate multiple differentiation status in the Arabidopsis root*, S Miyashima *et al.*, Development 138, 2303-2313. Copyright 2011 Company of Biolgists; (*c*), SE signal colour coded using the same key as *a*.

3.4 Discussion

The similarities in the data suggests that NanoSIMS analysis of a specific cross section is representative of surrounding root tissue on the order of ±10 µm. To check this is a reasonable assumption I considered the size of the cells relative to the scale on which the experiments take place. Root cells are typically several times longer than they are wide and since the 50µm image is represented by 256x256 pixels, we can calculate the size of the cells by measuring the width, in pixels, of the cells on the image:

$$1px = \frac{50}{256} = 0.195\mu m$$

Using this scale for some simple measurements on the sample revealed that the typical cells in the stele had a diameter of a few microns, a list of these measurements are provided in table 3.1. These measurements suggest that the cells are likely to be longer than the nine micrometers that were examined, and therefore provides additional evidence to suggest that there is little biological variation along the length of root at this scale.

Table 3.1: A table of cell dimensions along their longest and shortest cross sectional axes, all measurements in µm.

	Cell					
Axis	A	B	C	D	E	F
Axis-1	3.5	9.8	3.9	2.7	4.1	3.1
Axis-2	5.5	4.7	6.3	3.9	4.7	3.9
Mean	4.7					
StDev	1.9					

This same data also offers a very valuable opportunity to assess the repeatability of

NanoSIMS analysis and consequently the suitability for quantitative analysis.

3.4.1 Normalisation

In this section I will describe the method by which I proposed and tested various methods that could be used for normalising the NanoSIMS data in an attempt to correct some of the systematic variations present in the results.

As the structure of the root was so similar from one section to the next, it was possible to load the NanoSIMS data into the image analysis software, highlight a particular cell as a region of interest (ROI) and save the average counts within that ROI. In this way it is possible to compare a cell to exactly the same cell in another section. Even though the orientation of each image was slightly different, it was possible to identify each cell in all of these consecutive sections and compare the measured chemical composition between them.

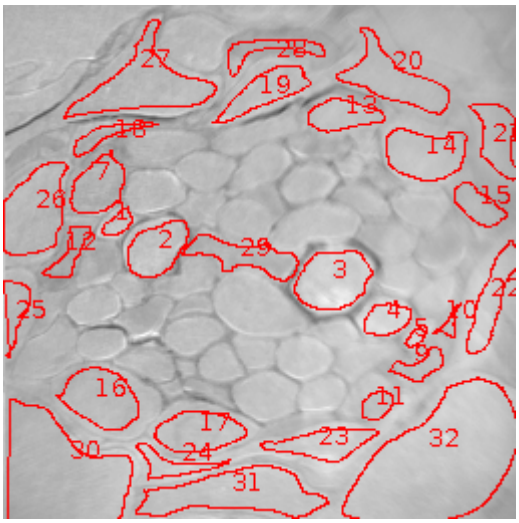

Figure 3.8: Example of how the root cells were identified and selected as regions of interest in the OpenMIMS software.

Therefore a range of different cell types within the root were identified and numbered.

In total 25 individual cells were labelled for this experiment, as shown in figure 3.8. The same cell was then identified as a ROI and given the same number in all of the consecutive sections. The mean ion intensity was then pulled from each of the numbered cells by highlighting them in the OpenMIMS software. This was repeated for each of the consecutively microtomed section of root such that the signal from all five detectors was collected from each numbered cell on each section.

I can then compare the mean ion intensity from each cell across all the sections. For example a graph containing all the $^{75}As^-$ data from the consecutive sections is shown in figure 3.9, where 'cell number' refers to the same cell as identified across all of the consecutive sections. The microtome sections from which the data was collected are identified in the legend.

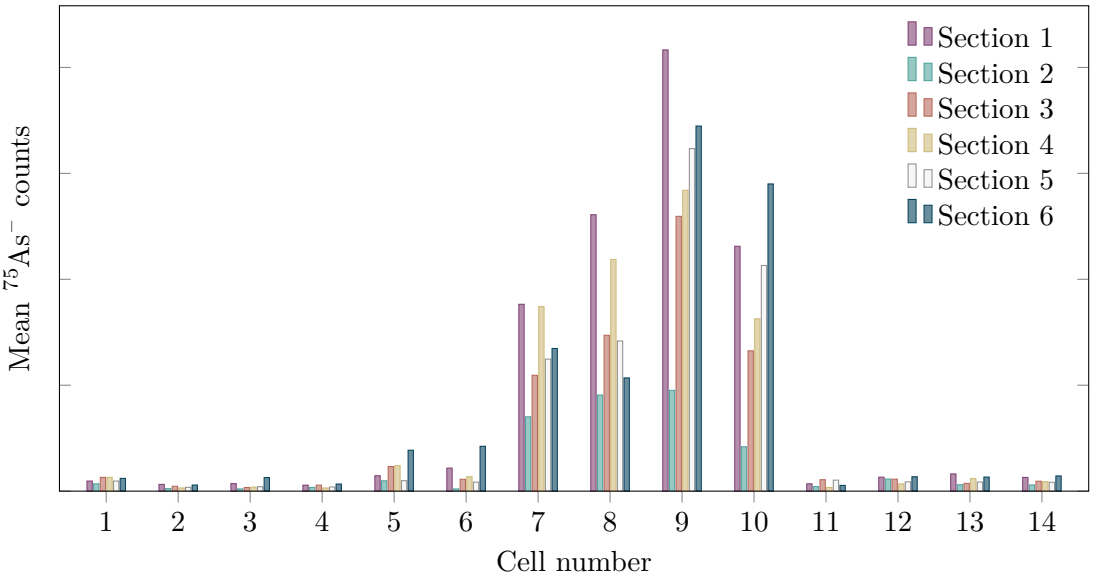

Figure 3.9: Mean $^{75}As^-$ counts recorded from each cell. The section number is given in the legend.

Some of the cells of interest fell outside of the analysed region in some sections, therefore

there are a few gaps in the data, for simplicity only the As signal recorded from cells 1 to 14 and in sections 1 to 6 are displayed in figure 3.9.

Cells 1-4 exhibited very low $^{75}As^-$ signal, and cells 7-10 recorded the highest. The intensities were similar across all the sections with the exception of section 2 which has a lower recorded values across almost all the cells. On further inspection of the data, it appears that the tuning for $^{75}As^-$ may have been slightly incorrect for this sample, and much less signal was recorded than expected. As will be discussed later, the As and S signals should be closely correlated in these samples, however in this particular case there was a large disparity between the two.

Although the general trends are quite clear, the variations from one section to another are quite large. In order to quantify these variations, the ion signals from each individual cell were combined together to provide a mean and standard deviation for that cell as recorded across all the different sections and plotted as a bar graph, figure 3.10.

If the recorded data was exactly the same we would expect to see very small standard deviations, but this is not the case despite the samples and the analytical conditions being as similar as reasonably possible from one section to the next. This demonstrates the difficulty with quantitative NanoSIMS analysis of biological materials, and the need for a normalisation method.

Even with the high variances the data still clearly shows some qualitative differences in the As concentration from different cells. For example a Student's *t*-test applied to the mean $^{75}As^-$ counts from cells 7-10 compared to the mean from cells 11-14 gave a probability of 8.8×10^{-11} that they were from the same population. This makes a very strong case for

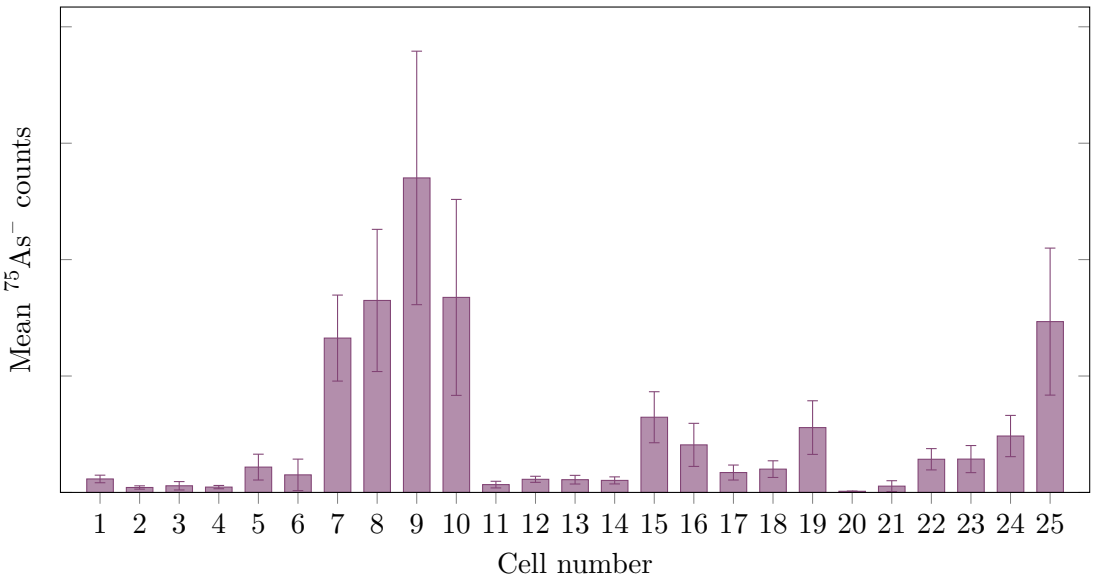

Figure 3.10: Mean $^{75}As^-$ counts recorded for each cell, averaged across all sections. Error bars represent ± one standard deviation

quantitative differences in As concentration in different parts of the root.

Normalisation methods

I proposed several methods of normalisation. The following list presents names of the normalisation methods along with a description of the method:

Mean Data before normalisation.

SIB CN The secondary ion beam (SIB) alignment data was recorded before each analysis, both on the sample and on a reference standard (typically GaAs). The signal from each sample was divided by the maximum $^{12}C^{14}N^-$ value from its corresponding SIB graph.

SIB Cl Same as above but the $^{35}Cl^-$ signal was used instead. Cl is present in large quantities in the resin used to preserve the samples, so both CN and Cl should consistently

be present in high concentrations with low variation in each sample.

Mean CN In this case the signal from each ROI was divided by the $^{12}C^{14}N^-$ signal from the same ROI.

Mean Cl Same as above but the $^{35}Cl^-$ signal was used instead.

Total CN This method involved dividing all the signals from each raster by the total $^{12}C^{14}N^-$ signal recorded over the entire image.

Total Cl Same as above but the $^{35}Cl^-$ signal was used instead.

Norm cx The signal from each sample was divided by the mean $^{12}C^{14}N^-$ signal from the central xylem of the respective sample. The central xylem is large and easily identifiable and we might assume that it contains approximately the same concentration of CN in each sample.

The sample standard deviation gives us an absolute value for how far the observed results fall from their mean, but it is not a useful tool for comparing how much spread there is in the data when considering different data sets. The sample standard deviation, s, divided by the sample mean, $\bar{x}$, provides a much more useful tool called the 'estimated coefficient of variation.'

$$\widehat{c_v} = \frac{s}{\bar{x}}$$

This provides us with a unitless value that can be used to compare variance between different samples. In order to assess the different normalisation methods listed on page 84,

I generated a table that contained the mean ion intensity from all of the cells analysed, with each column representing the measured intensity from a different ion detector. Additional columns containing the same data after normalisation were then appended to the table. The variances between cells from different sections were calculated for each of these columns, such that there was a measured variance for each cell before and after each normalisation was applied. The purpose of this was to establish how variance would be affected by the normalisations. The effectiveness of normalisation was determined by the variance in the data after the normalisation had been applied.

I then calculated the average variance for each of the ion detectors, repeating this for each of the normalisation methods. The mean variances are represented as a column graph in figure 3.11. In this graph the series titled "mean" is simply the mean of the variances between similar cells in the analysed data. The other series are calculated in the same fashion, but after the normalisation methods described on page 84 were applied.

Figure 3.11 shows that the data contains large variances between these sections on all the detectors and with all the normalisation methods. In many cases the normalisation increases the variance rather than decreases it. The elements of greatest interest for these samples are $^{32}S^-$ and $^{75}As^-$. For these elements it was typically the normalisation methods based around the chlorine signal that were most effective at decreasing the variance. We can expect that tuning to $^{35}Cl^-$ would provide a fairly strong and uniform signal across the whole sample (like that shown in fig. 3.4) because of the Cl present in the resin and therefore provide a useful standard against which to calibrate the rest of the associated data.

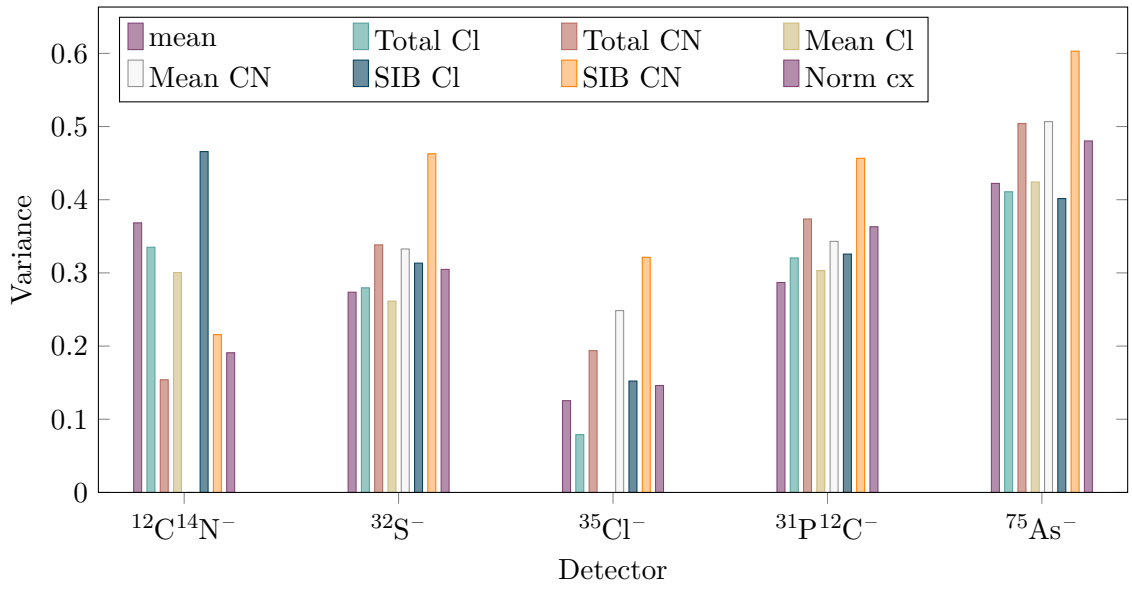

Figure 3.11: Mean variances of the cells analysed for each detector. Each series represents a different normalisation method, labelled in the legend and described on page 84.

This data shows that the normalisation methods tested decreased variance better when examining the data from some detectors than others. Averaging these variances across the detectors will give an indication of which normalisation methods are the best over all of the detectors. However for detectors tuned to $^{12}C^{14}N^-$ and $^{35}Cl^-$ some of the data is normalised against itself. This causes very apparent low variances in detectors that are not of particular importance for quantitative analysis, skewing the average variance downwards. Figure 3.12 contains the mean variances between samples after different normalisation methods had been applied.

From these results we come to the unfortunate conclusion that only one of the normalisation methods were effective at decreasing the variance from the raw data. The "Total Cl" normalisation technique is the only one examined that decreased the variance. It does, however, require tuning one of the detectors to a mass range that is not particularly relevant

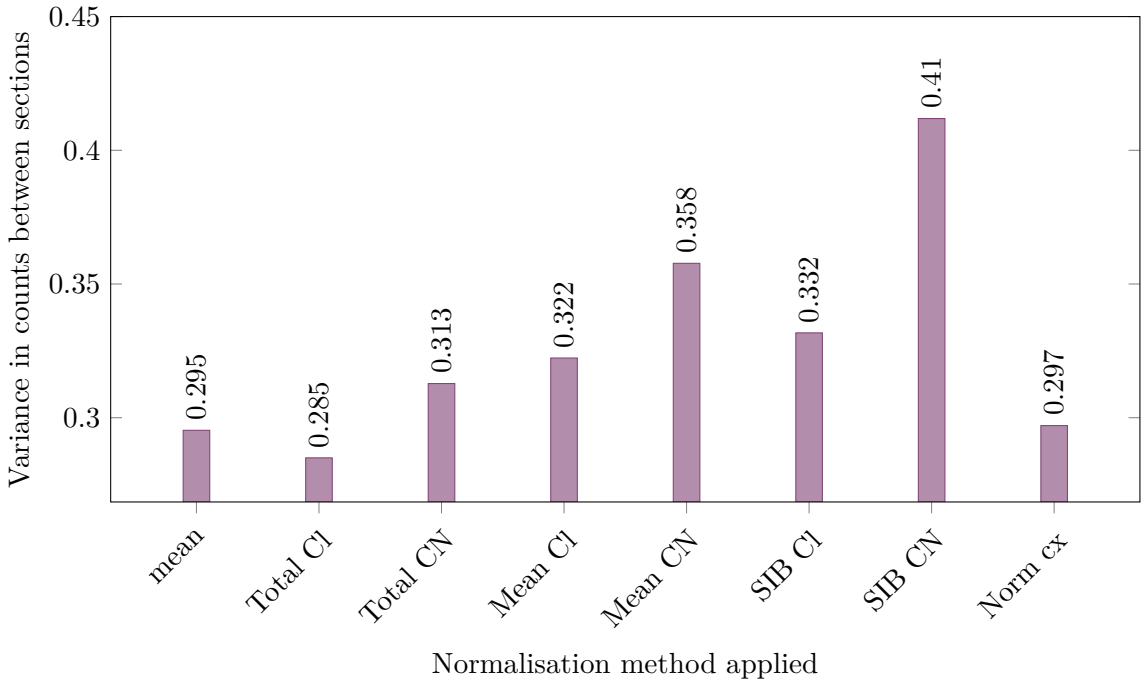

Figure 3.12: Mean variances in ion counts between sections after different normalisation methods have been applied.

to the aims of my later experiments. "Norm cx" where the $^{12}C^{14}N^-$ signal from the central xylem is used to normalise the rest of the data in the same scan, was the next best method and produced only a very small increase in variance.

The high variances and ineffective normalisation methods are likely to be due to the difficulty accurately tuning and recording data with NanoSIMS, the ambiguity of the location of cell boundaries when highlighting regions of interest, and the natural variation of biological samples. Despite this I maintain that it is still very important to apply some normalisation method. Changes in primary ion current, B-field, sputtering rate or dwell time can result in significant systematic variations that can be eliminated by this normalisation. The Cs source is consumed during use, causing the primary ion current to decrease.

In normal operation this can be corrected by increasing the heating current and extraction voltage on the source. However depletion of the source, occasional adjustments to source voltages and current, replacement of source once or twice a year, and source instability can result in significant changes in primary ion current over the course of several months.

For this experiment data was collected within the space of a week with a relatively stable source and with identical aperture and raster settings. There would have thus been little systematic variation in the ion intensities collected and consequently normalisation appeared to have very little effect. Despite this, from my experience with NanoSIMS operation, the primary ion current can be up to four times greater at the start of a source's life than that at the end of its lifetime.

Even with accurate knowledge of the primary beam current selecting different raster sizes, pixel size and dwell times could all contribute to two sets of data not being directly comparable without some form of normalisation. Additionally different concentrations of primary ion implantations prior to analysis is known to alter the work function and therefore ion yield of the sample surface.

For these reasons I believe it is very important to employ some normalisation method and for the psuedo-quantitative analysis in later chapters I will use the normalisation method "Norm cx" described on page 85.

An alternative method is to measure the beam current for every D1 aperture position at the start of each day of experiments using the faraday cup Fc0 and use this current to normalise the data. My experience was that readings from Fc0 were inconsistent, as evidenced by the 3.6% decrease in counts per second measured over an approximately

15 min period, figure 3.13. Either this data is accurate and the beam is very unstable, or this is not accurate and Fc0 measurements are unreliable. In both cases a method for more reliably normalising the data is preferable.

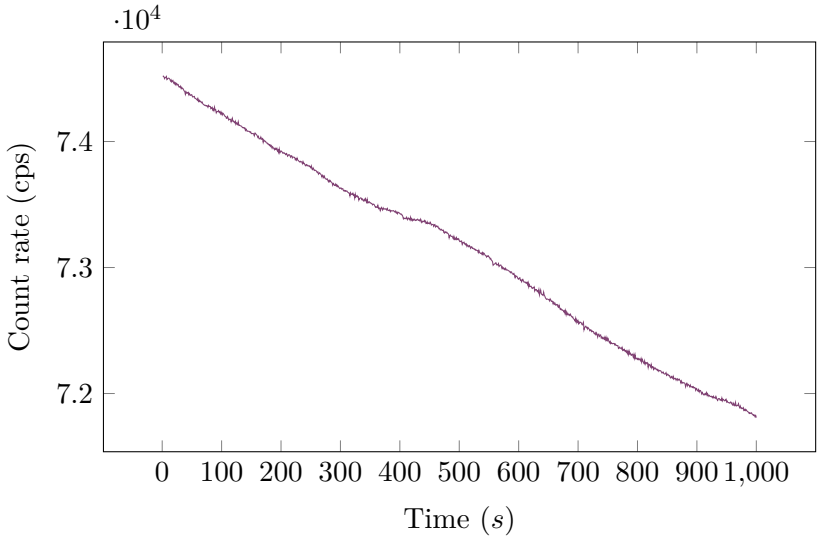

Figure 3.13: Beam stability data showing primary ion beam current as measured by Fc0. CT/Point: 1.000 s. Number of points: 1000

3.5 Conclusion

These experiments demonstrate that despite the NanoSIMS being able to detect very low concentrations of specific elements, minor analytical differences can result in relatively large varations in recorded ion concentrations between samples that should otherwise be almost identical. A selection of normalisation protocols did not significantly decrease the variance in this experiment, but one of the more successful and practical methods (Norm cx) will be employed in later experiments in order to compare samples that may have been analysed under different primary beam conditions.

Chapter 4

Lsi3 mutation

4.1 Aims

The recently discovered gene *Lsi3* is responsible for encoding a Si transporter that is suspected to also permit movement of As(III) ions. The aim of this chapter is to study the possible role of Lsi3 in the uptake of As. It is suspected that the expression of *Lsi3* may change along the length of the roots, so this experiment also aims to examine how the As and Si distributions change at different distances along the root tip.

4.2 Method

Two plant lines were grown at Rothamsted Research, an RNAi line of Lsi3 transporter defective *O. Sativa* (*lsi3*) and its respective wild type (WT). A description of the plant lines and growth conditions are given in Sections 2.2 and 2.3.

Small sections of root were cut at distances of 1 cm, 2 cm and 5 cm from the root tip, and preserved using the high pressure freezing (HPF) and resin embedding methods as described in Section 2.4.

The resin embedding process takes several days and does not always produce well preserved roots. The HPF process is also not always successful, but this process is relatively fast and damaged samples can immediately be identified and discarded. I made sure that for each of the samples listed in Table 4.1 four lengths of root, approximately 2 mm long,

Table 4.1: Samples prepared for HPF, their plant line, and the distance from the root tip from which they were harvested.

Preservation method	Sample number	Plant variant	Distance (cm)
HPF	397	WT	1
HPF	398	WT	2
HPF	399	WT	5
HPF	400	*lsi3*	1
HPF	401	*lsi3*	2
HPF	402	*lsi3*	5

were successfully frozen and could be reliably passed into the resin embedding process. This way I was able to maximise the chances of having several well preserved samples of the same type.

Following the preservation processes, the samples were microtomed, mounted on substrates, optically mapped, and loaded into the NanoSIMS.

The NanoSIMS was tuned to detect $^{12}C^{14}N^-$, $^{28}Si^-$, $^{32}S^-$, $^{31}P^{12}C^-$, $^{75}As^-$ ions as described in section 2.7.4.

4.3 Results

4.3.1 Sample Preservation

Thanks to the efforts of my collaborators at Oxford Brookes University the preservation of the samples was on the whole very good, as will be shown below. The preserved roots were uniformly aligned along the length of their respective resin blocks such that it was possible to microtome cross sections of the root.

The sections, once prepared on substrates ready for NanoSIMS, were first examined in an optical microscope. In addition to providing optical maps useful for navigating the samples

once in the NanoSIMS, this also allows easy to interpret micrographs to be recorded. Such inspection can reveal scratches, unevenness, breaks, tears or other defects in the sections.

Some of the root sections appeared to contain very few cells and it is possible that some biological material was lost during high pressure freezing because of the extreme physical conditions exerted by the process.

Before the root sections could be microtomed it was necessary to trim off the excess resin. Large microtome sections are difficult to handle, and it was possible to only cut a maximum thickness of 1 µm. Therefore I carefully removed as much resin as possible from around the root with a clean razor blade. Furthermore I cut off a few micrometers from the exposed end of the root, as it may have been damaged or contaminated when it was removed from the plant.

During the cutting and shaping process some of the preserved roots were accidentally damaged. Despite this, I still managed to prepare good quality cross sections from each of the samples. An example of such a cross section is shown in figure 4.1, where we can see four 1 µm thick microtomed samples of preserved root along with the resin medium in which they were embedded.

The more mature sections of root, taken 5 cm from the root tip, had a much larger diameter. Despite trimming the resin very close to the root itself the size of these samples meant that the microtome sections would frequently not lie flat on the substrate, and could consequently contribute to a decrease in mass and spatial resolution. For example the section shown in figure 4.2 is relatively large at 500µm and has not dried completely flat. As evidenced by the change in focus there is a raised ridge running north to south directly

through the middle of the root (A). Areas with poor adhesion to the substrate were avoided for SIMS analysis.

4.3.2 Optical micrographs

Two examples of typical optical micrographs represent sections cut at 1 cm and 5 cm from the root tip can be seen in figures 4.1 and 4.2, respectively. The scale bars on these images show that the sections from more mature root are considerably larger than those closer to the root tip.

4.3.3 NanoSIMS data

In total 107 measurements were made in the NanoSIMS on these samples. An example of some typical data can be seen in figure 4.3. It shows good preservation of the sample and sharp clearly defined outlines to most of the cells. Similar to the *A. thaliana* sections in chapter 3 a large cell with low $^{31}P^{12}C^-$ signal is visible in the centre of the root (A).

A ring of cells surrounded with a high $^{28}Si^-$ signal on their cell walls runs through the centre of the analysed area (B). The $^{32}S^-$ signal appears more evenly throughout the sample, but has high concentrations in a few specific cells (C) adjacent to cells with relatively low signal from most detectors, especially $^{31}P^{12}C^-$ (D). The $^{75}As^-$ signal is very low and appears predominantly in the same cells that produced the highest $^{32}S^-$ signal (C).

Comparing the NanoSIMS images with published data on *O. Sativa* roots, figure 4.4, we can confirm that the large central region is a metaxylem vessel. When studying Si transport Sparks *et al.* [178] determined that Si is predominantly "localized in the suberized

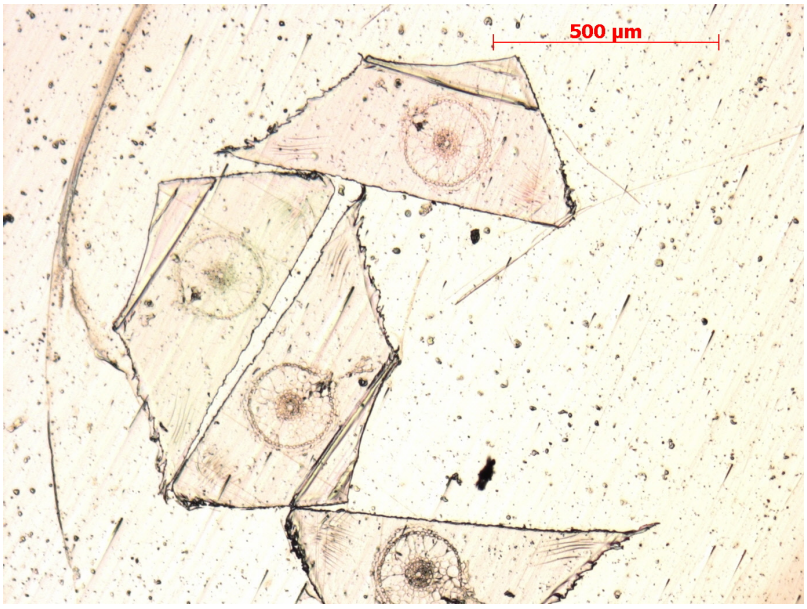

Figure 4.1: Optical micrograph of four preserved and microtomed sections of *O. Sativa* root, harvested 1 cm from root tip, mounted for analysis.

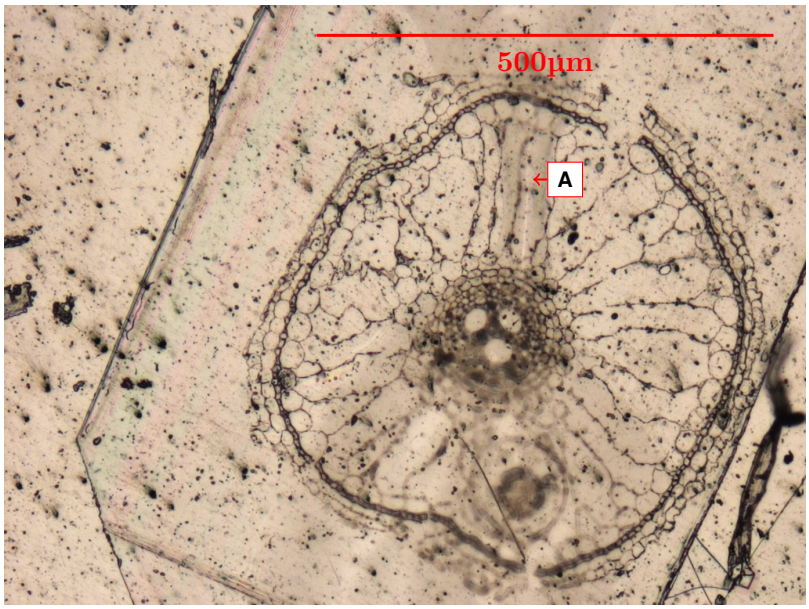

Figure 4.2: Optical micrograph of a preserved and microtomed section of *O. Sativa* root, harvested 5 cm from root tip, mounted for analysis.

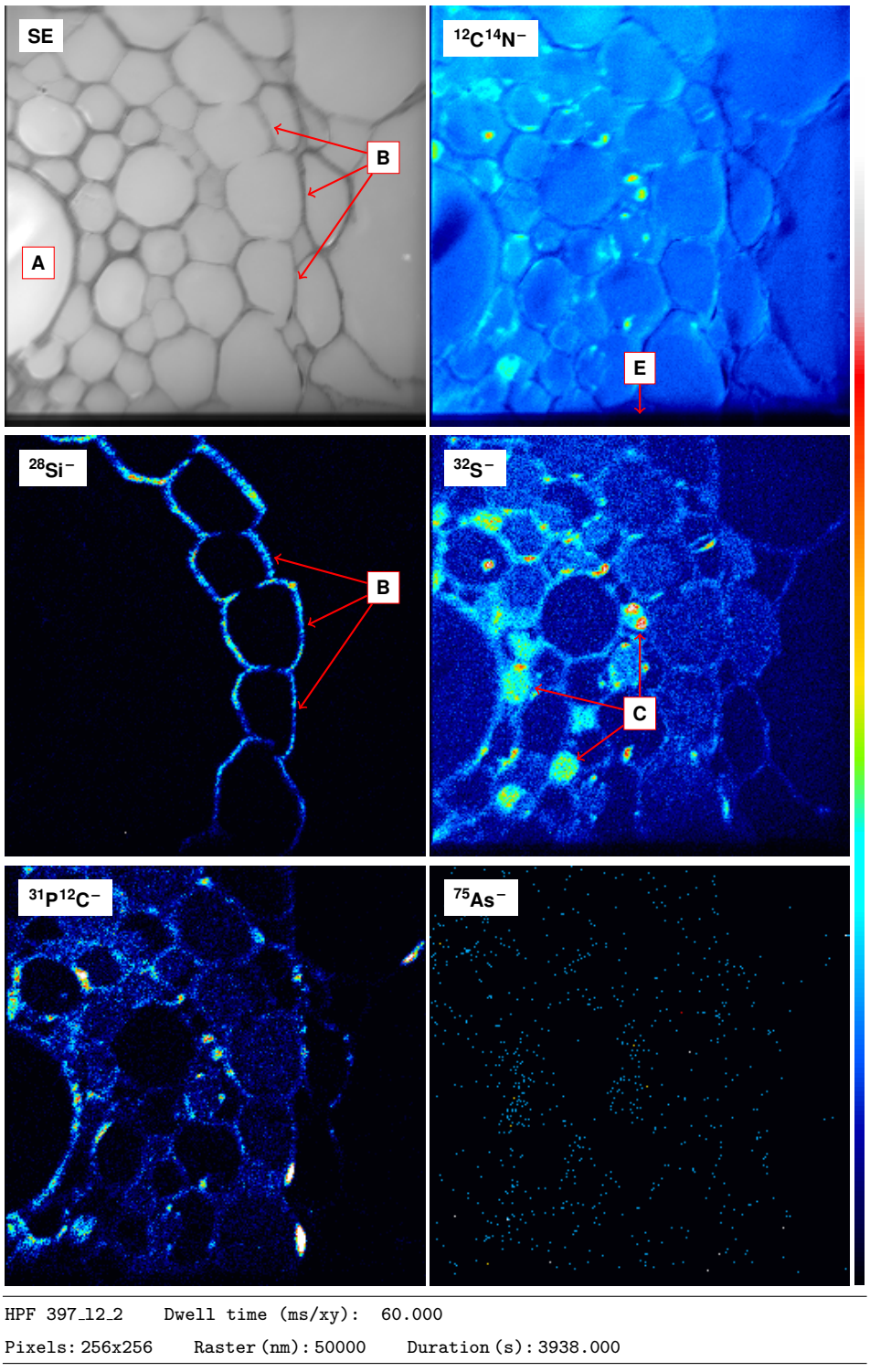

Figure 4.3: Typical NanoSIMS data set from one of the sections, showing signals from all five ion detectors and from the SE detector. (*a*) Central xylem, (*b*) endodermal cell walls, (*c*) regions in stele with high $^{31}S^-$ signal, (*d*) regions in stele with low $^{31}P^{12}C^-$ signal.

thick-walled region of endodermal cells [...] in close association to the Casparian strip." In addition to matching the shape and location of the cells I was therefore able to tune one detector to measure $^{28}Si^-$ so that I can identify the endodermis as the ring of cells surrounded by a strong $^{28}Si^-$ signal (see fig. 4.4 *e*). It follows that the layer of cells just inside this band form the pericycle — a cylinder of parenchyma or sclerenchyma cells. The very low $^{31}P^{12}C^-$ signal in the central xylem is also observed in other large cells with thick cell walls in the stele, it is possible that these are protoxylem.

This distribution of elements has previously been identified by Moore *et al.* [112, 179] in their study of *lsi2* mutants using a very similar method. They identified As accumulation "in the vacuoles of some xylem parenchyma cells and in some pericycle cells, particularly in the wild-type mature root zone" and that Si "was localized in the cell walls of the endodermal cells". These observations are in good agreement with the data presented in figure 4.3.

Comparing distances along the root

Figure 4.5 shows the data from three WT sections arranged in vertical columns, from left to right, representing 1 cm, 2 cm and 5 cm from the root tip. The central xylem vessel is visible in the lower left corner of all three of the SE images, demonstrating that they were taken in similar areas and with similar orientations. In the Si images at 1 cm and 2 cm the ring of cells that have a strong Si signal in their cell walls is clearly visible. At 5 cm this feature appears less distinct and two of the cells appear to not have Si accumulation on the cell walls.

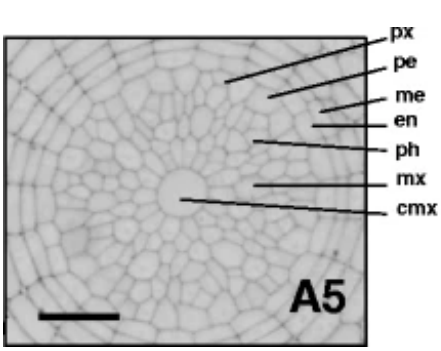

(A) Published optical image

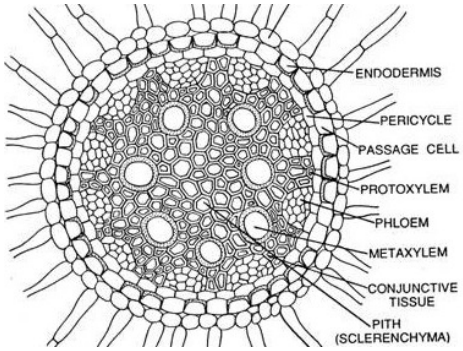

(B) Published diagram

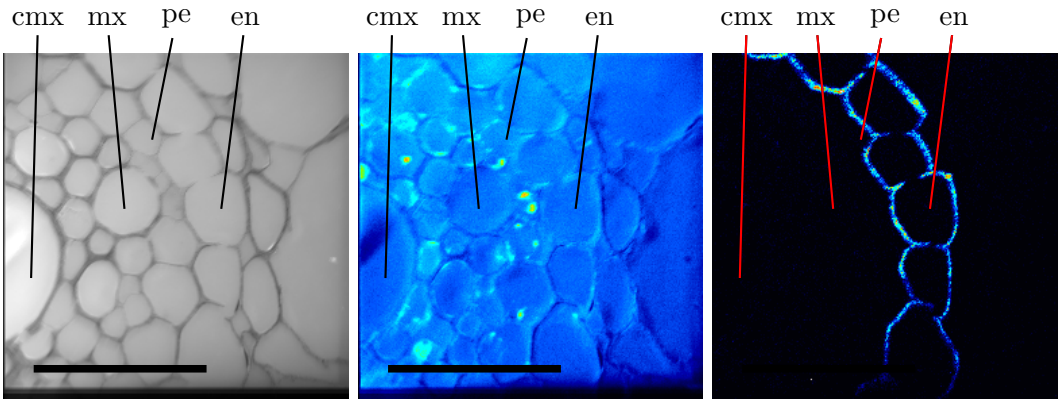

(C) SE signal **(D)** $^{12}C^{14}N^{-}$signal **(E)** $^{28}Si^{-}$ signal

Figure 4.4: Comparison of transverse sections of *O. Sativa* root with published data. (*a*) Labelled optical image from Molecular Genetics of Rice Root Development, J. Rebouillat et al [180]. (*b*) Labelled diagram of mature root section from Characteristics of Monocotyledonous Roots [181]. (*c-e*) NanoSIMS data as seen in figure 4.3. Scale bars 25µm. me, mesodermis; en, endodermis; pe, pericycle; cmx, central metaxylem; mx, metaxylem; ph, phloem; px, protoxylem.

The sulphur (S) signal across all three sections suggests an accumulation of S to much higher concentrations in specific cells, with proportionally much less appearing in the central xylem and cortex. At 1 cm, these differences in concentration are less obvious, and appear predominantly close to the central xylem, with very little S signal outside the cells that expressed higher Si concentration in their cell walls. At 2 cm, high S concentrations were detected in both the smaller cells near the central xylem and in distinct larger cells immediately outside of the boundary of the cells outlined with Si (annotation A). At 5 cm, the S appears concentrated within specific areas inside of the cells within the Si boundary, and more diffusely outside. The As concentrations, although very low, appear to follow a very similar trend to that of S.

Comparing WT and *lsi3* mutant

The same data from the WT section is presented alongside data from one of the *lsi3* sections in figure 4.6; both samples were taken at 1 cm from the root tip. Again the position and orientation is such that the central xylem can be seen in the lower left region of the images, with plenty of cells from the surrounding tissues visible.

The $^{28}Si^-$ signal looks similar in both samples, surrounding a ring of cells that form a boundary between smaller tightly packed cells on the inside and larger more diffuse cells on the outside. The $^{32}S^-$ signal, although appearing in very similar cell types in both samples, seems more localised in *lsi3*. As, again, follows a very similar trend to S in both sections.

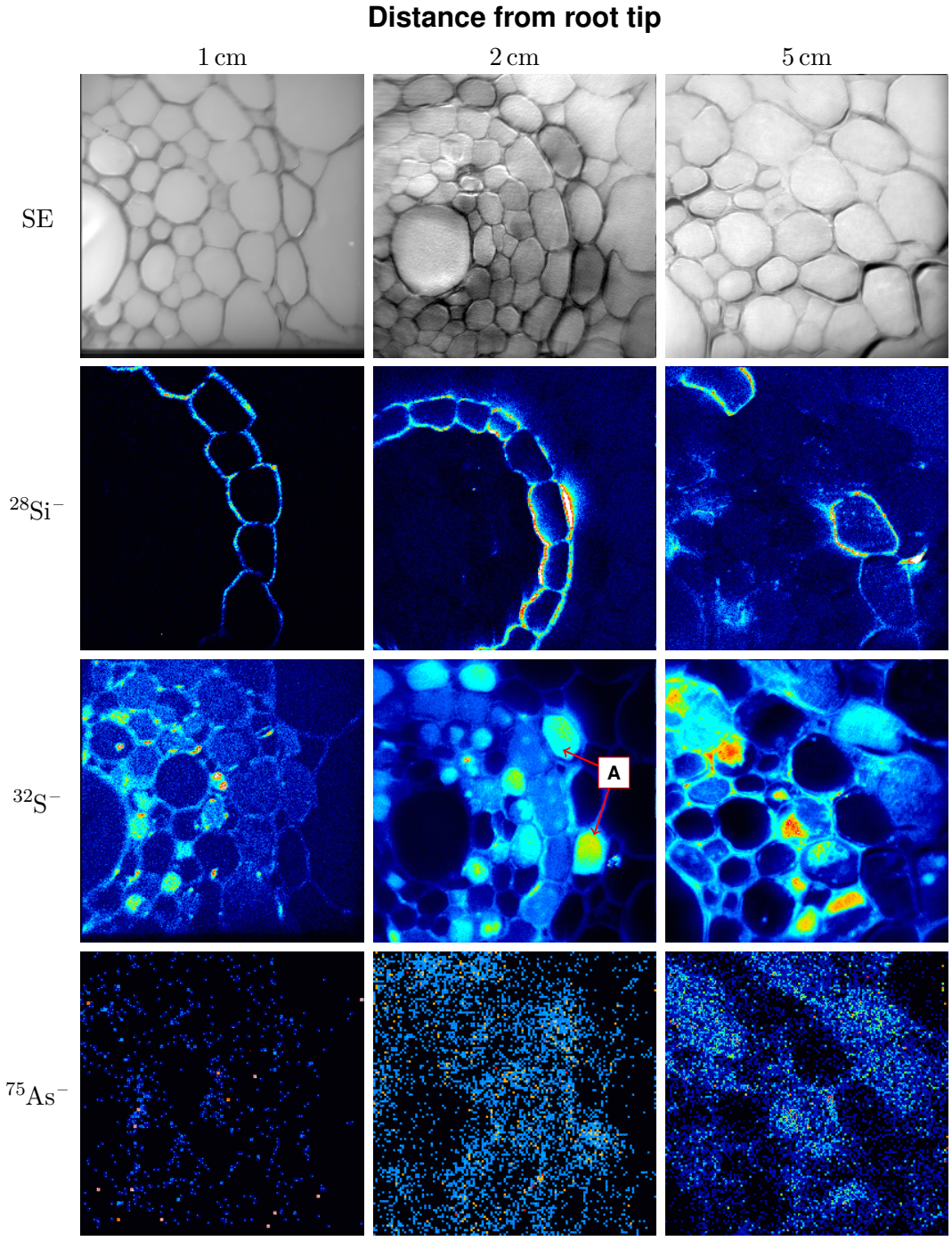

Figure 4.5: Three different wild type samples, cut at different distances from the root tip. (*a*) high $^{32}S^-$ signal containing regions in the cortex.

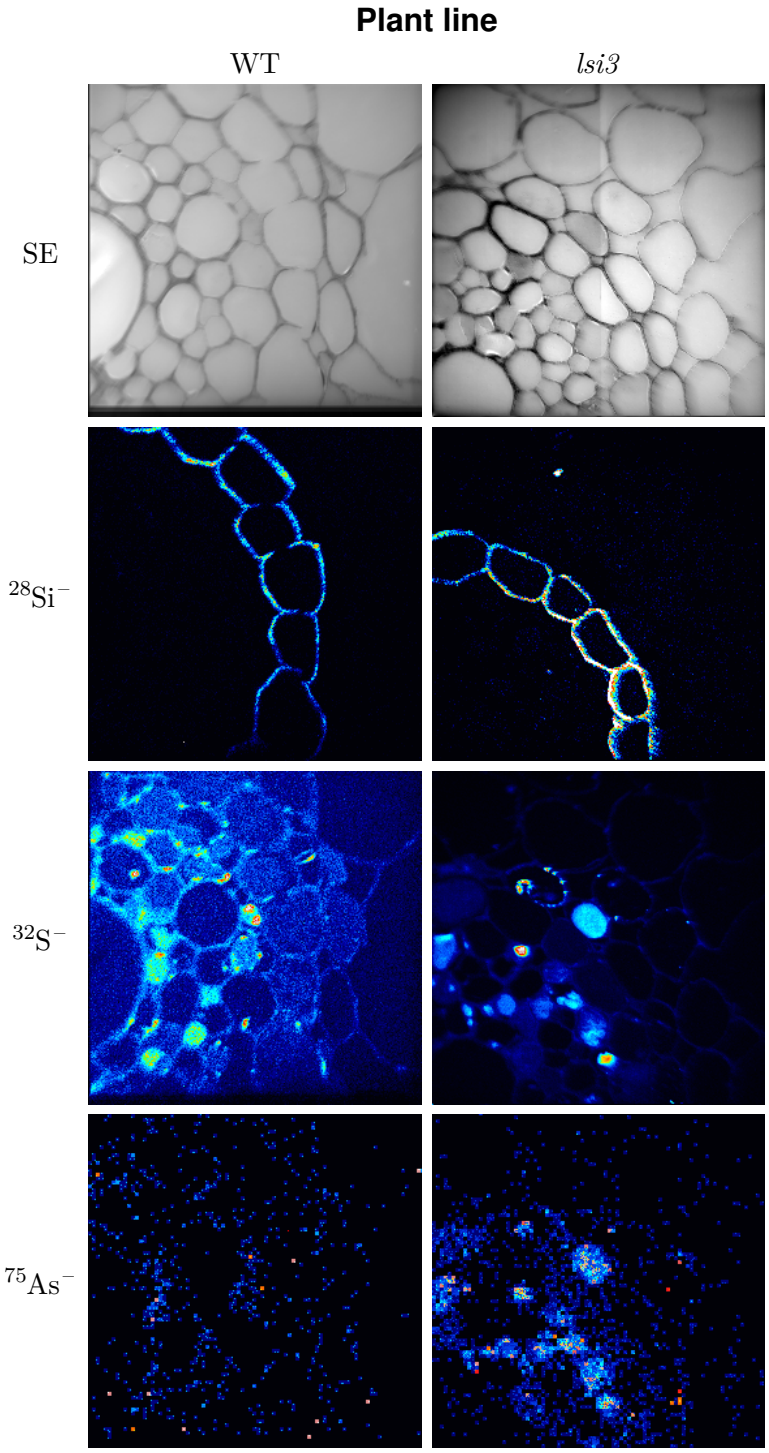

Figure 4.6: Comparison between a WT and an *lsi3* section, both samples 1 cm from root tip. $^{75}As^-$ signal contrast adjusted for visibility.

4.4 Analysis

The data in figures 4.5 and 4.6 are arranged in such a way that direct comparisons can be made between different distances along the root as well as between WT and *lsi3*. The observed differences were described in the results section, but these observations are only very rudimentary and do not allow for a reliable comparison for two main reasons. Firstly, the colour scales depicting ion intensity were calibrated individually for each image, so that no two images share the same scale. Secondly they are not normalised for primary ion current, or other factors that may cause systematic variation in the data.

Making visual comparisons of images in this way is only useful insofar as it can reveal qualitative information on the relative distributions of elements within each sample. For a more quantitative analysis, we must extract the data and attempt to normalise it.

4.4.1 Data analysis

Out of the 107 measurements made in the NanoSIMS, only 15 were chosen for quantitative analysis because the process was very time consuming, required sections of the best preservation, and also required the areas analysed to contain easily identifiable cell groups that also appeared in other samples, such that comparisons could be made. These were regions where expected to see changes in As distribution following the research conducted by Moore *et al.* [179].

In order to minimise selection bias samples were selected only on the following criteria: they contain the central xylem vessel, surrounding cells and cortex; they have no obvious

beam damage or HPF damage and there was good tuning on all 5 detectors. Some particularly notable results were also included despite not fully meeting these criteria. The sections that were selected are listed in table 4.2.

Table 4.2: Samples that were used for quantitative analysis.

Section name	Section type	Dist. from root tip (cm)
397_2a f1 l1_1	WT	1
397_2a f1 l2	WT	1
397_f3_l1_1	WT	1
397_l2_2	WT	1
397_l5_2	WT	1
398_2b f4 l1	WT	2
398 4a f2 l1_2	WT	2
398_f4_l1_6	WT	2
399 3b f1 l2	WT	5
399_f2_l1_1	WT	5
400_2ca_f1_l1_6	*lsi3*	1
400_f1_l1_3	*lsi3*	1
401_f1_l1_3	*lsi3*	2
402_f2_l1_1	*lsi3*	5
402 f3 l1_1	*lsi3*	5

In order to make a semi-quantitative analysis of this experiment I had to extract the NanoSIMS data in a format that would allow for comparisons to be made between samples. First I examined the data and compared it to published data (such as that shown in fig. 4.4) and chose several regions within the root that could easily be identified in all of the samples. The exact type of each cell could not be accurately deduced, therefore cells were instead identified by their position relative to prominent features. These regions are listed in table 4.3 and are labelled in figure 4.7A.

I then used the OpenMIMS software to select ROIs on the NanoSIMS data such that a few cells from each of the regions listed in table 4.3 were highlighted as ROIs. Figure 4.7B

Table 4.3: Areas identified for quantitative analysis.

Region name	Description	Biological feature
CSW	Cell walls containing high Si concentrations	Casparian strip
CSV	Vacuoles of cells surrounded by high Si	Endodermis
ICS1	Cells just inside of the endodermis	Stele\Pericycle
ICS2	Cells immediately inside the pericycle	Stele
OCS	Cells immediately outside the endodermis	Cortex
cx	Large central cell	Central xylem

contains these ROIs highlighted in red. Data (such as pixel value) could then be extracted from each of these ROIs by exporting it from OpenMIMS, and could be labelled according to the region they were associated with. Since these pixel values represent the ion count from their respective detector this gave me a table of relative ion intensities for each of the highlighted regions. This process was relatively simple, but required patience and accuracy to confidently identify and highlight cells of interest.

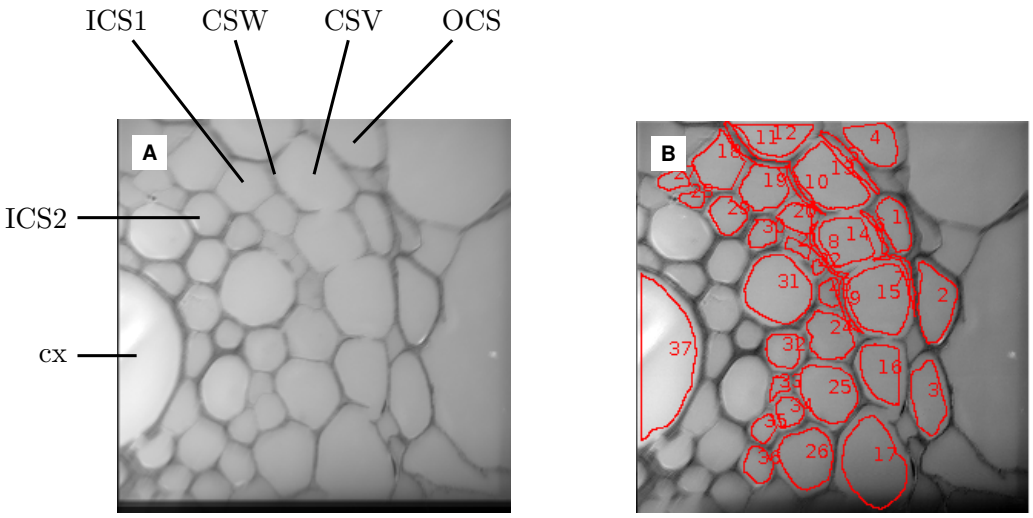

Figure 4.7: Selecting ROIs on a WT section at 1 cm from the root tip, only SE detector image shown. A, areas identified for quantitative analysis, each label points to a different layer of cells, except "CSW" which refers to the walls of the silicon rich cells and "cx" which represents the central xylem. B, NanoSIMS data from the sample after ROIs (marked in red) were selected in the OpenMIMS.

Carefully highlighting cell regions and labelling them was repeated for all of the samples listed in table 4.2. The end result of this analysis is a large spreadsheet that can then be used to compare normalised data between sections.

The first thing that I wanted to determine was how consistent the data was. Carbon-nitrogen bonds are very prevalent in biology and should not be significantly effected by knockout of *Lsi3*. These samples should therefore present relatively similar distributions and normalised counts of $^{12}C^{14}N^-$. In order to test this theory, I averaged the normalised $^{12}C^{14}N^-$ data for each cell region on each sample and added it to a bar graph. I expect that all the cells of the same type will have similar biology and therefore similar yield of $^{12}C^{14}N^-$. Each column in the graph shown in figure 4.8 represents the mean $^{12}C^{14}N^-$ signal from one ROI group averaged across all the cells in the same group in the same sample.

My expectations were proved incorrect; there is quite a large difference in normalised $^{12}C^{14}N^-$ counts between samples. The data suggests two possible sources of these differences. Firstly, on some sections (398_2b_f2_l1) the CN concentration recorded from the central xylem was lower than the rest of the cells analysed. In this case the effect normalising against the counts from the central xylem caused the mean $^{12}C^{14}N^-$ counts from all the other cell types to end up comparatively higher than from most other sections. Examining the NanoSIMS maps of these sections reveals the second possible cause of these results — differences in cell chemistry. This is not unexpected, as the cells were not identified by their biological function but by their relative position with respect to consistently observable and identifiable features. For example a cell labelled ICS1 or ICS2 could have been a phloem, protoxylem or companion cell, and each would have quite distinct biological function and

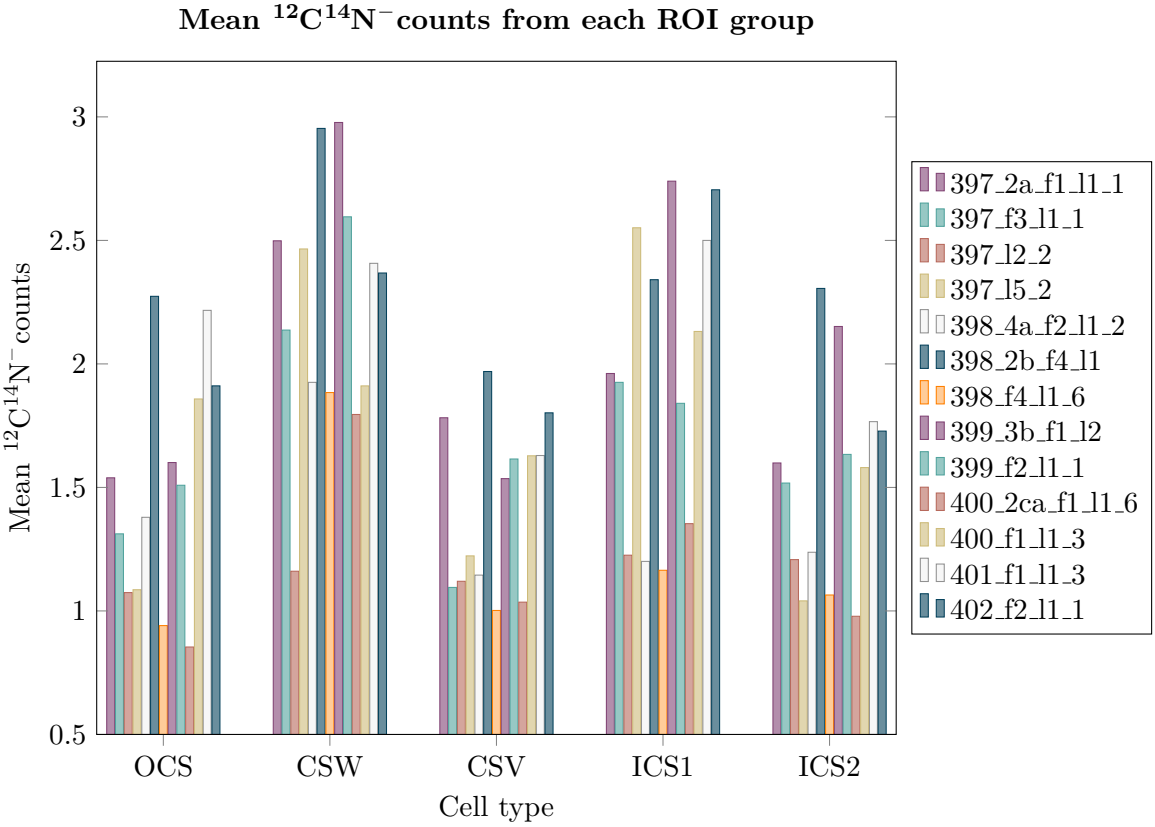

Figure 4.8: Average $^{12}C^{14}N^-$ signal from each of the different ROI groups, names of the sections used are given in the legend.

therefore contain different proteins, hence different $^{12}C^{14}N^-$ yield.

While it is useful to label and group the cells based on their position in the root, this demonstrates that cells from similar positions within the root should not be treated as if they were all identical. I will therefore present each cell as an individual entry on the column graphs, and the columns will be grouped by the cell's position within the root.

After careful analysis of the normalised data for all the sections listed in table 4.2 I chose to reject several of them. The rejected sections are listed in table 4.4 along with brief comments about why they were excluded. In order to make the best comparisons between

WT and *lsi3*, and between different distances from the root tip I was careful to only use the most accurate and representative sections. Unfortunately this meant that the total number of useful sets of data was very low.

Table 4.4: List showing whether sections were used or rejected for further quantitative analysis based on preliminary analysis of normalised data. Section names, plant lines and distance they were haravested from the root tip are also shown.

Section name	Plant line	Dist. (cm)	Used	Notes
397_2a f1 l1_1	WT	1	✓	
397_2a f1 l2	WT	1	✓	Epidermal region
397_f3_l1_1	WT	1	×	Close to lateral root
397_l2_2	WT	1	×	Low $^{75}As^-$ signal
397_l5_2	WT	1	×	Close to lateral root
398_2b f4 l1	WT	2	✓	
398 4a f2 l1_2	WT	2	×	Poor tuning
398_f4_l1_6	WT	2	×	Poor tuning
399 3b f1 l2	WT	5	✓	
399_f2_l1_1	WT	5	×	Low $^{75}As^-$ signal
400_2ca_f1_l1_6	*lsi3*	1	×	Close to lateral root
400_f1_l1_3	*lsi3*	1	✓	
401_f1_l1_3	*lsi3*	2	✓	
402_f2_l1_1	*lsi3*	5	✓	
402 f3 l1_1	*lsi3*	5	✓	

In the top left graph of figure 4.9 the $^{12}C^{14}N^-$counts from each highlighted cell has been plotted on a single bar graph for one section. Here it is possible to see quite significant variation in average $^{12}C^{14}N^-$counts from one cell to another, even within the same cell regions. It can be difficult to determine if these differences were biological or caused by analytical error, but since $^{12}C^{14}N^-$is a relatively easy mass to tune for in the NanoSIMS, it is more likely to be and indication of different biological functions of selected cells. Close to the root tip is a zone of cell division, at greater distances from the root tip there is a zone of elongation and then of differentiation and finally maturation. Regions closer to the root

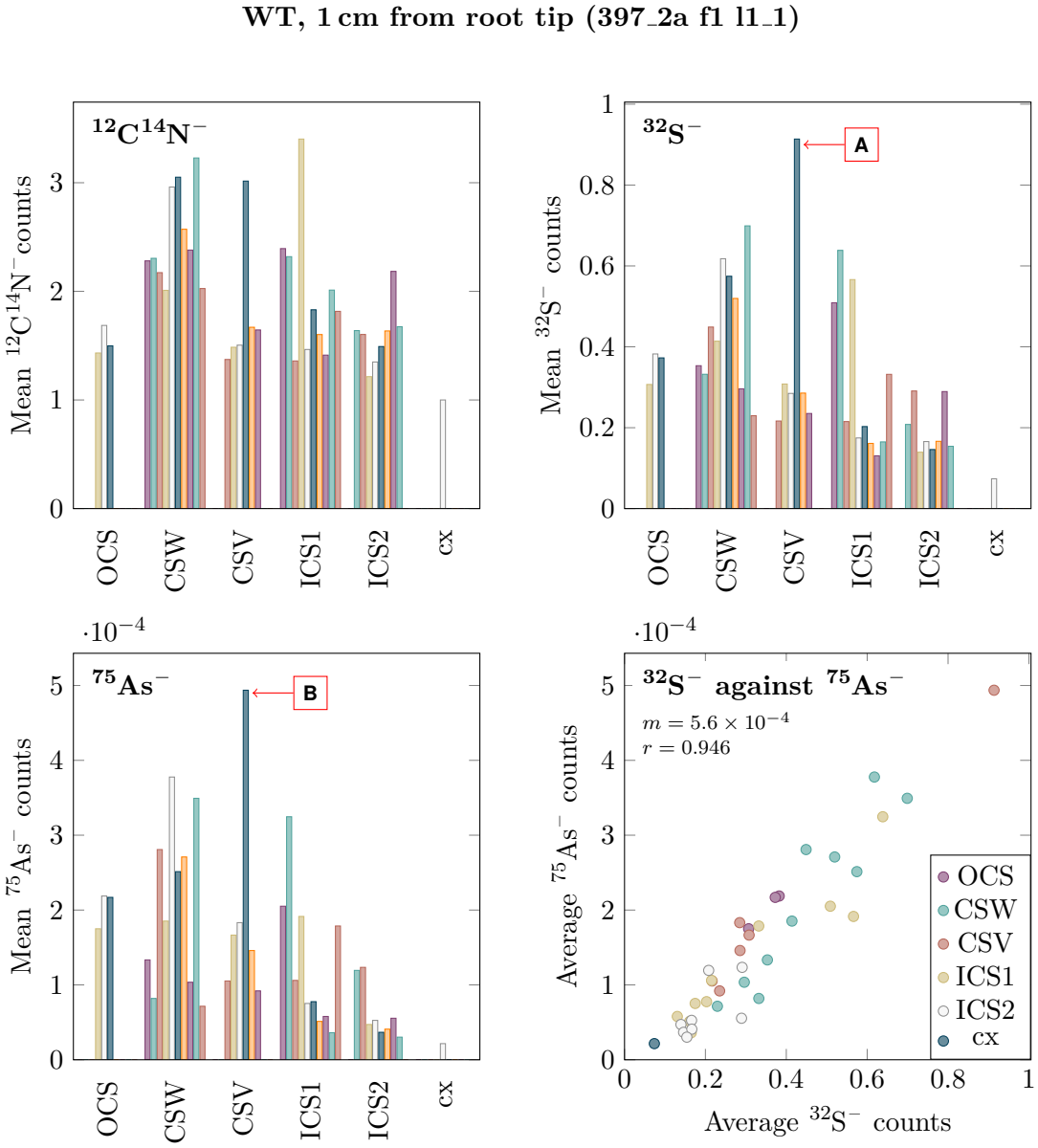

Figure 4.9: Bar graphs of average $^{12}C^{14}N^-$, $^{32}S^-$ and $^{75}As^-$ counts from each ROI. Scatter graph of average $^{75}As^-$ counts against average $^{32}S^-$ counts, (m) linear regression gradient given to two significant figures, (r) Pearson product-moment correlation coefficient give to three significant figures. WT, 1 cm from root tip.

tip therefore involve very high biological activity [180] and contain high concentrations of CN because the active division of cells produces a lot of proteins and small cells with dense protoplasts.

The $^{32}S^-$ signal (fig. 4.9 top right) and $^{75}As^-$ signal (fig. 4.9 bottom left) both show more variation than the $^{12}C^{14}N^-$signal. They share a similar distribution with the largest signal from CSV (annotations A and B), followed by a CSW and ICS1.

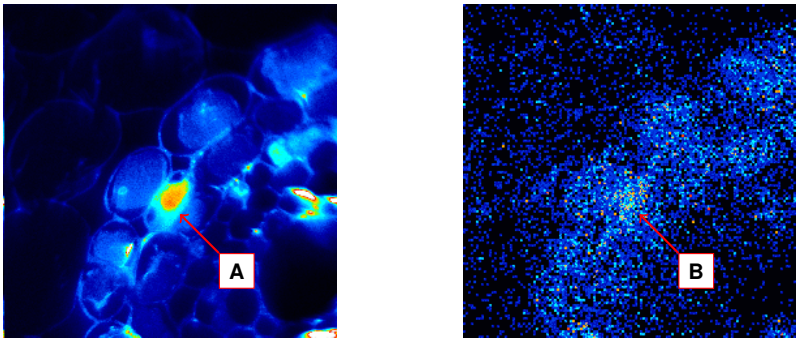

Figure 4.10: Arsenic and sulphur co-localisation, WT 1cm from root tip. Left, $^{32}S^-$ counts. Right, $^{75}As^-$ counts. (*a*) Pericycle cell with high S content, (*b*) the same region on the $^{75}As^-$ image showing high As content.

Plotting mean $^{75}As^-$ signal against mean $^{32}S^-$ signal for each ROI (fig. 4.9 bottom right) gives a correlation coefficient of 0.95, indicating a close relationship between these two elements. To explore the co-localisation of As and S more closely we can look at how they appear in the NanoSIMS ion intensity maps. Comparing $^{75}As^-$ and $^{32}S^-$ signals (eg fig. 4.10) it is quite easy to see that despite the much lower intensity and signal resolution of the As the elements are distributed in a very similar fashion. We can also see that the highest mean $^{32}S^-$ (fig. 4.9 annotation A) and $^{75}As^-$ (fig. 4.9 annotation B) both came from the same region in the pericycle (fig. 4.10 annotations A and B).

The main focus of these experiments is to see how As and S distributions may change

at different distances from the root tip, and if these trends are affected by knockout of *Lsi3*. To meet this aim I repeated this process for roots sections taken at 2 cm and 5 cm from the root tip. The normalised $^{32}S^-$ and $^{75}As^-$ counts from one section at each distance are shown in figure 4.11.

The $^{75}As^-$ graphs, left column, all share a same y-axis scale of between 0 and 5.5×10^{-4}. The $^{32}S^-$ graphs, right column, have an axis range of 0 to 1. This normalised data is clearly very similar in scale across all three sections. A high $^{32}S^-$ and $^{75}As^-$ concentration in one particular CSV region at 1 cm from the root tip (A and B) was not observed at 2 cm and 5 cm. The overall counts of these ions within CSV regions decreased with increasing distance from the root tip, most notably from 2 cm to 5 cm where the average counts of these elements decreased by 78% and 63% respectively. Conversely, within regions closer to the central xylem (ICS1 and ICS2), a slight increase in the concentration of these elements were observed.

Since these ROIs do not cover the whole sample, and because the data can be quite difficult to understand as column graphs, I have also included the NanoSIMS maps for $^{32}S^-$ and $^{75}As^-$ in figure 4.12. These images are not normalised, so care should be taken when comparing them.

The ion intensity maps show that while there was appreciable quantities of $^{32}S^-$ and $^{75}As^-$ measured in CSV at 1 cm and 2 cm from the root tip, there is very little of either in CSV at 5 cm. To better quantify this I plotted average $^{75}As^-$ counts from each ROI group against distance from the root tip, figure 4.13. This graph suggests that on average the concentration of As in the endodermis (CSV) decreases with increasing distance from the

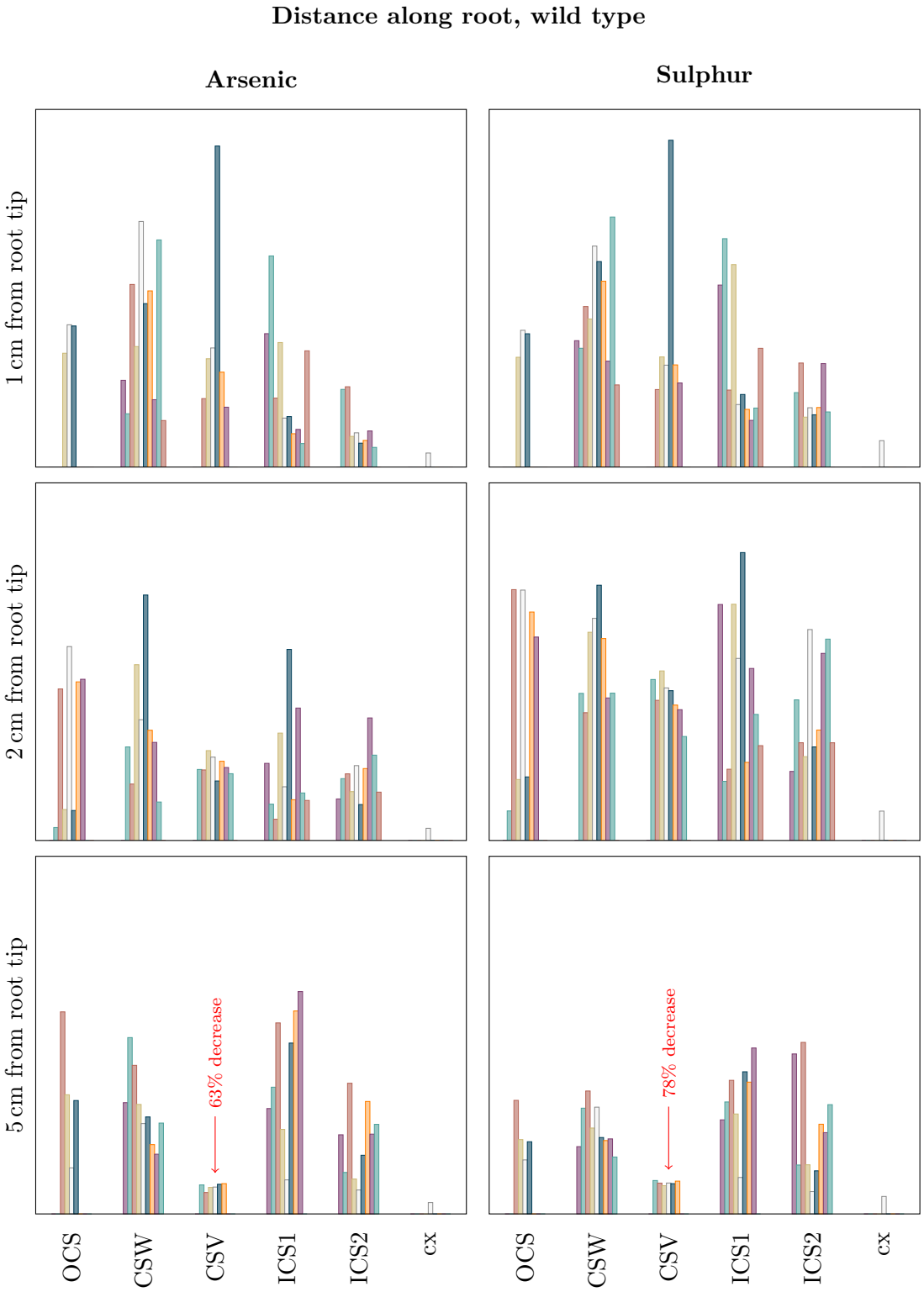

Figure 4.11: Normalised ion counts from WT sections at different distances along the root. Left column; $^{75}As^{-}$ counts, y-min 0, y-max 5.5×10^{-4}. Right column; $^{32}S^{-}$ counts, y-min 0, y-max 1

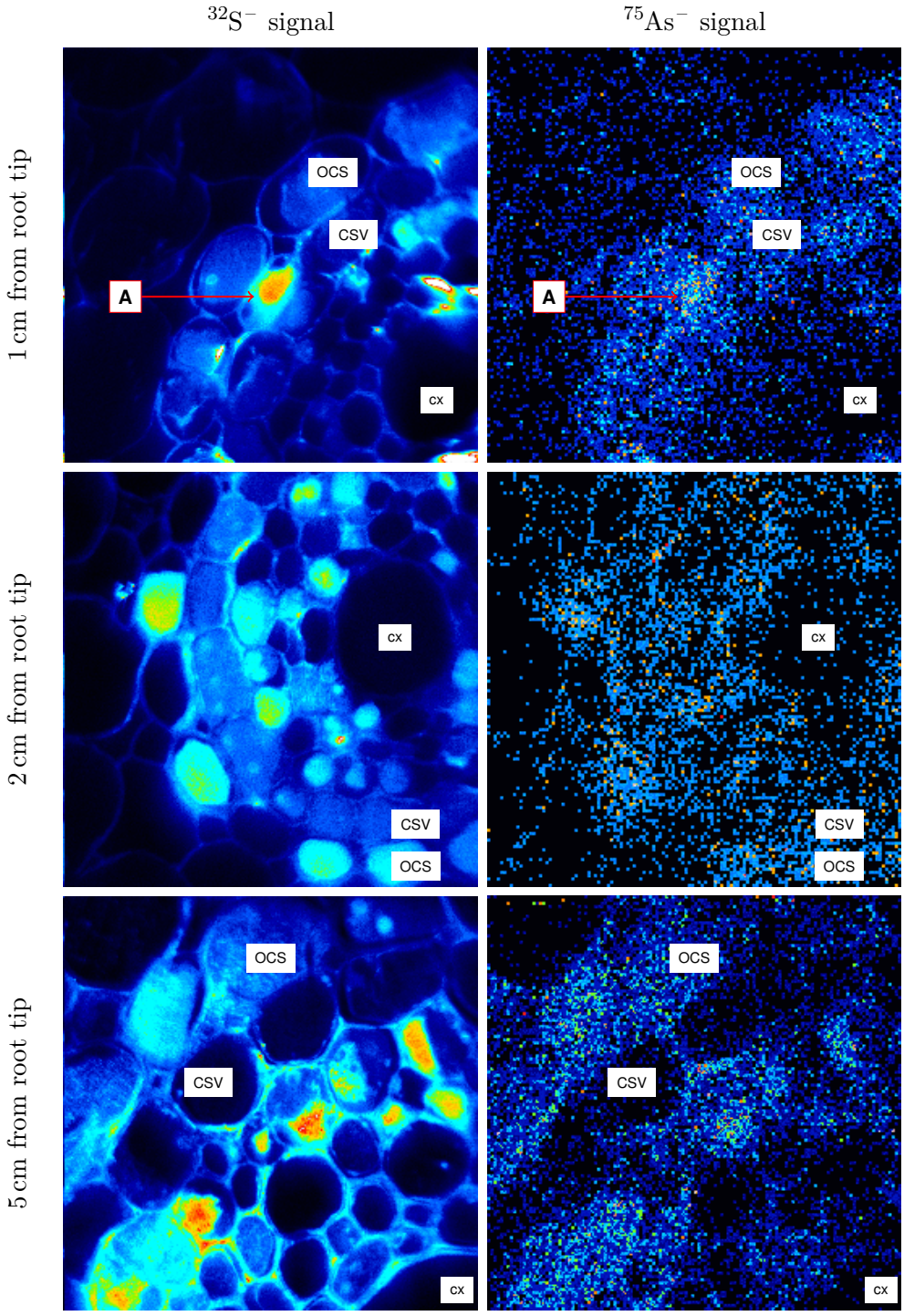

Figure 4.12: Maps of $^{32}S^-$ and $^{75}As^-$ counts at different distances from the root tip, WT. cx, central xylem; CSV, endodermis; OCS, cortex closest to endodermis.

root tip, and that it increases in the pericycle (ICS1).

The SIMS maps also show that the $^{32}S^-$ and $^{75}As^-$ signals are spread out over much of the analysed region. There are many cells in the samples containing slightly elevated concentrations of both elements. With the possible exception of one of the CSV regions at 1 cm, these elements do not appear to be hugely concentrated in any specific cells, but rather spread fairly evenly over many cells. In order to try to quantify the degree of localisation of As into specific cells I calculated the coefficient of variation, Cv, between the mean $^{75}As^-$ counts in different ROIs within the same group. Figure 4.13 also contains a plot of these Cv values against distance from the root tip. It shows that because of the high degree of localisation of As into one specific cell in CSV at 1 cm (fig. 4.12 A), the Cv value for this group is much higher at 1 cm than 2 cm and 5 cm. For most other groups Cv increases from 1 cm to 2 cm before decreasing again at 5 cm, with the exception of ICS2 where the opposite is true.

lsi3 mutants

So far only WT sections have been considered, I will continue the same analysis using the *lsi3* sections listed in table 4.4 to compare distributions of S and As at different distances from the root tip. Just as before I have arranged graphs of mean $^{75}As^-$ and $^{32}S^-$ from each ROI side by side for each distance from the root tip, figure 4.14.

For the *lsi3* section at 1 cm from the root tip the $^{75}As^-$ signal appears quite low across the CSV and CSW groups. It is comparatively higher in much of the ICS1 group and one ROI in OCS and ICS2 groups. Although the $^{75}As^-$ signals in ICS1 are on the whole higher

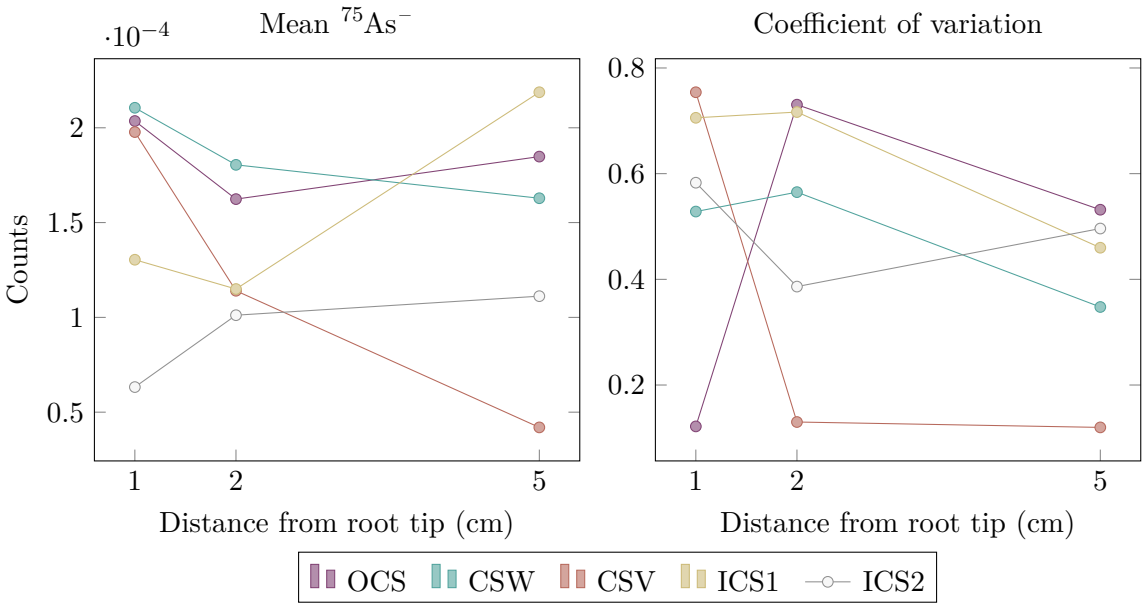

Figure 4.13: Changes in mean $^{75}As^-$ and coefficient of variation of mean $^{75}As^-$ in WT ROIs vs distance from root tip.

than in other regions there is still quite significant variation within that group; one region (annotation A) has some of the lowest average $^{75}As^-$ signal on that sample and could be a protoxylem.

At 2 cm from the root tip, there appears to be proportionately more $^{75}As^-$ and $^{32}S^-$ signal from the OCS, CSW and CSV groups. While the signals in ICS2 remain relatively low in these elements, ICS1 still appears to contain regions with the highest concentrations of them and again there is a lot of variation between different ROIs in the ICS1 group.

In section at 5 cm from the root tip the $^{75}As^-$ signal is more predominantly localised in the ICS2 group. There is also a relatively high average $^{75}As^-$ and $^{32}S^-$ signal two regions within the ICS2 group (annotations B_1 and B_2). While the relative proportions of these signals had been very similar for all other regions, these two specific regions had a much higher ratio of $^{32}S^-$ to $^{75}As^-$.

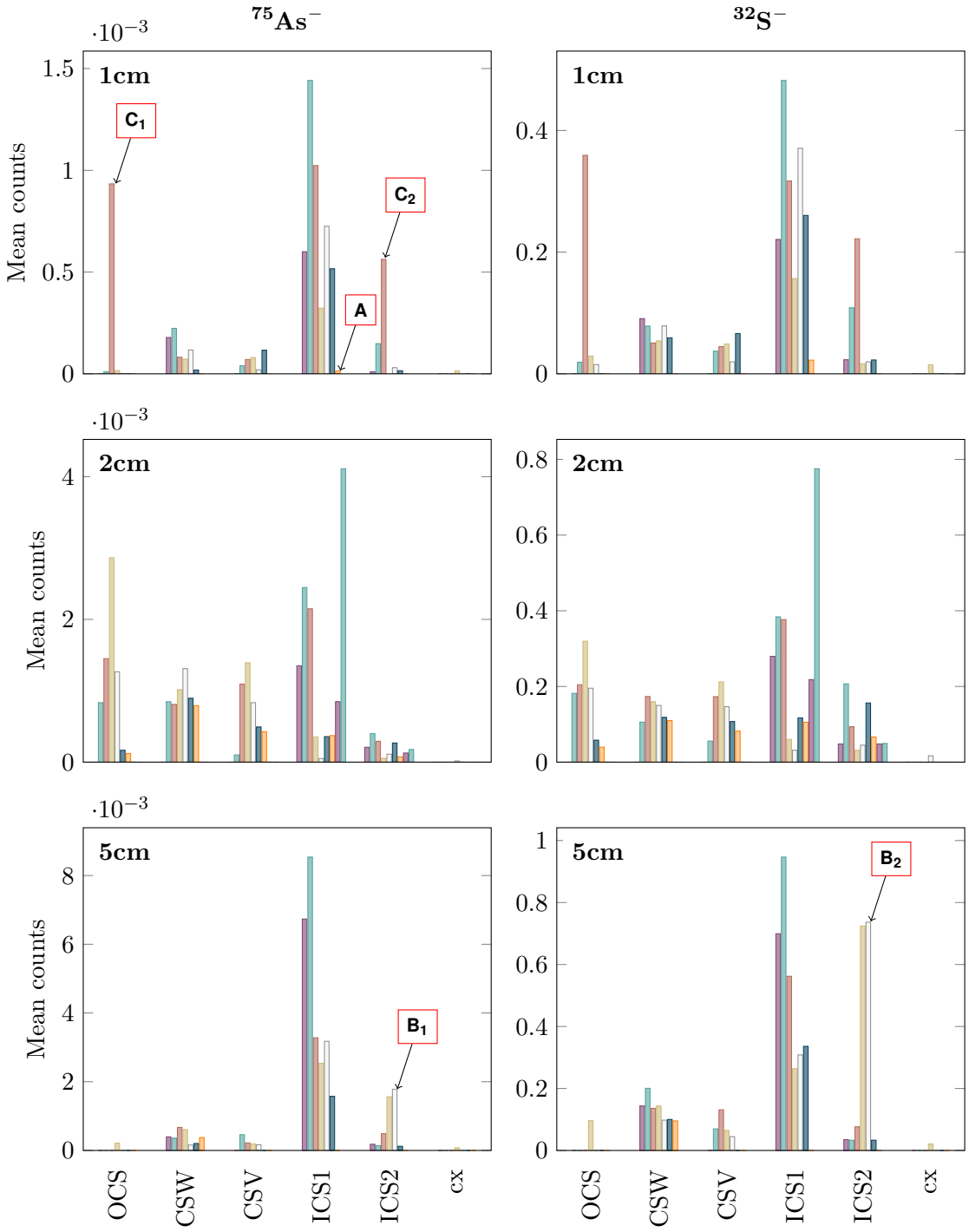

Figure 4.14: $^{75}As^-$ and $^{32}S^-$ signals from *lsi3* sections cut at different distances from the root tip. Left column mean $^{75}As^-$ counts, right column mean $^{32}S^-$ counts. (*a*) Unusually low As and S containing region just inside endodermis, possibly protoxylem. (*b*) High As and S containing regions in the ICS2 region. (*c*) As and S highly localised to specific cells in stele and cortex.

The differences in the scale bars in figure 4.14 show that there is a big increase in the $^{75}As^-$ and $^{32}S^-$ signals in the ICS1 group as the distance from the root increases and a slight increase in these elements in ICS2. At 2 cm, OCS, CSV and CSW seem to contain, on average, higher concentrations of As and S than ROIs from the same groups at 1 cm or 5 cm.

To help see these trends I have calculated the mean of the $^{75}As^-$ counts from in each ROI group and the coefficient of variation between ROIs within each group, figure 4.15. The coefficient of variance was calculated to give an indication of how much variation there was between ROIs in the same group, i.e. the degree to which As had been localised to specific cells in that group.

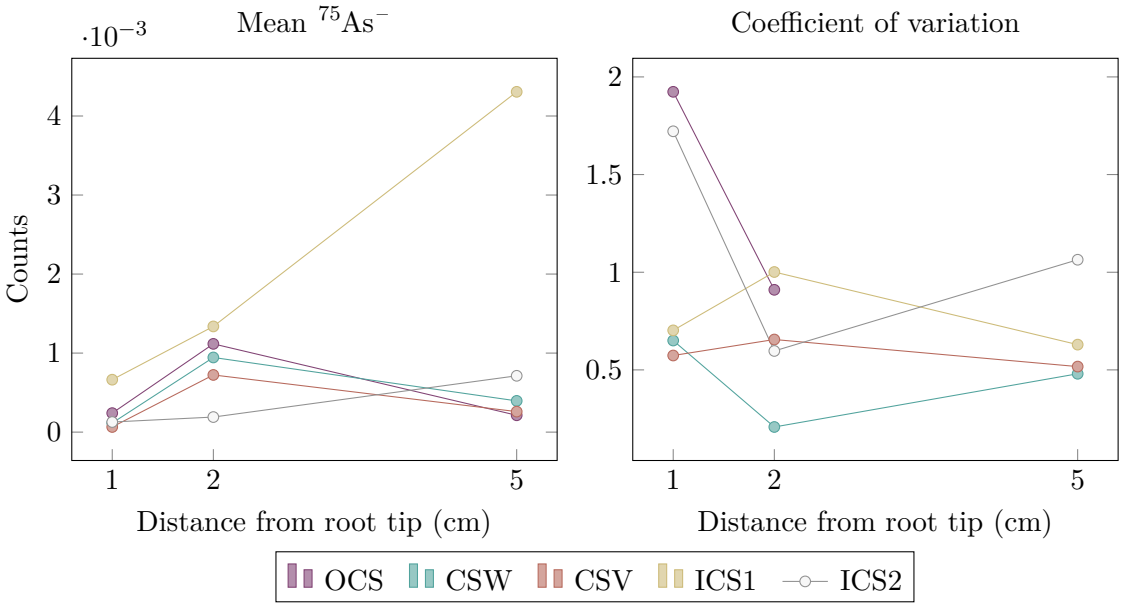

Figure 4.15: Changes in mean $^{75}As^-$ and coefficient of variation of mean $^{75}As^-$ in *lsi3* ROIs vs distance from root tip.

The graph of mean $^{75}As^-$ counts (fig. 4.15, left) shows that most of the groups contain similar concentrations of As at different distances from the root tip. The exception is ICS1

which sees a small increase in As concentration from 1 cm to 2 cm, then a proportionately far greater increase from 2 cm to 5 cm, ending several times higher, on average, than any other group.

The graph of coefficients of variation shows that there are quite large variations in $^{75}As^{-}$ counts within most group, which suggests that As is localised to specific cells within that group. The variation is especially the high for OCS and ICS2 at 1 cm from the root tip, where a very high $^{75}As^{-}$ signal was recorded from one or two cells (fig. 4.14 C_1 and C_2) while the adjacent cells produced a much lower signal.

Compared to WT, *lsi3* appears to have a more obvious trend with the changes in As and S concentration increasing in ICS1 with distance from the root tip. This becomes even more apparent when directly comparing $^{75}As^{-}$ signals from the three WT and three *lsi3* sections on adjacent graphs, figure 4.16. These graphs all have the y-axis scales adjusted to the same minimum (0) and maximum (9×10^{-3}). They provide reasonable evidence that *lsi3* contains much greater concentrations of As in the pericycle than WT, and that this concentration increases with distance from the root tip. These graphs also suggest a higher degree of localisation of As to specific cells in *lsi3* compared to WT, especially at greater distances from the root tip.

Student's *t*-tests on the average $^{32}S^{-}$ and $^{75}As^{-}$ counts showed no significant increase ($p < 0.05$) in $^{32}S^{-}$ counts between WT and *lsi3*, but a significant increase of $^{75}As^{-}$ counts ($p = 0.012$) in the ICS1 ROIs of *lsi3* over WT.

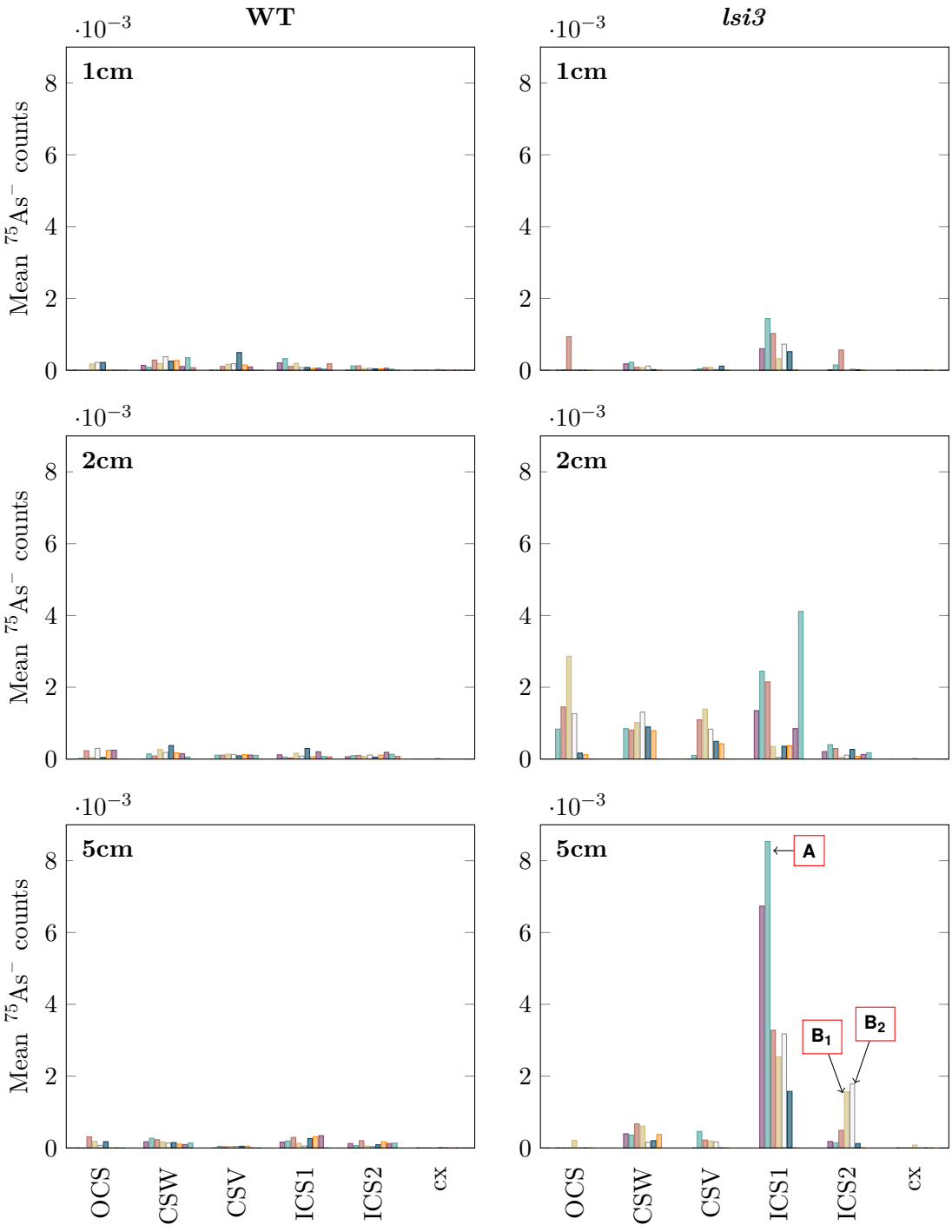

Figure 4.16: Mean $^{75}As^-$ counts in WT (left column) and *lsi3* (right column) at different distances from root tip. All graphs share the same y-axis limit of 9×10^{-3}.

4.4.2 Subcellular localisation

Correlating the high As containing regions (A, B_1, B_2) identified in figure 4.16 back to the NanoSIMS ion intensity maps, figure 4.17, shows that the highest average $^{32}S^-$ and $^{75}As^-$ signals were recorded in *lsi3* at 5 cm from the root tip from relatively large cells in the pericycle (e.g. fig. 4.17 *A*). These ions were also detected in high concentrations in a handful of much smaller cells (fig. 4.17 B_1, B_2) just inside the pericycle.

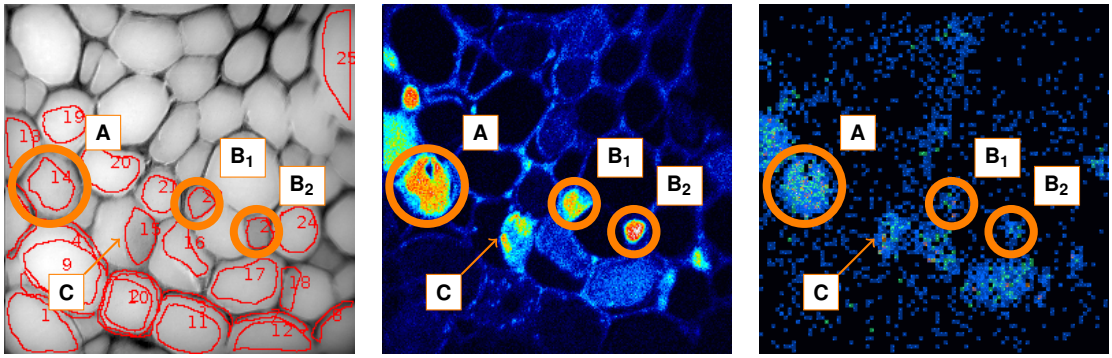

Figure 4.17: Detail of arsenic and sulphur localisation in an *lsi3* section at 5 cm from the root tip.

The intensity maps also show that these ions were not always detected uniformly within individual cells but that in some cases they were present only in a specific area within the cell (e.g. fig. 4.17 *C*).

4.5 Discussion

So far following trends have been identified for the sections listed in table 4.2:

1. As was localised to specific regions within cells

2. As and S concentrations were strongly correlated

3. As concentrations were highest in specific cells in ICS1 and ICS2

4. *lsi3* contained more As than WT

5. As in *lsi3* was more localised than in WT

6. As in *lsi3* became more localised with increasing distance from root tip

In the next few pages I will attempt to explain some of these observations.

1. Why is arsenic localised to specific regions within cells

The detection of some of the measured secondary ions in only part of a cell could be an artefact of the HPF process. If the cells were damaged during sample preparation it is possible that biological material could have been removed from part of the roots and later replaced with resin, resulting in lower than expected secondary ion counts in specific cells or parts of specific cells.

Since plant cells have large central vacuoles, as long as the cells are well preserved, it is possible that these regions are the vacuoles of these cells, where the As and S have been transported by the plant for storage. Vacuoles typically take up 30-80% of the volume of a cell, so it is not unreasonable, given the size of these features, to assume that they may be vacuoles. The converse could also be true — that the vacuoles contain very little As, and it is instead located within other organelles within the cytoplasm, or in the cytosol itself.

Both essential and non essential metal ions are potentially toxic to plants when present above threshold values. Heavy metals are known to hinder plant growth and can disrupt the function of enzymes and cause oxidative stress by replacing essential metals [182]. To

overcome these effects plants have developed mechanisms to detoxify and compartmentalise heavy metals. Ramsay *et al.* [183] demonstrated the importance of vacuoles for the detoxification of Co, Mn, Ni, Zn, by growing mutants devoid of vacuoles, resulting in increased sensitivity and decreased accumulation of these elements. However, they also noted that Cu, Cd, elements known to be mainly detoxified in the cytosol, were not significantly affected.

Yang *et al.* [184] discovered that in the As hyperaccumulator, *Pteris vittata*, As was strongly compartmentalised to vacuoles. By "isolating cell walls, protoplasts and vacuoles, and determining arsenic concentrations" they were able to determine that of the total As "about 94% was in the protoplast, and of that, 91% was present in the vacuoles, indicating that vacuoles are a major storage site for As in *P. vittata*."

More specifically, Song *et al.* [101] discovered a transporter, OsABCC1, responsible for "sequestering As in the vacuoles of phloem companion cells of the nodes in rice." They observed that "knockout of *OsABCC1* in rice resulted in decreased tolerance to As, but did not affect cadmium toxicity." Furthermore they found that *OsABCC1* was not only expressed in nodes but also "in many organs, including the roots, leaves, [...] peduncle, and rachis."

Given this information, it seems most likely that the subcellular regions in which we have observed the highest concentration of As are the vacuoles, where As is being sequestered as part of the plant's detoxification pathway.

2. Why were arsenic and sulphur concentrations strongly correlated

PCs are believed to be responsible for detoxification of As in plants via the formation of metal-peptide complexes. In their paper "Detoxification of arsenic by phytochelatins in plants" Schmöger *et al.* [98] noted that "an approximately 3:1 ratio of the sulfhydryl groups from PCs to As is compatible with reported As-glutathione complexes." They also reported the "unequivocal induction of PCs by As *in vivo* and *in vitro* and provide clear evidence for the formation of As-PC complexes, in accordance with a detoxifying role for the peptides."

Clemens [185] proposed that phytochelatin synthases (PCS) may have evolved specifically to help "cope with an excess of cadmium or arsenic ions." PCs are a class of thiol-rich peptides, which are able to chelate As by thiolate coordination [186]. As is therefore known to be chelated by complexation by organosulphur compounds.

Scatter plots of $^{32}S^-$ signal against $^{75}As^-$ signal, figure 4.18, demonstrate a strong co-localisation of As and S, as evidenced by Pearson product-moment correlation coefficients of between 0.83 and 0.98. This co-localisation is in agreement with the current scientific understanding of chelation by S containing complexes as part of the detoxification pathway.

Each element has different sputtering rates and electron affinity therefore in order to calculate the actual ratio of $^{32}S/^{75}As$ in the sample we must adjust the recorded data to account for this. Cameca have published relative sensitivity factors (RSF) for elements embedded in a Si matrix. The RSF for an element is defined as follows:

$$\frac{I_R}{C_R} = RSF_E \cdot \frac{I_E}{C_E} \tag{4.1}$$

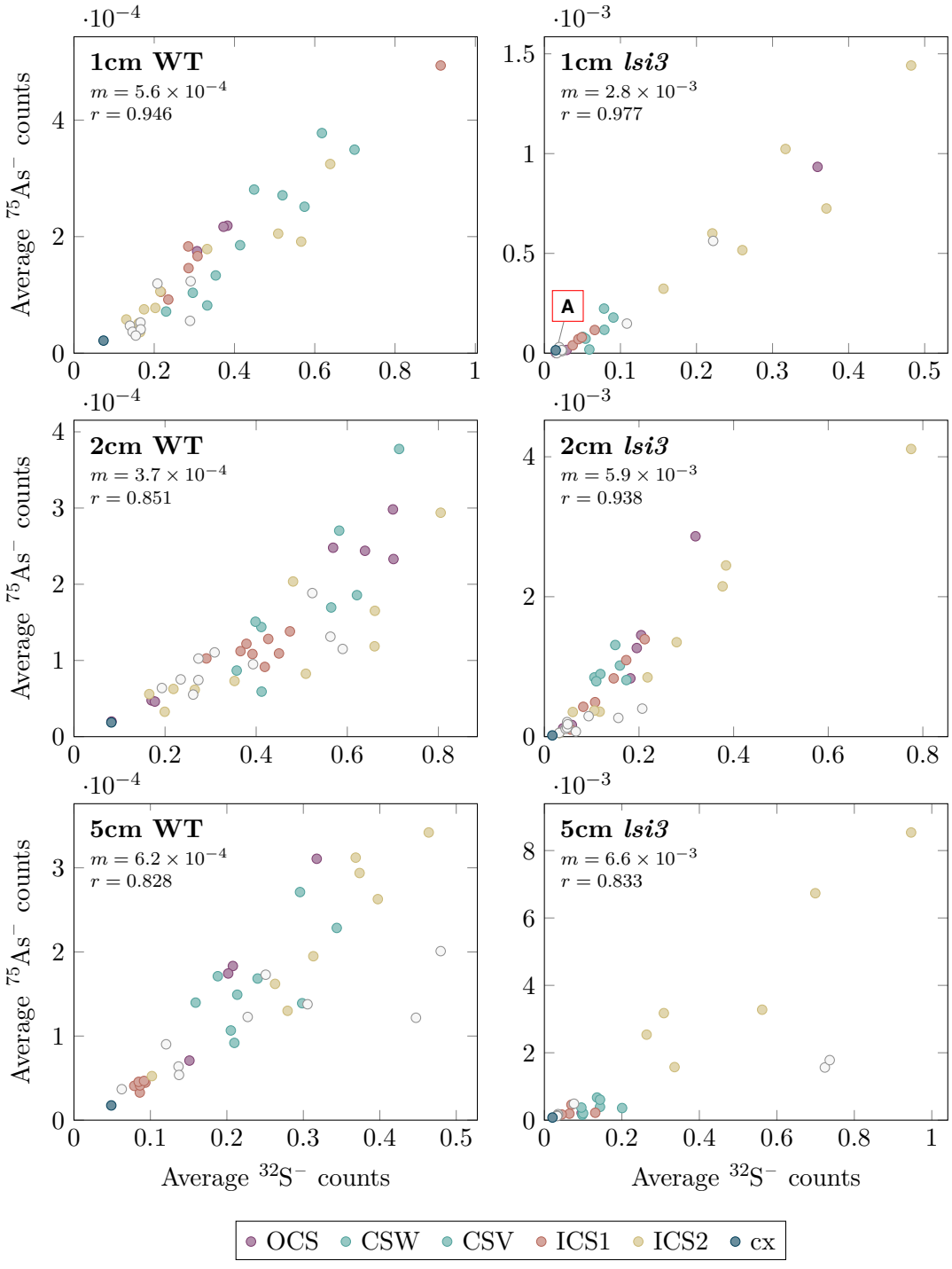

Figure 4.18: Scatter graphs of average $^{75}As^-$ counts against average $^{32}S^-$ counts for WT and *lsi3* sections at different distances from the root tip. (m) linear regression gradient given to two significant figures, (r) Pearson product-moment correlation coefficient give to three significant figures.

RSF_E	Relative sensitivity factor for element E
I_E	Secondary ion intensity for element E
I_R	Secondary ion intensity for reference element R
C_E	Concentration of E
C_R	Concentration of R

"The major (or matrix) element is usually chosen as the reference. Substituting M (matrix) for R (reference) and rearranging gives the following equation."

$$C_E = RSF_E \cdot \frac{I_E C_M}{I_M} \tag{4.2}$$

$$C_S = RSF_S \cdot \frac{I_S C_M}{I_M} \tag{4.3}$$

$$C_{As} = RSF_{As} \cdot \frac{I_{As} C_M}{I_M} \tag{4.4}$$

Dividing equation 4.3 by 4.4 gives the As to S ratio:

$$\frac{C_S}{C_{As}} = \frac{RSF_S \cdot \frac{I_S C_M}{I_M}}{RSF_{As} \cdot \frac{I_{As} C_M}{I_M}} \tag{4.5}$$

Which simplifies to:

$$\frac{C_S}{C_{As}} = \frac{RSF_S}{RSF_{As}} \cdot \frac{I_S}{I_{As}} \tag{4.6}$$

We can find the RSF values for As and S from published results. Wilson [187] published SIMS relative sensitivity for elements embedded in Si, GaAs, and diamond. The RSF of S in Si was 7×10^{21}, while for As it was 4.6×10^{23}.

This provides enough information to calculate the relative concentrations of As and S in the vacuoles from the measured ion intensities. In the case of figure 4.17 the pericycle cell vacuole with highest concentrations of As had an average of 9.5×10^{-1} $^{32}S^-$ counts and 8.5×10^{-3} $^{75}As^-$ counts.

$$\frac{C_S}{C_{As}} = \frac{7 \times 10^{21}}{4.6 \times 10^{23}} \cdot \frac{9.5 \times 10^{-1}}{8.5 \times 10^{-3}} \tag{4.7}$$

Which gives us an approximate value of 1.7 for the S to As ratio for the subcellular region measured in figure 4.17. We would expect a S to As ratio of 3 from PC coordination with As alone, which puts this first attempt at quantification within a factor of 2 of the expected value. Applying this method to the other sections provided figures of $^{32}S/^{75}As$ for each ROI. From this I have generated a graph, figure 4.19, which represents the data as a set of box and whisker plots.

On the accuracy of this information, some of the RSF values published by Wilson "are from one or two measurements and not the result of extended studies nor repeated measurements" and they propose that the experimental error should be assumed to be "a factor of 3 to 5." Secondly RSF values were also for these elements in an Si matrix, which may have very different relative RSFs compared to the organic matrix in these samples. Lastly small variation in the relative tuning of the two detectors could lead to significant systematic variation in the recorded ratios.

The median values across the *lsi3* sections in figure 4.19 varied from 3.3 to 10.7, which is within one order of magnitude of the ratios expected due to thiol-coordination. Given the possible errors this is close enough to provide evidence to support the theory that

detoxification and storage or As is taking place in the vacuoles of these specific root cells. The box-and-whisker plots show a higher median $^{32}S/^{75}As$ in WT than *lsi3* and the linear regression lines on the scatter plots, figure 4.18, have lower gradients in WT than *lsi3*. Together this information suggests a fairly strong co-localisation of As and S in both WT and *lsi3*, with *lsi3* having a higher ratio of As to S compared to WT. The median ratios in WT varied from 28 to 52, which suggests a larger proportion of S that exceeds the quantity expected for thiol coordination with As alone.

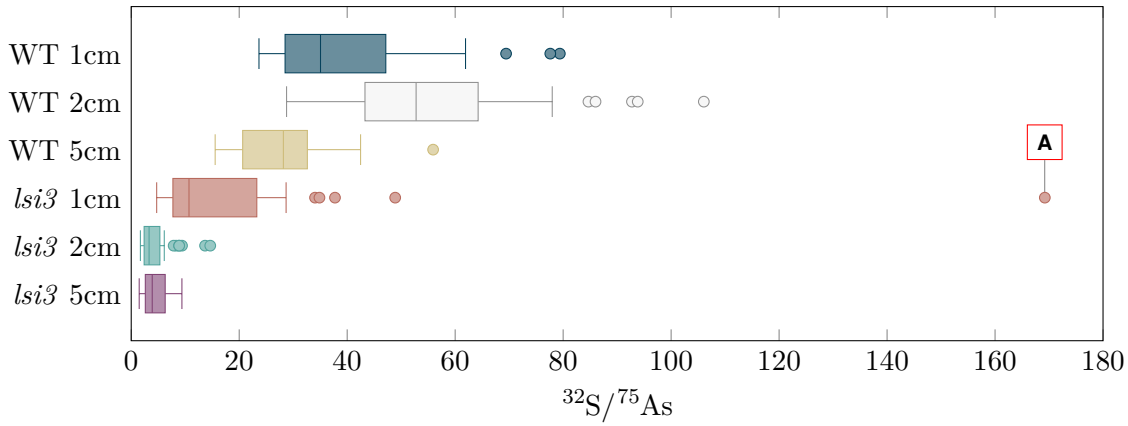

Figure 4.19: Box and whisker plots of estimated sulphur to arsenic ratios for different sections of *O. Sativa*. Top and bottom whiskers are the furthest points from the median within 1.5 times the inter quartile range. Outliers represented as points.

The *lsi3* section at 1 cm from the root tip had one ROI with a $^{32}S/^{75}As$ far higher than other ROIs from the same sample (fig. 4.19 *A*). This originated from a mesodermal cell with very little $^{75}As^-$ signal, the correspondingly high proportion of $^{32}S^-$ signal may have originated due to crater edge effects from the cell walls, which are known to sputter at a different rate than cell interiors in SIMS analysis. This ROI has so little signal from either detector that it is barely noticeable in the scatter plot (fig. 4.18 *A*), which leads me to conclude that scatter plots are a more useful tool for analysing the relationship between

two elements measured by SIMS in situations where the signal is so low that noise can significantly alter the ratios.

3. Why are arsenic concentrations highest in ICS1 and ICS2

The evidence so far, in agreement with previous research [98, 100], suggests detoxification of As by coordination with induced PCs in the vacuoles of specific cells within the stele. Now it is of interest to determine what the cells are and what their functions might be.

My experiments have demonstrated that As appears to be sequestered, along with S, in specific cells within "ICS1" and "ICS2." ICS1 refers to the pericycle, which forms a cylinder of cells, some of which will be parenchyma cells that surround the vascular tissue and take part in short distance transport and storage of nutrients. They have large central vacuoles to allow them to store and regulate ions, waste products, food and water. The ROIs in the group ICS2 were cells one layer inside of ICS1. The cells in this part of the root likely include more parenchyma cells as well as sclerenchyma cells and vascular bundles.

In their study of As detoxification in *O. sativa* Song *et al.* [101] found that "a member of the *Oryza sativa* C-type ATP-binding cassette transporter (OsABCC) family, OsABCC1" played an important role in "vacuolar sequestration of As [...] reducing As accumulation in rice grains." Their study revealed that *OsABCC1* was expressed in the "exodermis and pericycle of roots and in the phloem companion cells of both the [enlarged vascular bundles] and [diffuse vascular bundles] at the basal node and node." They determined that "OsABCC1 is mainly localized to the tonoplast of phloem companion cells" and that their results indicate "that As was sequestered into the phloem cells before translocation

to the grain." They conclude that "Localization of OsABCC1 to these organs also likely reduces As movement up to the grain by sequestering As into the vacuoles of the phloem companion cells. This notion is supported by a previous report describing As accumulation in the phloem region of these organs."

Given this information it is likely that the vacuoles in which we find strong co-localisation of As and S, as observed in figure 4.17 (B_1 and B_2), are companion cells. These companion cells could be regulating the flow of nutrients and ions into vascular tissue; in this case the flow of As, where it is either stored in the companion cell or released into the vascular tissue system to be translocated to different organelles at the nodes.

4. Why does *lsi3* contain more As than WT

A study of Si hyperaccumulation in rice by Yamaji *et al.* [102] revealed some details on the organisation of Si transport. Their study examined three transporters (Lsi2, Lsi3, Lsi6) and their role in intravascular transfer of Si. The study focussed on the node, but their results reveal useful information about these transporters, the Si pathway and by extension the As pathway.

Their research proposed the subcellular localisation and function of Lsi3. They determined that "[s]imilar to Lsi2, Lsi3 also showed efflux transport activity for Si" and that "Lsi3 is a plasma membrane-localized efflux transporter of silicic acid."

In a paper published a few years earlier Yamaji *et al.* [188] wrote that "expression of *Lsi3* was mainly detected in the roots and upper nodes. Immunohistological staining revealed that Lsi3 is localized at the pericycle cells of the roots. The Si uptake as well as Si

concentration in the xylem sap was slightly increased in a *Lsi3*-enhanced line, suggesting that Lsi3 is involved in the xylem loading of Si."

They believe Lsi3 in the node to be responsible for effluxing Si from parenchyma cell bridges between enlarged and diffuse vascular bundles. They also found *Lsi3* expressed in pericycle cells in the root, where it may be responsible for effluxing Si from pericycle cells into vascular bundles. Since As(III) is thought to share the Si transport pathway, knockout of *Lsi3* may result in a reduced capacity for the parenchyma cells to effectively efflux As, resulting in an accumulation of As in the parenchyma cells. This would explain the higher concentrations of As found in the pericycle (ICS1) cells in the *lsi3* samples in this experiment, compared to WT.

5. Why is As more localised in *lsi3* than WT

This result may have also been caused by the lack of Lsi3 leaving specific cells unable to efflux As. If *Lsi3* is only expressed in a few specific cells it could have disproportionately affected some cells over others, causing the observed increase in localisation of As in *lsi3* over WT.

6. Why did arsenic in *lsi3* become more localised with increasing distance from root tip

If Lsi3 is responsible for efflux of As into the xylem, then this could explain why in more mature root sections *lsi3* demonstrates an increasing localisation and increasing concentration of As in small number of cell vacuoles. Disruption of *Lsi3* could cause efflux to be

reduced from parenchyma cells, but without slowing influx, resulting in accumulation of As within these cells. The more mature the root section, the longer As influx has exceeded efflux, and the greater the accumulation. In less mature root sections the cell differentiation and influx of As into these cells may also be less pronounced, hence the lower concentration of As observed.

Chapter 5

Lateral Roots

While microtoming sections of rice root during the experiments detailed in the previous chapter, I noticed that there were small lateral roots growing perpendicularly out of the sides of the root. This presented me with the interesting possibility of sectioning through the lateral root, along its direction of growth, and across the junction where the lateral root met a higher order root.

I found that it was possible to cut such a cross section through a lateral root, as observed in the optical micrograph shown in figure 5.1. While it was difficult to repeat this, and required removing a lot of material, it presented a rare opportunity to study something of potential significance that had not previously been analysed.

The role of lateral roots and the surrounding cells in the uptake of heavy metals is not understood, and therefore this sample may provide useful information regarding the uptake of heavy metals in this study and in future studies.

A lateral root is a root that grows out the side of an existing root. They form slightly differently in dicots and monocots. Eudicots such as *Arabidopsis thaliana* form a primary root, out of which lateral roots will begin to form, branching several more times into higher order lateral roots. The mature root system of monocots such as rice are instead mainly composed of adventitious roots - that is, roots that grow outwards from the base of the stem rather than from a primary root. These adventitious roots then branch into several further orders of lateral roots.

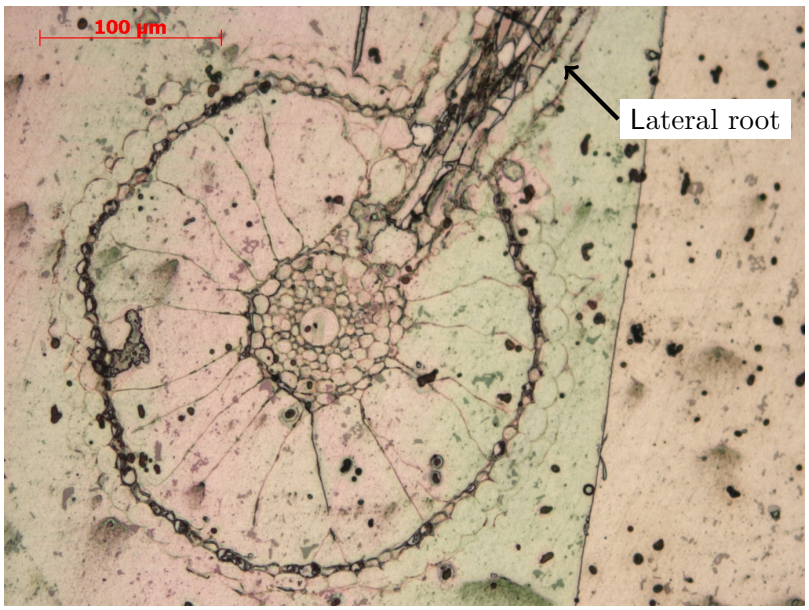

Figure 5.1: Optical micrograph of a preserved and microtomed section of *O. sativa* root featuring a prominent side root.

The growth of lateral roots is "regulated by nutrient and hormonal signals which act locally to induce or inhibit root branching" [189, 190]. Once initiated by the necessary stimuli, the lateral root will protrude from the side of a higher order root and begin to grow in the same fashion as higher order roots, typically in the direction of water and nutrients.

The lateral roots increase the surface area of the root system, allowing greater potential for nutrient uptake. They are able to grow in response to the availability of water; experimental results demonstrate a suppression of lateral root growth in the absence of moisture. Lateral root growth also increases the anchoring of the plant in the soil.

If lateral roots are an important pathway in the uptake of nutrients then examining them in their early developmental stage may deliver some useful information on how the transporters being examined are effecting the uptake through lateral roots.

5.1 Aims

There are several things that I wished to examine in this experiment.

1. The lateral roots that I examined were close to the root tip of a higher order root; they were very small young roots approximately a few hundred microns in width. Since they appear to be at an early stage of development, it could give insight into development of lateral roots and transporters therein.

2. At the lateral root junction it might be possible to see the transfer of As from lateral root into a lower order root. If there are cells responsible for storing or loading As between transport vessels it may be possible to identify these cells by examining the junction of a lateral root. The three dimensional nature of these features may, however, make it challenging to identify such features in the two dimensional cross sections prepared for SIMS analysis.

3. Disruption of Lsi3 transporters could result in some cells being unable to unload As, resulting in high concentrations of As in affected cells. This could also show sequestration of As to specific cells before being loaded into transport vessels.

Therefore, more simply, my aims were to determine if and where As appears in side roots; whether there are higher concentrations of As in sections of roots near lateral roots than sections not near lateral roots; and whether or not there is a difference in these trends between WT and *lsi3*.

5.2 Method

The methodology for this experiment was very similar the other experiments on the rice plants from G1 described in Chapter 4. The same samples were used, with the only difference to the sample preparation being during the microtomy where the resin block had to be prepared in such a way as to include some of the lateral root in addition to the main root cross section. As represented in the diagram in figure 5.2 the lateral roots only occurred at a few intervals along the root. This meant that there was only a few depths at which it was possible to get suitable sections. The sections would also have to be physically larger in order to include both the main root and the lateral root.

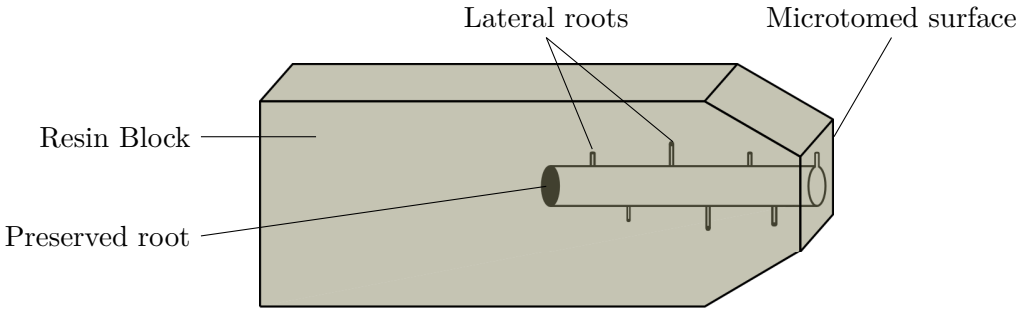

Figure 5.2: Schematic of a preserved section of root embedded in resin. The resin is sculpted such that sections can be microtomed from one of the cut ends of the root, in this example a lateral root would also be included in the section.

5.3 Results

During the microtomy process I found that the larger section required to include all the features of interest resulted in some difficulty in microtoming good quality sections. If the block was not shaped carefully and the microtome appropriately adjusted it was possible to

develop a rough surface, for the sections to fold up on themselves, for some of the biological material to lose adhesion to the rest of the sample, or even for sections to break apart. Furthermore when the sections were laid on a substrate they would sometimes dry with wrinkles or folds in them, making NanoSIMS analysis difficult or impossible. The best sections were obtained by carefully shaping the resin block around the main root slightly in front of a lateral root, then microtoming back towards the lateral root, continually making adjustments so that the best possible sections are obtained, then once the lateral root has been reached it should be possible to continue cutting good quality sections.

In figure 5.3 I have demonstrated some of the typical results obtained from this experiment. In the left hand column are regular sections of the main root of interest, in the right hand column is another root but this time featuring a lateral root that extends to the top right of each image. In the schematic images the layers represented from outside to inside; epidermis, endodermis, and pericycle.

We can see from the optical images that the lateral root appears to extend from either the endodermis or pericycle cells, with the stele at the centre of the root appearing mostly unchanged relative to the sections without lateral roots. The lateral root then extends through the cortex and penetrates through the outer layers of the root, leaving the structure of the root disrupted only for the cells in the direction in which it extends. The distal side of the root appears to be unchanged when compared to sections without lateral roots.

The large size of some of these sections made it difficult to conduct NanoSIMS analysis on the whole root at once, as the apertures did not allow for a large enough area to be rastered without a very significant decrease in resolution. The images at the bottom of

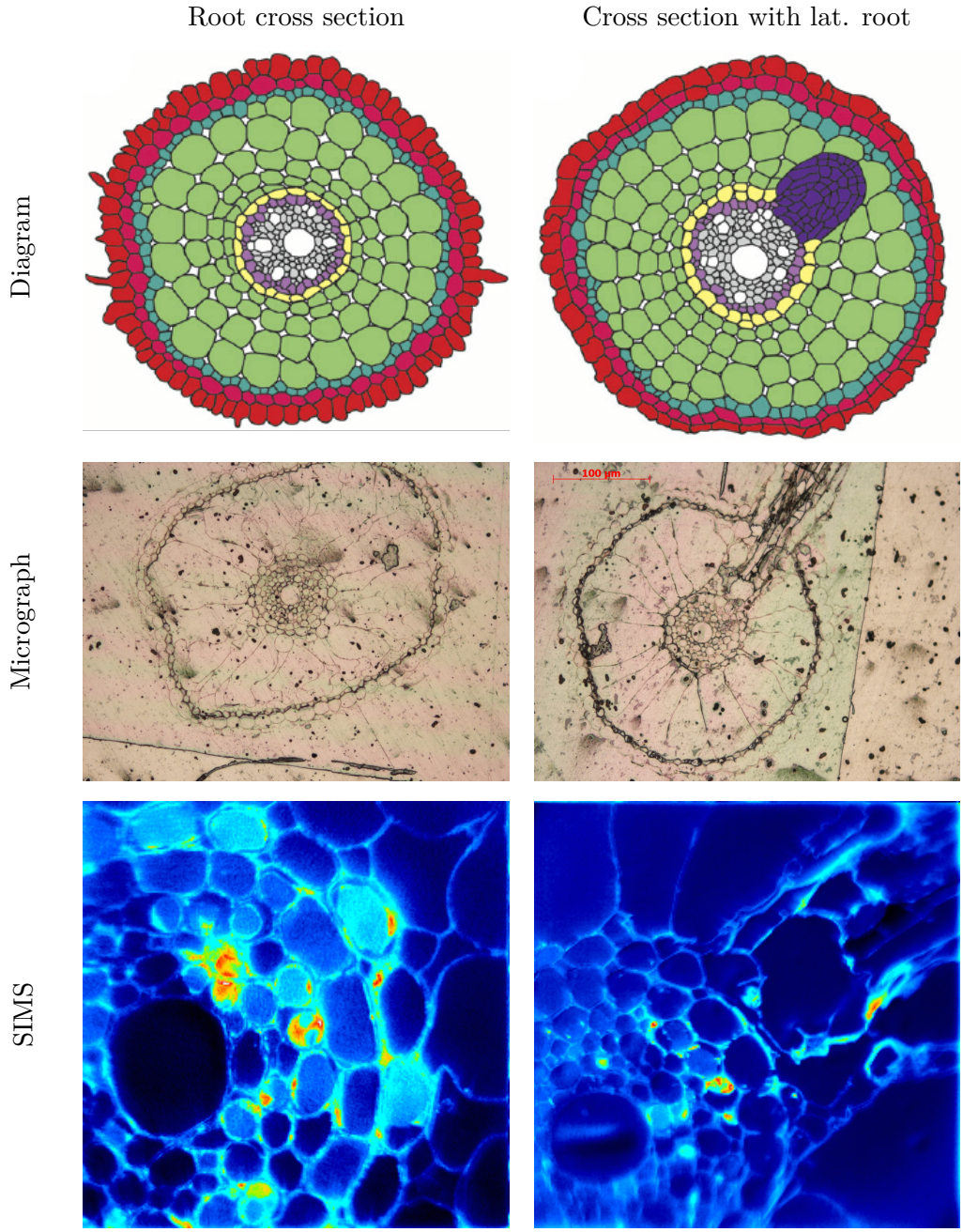

Figure 5.3: Diagrams, optical micrographs, and NanoSIMS $^{12}C^{14}N^-$ ion maps demonstrating the difference between a normal root section (left column) and one with a lateral root (right column). In all the lateral root examples the lateral root extends to the top right of the image. Data from WT. Diagrams from Péret et al., Lateral root emergence: a difficult birth, Journal of Experimental Botany, 2009, 60, 3639, by permission of Oxford University Press [191].

figure 5.3 demonstrate this phenomenon, with the left hand image having a size of 50 µm and the right hand image having a size of 100 µm. While the latter allows us to see a greater proportion of the cortex there is also a very evident drop in resolving power as a result of large deflections in the beam required for a raster of this size causing a loss of focus towards the edges. Such a phenomenon cannot be easily corrected, instead I opted, where necessary, to take multiple smaller sized rasters of the sample and to stitch them together. Of course, due to challenges with repeatability in the mass spectrometer and slow acquisition times we may find systematic variations appear even if the analysis of one was done immediately after the other.

The images in figure 5.3 are just small examples to demonstrate how samples with lateral roots compare to other data in this set of experiments. Let us now look more closely at a specific example. In figure 5.4 I have presented an optical micrograph of a cross section through a WT root 1cm from the root tip that included a lateral root. I have annotated the micrograph with boxes representing two of the regions of the sample that were analysed with the NanoSIMS.

The NanoSIMS results from the larger area near the stele, figure 5.5, is generated by a 100 µm raster, which is large enough to cause some aberrations towards the edges of the image, as can be seen particularly clearly from the SE detector. Despite this the cell walls are clear and distinct across most of the $^{12}C^{14}N^-$ map. We can see a quite sharply defined dark region at the bottom right of the SE image that also appears dark in the $^{12}C^{14}N^-$ and $^{32}S^-$ data but very bright in the $^{28}Si^-$, $^{31}P^{12}C^-$ and $^{75}As^-$ data. This is likely a hole in the sample where some biological material is missing and signal is being picked up from

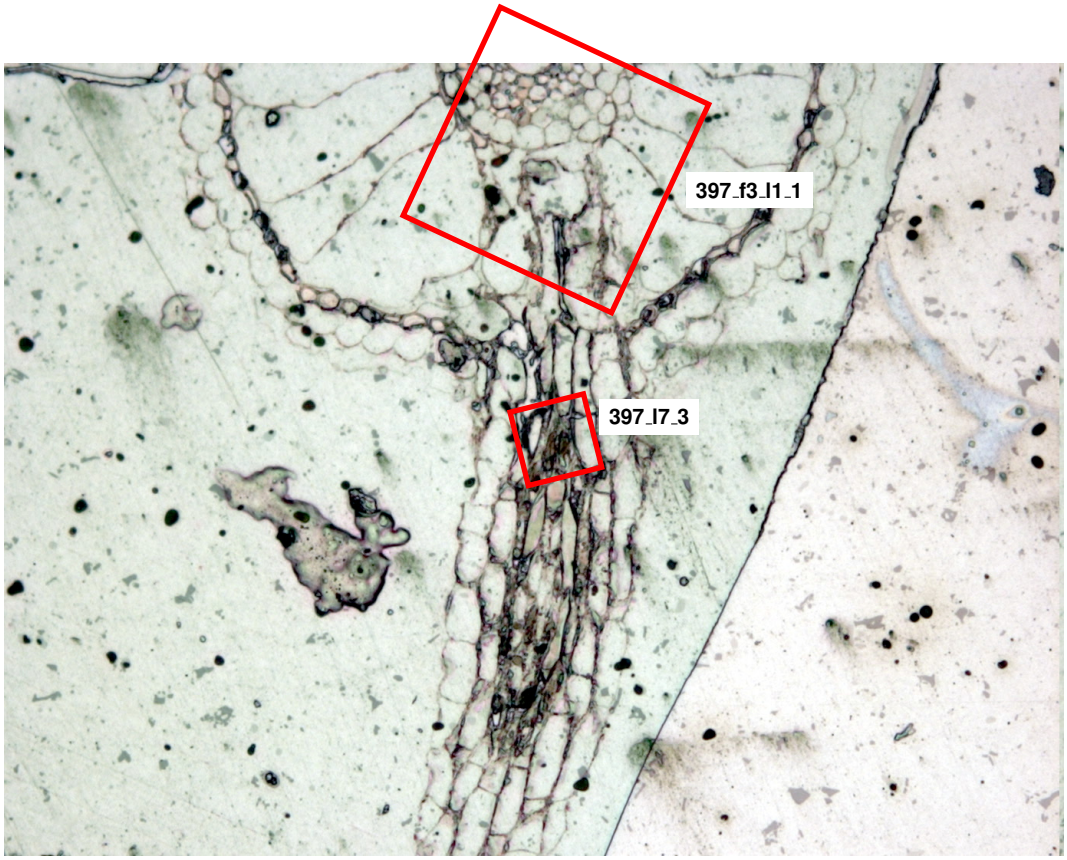

Figure 5.4: Optical micrograph of a root section that features a side root. Marked in red are two of the areas that were analysed with SIMS. Top square, 100 µm; bottom square, 30 µm.

the substrate underneath.

Similar to the sections without lateral roots Si is strongly localised to the cell walls of a ring of cells on the outer edge of the stele. But in this case appears more concentrated on the cells closest to the direction in which lateral root extends.

The S and As signals exhibit strong co-localisation in a small number of specific cells within the stele. These cells predominantly appear in parts of the stele closest to the lateral root. This is a possible trend deserving of further investigation.

There also appears to be a strong S and As signal in the middle of the "hole" in the

sample. Possibly a small amount of biological material remains with very high sequestration of these elements, but it could be some dirt or other contaminant.

The smaller 30 µm region (fig. 5.6) was identified as a region of potential interest on account of the high S and As observed in other low resolution scans. In this higher resolution image we again see some regions with very high $^{31}P^{12}C^-$ signal that is likely being collected from the substrate through holes in the sample. The SE image appears to show that some of the cells have cracked, broken, or fallen apart. There are, however two regions of seemingly intact biological material that are much higher in $^{12}C^{14}N^-$, $^{32}S^-$ and $^{75}As^-$ than the rest of their surroundings. While it is very common to see S and As in the same features, it is unusual to also get a strong $^{12}C^{14}N^-$ signal from that same cell. These features are relatively small (approximately 5 by 10 µm) and were found in the centre of the lateral root approximately 200 µm away from the centre of the main root, just outside of the epidermis.

There is an apparent trend of higher S and As localisation in the parts of the stele closer to the lateral root. In order to examine this more clearly I have produced a composite of several NanoSIMS rasters that were taken across the stele, figure 5.7.

In figure 5.7 I have arranged the $^{32}S^-$ signal from the NanoSIMS data shown in figure 5.5 in a composite image with with two more scans, at slightly higher resolution, that include other parts of the stele from this section. While we are primarily concerned with the $^{75}As^-$ signal, the $^{75}As^-$ tuning was too inconsistent between each of these scans to be useful. Instead I have used the $^{32}S^-$ signal, since as we have seen above that it is correlated closely with As. The contrast of the images has been adjusted to be as consistent as possible in order to most accurately represent the variation of $^{32}S^-$ concentration across the three ion

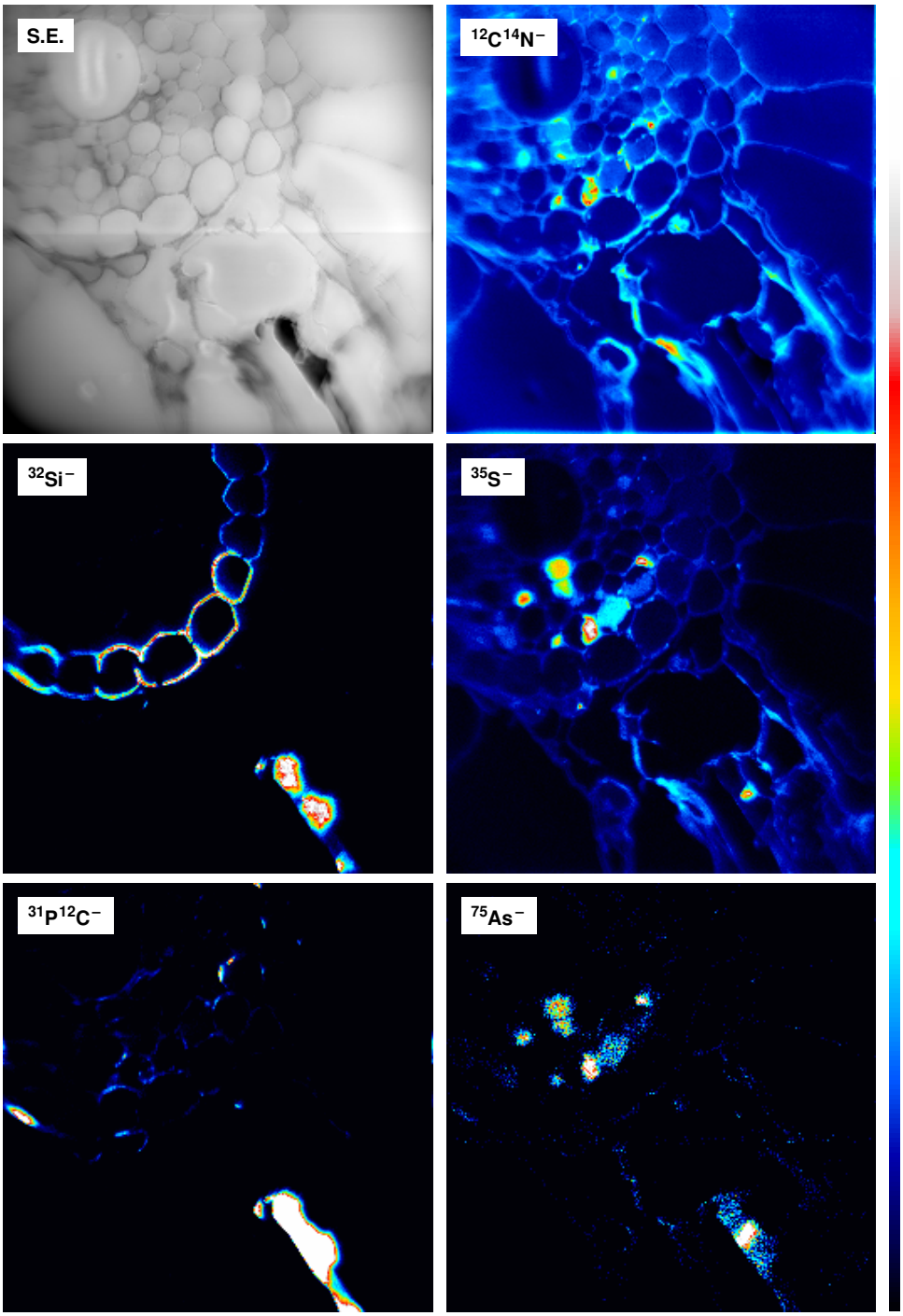

Figure 5.5: An example of NanoSIMS data from one of the sections containing a lateral root, showing signal from all five ion detectors and the SE detector.

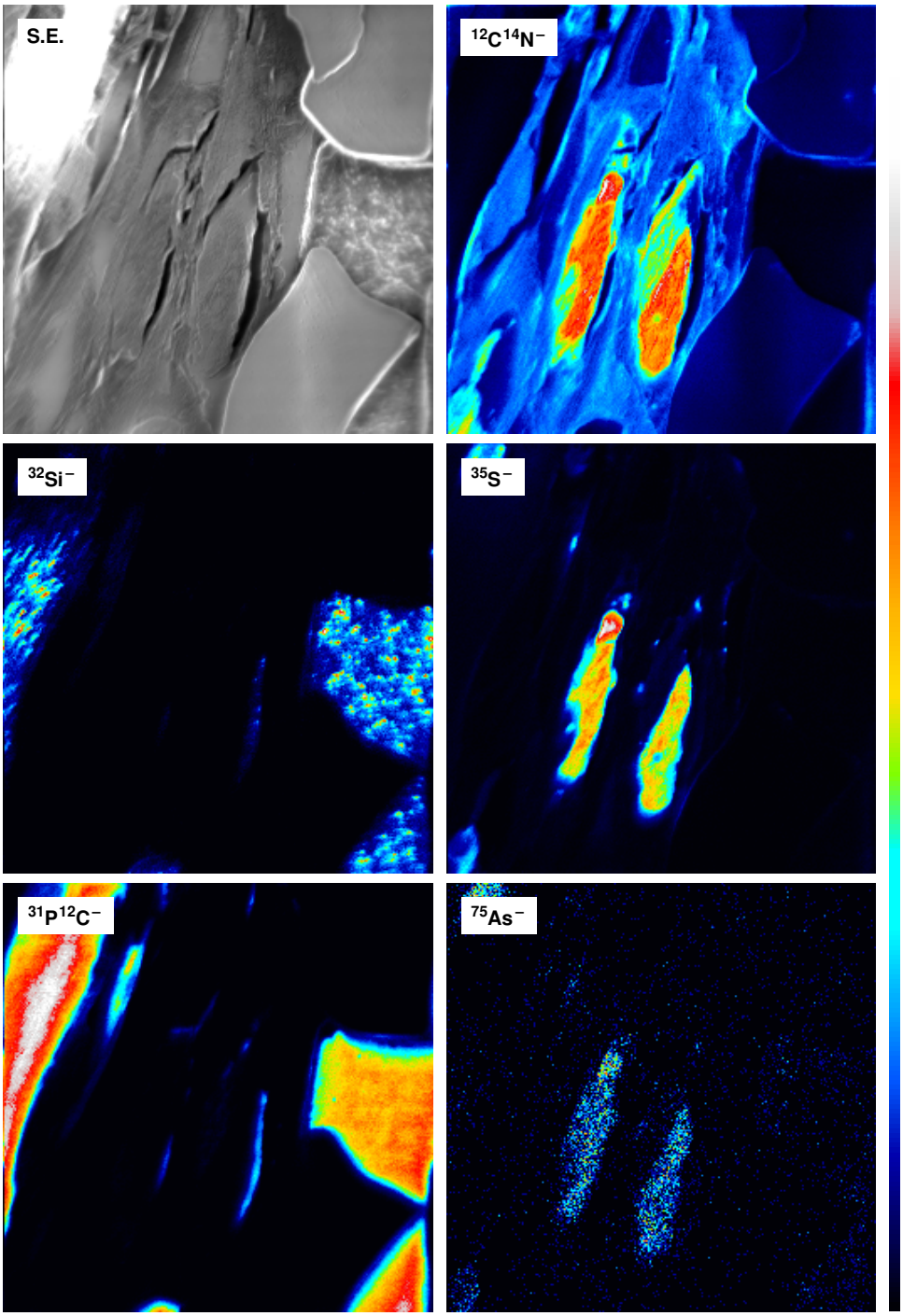

Figure 5.6: An example of NanoSIMS data from part of a lateral root, showing signal from all five ion detectors and the SE detector.

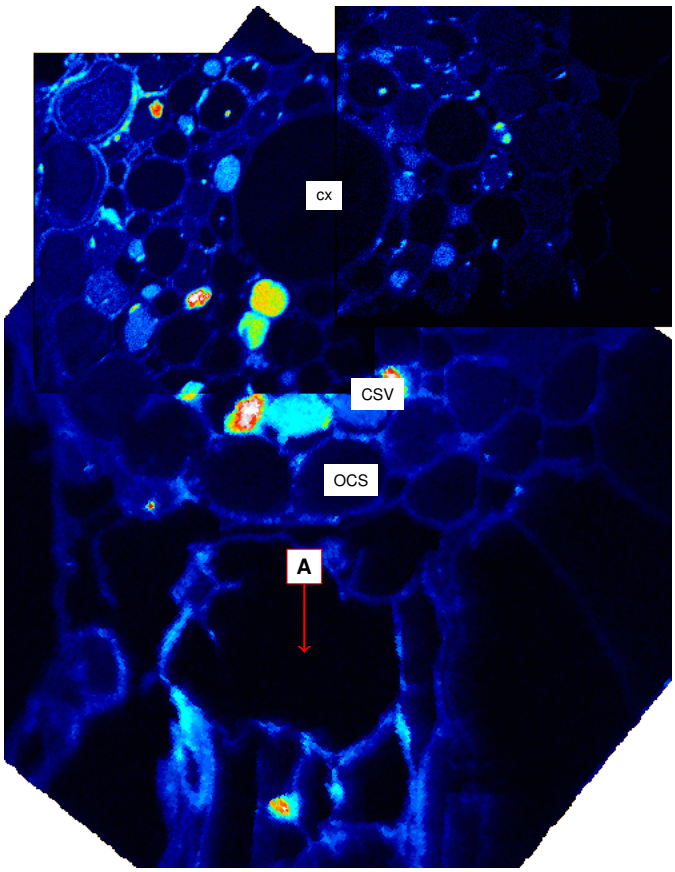

Figure 5.7: Three NanoSIMS maps of $^{32}S^-$ stitched together, the stele is visible at the top of the image, and a side root protrudes from the lower part of the image. *A,* direction of lateral root growth; *cx*, central xylem; *CSV*, endodermis; *OCS*, mesodermis.

maps. Here we can see more clearly that, as suggested by figure 5.5, the S concentration on the part of the stele adjacent to the side root (proximal side) is much higher than on the opposite (distal) side.

5.3.1 Wild types, with and without lateral roots

In the WT sections at 1 cm from the root tip regions without lateral roots appear to have fairly diffuse S and As throughout the stele, with relatively low concentrations of both being slightly elevated in a small number of the cells within the stele.

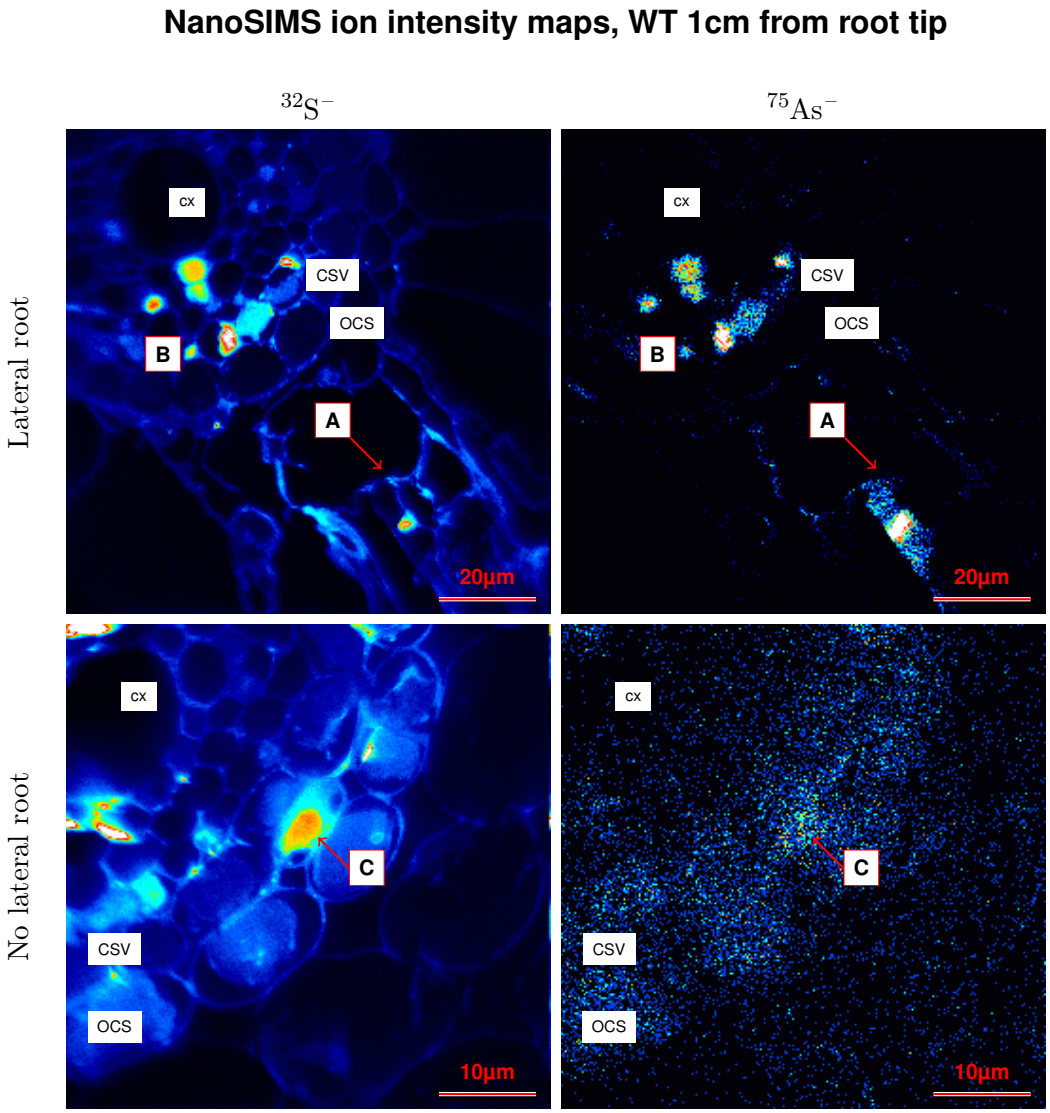

Figure 5.8: The $^{32}S^-$ and $^{75}As^-$ signals recorded for two WT sections 1cm from the root tip, with a lateral root (top) and without (bottom). *A*, direction of lateral root growth; *B*, region of high $^{32}S^-$ and $^{75}As^-$ signals; *cx*, central xylem; *CSV*, endodermis; *OCS*, mesodermis.

In the examples shown in figure 5.8 the WT section without a lateral root (bottom row) appears to have one pericycle cell that contains a much higher S concentration (annotation *C*) than the rest of the analysed region with the exception of some regions close to the central xylem. There also seems to be an appreciable but much lower concentration in the vacuoles of the endodermal and pericycle cells as well as many of the cells in the stele. Because this region is only 50 µm in size we can only see a small portion of the root.

The WT with a lateral root instead appears to have a cluster of cells (annotation *B*) on the proximal side of the stele with greatly elevated concentrations of both As and S. Normalised $^{75}As^-$ signal in the two most concentrated regions were 5.5×10^{-3} and 4.8×10^{-3}, both were located in the pericycle on the proximal side of the root. This is approximately ten times greater than the highest concentration of $^{75}As^-$ signal (4.9×10^{-4}) recorded from the section without a lateral root. The As seems to be almost exclusively in these cells, with the exception of some appearing at lower concentrations along many of the cell walls.

5.3.2 *lsi3*, with and without lateral roots

The *lsi3* sections, figure 5.9 show that whether a lateral root is present or not the $^{32}S^-$ and $^{75}As^-$ signals are predominantly localised to specific small cells in the stele. Elevated $^{32}S^-$ and $^{75}As^-$ signals were also recorded from larger cells in lateral root itself (annotation *A*) but at lower concentration than found in the stele.

Visually comparing WT and *lsi3* ion maps suggests that regions of high S concentration in the latter appeared mainly on the side proximal to the lateral root. However, in *lsi3*

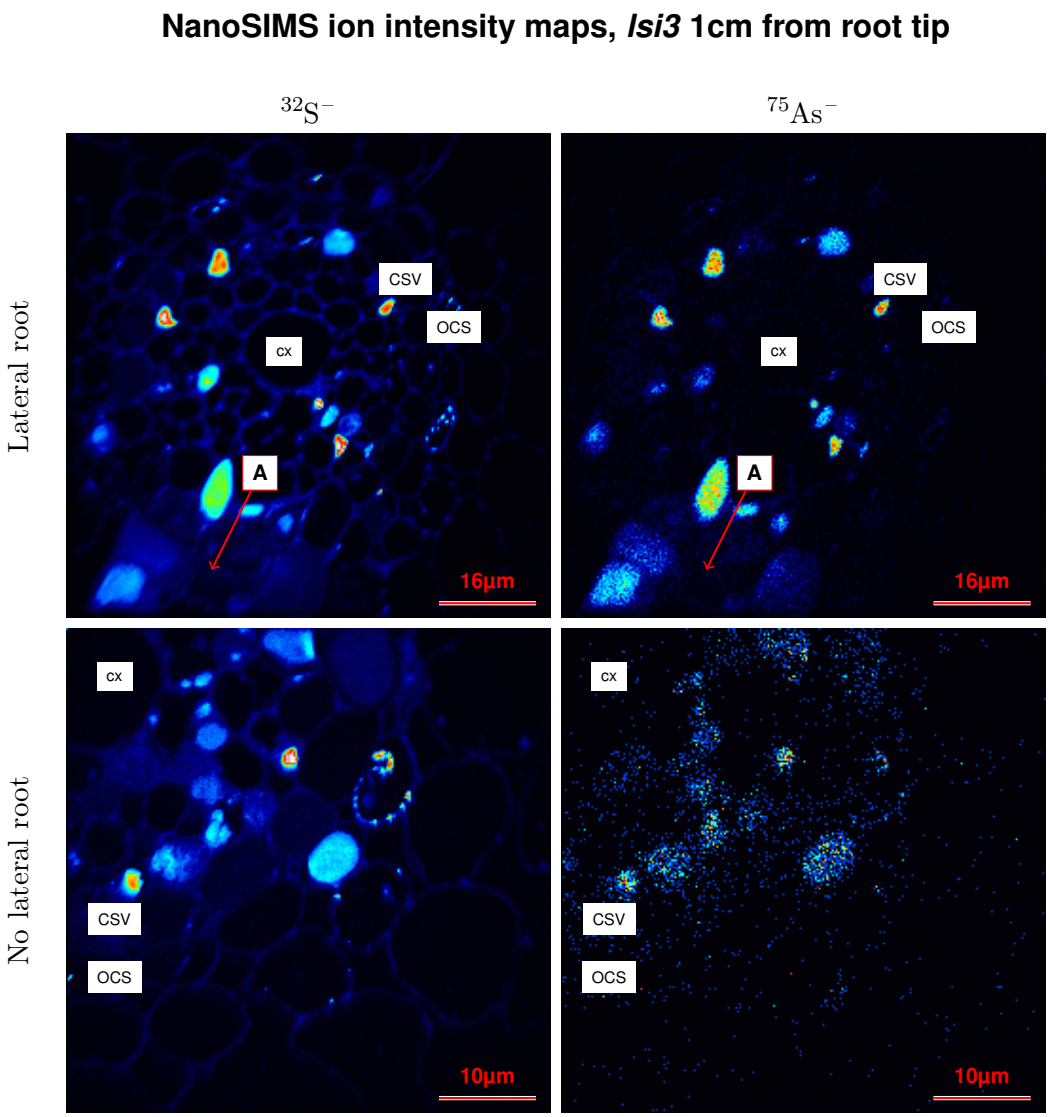

Figure 5.9: The $^{32}S^-$ and $^{75}As^-$ signals recorded for two *lsi3* sections 1cm from the root tip, with a lateral root (top) and without (bottom). *A*, direction of lateral root growth; *cx*, central xylem; *CSV*, endodermis; *OCS*, mesodermis.

such a correlation appears to not exist.

Since visual comparison between NanoSIMS ion intensity maps is limited to very basic qualitative assessment it is necessary to extract and normalise numerical data from regions of interest for a more robust analysis.

5.4 Discussion

Using the same method as the previous chapter, regions of interest were highlighted according to groups named OCS, CSV, CSW, ICS1, ICS2 and cx. These groups corresponded to areas within the root that could be easily and consistently identified from one sample to the next. They are described in table 4.3 and the supporting images in figure 4.7.

These regions, such as those given as an example in figure 5.10, can then be used to provide normalised mean data from different regions of the root, allowing for much more reliable comparisons between samples.

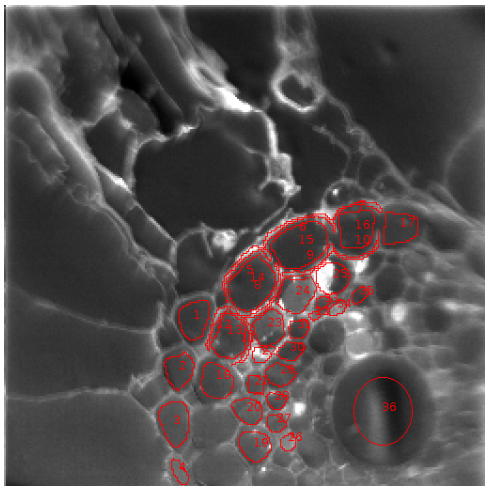

Figure 5.10: Regions of interest highlighted on sample 397_f3_l1_1, ready to be extracted by the OpenMIMS software for further analysis.

The process of data extraction and normalisation was repeated for one of each WT and *lsi3* with and without lateral roots. This data was used to plot column graphs of As concentration, figure 5.11, for each of these sections. These graphs have been scaled to the same y-axis limits for easier comparison.

The top two graphs are from WT sections, and the bottom two for the *lsi3* sections. The graphs very clearly show that sections with a lateral root contain regions with vastly more concentrated As than sections without lateral roots.

The WT sample with the lateral root had on average across all the ROIs over five times more As than the sample without a lateral root. The most notable increase was in the ICS1 group, where the lateral root containing sample had an average of more than sixteen times higher As concentration than the non-lateral root counterpart. The highest As concentration in the lateral root was also eleven times higher than that in the non-lateral root sample. Therefore it was not only greater on average across the sample, but was much more highly concentrated into specific regions within the root.

While in the non-lateral root section, the As had been measured as fairly diffuse throughout the sample, in the lateral root section it seems to be highly concentrated into specific cells within the stele, as well as there being some elevated concentrations on the cell walls at the edge of the stele.

Despite *lsi3* sections typically containing higher As than WT, the average $^{75}As^{-}$ in the lateral root containing section was 3.6 times higher and the maximum $^{75}As^{-}$ in the lateral root section was 10.9 times higher. In the case of the *lsi3* section, the localisation was also more severe. Most of the cells identified in the stele contained relatively low As, it was only

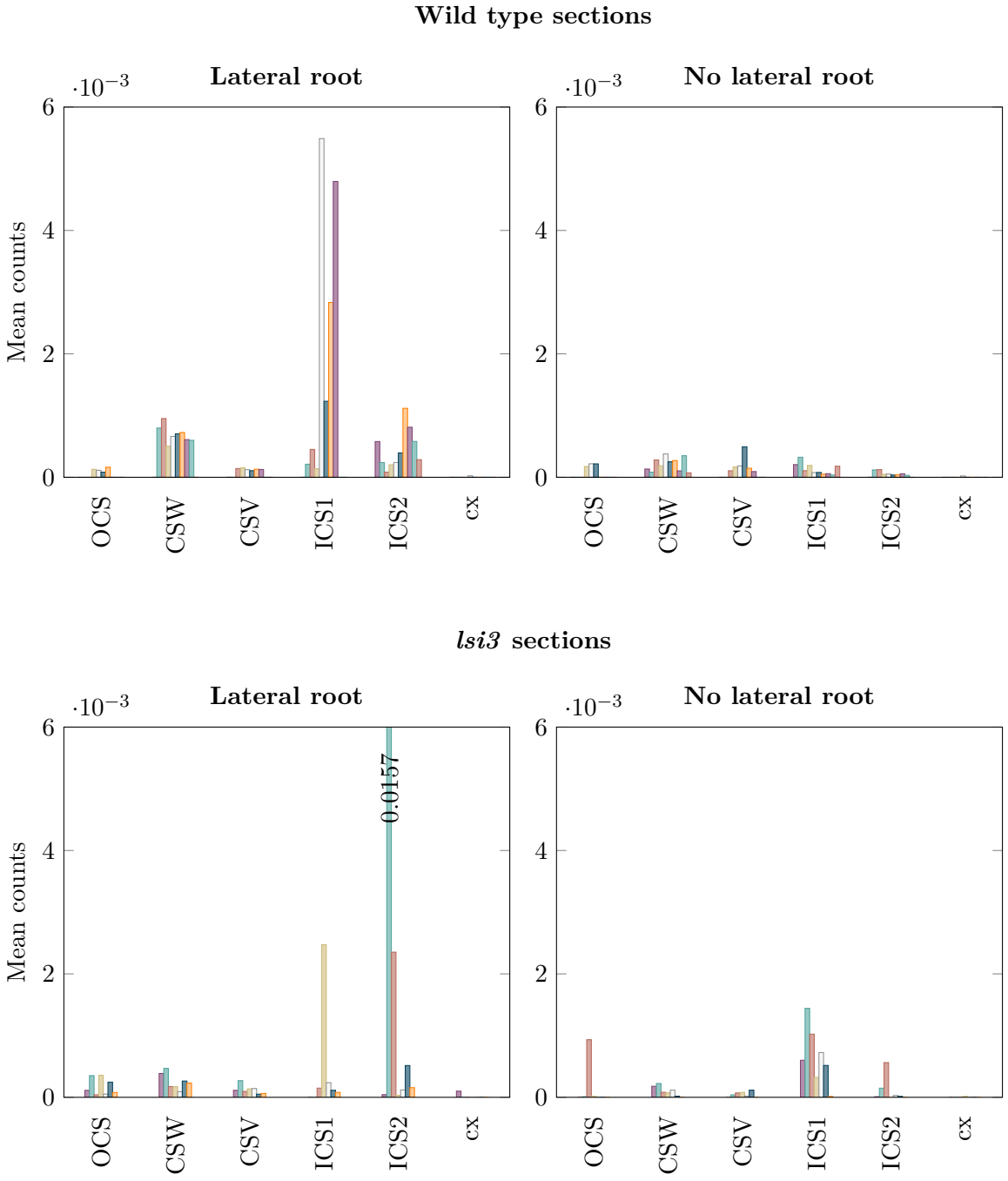

Figure 5.11: Arsenic concentration of both WT (top) and *lsi3* (bottom) with and without lateral roots.

two cells with markedly increased As, and one further with hugely increased concentration of the element. It contains such a greater quantity of As that it exceeds the y boundary of the graph by more than two and a half times.

The trend observed was therefore an increase of As in the lateral root containing sections, particularly in some of the cells in the stele. In the *lsi3* samples the increase was much larger but also more specifically occurring only in a small number of ROIs in the stele.

Distal vs. proximal side of lateral roots

While normalising the data, a slightly less obvious trend began to emerge; a trend of higher As and S concentrations in the ROIs closer to the lateral root.

In order to examine this further, I selected and ordered the ROIs within each group in increasing distance from the lateral root. This was done by first selecting the ROIs of each group that were closest to the lateral root, then selecting the next closest, and so on, until the furthest one was selected. After normalising the data using the 'norm cx' method (described in section 3.4.1) I can then graph the mean ion counts from each ROI against distance from the lateral root.

The results of this, figure 5.12, are quite interesting. For easier comparison both the *lsi3* (top) and WT (bottom) samples are drawn with the same y-axis range.

The trend of decreasing mean As concentration with increasing distance from the lateral root can clearly be seen in WT from the graph of $^{75}As^{-}$ signal against distance from the lateral root. The ICS1 and ICS2 regions that contained the higher $^{75}As^{-}$ signal were close to the lateral root. Even the ICS1 cells with the lowest $^{75}As^{-}$ signal were higher than their

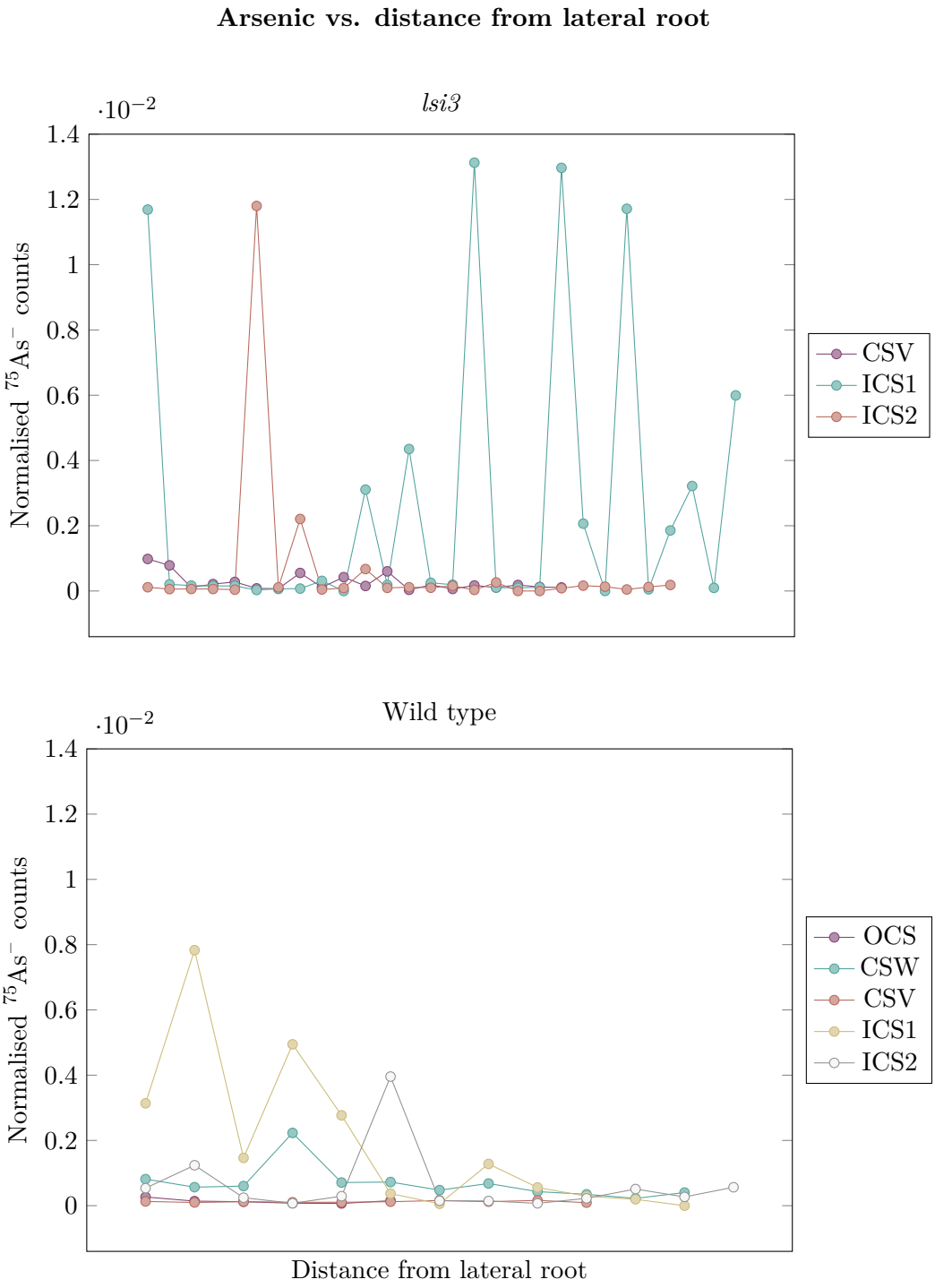

Figure 5.12: Average arsenic counts in cells in *lsi3* and wild type vs. distance from the lateral root.

counterparts on the distal side of the root.

Conversely the results from *lsi3*, top graph, show no such trend. The cells in both the ICS1 and ICS2 groups that had high $^{75}As^{-}$ signal are quite uniformly arranged around the stele. The normalised data shows that compared to WT, *lsi3* had a greater number of regions with high $^{75}As^{-}$ signal, and several of those regions contained higher mean signal than any region in WT.

The data used here for *lsi3* was taken from a large raster that included most of the stele. This allowed the ROIs to be selected from the regions closest to the lateral root all the way around to the opposite side of the stele. For WT the raster was centred slightly away from the middle of the stele, so such a comprehensive set of data could not be recorded; hence the smaller number of data points on the graph.

There is more data available from WT, but it is segmented into different rasters that were combined together in figure 5.7. Such a composite image allows us to see that, for the most part, the trend observed for this particular sample continues — with fewer regions of localised As and S occurring on the distal side of the root.

Because of the way data was selected, the ROIs used for these graphs were only from the first two or three rows of cells within the stele. Regions closer to the central xylem were not used. As seen in the NanoSIMS composite, figure 5.7, there are some regions of elevated S (and also As) close to the central xylem. This is something worth investigating, along with the relationship between S and As concentrations in these regions.

For this purpose I have created a new ROI group called “nearcx” that contains regions close to the central xylem. Adding this to the existing groups, I am able to plot a column

graph of mean S from some of these groups together, figure 5.13. Also included, on a separate scale (right), is the normalised mean $^{75}As^-$ signal from the same ROIs. The mean $^{75}As^-$ and $^{32}S^-$ signals in CSV, CSW and OCS were uniformly quite low in comparison to the cells closer to the centre of the root and have therefore been omitted for the sake of simplicity.

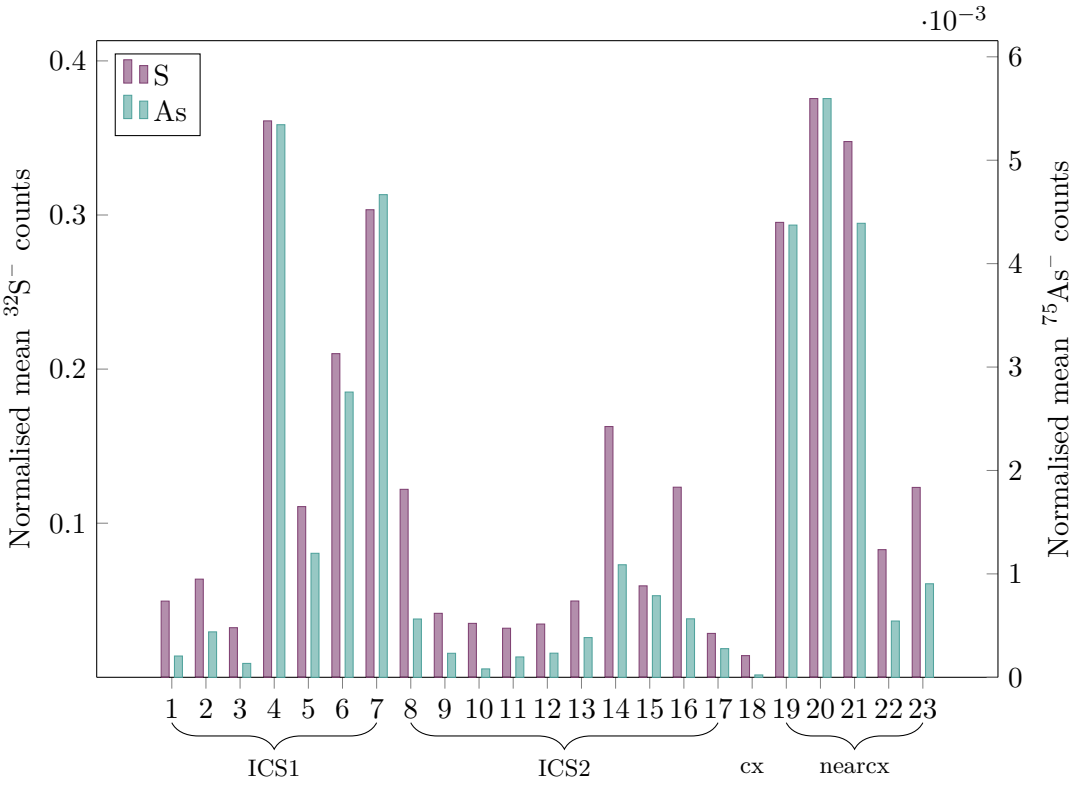

Figure 5.13: Mean normalised $^{32}S^-$ (left axis) and $^{75}As^-$ (right axis) counts in the root cells near a side root. Wild type sample, taken 1cm from the root tip; 397 f3 l1 1.

The graph shows that $^{32}S^-$ and $^{75}As^-$ signals from some cells near the central xylem (19-21) were much higher than average and comparable to the ICS1 cells that were also high in these signals (4,7). ICS2 regions were on average much lower and did not contain a cell with similarly elevated concentration of $^{32}S^-$ or $^{75}As^-$. The ratio of $^{32}S^-$ to $^{75}As^-$

signal appears lowest in the regions with the highest As concentrations.

Since I used the same method for highlighting ROIs as in the previous chapter (also on the roots of *O. sativa*) it is fairly straightforward to identify the types of cells that were examined. The endodermis (CSV) is very easy to identify because of the band of Si surrounding it (see fig. 5.5). Just inside of the endodermis is a cylinder of parenchyma or sclerenchyma cells forming the pericycle (ICS1) and just outside of the endodermis is the mesodermis (OCS). These features are labelled on the NanoSIMS maps in figure 5.14. The cells inside the pericycle (ICS2 and nearcx) are a mixture of sclerenchyma, parenchyma and vascular tissues, making it much harder to determine the exact function of specific cells in these regions.

It is also very difficult to determine how far through the lateral root junction these sections were microtomed. Since a lateral root junction is likely a fairly complex three dimensional structure, it is possible that taking cross sections through different planes of the junction could reveal quite different information, this possibility was not explored in these experiments. The results do, however, show strong evidence of very highly concentrated As and S in the lateral root junction in both the WT and *lsi3*.

The high concentrations of As and S in specific cells could be related to the loading of these elements into xylem, as proposed in the previous chapter. Ma *et al.* grew rice *O. sativa* defective in the formation of lateral roots (RM109) and found that Si uptake in the mature zone (1-4 cm from the root tip) was "significantly lower in RM109 than in WT." They concluded that lateral roots likely contain a specific transport system for Si [68]. Since lateral roots are understood to originate from the pericycle cells, is possible that

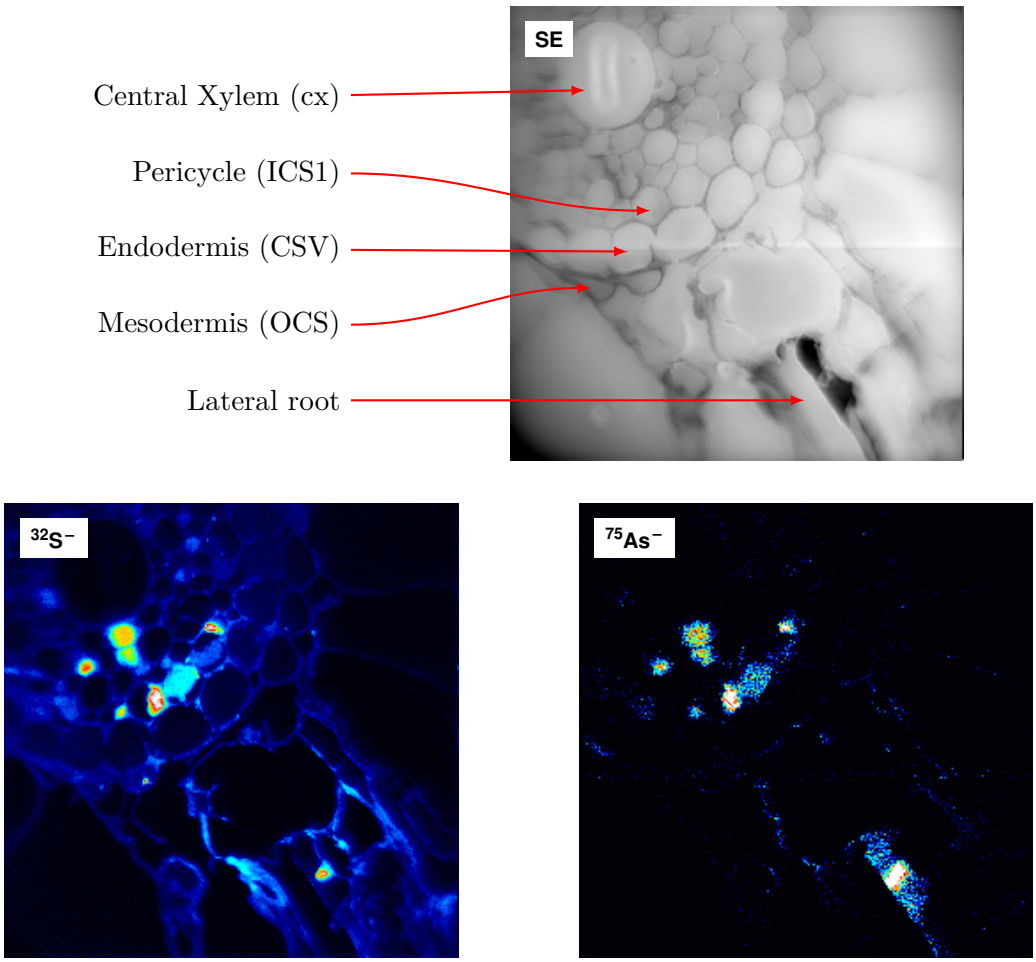

Figure 5.14: The Secondary election (a), sulphur (b), and arsenic (c) NanoSIMS results from 397 l3 f1 1. A wild type sample with a lateral root, 1cm from the root tip. The raster was 100µm in size.

As is taken up by the same transport system as Si and transported along the lateral root towards the pericycle cells of a higher order root where they form As-PC complexes. My data suggest that this process may be disrupted in *lsi3*, if Lsi3 is an efflux transporter used by As, then *lsi3* may not be able to load As into the pericycle cells of higher order roots, which could explain the observed result that there was no increase in As concentration in pericycle cells near lateral roots. The higher observed concentrations of As in *lsi3* could

again be explained by an inability of the plant to effectively efflux As from the pericycle of the higher order root into xylem, in agreement with the conclusion from the previous chapter.

Chapter 6

PT8-Ov mutation

In aqueous solutions As, as discussed earlier in section 1.2.1, typically exists as either As(III) or As(V) [38, 39]. The exact chemistry taking place in the rhizosphere is an area of ongoing study and not fully understood. It is complicated further in the case of *O. sativa* by the ability of rice to grow in flooded soils by transporting oxygen to root tissue by internal gas channels [192] causing a change in oxidative environment near the roots. Rhizosphere chemistry can also be altered by the presence of bacteria, an iron plaque [86], variations in soil aeration between the two growing seasons and changes in farming practices such as the relatively recent phenomenon of boro rice cultivation in the Bengal lowlands [193]. "Boro" refers to rice planted during the dry season (December-February) in Bangladesh and north eastern India, typically requiring groundwater irrigation. The different forms of As, which are believed to be taken up by different mechanisms, can therefore be present in the rhizosphere in different proportions depending on these variables.

Consequently in order to understand the uptake of As, not only is it important to study As(III) (arsenite) uptake pathways, as in the previous chapter, but to also examine possible pathways for the uptake of As(V) (arsenate).

Inorganic phosphate (Pi) competes with As(V) for uptake, leading to the Pi pathway being identified as a potential mechanism for the uptake of As(V) [53].

A rice mutant "defective in OsPHF1 (for phosphate transporter traffic facilitator1)" was shown by Wu *et al.* [80] to lose much of its ability to uptake and translocate both

Pi and As(V). As part of these experiments Wu *et al.* also prepared a transgenic rice overexpressing the Pi transporter OsPht1;8 (OsPT8). They found OsPT8 "to have a high affinity for both Pi and As(V), and its overexpression increased the maximum influx by 3- to 5-fold." Their experiments also included the use of HPLC-ICP-MS to measure speciation in xylem sap, revealing that As(V) was rapidly reduced to As(III) in the roots and shoots.

Analysis of 26 potential phosphate transporter (PT) genes by Liu *et al.* [194] showed that "Most PHT1 genes are strongly expressed in roots", and identified *OsPT8* as one of fifteen *OsPT* genes with "high or detectable expression simultaneously in root" in each of the three genotypes studied; Minghui 63, Zhenshan 97, and Shanyou 63. They used microarrays to assess expression of these PTs and found the average signal values of *OsPT8* genes in seedlings at the two-tillers stage were approximately six times higher in the root than the shoot.

Wang *et al.* [82] discovered that the japonica variety of rice *Nipponbare* took up more Pi and As(V) than the aus variety *Kasalath*, the former having more than twice the expression of Pi transporter genes *OsPT2* and *OsPT8*. Aus type rice are known to be highly tolerant to environmental stresses, they are typically sown in the summer along with the pre-monsoonal showers and harvested in autumn. Wang *et al.* isolated *ospt8* mutants in *Nipponbare* and *Kasalath*, and found that in hydroponic conditions the mutation "decreased As(V) uptake by 33-57%" in both backgrounds, concluding that "OsPT8 plays a key role in As(V) uptake"

6.1 Aims

Since Pi is an important nutrient for plants, the interaction of Pi and As uptake in As contaminated soils is an important area of study. Varieties of rice with a higher *OsPT8* expression could inadvertently take up more As at a higher rate, potentially allowing more As to be translocated to the grain. Alternatively, As(V) could be reduced to As(III) in the roots, then transported not by the phosphate pathway but instead via the silicic acid pathway.

In order to study this process we have grown and treated an *OsPT8*-overexpressing line (*PT8-Ov*) along with a WT counterpart for NanoSIMS analysis. This analysis aims to determine cellular and subcellular localisation of P and As, and how they are affected by overexpression of *PT8*. Since we are only interested in P and As transport in this experiment, Si was not included in the nutrient solution.

6.2 Method

The *PT8-Ov* lines (G2) were prepared in mostly the same way as the *lsi3* lines (G1) which are described in section 2.3, using the same half strength Kimura nutrient solution described in table 2.2. After 20 d they were exposed to 5 µmol L^{-1} As(V) (in the form Na_2HAsO_4) for 3 d instead of the 10 µmol L^{-1} As(III) used for G1. The lower concentration of As was necessary because *cad1-3* were particularly sensitive to As.

The plants were then rinsed in deionised water and preserved using HPF and the freeze substitution protocols detailed in section 2.4. Sections 1 µm in thickness were microtomed

from the preserved root and allowed to dry onto a Pt coated substrate, and coated with a further 5 µm Pt.

The NanoSIMS was tuned to detect $^{12}C^{14}N^-$, $^{28}Si^-$, $^{31}P^-$, $^{32}S^-$ and $^{75}As^-$ ions as described in section 2.7.4. Detector 4 was tuned to the $^{28}Si^-$ signal for comparison with G1 despite Si not being present in the G2 nutrient solution. Both the endodermis and exodermis were expected to be affected by *PT8-Ov*8 therefore NanoSIMS data was taken for parts of the stele that included the endodermis and central xylem, and for regions that included part of the epidermis including some of the exodermis, sclerenchyma and cortex.

6.3 Results

6.3.1 Sample preservation

The high pressure freezing and resin substitution was largely successful. Five root cuttings from *PT8-Ov* and five from WT were taken so that if any were damaged during HPF there would still be plenty of remaining samples. At the end of the resin embedding most samples appeared well preserved. Some of the roots had a large diameter, making them difficult to microtome without tearing. The large microtomed sections also frequently folded or wrinkled when deposited onto the substrates.

Some optical micrographs of typical sections of *PT8-Ov* and the corresponding WT are shown in figure 6.1 and figure 6.2 respectively, after they have been microtomed and deposited on platinum coated discs. The micrographs reveal good preservation of the root structure was achieved from HPF and resin embedding. There are some large scratches

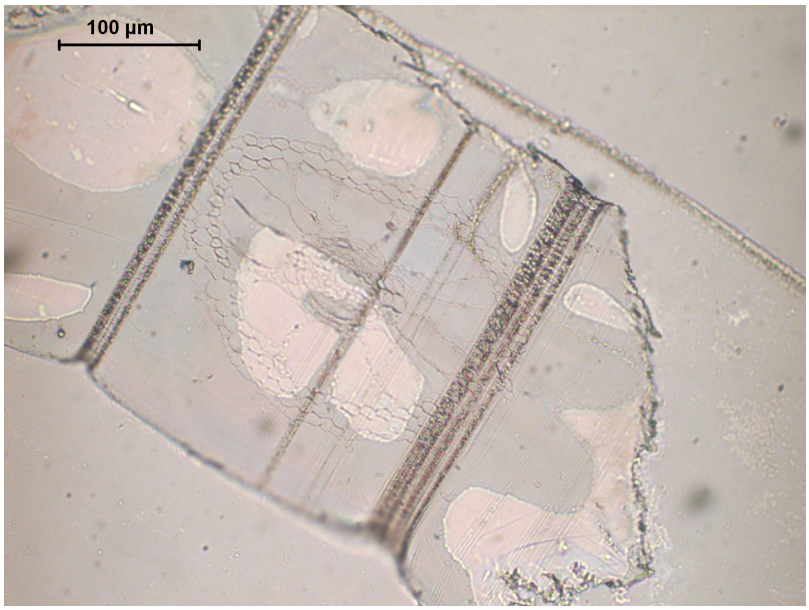

Figure 6.1: Optical micrograph of a preserved and microtomed section of mature root, WT.

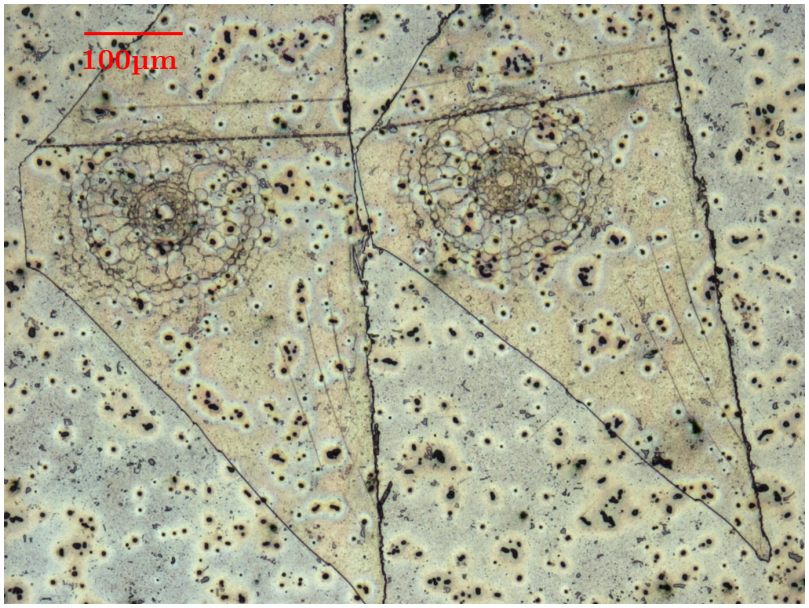

Figure 6.2: Optical micrograph of preserved and microtomed sections, *PT8-Ov*.

visible across the sections, they are especially prominent in figure 6.1. Previous damage to the diamond microtomy knife was responsible for these scratches. Care was taken in later samples to avoid the damaged sections of the diamond blade. Also visible in figure 6.1 are some lighter regions. These are areas where the sample is not sitting flat on the substrate. The risk of this occurring was reduced by making sure that the sections produced from microtomy were as small as possible while maintaining a suitable shape and structure to produce good sections. This could be achieved by very carefully using a razor blade to trim away excess resin.

6.3.2 NanoSIMS maps

I have provided two examples of some typical NanoSIMS data, one focussed on the stele, figure 6.3, and one focussed on the exodermis, figure 6.4. Both of these examples are from the same WT sample and the same growth line (G2). Some features are similiar to those observed in the WT from the *lsi3* growth line (G1) (see fig. 4.3); a diffuse $^{75}As^{-}$ signal present in the stele roughly correlated with the $^{32}S^{-}$ signal. The nutrient solution in G2 did not include Si, and therefore the very localised Si accumulation seen in G1 is not present in this sample.

The data for the $^{31}P^{-}$ signal suggests that the phosphorus is predominantly present within the stele (fig. 6.3) and sclerenchyma (fig. 6.4), with relatively little present in the cortex. In the sclerenchyma it appears to be distributed in a very similar fashion to both $^{32}S^{-}$ and $^{75}As^{-}$. While in the stele these elements also appear to share a similar distribution, the signal from $^{32}S^{-}$ and $^{75}As^{-}$ appears to have some concentration in regions within specific

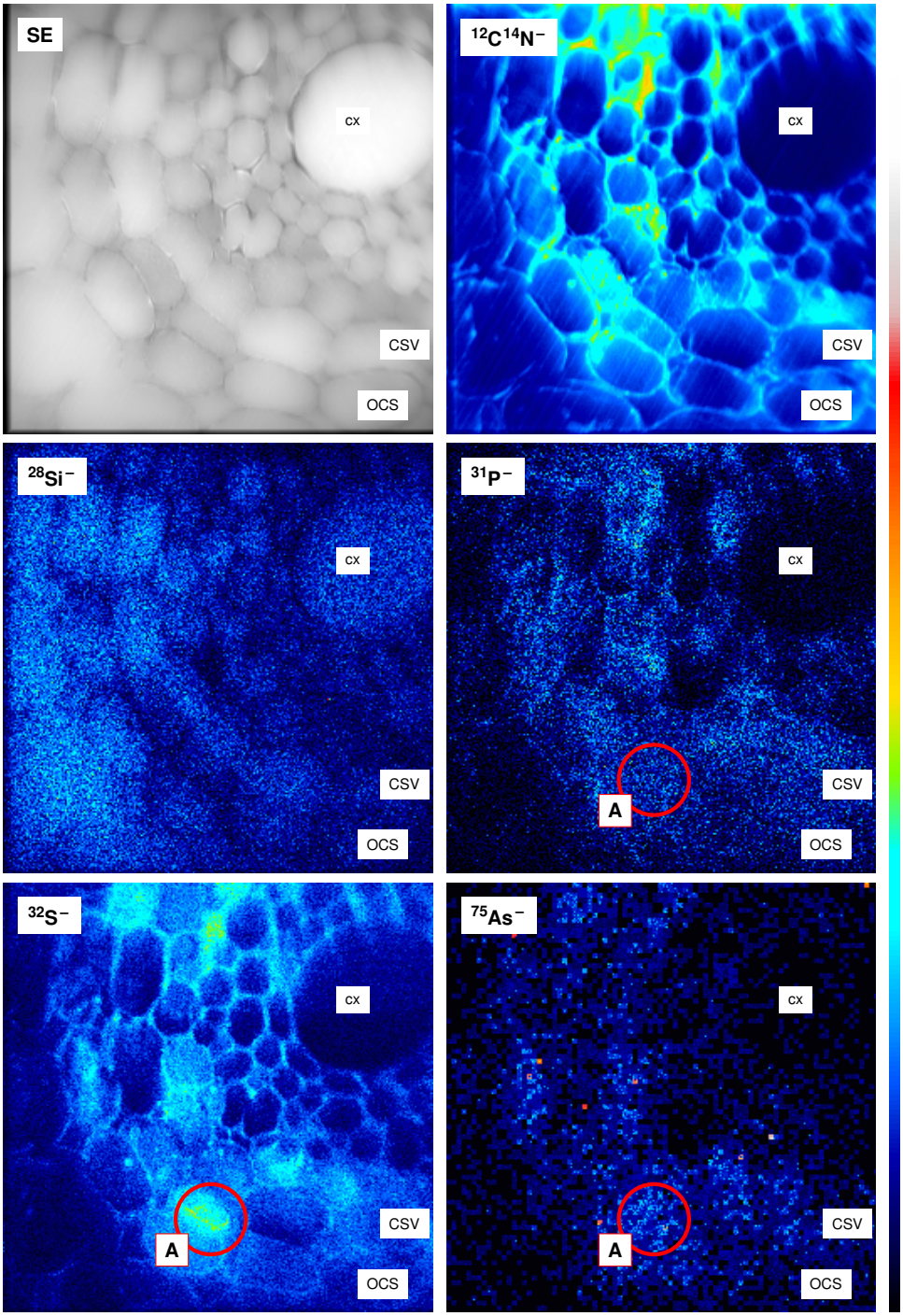

Figure 6.3: Example of SIMS data from a region in the stele, G2 WT. *A*, region of elevated $^{32}S^-$ and $^{75}As^-$ but not $^{31}P^-$; *cx*, central xylem; *CSV*, endodermis; *OCS*, mesodermis.

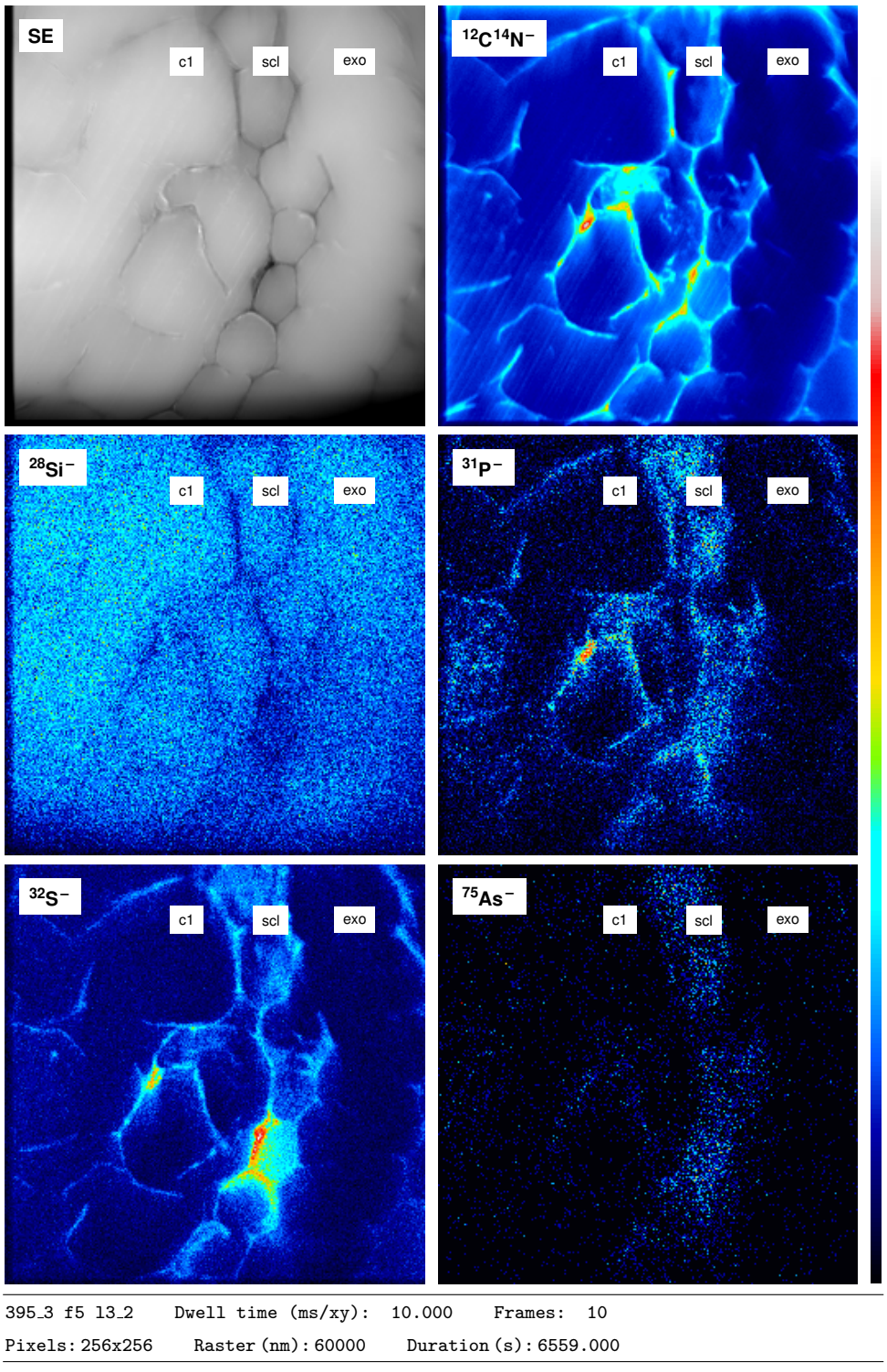

Figure 6.4: Example of SIMS data from a region around the exodermis, G2 WT, showing co-localisation of $^{32}S^-$, $^{31}P^-$ and $^{75}As^-$. *c1*, outermost cortex cells; *scl*, sclerenchyma; *exo*, exodermis.

cells that are not shown by the $^{31}P^-$ signal. For example, towards the bottom centre of the $^{32}S^-$ and $^{75}As^-$ maps, there is a region of higher ion intensity that is not associated with a higher $^{31}P^-$ signal (see fig. 6.3 annotation *A*).

This gives an idea of what some of the typical NanoSIMS data looks for WT sections from G2. To better compare WT and *PT8-Ov* I have arranged some *PT8-Ov* data side by side with the already seen WT data both for the stele (fig. 6.5) and the exodermis (fig. 6.6).

In both cases the similarity between detectors tuned to $^{32}S^-$ and $^{75}As^-$ suggests a co-localisation of S and As within the stele despite the low and diffuse signal. The endodermis (CSV), mesodermis (OCS) and central cortex (cx) are labelled on the image. The data suggests that most of the P, S and As is found within the endodermis, mesodermis, and specific cells with in the stele. There are a few regions that appear to contain very little of any of the elements displayed here. One of these is the central xylem (cx), and it is possible that the other such regions are metaxylem or protoxylem vessels, such as annotation B, fig. 6.5. This labelled region is neighboured by two cells that appear to have unusually high concentrations of both As and S. It is possible that these are xylem parenchyma cells, responsible for loading and unloading nutrients from the xylem vessel.

In the exodermal regions, figure 6.6, the outermost part of the root is to the right on the WT data and to the top right of *PT8-Ov*. The structure of these regions look very similar between the SE images for WT and *PT8-Ov*. In the former, the cells in the cortex are perhaps slightly larger and irregular, with what appears to be some damage to the cell walls, likely as result of the HPF process.

At first glance in both WT and *PT8-Ov* the concentrations of S and As again appear

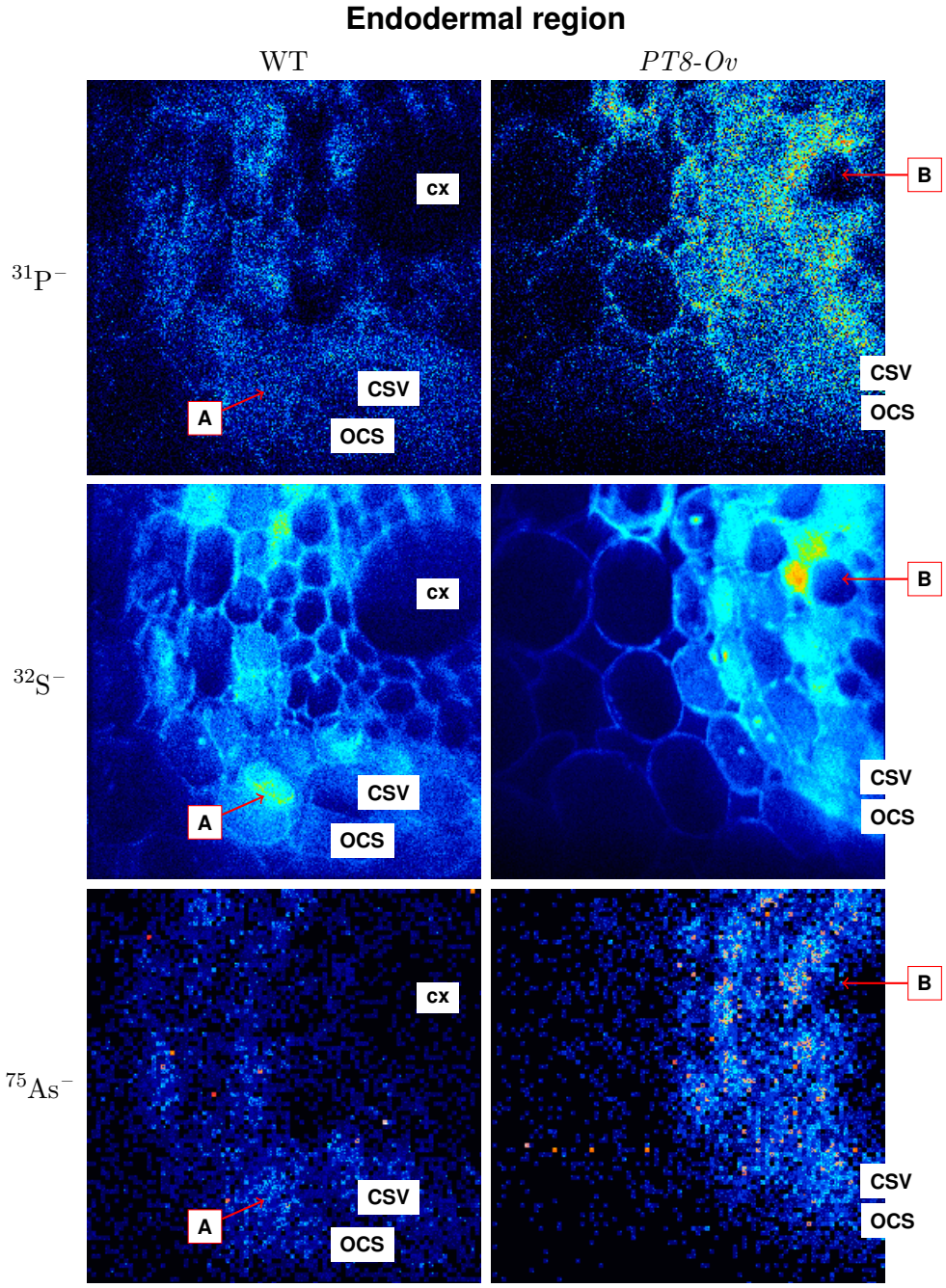

Figure 6.5: NanoSIMS ion maps of WT and *PT8-Ov* sections near the stele, both rasters 60µm in size and had a duration of 6559s, $^{75}As^-$ contrast increased. *A*, region of elevated $^{32}S^-$ and $^{75}As^-$ but not $^{31}P^-$; *B*, region low in all ions, adjacent to regions high in $^{31}P^-$, $^{32}S^-$ and $^{75}As^-$, possibly metaxylem; *cx*, central xylem; *CSV*, endodermis; *OCS*, mesodermis.

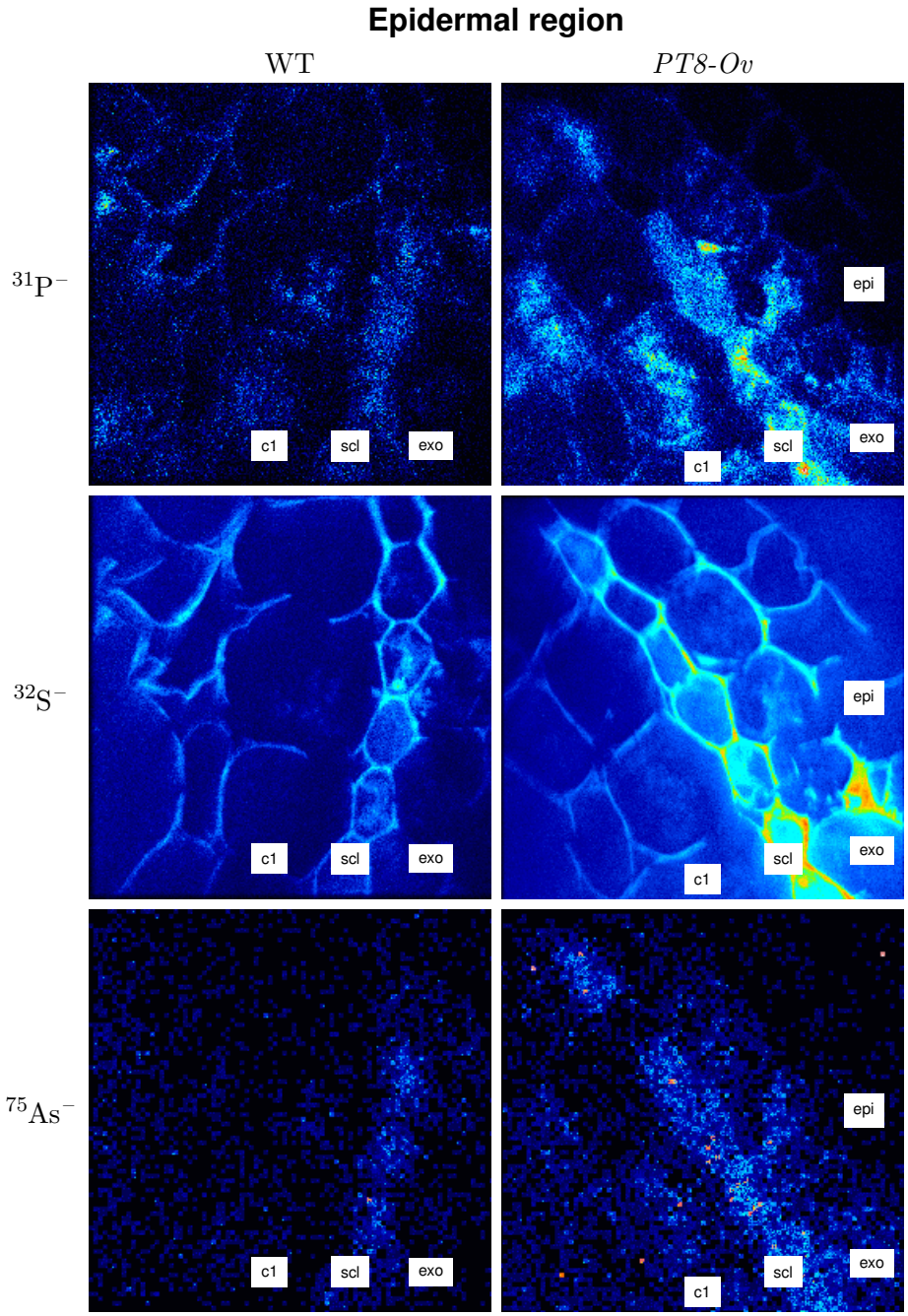

Figure 6.6: NanoSIMS ion maps of WT and *PT8-Ov* sections near the exodermis, both 60µm in size and had a duration of 6559s, $^{75}As^-$ contrast increased. *c1*, outermost layer of cortex; *scl*, sclerenchyma; *exo*, exodermis; *epi*, epidermis.

to be similarly distributed; both appearing in the thin distinct strip of small cells that form the sclerenchyma. The *PT8-Ov* data, for the ions measured here, demonstrates a possible trend of phosphorus being more localised to subcellular regions than is observed for WT. Additionally As appears to be not just predominantly in the sclerenchyma (as is the case with WT) but also extending fairly significantly either side of it in a manner that more closely resembles the phosphorus distribution.

6.3.3 Data analysis

Since the data in these images is not normalised and the images only show relative proportions of signal from each detector, it is not possible to make straightforward comparisons between WT and *PT8-Ov*. For example, one image appearing brighter in the NanoSIMS data does not necessarily mean more of that element was present. It can also be challenging to compare information from several images as they will be in different orientation and it is easy to confuse different regions from different roots. In order to make semi-quantitative analysis I chose to use a technique similar to geostatics; I first identified the samples of best quality, then selected regions of interest within these samples based on their relative positions within the root and normalised them using the normcx method determined in Chapter 3. This method allowed me to compare the recorded number of counts from different parts of the root between different samples.

For the NanoSIMS data centred around the stele, I used the same methods as described in section 4.3.3 and figure 4.4. This involved identifying and highlighting individual cells within concentric rings as the regions of interest. It had been relatively trivial in the case of

the previous growth line, G1, to identify the same type of cells in each sample, because the endodermis was surrounded in a very distinct layer of Si decorating the cell walls. These Si surrounded cells were then selected as ROIs belonging to the group labelled "CSV," and the other groups were identified based on their position relative to this, as demonstrated in figure 6.7.

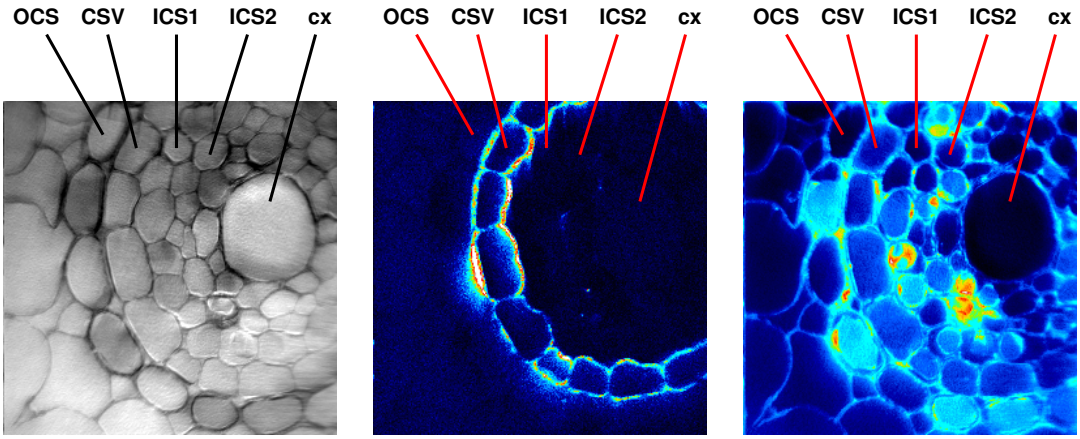

Figure 6.7: The regions of interest for the *lsi3* growth line (G1). SIMS images from left to right; SE, $^{28}Si^{-}$, $^{12}C^{14}N^{-}$. "CSV" can be easily identified by the strong Si accumulation on the cell walls.

In G2 such a feature was not present, as the nutrient solution did not contain Si, and therefore the plants could not deposit any on the endodermis. Instead I had to carefully observe the relative shapes of the cells, and compare them to samples from G1 in order to positively identify the cell types. For example figure 6.8 shows some data from the G2 growth line, marked and labelled with the same ROI group names. The middle of the three images contains the data from the detector tuned to $^{28}Si^{-}$. In this case there is no visible deposition of Si present on the endodermis.

I found it useful to use both the $^{12}C^{14}N^{-}$ and the SE data to determine the areas of

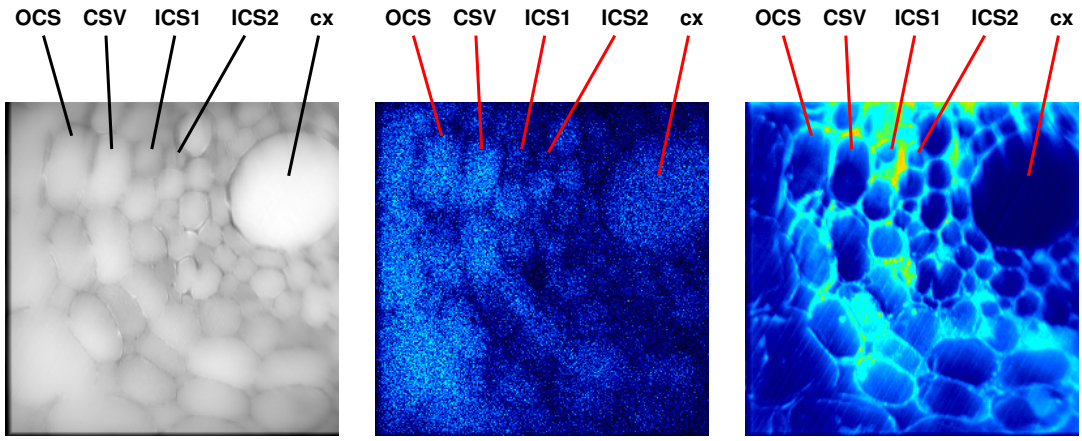

Figure 6.8: The regions of interest for the *PT8-Ov* growth line (G2). SIMS images from left to right; SE, $^{28}Si^-$, $^{12}C^{14}N^-$. No strong Si accumulation was present on the cell walls, making identification of "CSV" more challenging.

each cell, since using just one detector on its own often did not provide enough information to accurately select individual cells. In most cases the shapes of the features were sufficient to confidently mark the ROI groups the same as in the previous chapter.

For the epidermal regions I identified the outermost layer of cells, highlighted them as individual ROIs, and labelled them as belonging to the ROI group "epi." I repeated this for the next layer of cells, and so on, labelling them "exo," "scl," "c1" and "c2" respectively, as shown in figure 6.9. These abbreviations were chosen to refer to the root epidermis (rhizodermis), exodermis, sclerenchyma, and the two outermost layers of the cortex. This reflects the conventions used by Tabuchi *et al.* [195], Ranathunge *et al.* [196], Syu *et al.* [197] and others in their respective studies of uptake of ammonium ions, water, and As in *O. sativa*.

Once all the ROIs had been identified on a particular data set, the mean counts over each ROI could be extracted by the OpenMIMs software for each detector. This was done

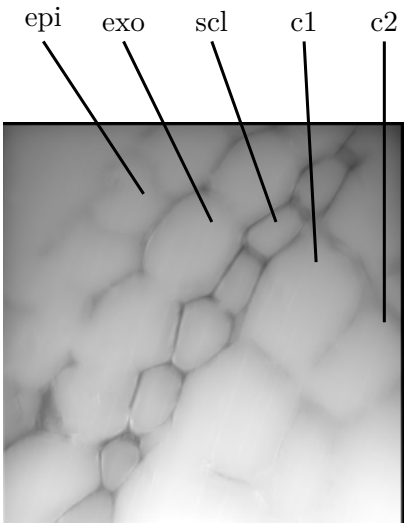

Figure 6.9: Regions of interest around the epidermis, each layer of cells is assigned to an ROI group as labelled in this example.

for all of the samples and added to a spreadsheet. In order to normalise the data, the "norm cx" method, detailed in section 3.4.1, was applied. This involved simply dividing all the data for each sample by the mean $^{12}C^{14}N^-$ counts from the central xylem. This effectively normalised changes in primary ion intensity, secondary ion transmission, and dwell time.

Normalised ion counts can then be extracted from the NanoSIMS data, allowing comparisons to be made between the compositions of different cells. An illustrative example of how some data was mapped from images to numerical values is shown in figure 6.10 using the same *PT8-Ov* data that was shown in figure 6.5. Handling the data in this way allows numerical values to be produced that can then be used to compare between cells in different regions of the root and between different samples. For example in figure 6.10 we can see not only that the As is found predominantly in the stele (OCS, CSV, ICS1 and ICS2) as opposed to the cortex (OCS2) but that the most As rich regions were found in the pericycle (ICS1). Less obviously it shows that the pericycle contains regions regions highly

Table 6.1: Samples that were used for quantitative analysis

Sample name	Sample type	Analysed region
395_3 f5 l2	WT	Stele
395_3 f6 l1_1	WT	Stele
395_3 f7 l1	WT	Stele
395_4 f7 2	WT	Stele
395_4 f8 1	WT	Stele
395_f4_l1_1	WT	Stele
395_3 f5 l3_2	WT	Epidermis
395_3 f6 l2_1	WT	Epidermis
395_4 f8 4_2	WT	Epidermis
395_4_f1_2	WT	Epidermis
396_3_f4_4	*PT8-Ov*	Stele
396_3 f5_3	*PT8-Ov*	Stele
396_3 f7 l6	*PT8-Ov*	Stele
396_3 f7 l3	*PT8-Ov*	Epidermis
396_3 f7 l2	*PT8-Ov*	Epidermis
396_3 f7 l5	*PT8-Ov*	Epidermis

concentrated in As (annotation A) and also containing relatively little As (B), suggesting different cell types in this part of the root.

Not all of the data collected was suitable for quantitative analysis. This could be due to improper calibration of the machine, incorrect settings, or insufficient useful data in the rastered area. Out 41 sets of data collected, the 14 NanoSIMS acquisitions used for quantitative analysis are listed in table 6.1. In order to minimise selection bias I only omitted samples that contained too few cells of interest or suffered from poor preservation or beam damage.

The method of mapping of NanoSIMS data from regions of interest to numerical values as illustrated in figure 6.10 was carried out for the samples in table 6.1. This produced a large quantity of data that is given in appendix A for reference.

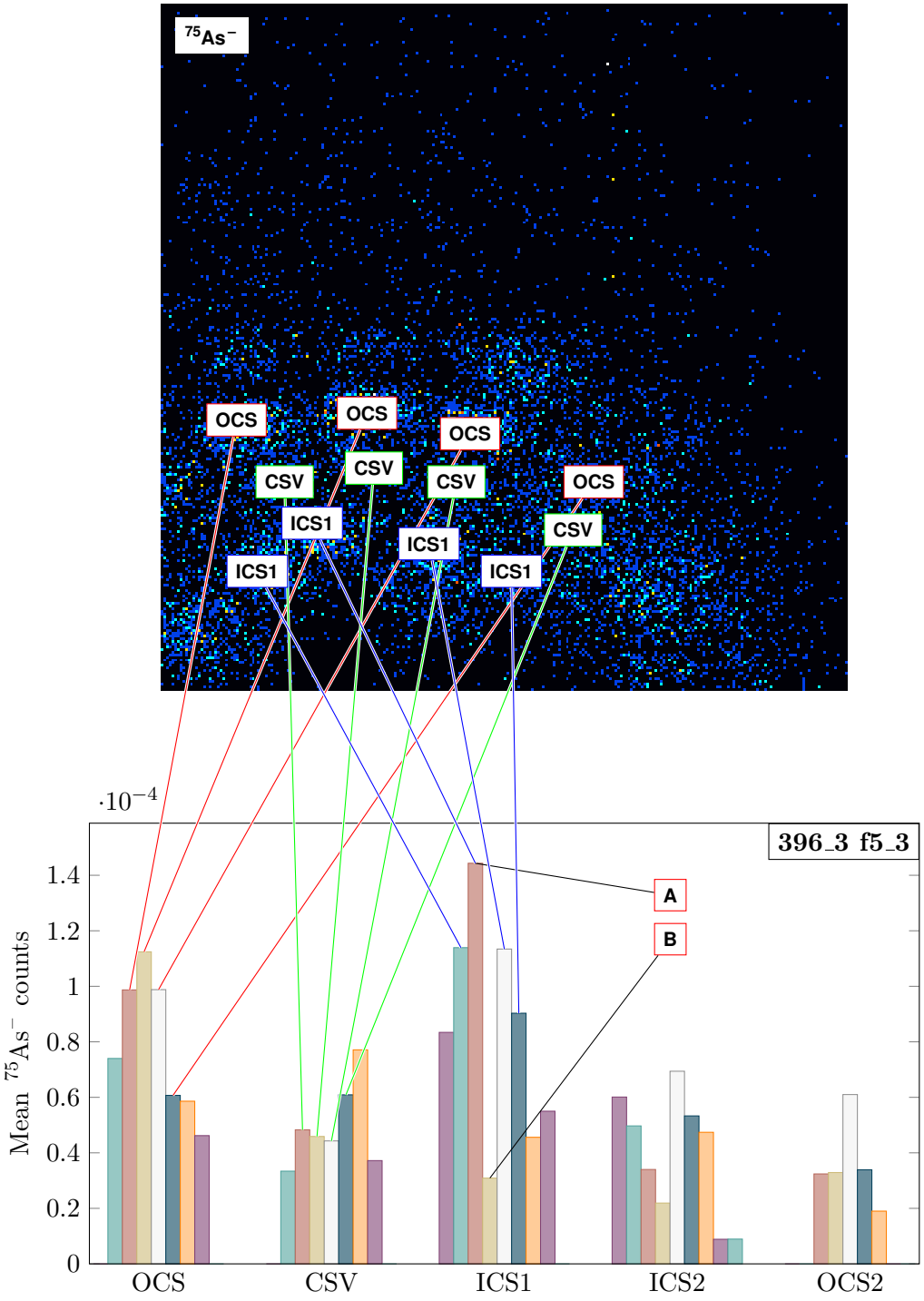

Figure 6.10: Diagram showing relationship between ion counts from a small number of ROIs and the respective numerical data for $^{75}As^-$ signals in the stele of *PT8-Ov* root. Highest counts were recorded in ICS1. *OCS*, mesodermis; *CSV*, endodermis; *ICS1*, pericycle; *A* pericycle cells with high average $^{75}As^-$ signal; *B* pericycle cells with low average $^{75}As^-$ signal.

Average signals in different root regions

In order to make overall comparisons between distributions of $^{32}S^-$, $^{32}P^-$ and $^{75}As^-$ in these samples I calculated averages and standard deviations of these signals for all OCS regions across all WT samples, and then for all CSV regions, and so on. Repeating this again for *PT8-Ov* allows rudimentary comparisons to be made in the distributions of these signals, figure 6.11.

The averages counts from the endodermal regions (left column, fig. 6.11) suggest that for both WT and *PT8-Ov* P and As are slightly more concentrated in the stele than the cortex, whereas S is more uniformly distributed. Data from the epidermal regions (right column, fig. 6.11) suggest P and As are predominantly localised to the sclerenchyma whereas S is again more uniformly distributed. Lastly it appears that in almost all regions P and S concentrations are higher in *PT8-Ov* than WT, and for As distributions in the stele, but near the outer edges of the root As concentrations were higher in WT.

Student's t-tests between these populations indicate a significant ($p < 0.05$) increase in $^{31}P^-$, $^{32}S^-$ and $^{75}As^-$ signal for *PT8-Ov* over WT for all regions near the stele except the central xylem. Near the outer edge of the roots a significant increase in $^{31}P^-$ was recorded in the epidermis, exodermis, and sclerenchyma for WT over *PT8-Ov*, whereas there was a significant decrease ($p = 0.04$) in $^{75}As^-$ counts from the epidermis.

Cells with high concentrations of particular elements

While these trends appear quite strongly in figure 6.11, the large standard deviations (indicated by the error bars) are evidence of the large variations not only between samples but

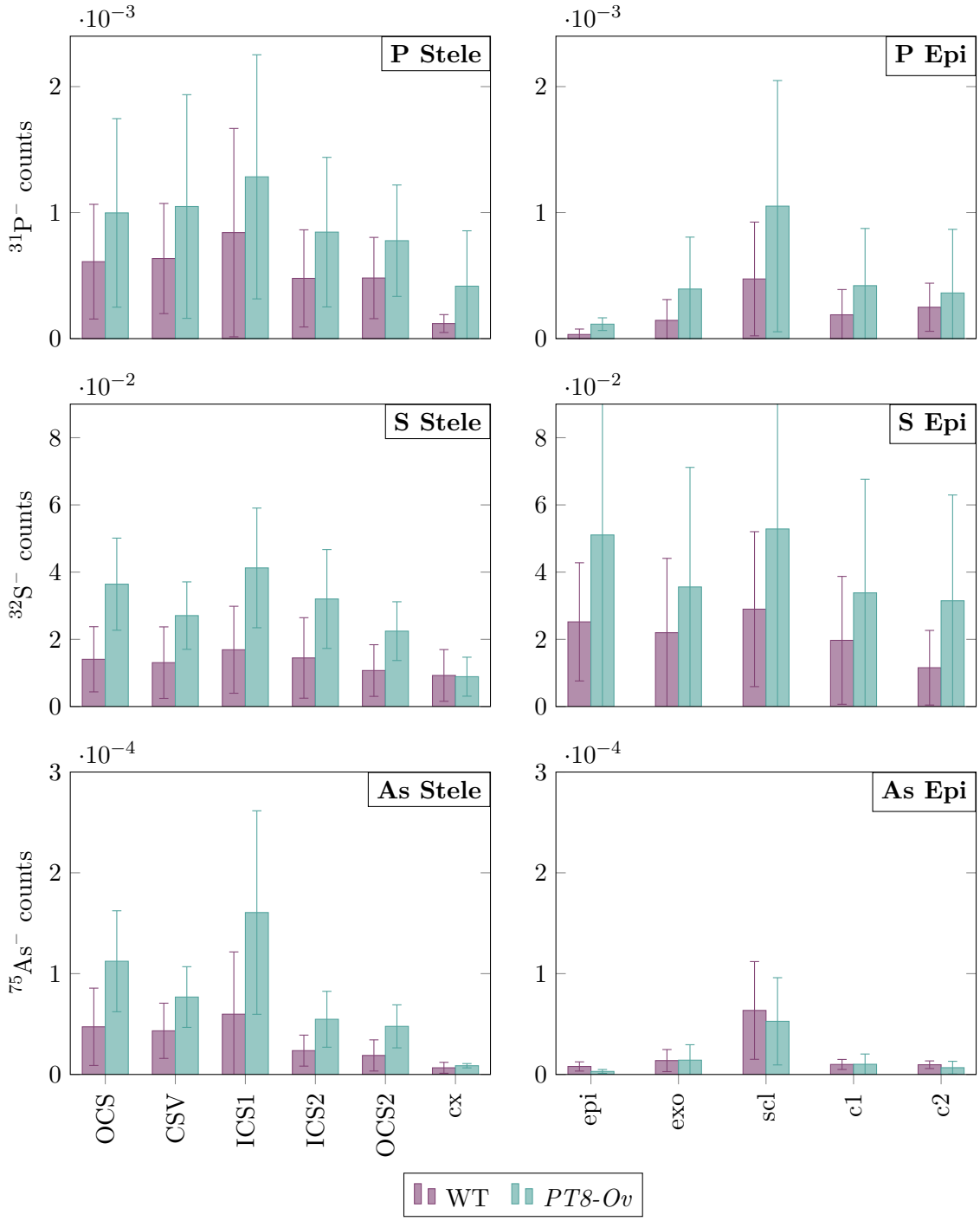

Figure 6.11: Average normalised counts recorded from different cells averaged across all WT (purple) and *PT8-Ov* (teal) samples for areas near the endodermis (left column) and epidermis (right column). Error bars represent one standard deviation in the mean counts between cells in the same region. *OCS*, mesodermis; *CSV*, endodermis; *ICS1*, pericycle; *ICS2*, cells just inside of pericycle; *OCS2*, cells just outside of mesodermis; *cx*, central xylem; *epi*, epidermis; *exo*, exodermis; *scl*, sclerenchyma; *c1*, cells just inside sclerenchyma; *c2*, cells just inside c1.

also between different cells within the same region of the same sample. For example, within the stele it is not possible to accurately determine the type of each individual cell using NanoSIMS data alone. I selected cells just inside the endodermis as a region of interest because they could be easily identified and some of them produced relative high $^{75}As^-$ signals, but some of these cells appear to contain very little of any of the elements of interest (*e.g.* fig. 6.5 annotation A), while others were highly concentrated in As and S. It is likely the "ICS1" contains an average of data from several different types of cells such as phloem, metaxylem, and companion cells. By taking an average information on the localisation of signal to these specific cells is lost.

Averaging the data also hides large variances between samples of the tame type. Therefore it might be more accurate to try to quantify the relative localisation of elements within each sample, since this would not require normalisation. This would provide an indication of the distributions of key elements and could help quantify any changes distribution of these elements resulting from overexpression of *PT8*.

In order to achieve this I calculated the number of cells in each sample that contained 50% more $^{31}P^-$, $^{32}S^-$ or $^{75}As^-$ counts than the average for the rest of the sample. This provides an absolute number of cells highly concentrated in P, S and As. Dividing this by the number of cells in each region within the sample gives a relative number of concentrated cells per root region, which can then be used to compare WT to *PT8-Ov*. Such a comparison is made in figure 6.12 and gives an idea of where the cells with the greatest concentrations of P, S and As are most likely to be found.

In combination with the data from figure 6.11 this suggests that cells in the pericycle and

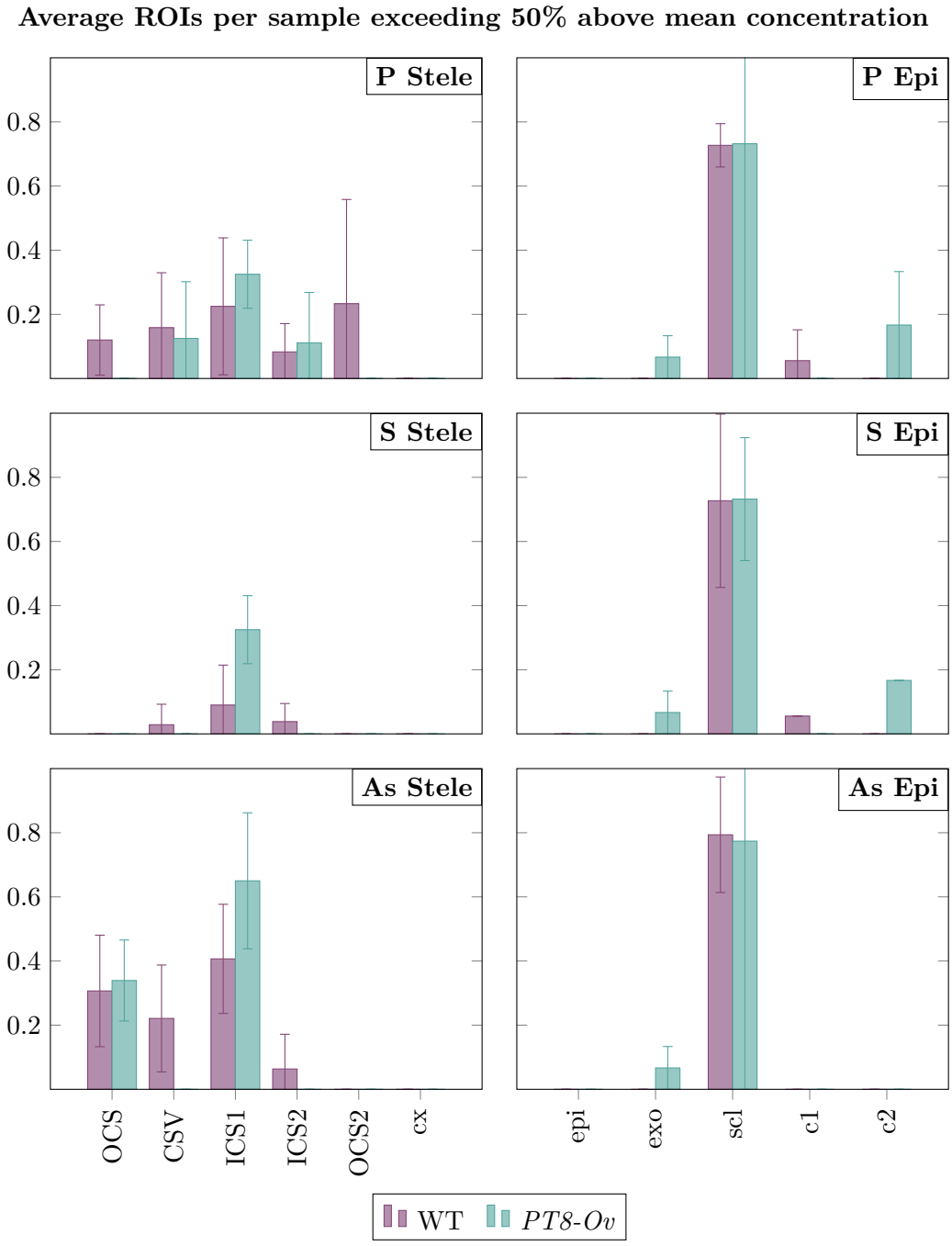

Figure 6.12: Average number of ROIs root region containing more than 50% higher than the mean concentration of each respective element. Left column regions near stele. Right column regions near epidermis. *OCS*, mesodermis; *CSV*, endodermis; *ICS1*, pericycle; *ICS2*, cells just inside of pericycle; *OCS2*, cells just outside of mesodermis; *cx*, central xylem; *epi*, epidermis; *exo*, exodermis; *scl*, sclerenchyma; *c1*, cells just inside sclerenchyma; *c2*, cells just inside c1.

Table 6.2: *p*-values from Student's *t*-tests for different ions between WT and *PT8-Ov* sections for high $^{75}As^-$ signal regions near the Stele and Epidermis.

	Detector		
Region	$^{31}P^-$	$^{32}S^-$	$^{75}As^-$
Epi	0.0981	0.1223	0.4281
Stele	0.2515	0.0004	0.0260

sclerenchyma contain both the highest average concentration of all three of these elements and the greatest number of cells containing high concentrations of these elements.

To determine if there was a significant difference in high As containing regions between WT and *PT8-Ov* I conducted Student's *t*-tests on the three ROIs from each section with the highest $^{75}As^-$ signal, associated *p*-values are given in table 6.2. There was no significant difference ($p < 0.05$) between WT and *PT8-Ov* for the epidermal regions, but there was significant difference between WT and *PT8-Ov* in the distributions of high $^{32}S^-$ and $^{75}As^-$ signal producing cells near the stele.

This data suggests no difference between WT and *PT8-Ov* in the relative distribution of elements near the edge of the root, but that overexpression of *PT8* may have caused S and As to be more highly localised to the pericycle.

Arsenic sulphur and arsenic phosphorus ratios

Examining the relative ratios between these elements could shed some more light on how PT8 affects transport and detoxification of As. In order to do this I used the normalised average signals from all the ROIs to plot scatter graphs of $^{75}As^-$ against $^{32}S^-$, some typical examples are given in figure 6.13. This figure only contains one example of WT and *PT8-Ov* sections for near the epidermis and stele, the rest of the data can be found in appendix B.

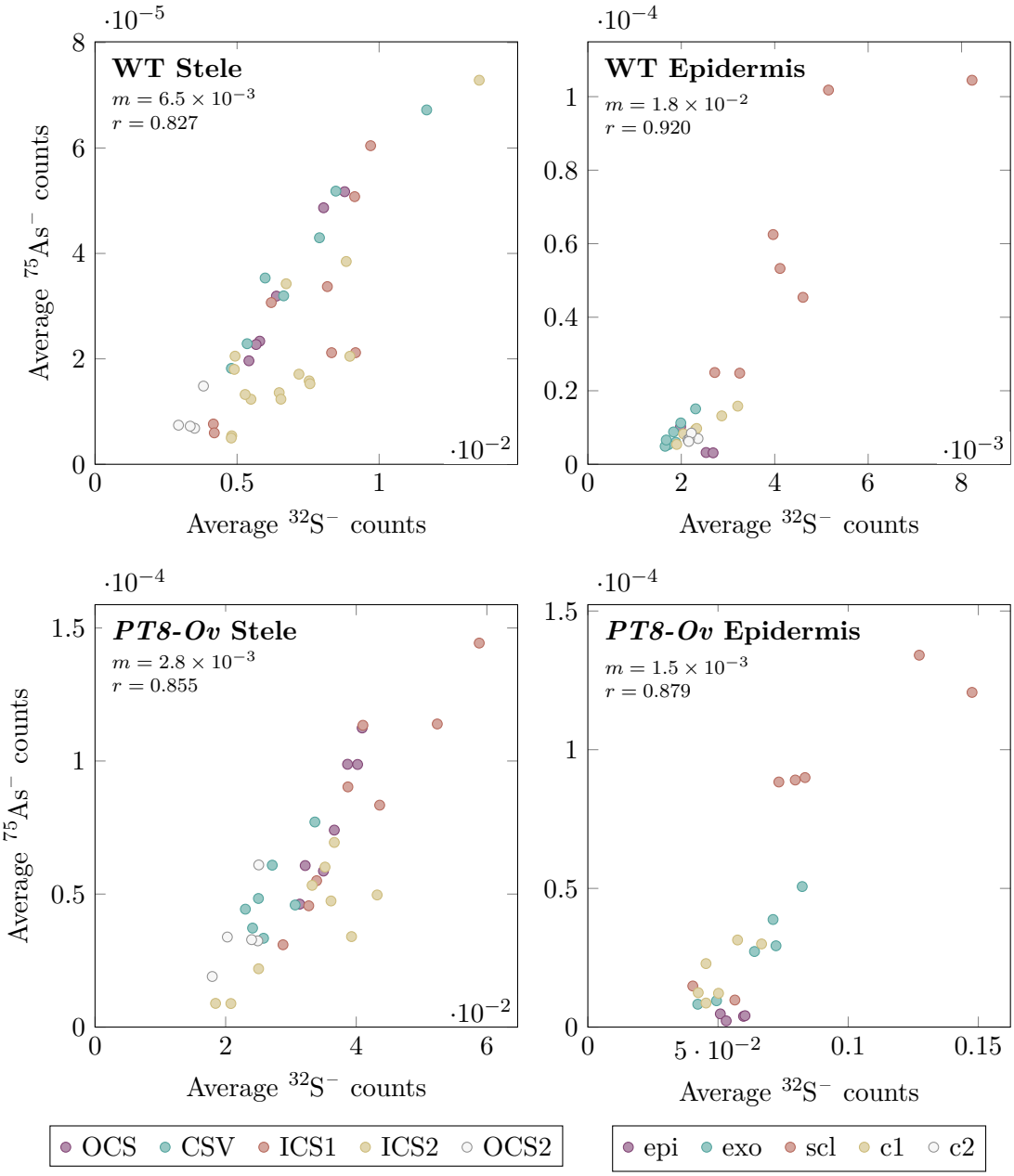

Figure 6.13: Scatter graphs of mean normalised $^{75}As^-$ counts against mean normalised $^{32}S^-$ counts from each region of interest, ROI groups are plotted in seperate colours as indicated in the legend. Data from one example of WT and *PT8-Ov* sections recorded near the stele and near the epidermis. (m) linear regression gradient given to two significant figures, (r) Pearson product-moment correlation coefficient give to three significant figures.

The ratios between ion counts will depend on the relative tuning on the detectors. As already demonstrated in figure 4.18 there are large errors in this tuning that is not accounted for by the normalisation method used. This error is evident again here by the different scales on the scatter plots in figure 6.13. I calculated the Pearson product-moment correlation coefficient (PPMCC) and the gradients of the line of best fit using the linear regression method (least squares), the results of each are shown in the top left of the scatter plots.

The process of calculating gradients and correlation coefficients was repeated for $^{75}As^{-}$ signal against $^{32}S^{-}$ signal and $^{75}As^{-}$ against $^{31}P^{-}$. The results are presented as bar graphs in figures 6.15 and 6.14 respectively. One of the correlation coefficients was negative so the modulus was used, and the gradients varied to such a degree that they are plotted on a logarithmic axis.

The graphs in figure 6.14 show that the correlation between $^{32}S^{-}$ and $^{75}As^{-}$ signals is quite good ($r > 0.8$) for most sections but very poor in two of the sections. The highest gradients were from the two sections with the worst correlation.

6.4 Discussion

The average $^{31}P^{-}$, $^{32}S^{-}$ and $^{75}As^{-}$ signals, figure 6.10, indicate that these elements are predominantly located in the stele and sclerenchyma of both WT and *PT8-Ov*. This data suggests more of all of these elements in *PT8-Ov* compared to WT for all regions with the exception of the epidermal regions where lower $^{75}As^{-}$ signals were recorded.

When analysing just the regions with highest concentrations of P, S and As *PT8-Ov*

had significantly higher average normalised $^{75}As^{-}$ ($p = 0.0260$) and $^{32}S^{-}$ ($p = 0.0004$) counts, suggesting that *PT8-Ov* had taken up more As and P. This agrees with previous observations made by Chen *et al.* [198] and Nussaume *et al.* [199] that OsPT8 plays an important role in Pi uptake; and observations by Wu *et al.* [80] and Wang *et al.* [82] that As(V) uptake increases along with Pi uptake with overexpression of *OsPT8*. Higher S concentration could be caused by increased production of PCs as part of the detoxification mechanism in response to the higher As uptake.

The approximately 5x increase in root As in *PT8-Ov* recorded by Wu *et al.* in rice grown in similar conditions was not observed in this thesis. Taking this discrepancy, as well as the large variance between samples (see appendix A) and small sample size into consideration, suggests that these results wholly conclusive. The high variances could be caused by changes in the relative tuning between detectors, creating systematic error which would persist despite normalisation as the method used only normalises against data from the first detector, tuned to $^{12}C^{14}N^{-}$. However the results were close to agreement and only a relatively small quantity of additional data could allow a much more definitive conclusion to be drawn.

Jia *et al.* [81] used green fluorescent protein markers to show that *OsPT8* is strongly expressed in both the epidermis and endodermis. These results showed that As and P were present in relatively low concentrations in the epidermis, and in elevated concentrations in the sclerenchyma. Lower As concentrations in *PT8-Ov* near the edge of the root could have been caused by increased rate of translocation of As away from the epidermis.

Similar to G1 sections, high proportions of $^{75}As^{-}$ signal were observed in smaller cells

adjacent to larger cells with much lower signal from all detectors (figure 6.5 annotation *B*). This could represent protoxylem or metaxylem surrounded by parenchyma cells, where the parenchyma are used for storage and loading of ions into xylem vessels. The similar ratios of As to S counts between WT and *PT8-Ov* suggest that As is being rapidly reduced from As(V) to As(III) and detoxified by PCs in the roots of both lines. It is possible that As(V) is being reduced in the sclerenchyma, and chelated in the stele. This would explain the strong correlation of As and P near the edge of the root as As(V) and Pi share transport a transport pathway, once As is reduced to As(III) it would likely move via a different transport pathway, and therefore correlate less well with P, as seen in the stele. It would also explain and the strong correlation of As and S near the centre of the root, where as As(III) can be readily detoxified by chelation with thiol containing PCs.

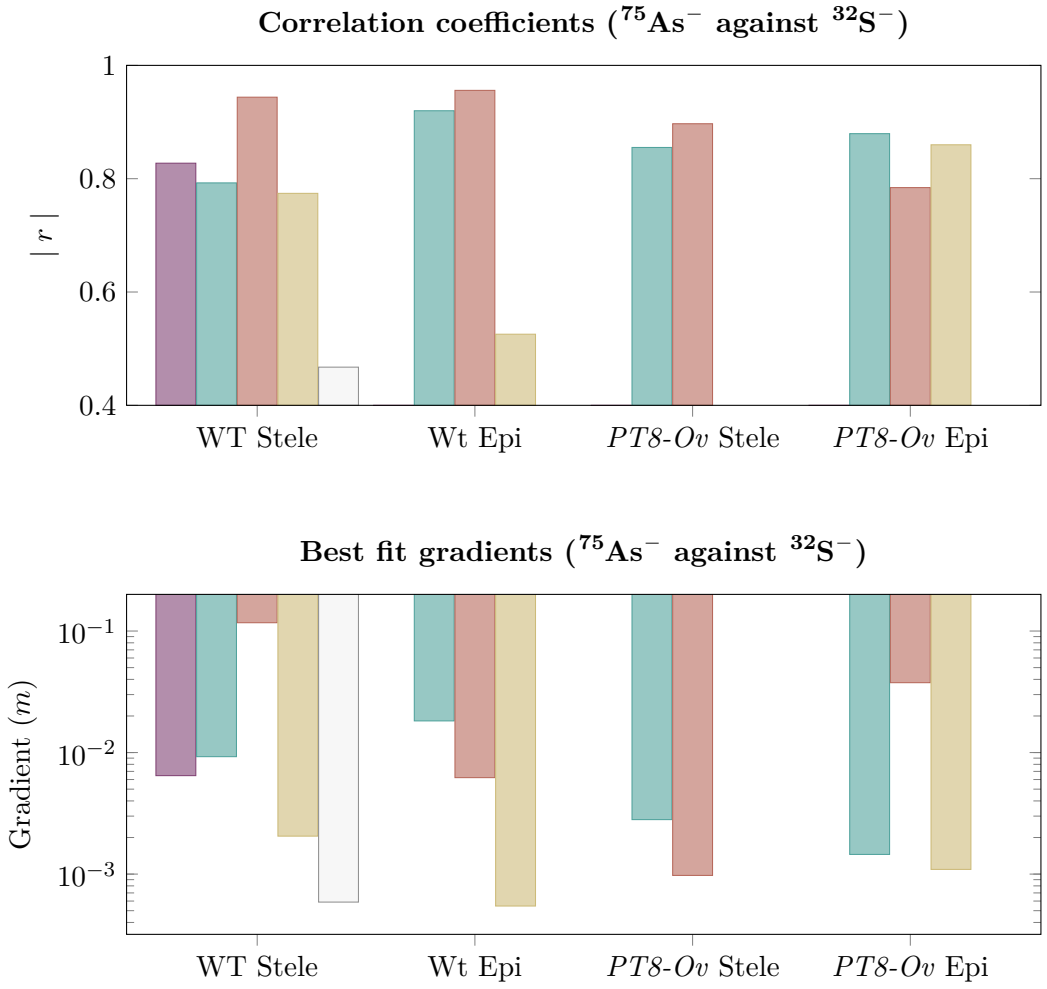

Figure 6.14: Pearson product-moment correlation coefficients (r) and gradient of line of best fit (m) for the mean normalised $^{32}S^-$ and $^{75}As^-$ counts in each ROI from different sections. Gradients calculated using the linear regression "least squares" method.

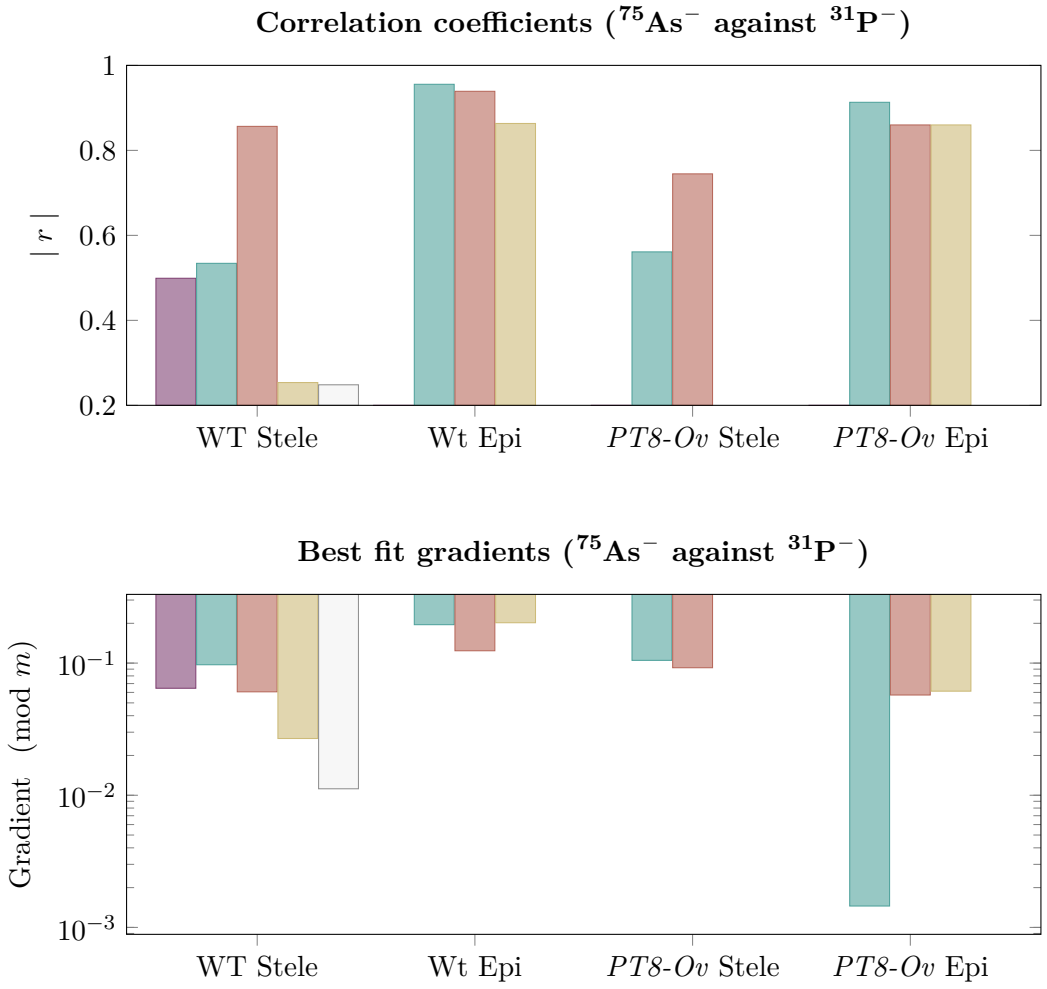

Figure 6.15: Pearson product-moment correlation coefficients (r) and gradient of line of best fit (m) for the mean normalised $^{32}S^-$ and $^{75}As^-$ counts in each ROI from different sections. Gradients calculated using the linear regression "least squares" method.

Chapter 7

Arabidopsis

Detoxification of heavy metals in plants is believed to involve chelation by phytochelatins (PCs) followed by the transport of metal-PC complexes into vacuoles. PCs are thiol containing peptides that are known to be synthesised from glutathione in plants exposed to heavy metals [200]. More specifically, they are synthesised "from glutathione by a specific γ-glutamylcysteine dipeptidyl transpeptidase" named PC synthase [201]. In *Arabidopsis* mutation in the *CAD1* gene confers cadmium (Cd) sensitivity, investigation into the function of this gene suggested that it encodes PC synthase [170]. Further experiments by Ha *et al.* demonstrated this to be the case; they observed that *cad1-3* lacked detectable PCs, even when exposed to cadmium and were "highly sensitive" to the element [95]. The *cad1-3* mutation was brought about by "a G-CtoC-G transversion generated by 1,2:3,4-diepoxybutane."

C-type ATP-binding cassette (ABC) transporters are believed to be involved in detoxification of As. Song *et al.* showed that "in the absence of two ABCC-type transporters, AtABCC1 and AtABCC2, *Arabidopsis thaliana* is extremely sensitive to arsenic and arsenic-based herbicides [168]." Their further experiments connected these transporters to PC_2 transport activity. They concluded that these were the "long-sought and major vacuolar PC transporters" and that "the sequestration of PCAs complexes into vacuoles is as critical for the detoxification of arsenic as the synthesis of PCs."

Later research identified that OsABCC1 expressed in rice roots is able to "mediate

AsIII-PC sequestration, thus reducing As accumulation in the rice grains [101]." Despite not decreasing root As, knockout of OsABCC1 resulted in several times more As in the grain compared to WT [101]. Ueno *et al.* suggested that selective sequestration of heavy metals to root vacuoles could limit root to shoot transmission [202]. Using this information Deng *et al.* were able to reduce grain As in rice by overexpression of OsABCC1, ScYCF1 and γ-glutamylcysteine synthetase [203].

7.1 Aims

The exact role that these transporters take in the uptake of As is not fully understood. Here I use NanoSIMS analysis to map the distribution of key elements in the roots of *Arabidopsis thaliana* mutants at both high spatial resolution and high sensitivity. The aim is to observe changes in the transport and chelation of As as a result of disrupting key genes (*ABCC1*, *ABCC2* and *CAD1*) identified as being relevant to important stages of heavy metal detoxification.

7.2 Method

Arabidopsis WT and mutants (Columbia ecoline) were grown to flowering stage, 16-h light/8-h dark cycle at 22°C/18°C, appended with $10\,\mu mol\,L^{-1}$ As(V) for 5 days before harvesting as described in section 2.3. The growth line consisted of WT (Col-0), *cad1-3* (PC synthase deficient mutant) and *abcc1-2* (double knockout mutant where ABCC1 and ABCC2 transporters were non functional and cannot transport PC-As(III) complexes into

Table 7.1: List of root sections cut for this experiment

Name	Mutant	Distance from root tip
742	Col-0	2 cm from tip
743	Col-0	5 cm from tip
744	*cad1-3*	2 cm from tip
745	*abcc1-2*	2 cm from tip

vacuole).

Small lengths of root were cut from near the root tip and preserved according to the HPF and resin substitution methods described in section 2.4. Based on research by Blum *et al.* [204] regions 2 cm from the root tip were expected to have high PC activity and therefore be of interest in this study. Lengths of root were cut 2 cm from the root tip for all plant lines, and additional lengths 5 cm from the root tip were cut for Col-0 in order to examine any changes in As and S distributions at different distances from the root tip. The difficulty and time intensive nature of both the sample preparation and NanoSIMS analysis meant that only a limited number of samples could reasonably be chosen, and therefore lengths of mutant root were only taken at one distance from the root tip. A list of the plant lines are shown in table 7.1, a minimum of four lengths of root were cut for HPF from each plant line.

The NanoSIMS was tuned to detect $^{12}C^{14}N^-$, $^{32}S^-$ $^{35}Cl^-$, $^{31}P^{12}C^-$ and $^{75}As^-$ ions as described in section 2.7.4.

7.3 Results

7.3.1 Optical micrographs

Some example micrographs of the preserved and microtomed sections of root are shown in figure 7.1. They give an indication of the condition and quality of the samples prior to SIMS analysis. The sections are very large, and contain only a small quantity of biological material relative to the size of the section. It may have been possible to obtain better sections by trimming away more of the resin with a razor blade. Smaller sections are typically less likely to have folds or tears in them, increasing the proportion of usable samples.

The first example, Col-0, taken at 2 cm from the root tip, figure 7.1A, contains two different roots that were preserved together in the same resin. There seem to be two visible steles (red arrows), with some irregularities in the formation of the cortex and some of the cells appearing very distorted.

Two of these samples, figures 7.1B and 7.1C, don't contain a whole cross section of the root. It is hard to tell if the sample was damaged during HPF or when the root was cut from the plant. It is possible that taking sections from further into the resin block would yield better preserved sample, and that this may not have been done owing to a lack of microtomy experience.

These two also have some folds or bubbles in the section, which could result in inconsistent SIMS data. It looks as though there are some small lenticular shapes in the regions where the section is raised from the substrate. This may be small bits of the sample that have broken loose and become deposited underneath the sections.

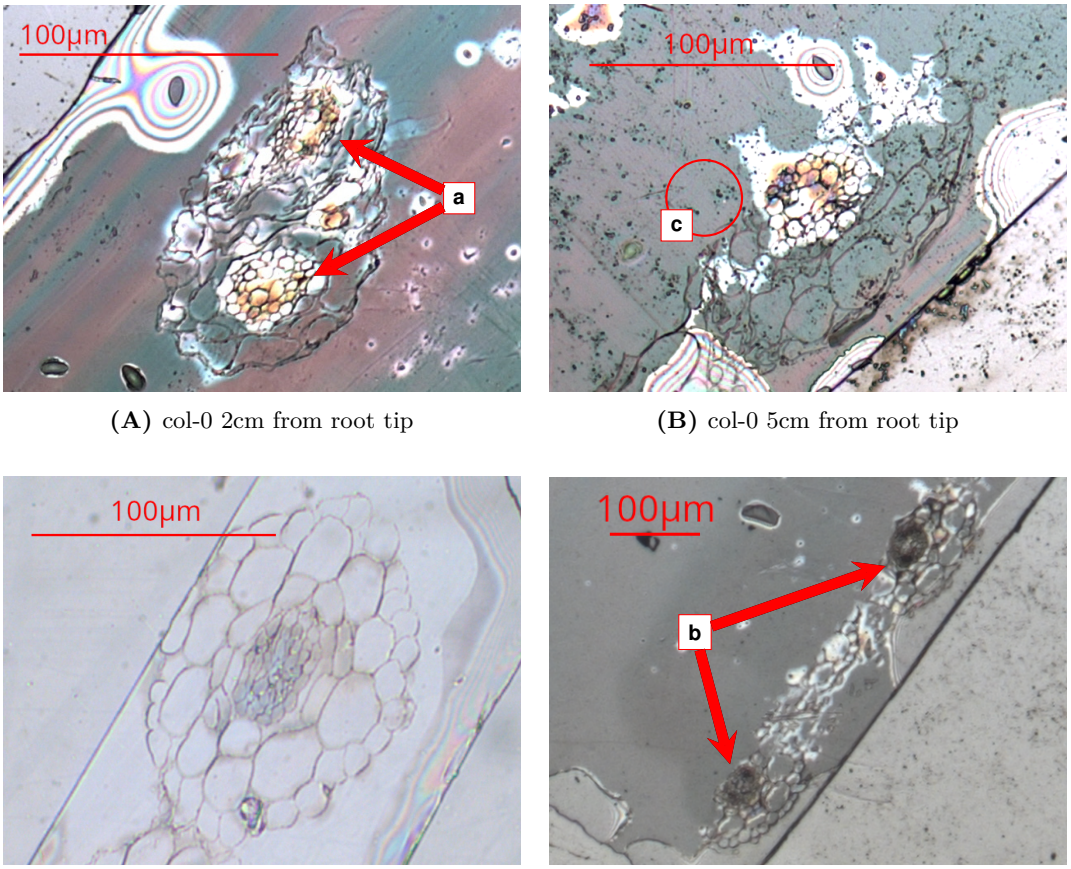

(A) col-0 2cm from root tip

(B) col-0 5cm from root tip

(C) *cad1-3* 2cm from root tip

(D) *abcc1-2* 2cm from root tip

Figure 7.1: Optical micrograph of preserved and microtomed sections. *a,b*, two different roots preserved in the same resin block; *c* part of the cortex missing from the section.

The best section, figure 7.1D, contains two well preserved root sections with very little surrounding resin and appears to have dried flat on the substrate with very little contamination. Despite these issues almost all samples had well preserved and sectioned steles that could be analysed.

7.3.2 NanoSIMS data

Some typical NanoSIMS data, figure 7.2, demonstrates the general appearance of these samples. In this case, the sample is the same Col-0 section cut 2 cm from the root tip

shown in the first optical micrograph, figure 7.1A. The data reveals clear and distinct cells throughout most of the stele. The $^{32}S^-$ and $^{75}As^-$ signals reveal strong localisation of these elements to specific cells. The uniformity of the $^{35}Cl^-$ signal indicates the the sample is mostly flat and well preserved with perhaps the exception of the spaces in between some of the cells.

Towards the edges the image becomes out of focus, and the definition between cells is slightly lost. This sample was identified in the optical micrographs as having a 'squashed' appearance with the cells being distorted. These distortions are also evident in the NanoSIMS data and could make it difficult to accurately identify the cell types.

In this example As and S appear to be predominantly located within a handful of cells around the edges of the stele. To get an idea of how other samples compared I have arranged into one image, figure 7.3, the data collected from ion detectors tuned to $^{32}S^-$ and $^{75}As^-$, and the S.E. detector from this sample and one example from each of the other samples listed in table 7.1.

Col-0 sections at 2 cm and 5 cm from the root tip appear similar in both shape and distribution of elements. Signals for $^{75}As^-$ and $^{32}S^-$ predominantly came from a small number of cells near the edge of the stele in both samples with the localisation of these elements appearing slightly stronger from the latter.

These elements were typically not found uniformly across whole cells but within a part of the cell. This can perhaps be seen most clearly in the region highlighted in red in Col-0 at 5 cm from the root tip (fig. 7.3). I re-imaged this area in the NanoSIMS at a higher magnification, figure 7.4. This clearly shows that the area responsible for the highest counts

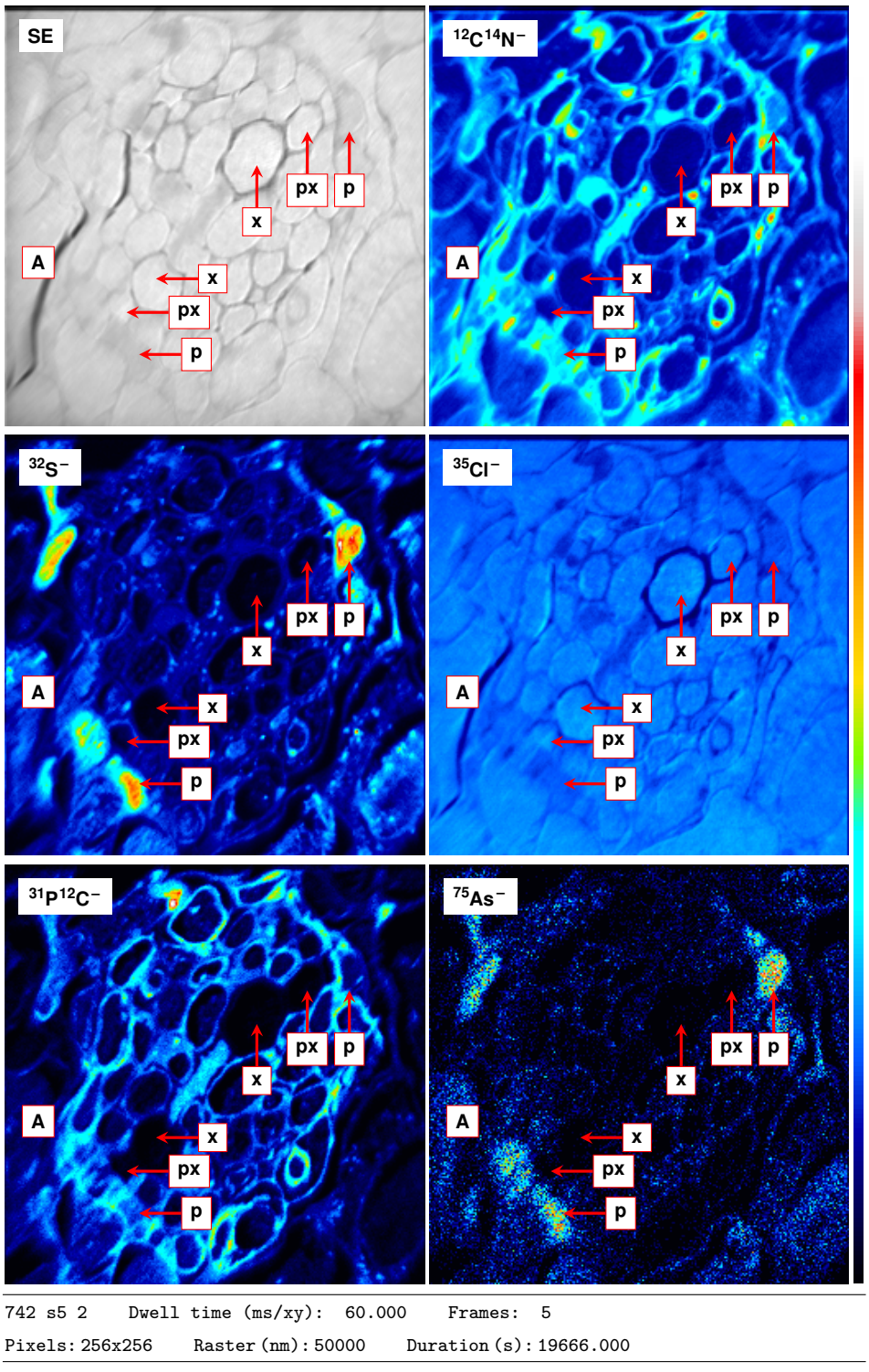

Figure 7.2: Typical SIMS data from an arabidopsis sample. Col-0, 2 cm from root tip, showing strong $^{75}As^-$ and $^{32}S^-$ signals from pericycle cells on the xylem pole. *A*, preservation damage; *x*, xylem; *px*, protoxylem; *p*, pericycle.

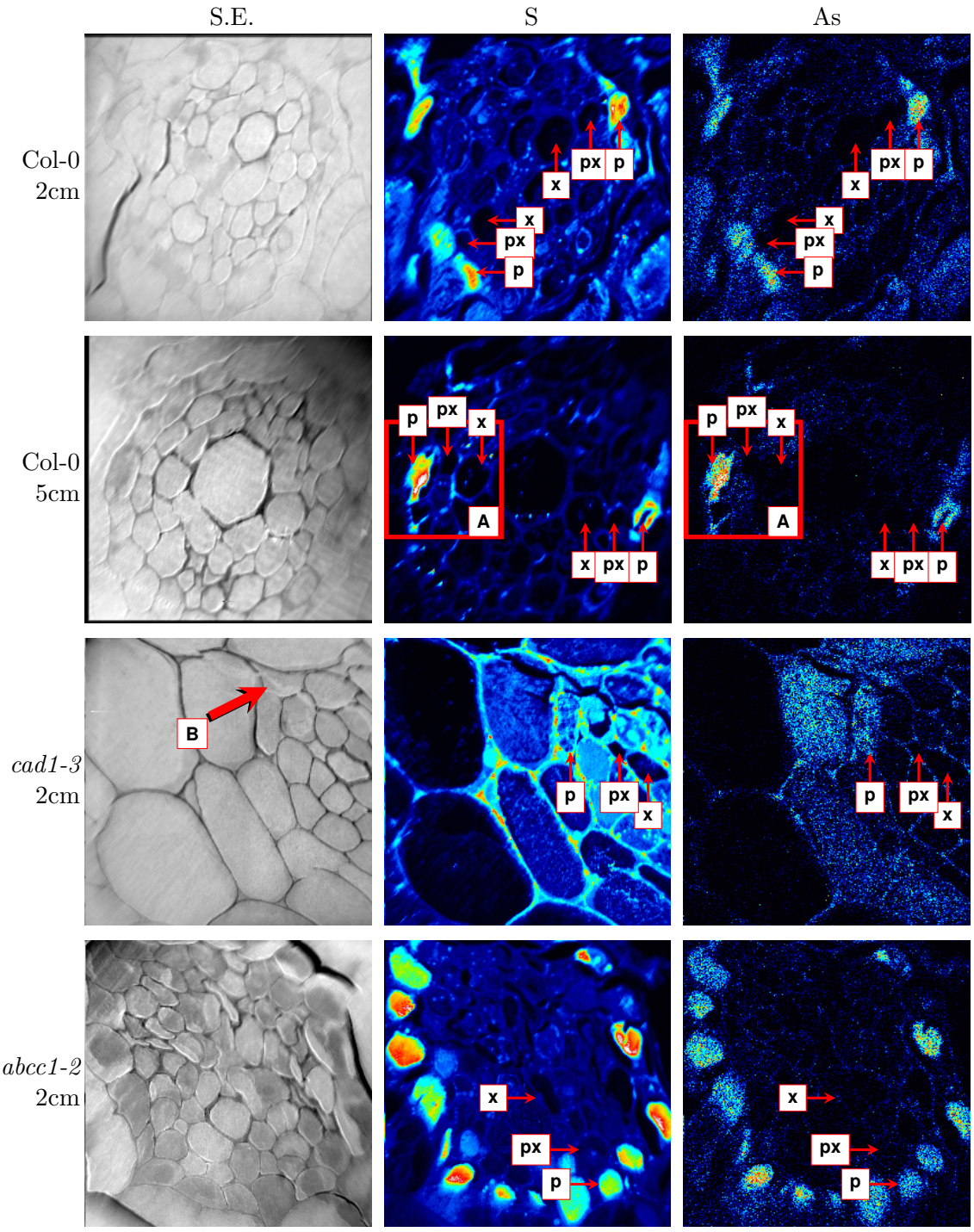

Figure 7.3: Secondary electron, $^{32}S^-$ and $^{75}As^-$ data collected from one of each of the arabidopsis mutants, all rasters 50 µm. $^{32}S^-$ and $^{75}As^-$ signals strongly localised to specific pericycle cells in Col-0, all pericycle cells in *abcc1-2* and diffusely localised in *cad1-3*. *A*, region analysed at higher resolution; *B*, perservation damage; *x*, xylem; *px*, protoxylem; *p*, pericycle.

of $^{32}S^-$ and $^{75}As^-$ is a region within the cell that extends to some of the edges of cell, but appears pulled away from some sections of the cell wall. This feature could be a vacuole, or the cytoplasm if the cell became plasmolysed during one of the sample preparation steps.

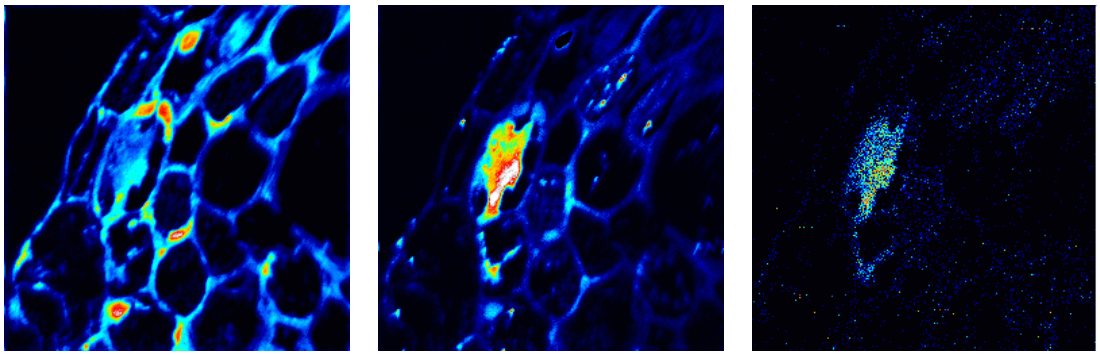

(A) $^{12}C^{14}N^-$ **(B)** $^{32}S^-$ **(C)** $^{75}As^-$

Figure 7.4: Col-0 at 5 cm from the root tip, higher resolution image of area identified in figure 7.3. Data acquired over a 30 µm raster with a 3938 s duration.

Data from the *cad1-3* section also suggests a concentration of As and S in cells towards the edge of the stele, but in this case it seems more diffuse and much less localised. A crack can be seen in the upper right quadrant of the sample (red arrow), suggesting damage was sustained during HPF. It appears as a faint grey line in the SE image and a black line in the $^{32}S^-$ data.

For the *abcc1-2* section S and As appear highly localised similar to the Col-0 sections, but this time not just in one or two cells but in a whole ring of cells at the edge of the stele.

7.3.3 Cell types

I attempted to identify the high As containing cells observed in the high resolution scan, figure 7.4, and several other cell types within the root. To do this I compared my data to published information on the structure of *Arabidopsis* roots using both optical micrographs

taken prior to SIMS analysis in addition to the SIMS data to best identify the cell types present in each scan. Some of this data and an example of this process is shown in figure 7.5.

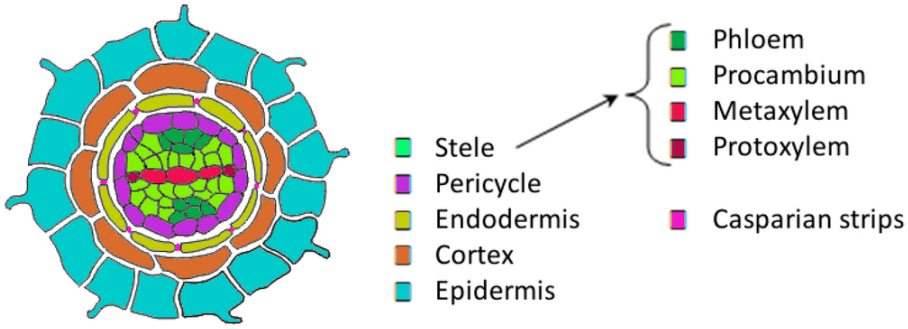

(A) Root structure of *Arabidopsis Thaliana*

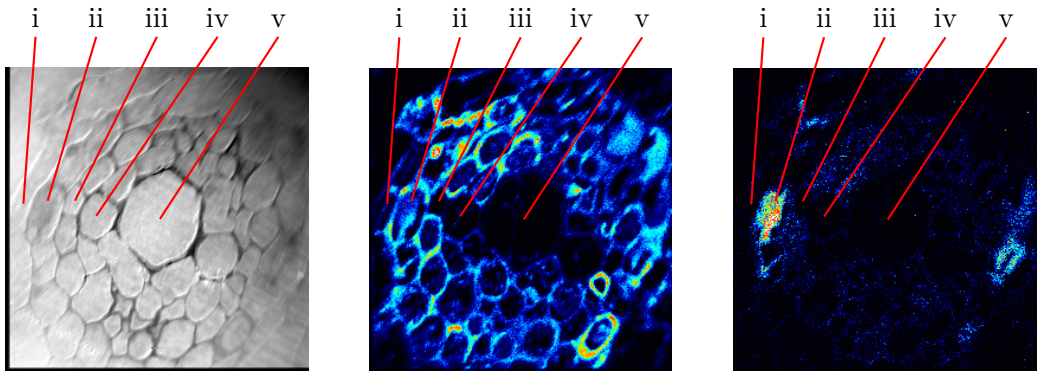

(B) SE **(C)** $^{31}P^{12}C^-$ **(D)** $^{75}As^-$

Figure 7.5: Identifying cell types. A, Diagram of cell types in Arabidopsis root from Petricka *et al.* [205] reprinted with permission Copyright 2012 Annual Reviews; B-D, NanoSIMS data from a cross section of arabidopsis root, Col-0, 5 cm from the root tip. *i*, endodermis; *ii*, pericycle; *iii*, protoxylem; *iv*, metaxylem; *v*, central xylem.

In this way I was able to quite consistently identify five cell types, labelled i-v in figure 7.5, that could be used to compare data between different sections. Starting from the centre of the image (v) was a large cell with thick walls and low counts from most detectors that is likely a xylem vessel. Similar cells (iv) appear either side of it that I identified as metaxylem. Adjacent to these are much smaller cells (iii) also with thick walls and low counts from most detectors I believe are protoxylem. This suggests that the cells in the

next layer out (ii) were pericycle cells. Further out again are longer thinner cells (i) which I deduced were likely endodermal cells. Beyond this the cells became much larger and probably form the cortex.

The diagram also showed the position of the phloem, but there were no obvious differences between procambium and phloem cells in most of the NanoSIMS data, so I was unable to determine with much certainty which cells these were. *A. thaliana* roots have radial vascular bundles with one protoxylem pole (diarch) [206], therefore I assumed that the phloem were 90° opposite the xylem pole even though I couldn't directly identify them.

7.3.4 Regions of interest

Using this information I deduced a method for analysing the data by highlighting ROIs based on the cell types and their position in the root. First I highlighted the xylem vessels, including the metaxylem and protoxylem. This provides a very consistent and easily identifiable feature across all the samples that can be used, as in previous chapters, to normalise the data. Since the central xylem varied from one sample to another I created the ROI groups cx, mx, and px for the central xylem, metaxylem and protoxylem respectively.

In the Col-0 samples the regions with the highest $^{75}As^-$ and $^{32}S^-$ signals often originated from the pericycle cells, specifically the ones closest to the protoxylem as seen clearly in figure 7.5D (ii). The high resolution image, fig 7.4, showed these elements not in the whole cell, but a part of it — which could be a vacuole or a cell that has plasmolysed. Therefore when selecting ROIs I used my best judgement to include these features with as little of the empty space around them. Following this observation I also separated the pericycle cells

into three separate groups; those near the protoxylem (pex), those near phloem (pep) and those in between (pef).

These formed the main ROIs used for analysis. There were one or two examples of high concentrations of As in other places within the roots, such as the endodermis, which were also selected for analysis. Additionally some samples contained some unusual or interesting features that were highlighted on a case by case basis. Highlighted regions within a sample typically looked like those given in figure 7.6. To the left and right of the image (regions 6 and 7) are the high $^{75}As^{-}$ signals from near the xylem poles. At the top and bottom of the image (regions 9-11) are the regions near the phloem poles.

This process was repeated for all the samples listed in table 7.2 and the average counts from each detector in the ROIs were saved to a spreadsheet and normalised.

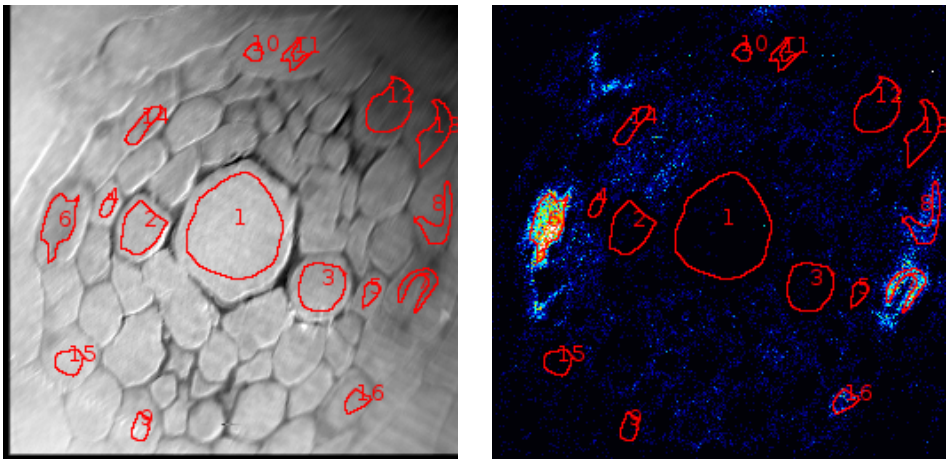

(A) S.E. **(B)** $^{75}As^{-}$

Figure 7.6: A Col-0 sample with the ROIs used for analysis displayed in red.

Table 7.2: List of sets of NanoSIMS data collected for this experiment, the associated plant line, and the distance they were recorded from the root tip.

Sample name	Plant line	Dist. (cm)
742 4a f1 1	Col-0	2
742 1d 3	Col-0	2
742 s5 2	Col-0	2
743 1b f1 1	Col-0	5
743 1b f1 2	Col-0	5
743 1b f1 3	Col-0	5
743 1a f5 l1	Col-0	5
743 1a f7 l2	Col-0	5
743 2a f3 l3	Col-0	5
743 2a f4 l1	Col-0	5
743 2a f4 l2 2	Col-0	5
744 1b f3 2	*cad1-3*	2
744_4a_f3_1	*cad1-3*	2
744_5a_f1_5	*cad1-3*	2
745 2c f4 01	*abcc1-2*	2
745_1b_f4_5	*abcc1-2*	2
745_4b_f5_1	*abcc1-2*	2
745_6a_f1_5	*abcc1-2*	2
745_6a_f1_7	*abcc1-2*	2
745_6a_f1_8	*abcc1-2*	2
745_7a_f5_1	*abcc1-2*	2
745_7a_f5_4	*abcc1-2*	2
745 2b f1_1	*abcc1-2*	2

7.3.5 Arsenic localisation

Plotting the normalised average $^{75}As^-$ counts from each ROI demonstrated similar trends to that observed initially in figure 7.3. Looking at just one example from each mutant, figure 7.7, we can see that in Col-0 at 2 cm and 5 cm the pericycle cells near the xylem pole (pex) contain the highest concentrations of As, with very little in other cells. *cad1-3* additionally had high As concentrations in cells between the xylem and phloem poles (pef) as well as nearby cells in the cortex (cortf), but similar to Col-0 most of the As was in

pericycle cells near the xylem pole. The As in *abcc1-2* appeared evenly distributed across all pericycle cells (pex, pep and pef) and not just concentrated in those nearest the xylem pole. Data from the rest of the samples is given in Appendix C.

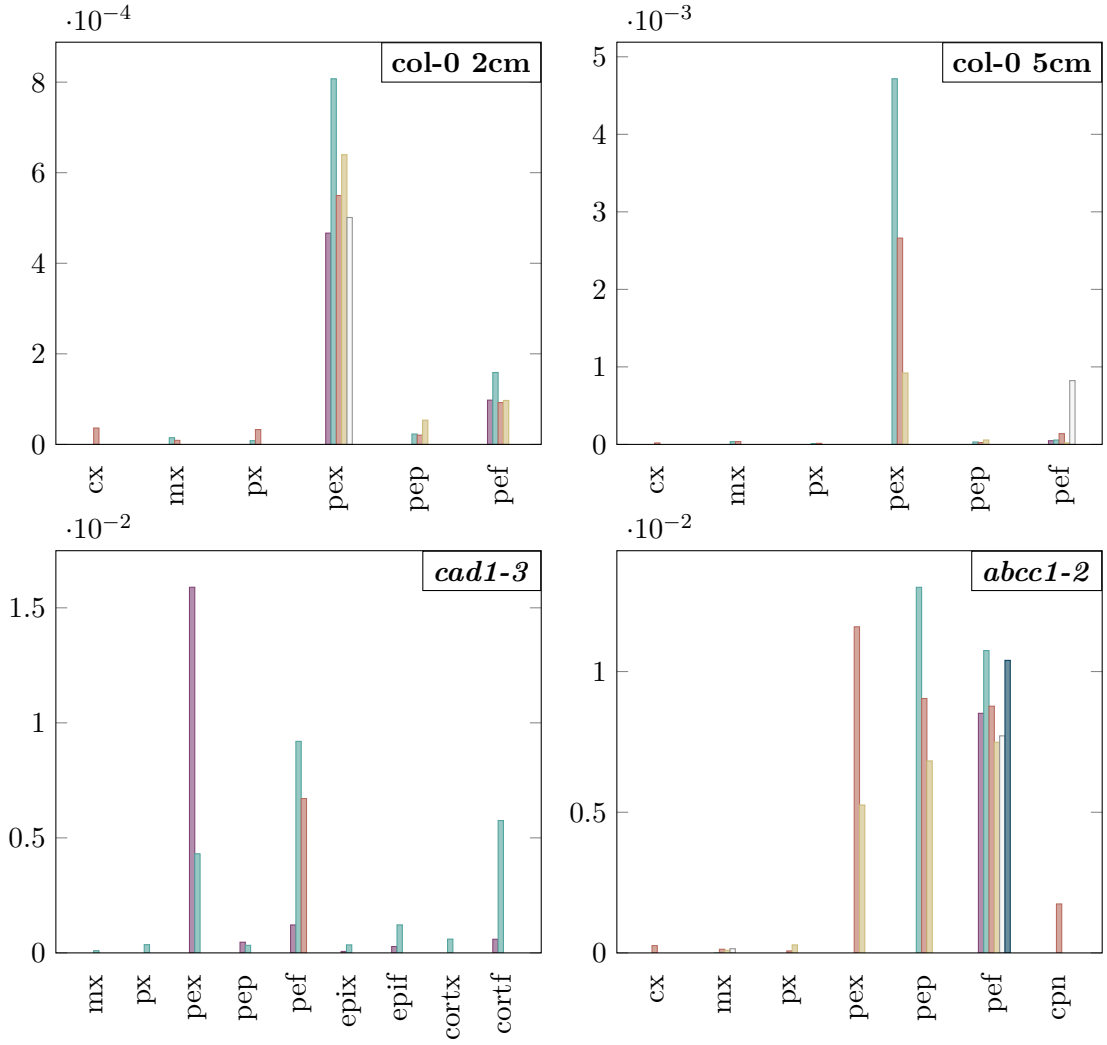

Figure 7.7: Average $^{75}As^-$ signals recorded from some arabidopsis ROIs. Data from 742 1d 3, 743 2a f4 l1, 744_4a_f3_1, 745_6a_f1_7

Taking an average of the $^{75}As^-$ counts for the main ROI groups within each sample set, fig 7.8, further illustrates this trend. This suggests that As concentrations were higher in *cad1-3* than Col-0, and higher still in *abcc1-2*. Only three *cad1-3* samples were used for

analysis and the $^{75}As^-$ counts varied in these samples by more than one order of magnitude. Students' t-tests revealed that significantly ($P < 0.05$) higher proportions of $^{75}As^-$ and $^{32}S^-$ signal were found in pericycle cells near the phloem pole in *abcc1-2* compared to WT.

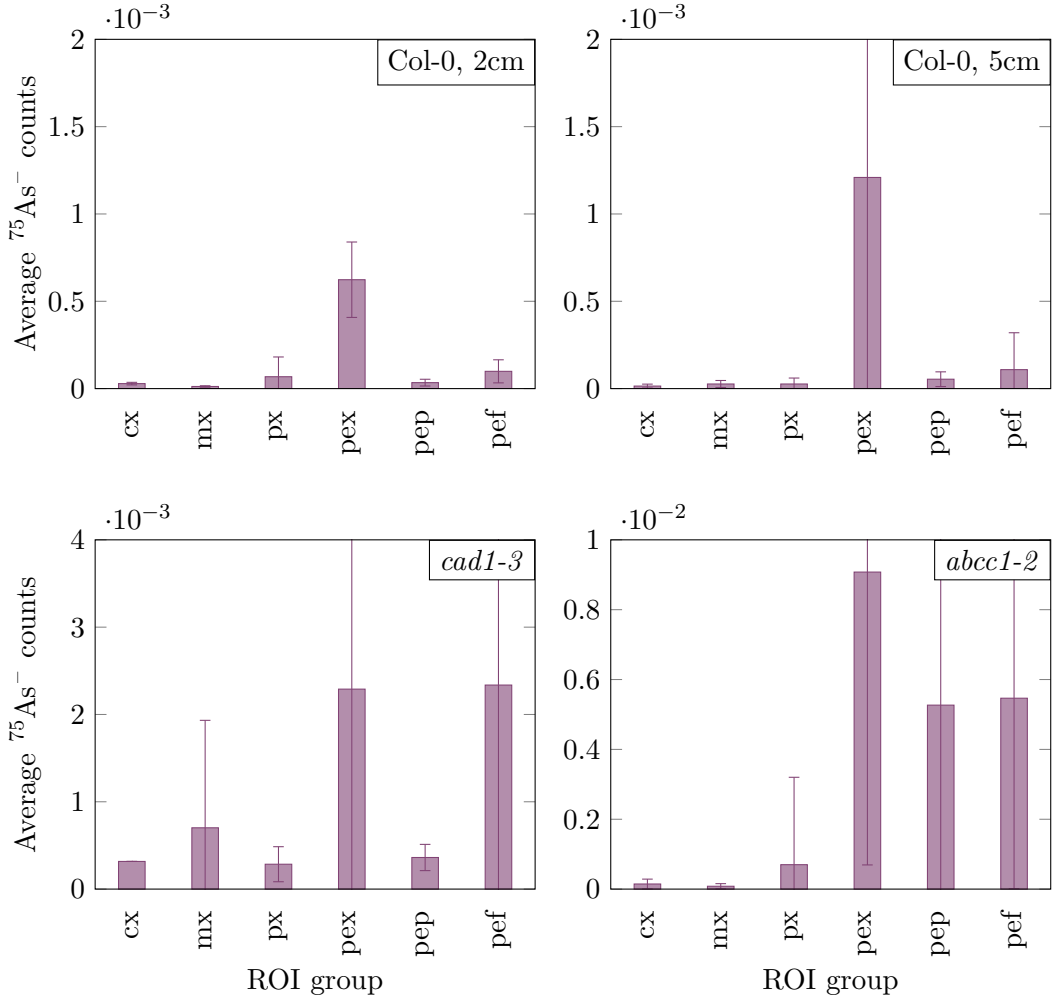

Figure 7.8: Average $^{75}As^-$ signal recorded from each ROI group.

The distributions of elements between the ROI groups within each plant line are quite consistent, but as seen in previous chapters there are large systematic variations causing an upwards or downwards shift in the signals recorded from some samples. This has caused very large error bars in figure 7.8 and makes it difficult to accurately quantify the differ-

ences in $^{75}As^-$ signal between different sections. Therefore I decided to look instead at the relative distributions of $^{75}As^-$ signals between ROIs within each sample. Most samples demonstrated a high concentration of As in the pericycle cells near the xylem pole, which were ROIs referred to in the data as "pex". Using the pex ROI with the highest average $^{75}As^-$ counts in each section as a reference point (pexmax) I calculated the relative proportion of $^{75}As^-$ found in the other pericycle cells in that section.

This gave an indication of how much higher the As concentration was in pericycle cells near the xylem pole (pex) were than pericycle cells near the phloem pole (pef) or between the two poles (pef) that could be compared reliably between samples. The proportion of $^{75}As^-$ signal recorded from pericycle cells relative to pexmax is represented as a box and whisker plot, figure 7.9. This shows how As was very highly localised to pericycle cells near the xylem pole in Col-0 at 2 cm; slightly less at 5 cm, and with greater variance between samples. *cad1-3* had higher variance again and a higher proportion of As in the pericycle cells near the phloem. *abcc1-2* contained even greater variance and, as the data in figure 7.8 showed, only about 50% less $^{75}As^-$ counts measured in pericycle cells (compared to a six fold decrease in Col-0 at 2 cm). Suggesting that As is highly localised to pericycle cells on the xylem pole in Col-0, and much more evenly distributed across all pericycle cells in *abcc1-2*.

7.3.6 Arsenic sulphur ratios

In order to investigate the co-localisation of S and As in these samples I decided to plot scatter graphs of the counts from the $^{32}S^-$ detector against the $^{75}As^-$ detector. This could

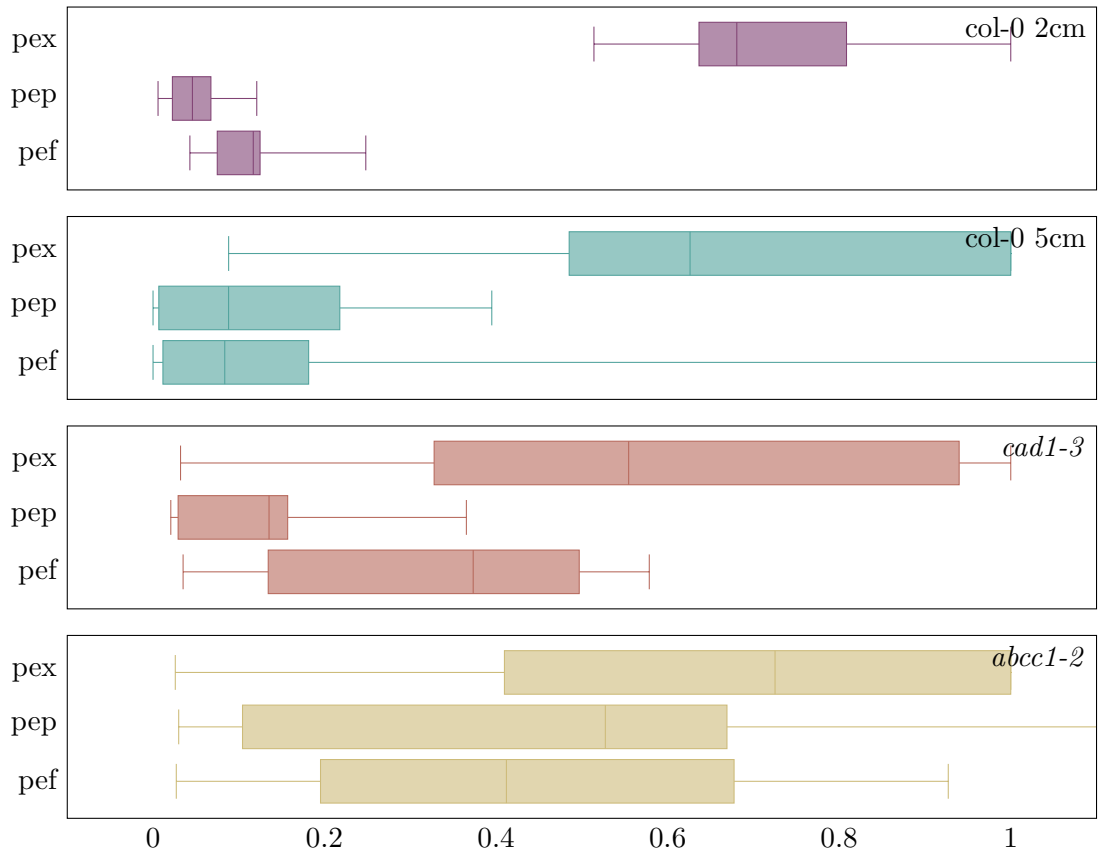

Figure 7.9: $^{75}As^-$ counts in pericycle cells relative to the highest mean counts of $^{75}As^-$ in a pericycle cell on the xylem pole. Data presented as a box and whisker plots where lower and upper whiskers represent minimum and maximum values, and the box represent interquartile ranges.

be done using the ROIs but only a small number were selected for most of these samples, meaning there would be very few data points. All of my NanoSIMS data was collected over 256x256 rasters, so plotting the ratio of $^{32}S^-$ to $^{75}As^-$ for every pixel in a scan was possible but would have required over 65,000 data points. In addition to being cumbersome there was the issue that the $^{75}As^-$ counts were so low that most pixels contained zero counts and was too low to make useful correlations.

To overcome this I used OpenMIMS to batch export drift corrected NanoSIMS files as

nearly raw raster data (nrrd) binaries. I wrote a program in c[1] to split the data into 8x8 pixel "blocks" (figure 7.10) and sum up all counts in each block. The program is also able to add together counts across multiple frames where necessary. Data was exported as CSV files containing a list of sum counts from every block, the most relevant sections of the code is given in Appendix D. This allows the sampling of 1024 equally sized areas within each image from which ratios between $^{75}As^-$ and $^{32}S^-$ counts can be calculated.

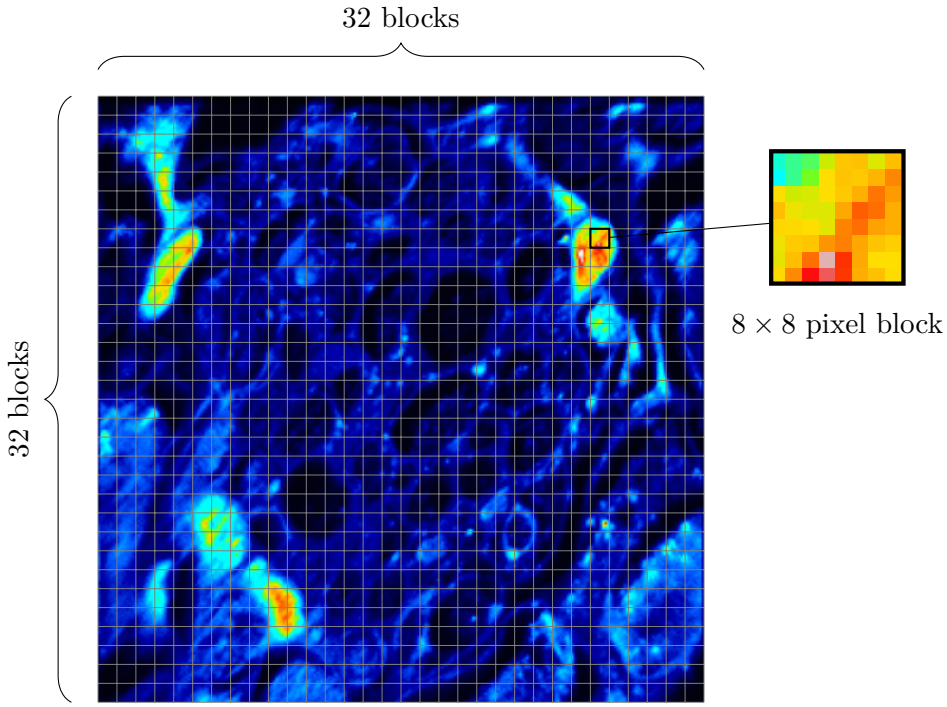

Figure 7.10: SIMS data with grid showing how image was split into sample sections

A typical example from each sample type, figure 7.11, reveals $^{32}S^-$ $^{75}As^-$ ratios were similar for Col-0 at 2 cm and 5 cm with the correlations at 2 cm appearing slightly stronger than those at 5 cm. Most of the *cad1-3* data shows low but closely correlated counts, but in regions with higher counts of $^{32}S^-$ or $^{75}As^-$ the data appears to split into two separate

[1]Scripts available online at gitlab.com/HughTaylor/nanosims-scripts

lines, one of proportionately much higher $^{75}As^-$ (red circle) and one of much higher $^{32}S^-$ (green circle). Most of *abcc1-2* had the same shape as Col-0. Data from the rest of the analysed samples can be found in Appendix C.

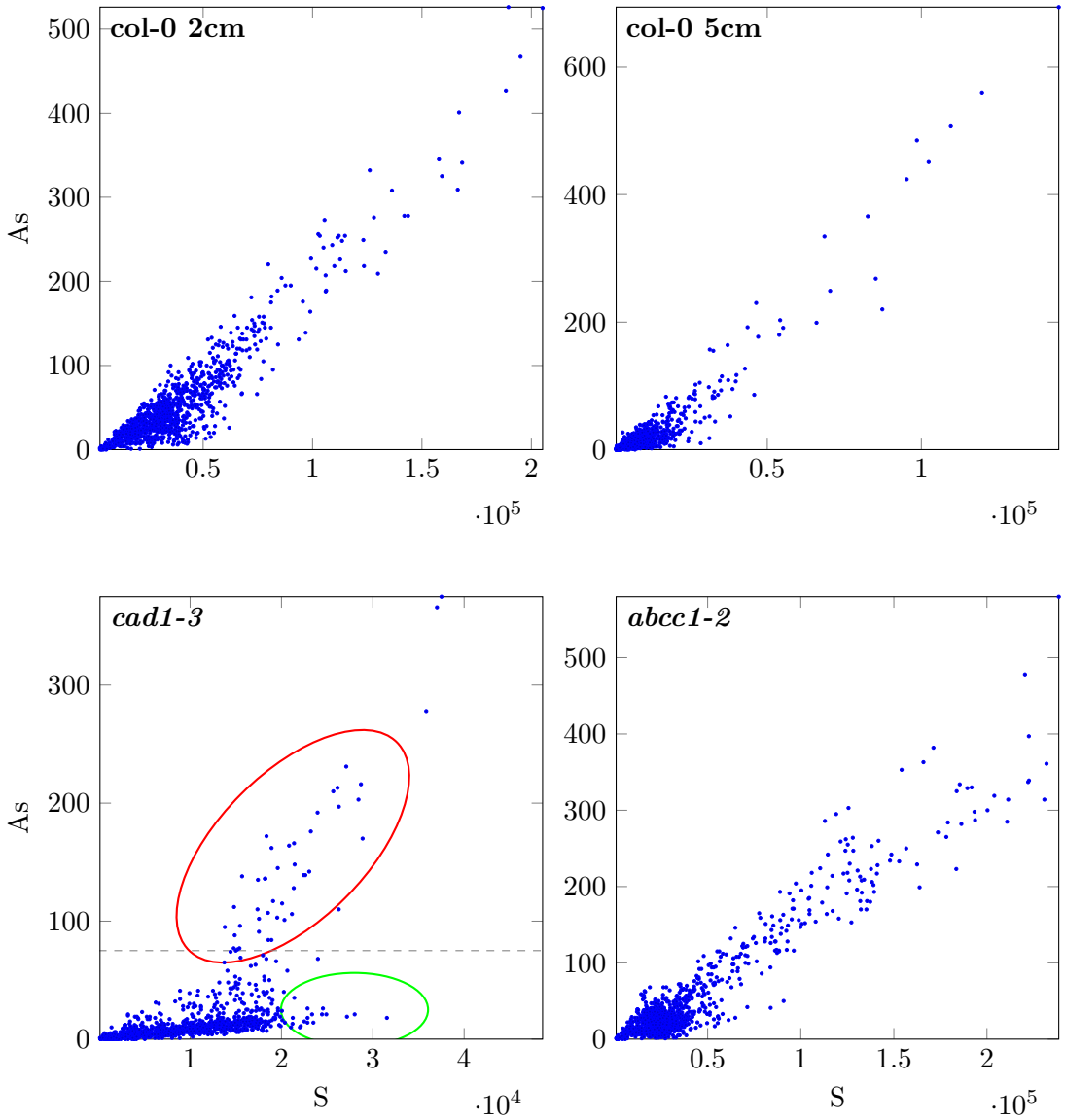

Figure 7.11: $^{75}As^-/^{32}S^-$ detector ratios for four different sections

Applying linear regression statistical analysis to the data corroborates these observed trends. I calculated the Pearson product-moment correlation coefficients (PPMCCs), and

gradients of the regression lines (assuming axis intercept at $y = 0$) and plotted them, figure 7.12. As expected from looking at the scatter plots, *cad1-3* sections had lower correlation than the other samples. The gradients don't reveal an obvious trend, but the relative tuning of the detectors and other changes in analytical parameters can result in very large systematic changes in the count ratios making it hard to compare between samples.

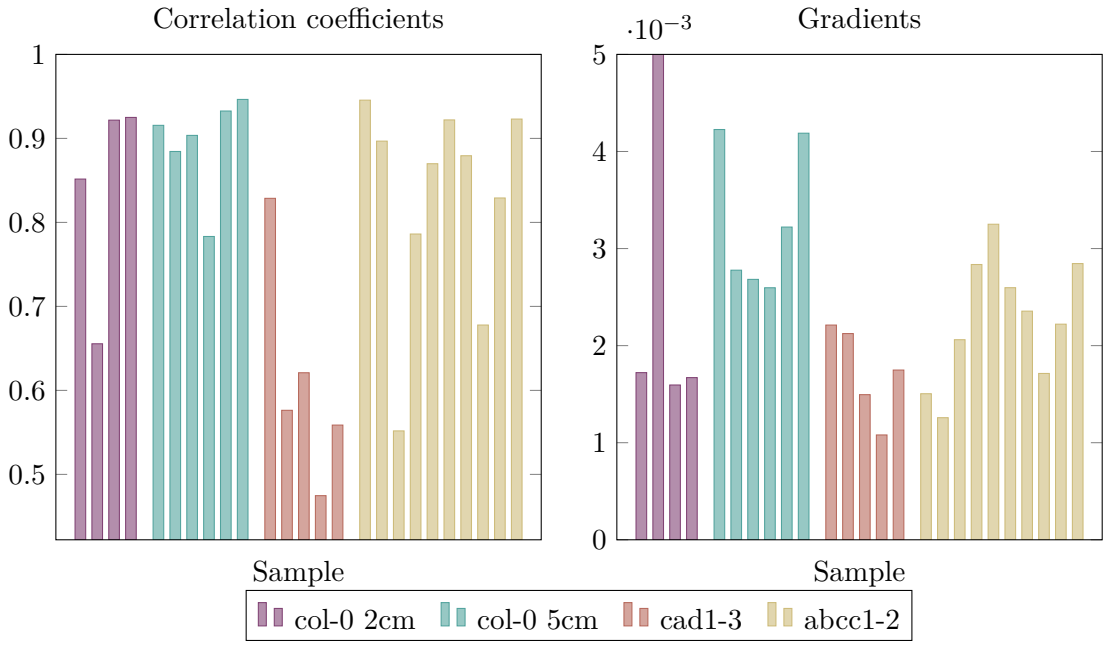

Figure 7.12: Sample correlation coefficients (left) and sample gradients of $^{75}As^-$ regressed on $^{32}S^-$ (right) showing strong correlation of As and S in Col-0 and *abcc1-2* but not *cad1-3*; and higher As to S ratios at greater distances from root tip.

For example, the gradient of the second Col-0 sample in these graphs far exceeds the boundaries of the chart, implying a much higher proportion of S to As in this one sample. The map of $^{32}S^-$ counts was also very different to the other samples. A possible explanation is that Detector 2 could have been accidentally tuned to measure superoxide anions ($^{16}O_2{}^-$) instead of $^{32}S^-$, the former having a yield approximately five times greater than the latter in these samples. An HMR scan taken just before this data was collected is shown in

appendix F, with the peaks for $^{16}O_2^-$ and $^{32}S^-$ clearly visible.

To see where the higher proportion of $^{75}As^-$ counts in the *cad1-3* data (red circle, fig. 7.11) originated from I wrote a script that found blocks that contained greater than a specific number of total $^{75}As^-$ counts (75 in this case, grey dashed line, fig. 7.11). The script provided Cartesian coordinates for the regions that met this criteria. I used PGF/Ti*k*Z to overlay rectangles with these coordinates on the original $^{32}S^-$ and $^{75}As^-$ maps. This shows that the high As to S regions (red squares, fig. 7.13) were from the high As containing pericycle cells.

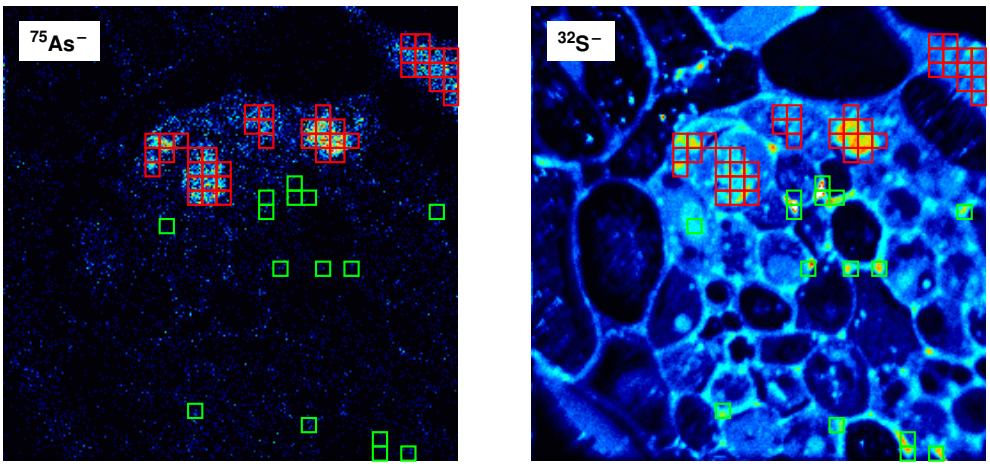

Figure 7.13: 8×8 pixel regions from the *cad1-3* sample, 744_4a_f3_1, that contained greater than 75 total $^{75}As^-$ counts (red squares), and regions that contained both more than 22000 $^{32}S^-$ counts and less than 50 $^{75}As^-$ counts (green squares).

This suggests a marked increase in proportion of As to S in the vacuoles of high As containing *cad1-3* cells near the edge of the stele. I recalculated the regression lines for this sample for only the data either above or below 75 $^{75}As^-$ counts (grey line, fig. 7.11) and found them to have gradients of 0.00716 and 0.00116 respectively, with correlation coefficients of 0.8949 and 0.5852 (compared to 0.5763 for the whole data set).

I applied this same method to the high $^{32}S^-$ part of the graph (green circle, fig. 7.11), this time filtering for regions that exceeded 22000 $^{32}S^-$ counts and also had fewer than 50 $^{75}As^-$ counts. I drew the corresponding regions on the NanoSIMS image (green squares, fig. 7.13). These appear in scattered locations throughout the stele, mainly on cell walls. They could be caused by high S containing features on the cell walls or they could be false counts caused by crater edge effects due to the different rate of sputtering for cell walls and vacuoles.

I repeated this process for the other *cad1-3* data; splitting the scatter graphs into regions of different $^{75}As^-/^{32}S^-$ ratios and calculating corresponding correlation coefficients and linear regression gradients. The data, figure 7.14, suggests that the As rich regions typically have a higher correlation between As and S, and that the proportion of As to S is much higher. The exception, 744_5a_f1_5, exhibited no correlation between $^{75}As^-$ and $^{32}S^-$, the most concentrated $^{75}As^-$ regions did not see any increase in $^{32}S^-$.

Excluding this result, the averages of the gradients of regression lines, figure 7.15, suggest an increase in As to sulphur ratios from 2 cm to 5 cm from the root tip in Col-0 and a much higher ratio in *cad1-3*. The ratios in *abcc1-2* (at 2 cm from the root tip) were comparable to those observed in Col-0 at 2 cm. The error bars on this graph represent one sample standard deviation from the mean.

This implies that the ratio of As concentration to S concentration in the root increases with increasing distance from the root tip in Col-0, and with mutation of *CAD1*. Increased As concentration in *abcc1-2* was matched by a proportional increase in S concentration.

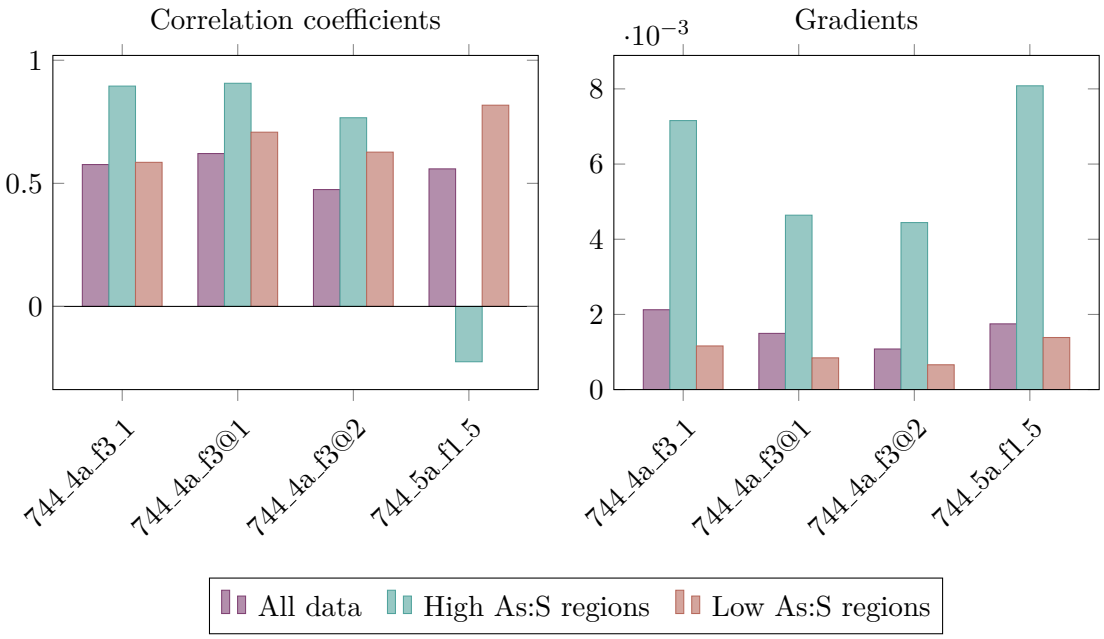

Figure 7.14: *cad1-3* correlation coefficients and gradients for high and low As:S regions

7.4 Discussion

The strong correlation observed between As and S in WT agree with the previously understood mechanism of As detoxification by complexation with thiol containing PCs. The highest concentration of these elements were observed in pericycle cells near the xylem poles. These are possibly parenchyma cells that are involved in loading the xylem vessels.

A modification in localisation and decrease in the correlation of As and S in *cad1-3* mutants agrees with research by Ha *et al.* [95] into *CAD1*. *cad1-3* is unable to produce PCs, resulting in the observed regions with very high As that lack the corresponding increase in S expected from complexation with thiol containing PCs. Despite this, the As still appears to be partially localised to the pericycle cells near the xylem pole as in WT, which could be due to transport of uncomplexed As into these cells. High concentrations of uncomplexed

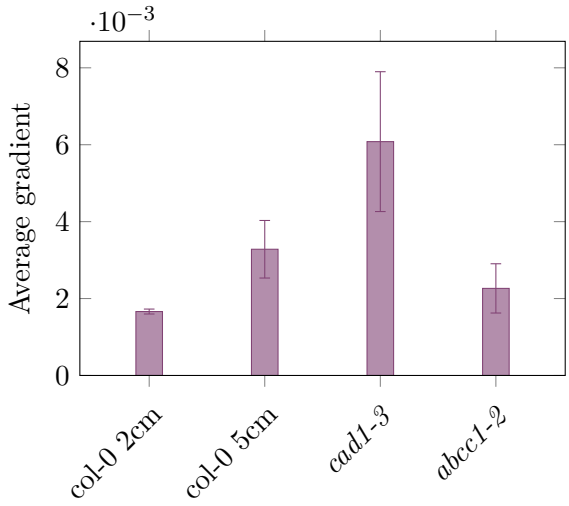

Figure 7.15: Average linear regression gradients from arabidopsis samples

As in the root pericycle could have significant toxic effects on the plant which may explain the sensitivity of *cad1-3* to As.

Geisler *et al.* used membrane fractionation to determine that ABC transporters were localised "to the central vacuolar membrane" [207], and Park *et al.* used "microscopic analysis using a Cd-sensitive probe" to demonstrate that in *abcc1-2* double mutants exposed to cadmium (Cd) the Cd was mostly located in "the cytosol of protoplasts" while in WT it was mainly found in vacuoles [208].

This strongly suggests that As(III)PC_2 complexes in *abcc1-2* exist outside of vacuoles. While my data has clearly demonstrated the cells where As can be found, it is not possible to corroborate these findings as with NanoSIMS alone it is difficult to determine exactly what subcellular structures contain the As.

Song *et al.* found that *abcc1-2* "exhibited a very low residual As(III)PC_2 transport activity" and produced less PC when exposed to As compared to WT [168]. My results

demonstrate that high concentrations of both As and S are found in most of the pericycle cells in the roots of *abcc1-2* mutants. It is possible that *abcc1-2* mutants are chelating As in the pericycle but are unable to transport As(III)PC_2 complexes towards the xylem pole. This supports data showing increased As concentration in roots of *abcc1-2* over WT [168] and immunostaining data of the similar OsABCC1 transporter in rice where signal was "observed in the exodermis and pericycle of roots" [101].

Chapter 8

Conclusions

This thesis supports previously observed results that NanoSIMS is a powerful tool for measuring the distribution of trace elements and is capable of mapping them at high resolution in preserved sections of biological material. By attempting to better quantify NanoSIMS data I have shown that systematic variations can be very large, even when good care is used to check and maintain tuning of the detectors. The different normalisation methods I proposed were unable to decrease the variance between similar sections that were measured while conditions were kept as identical as possible. Under differing analytical conditions the normalisation method used can correct for changes in primary ion current and dwell time. The long time required to gather good quality data meant that only a small number of ion maps were used for analysis, and therefore it was difficult to draw strong conclusions on quantitative changes between samples. Even though it is difficult to quantify absolute concentrations using SIMS, the relative distributions of elements can be measured quite reliably.

The distributions of As and S suggest a co-localisation of these elements particularly in specific regions of the cortex that appear to be the vacuoles of parenchyma cells. This agrees with published results and current theoretical understanding of As detoxification by complexation with thiol containing phytochelatins (PCs). Knockout of *Lsi3* resulted in a significant increase the $^{75}As^{-}$ signal recorded from pericycle cells, which could have been caused by a decreased ability for the pericycle to efflux As in the absence of LSi3. High

concentrations of As found in lateral root junctions agrees with literature that suggests lateral roots are an important part of the As uptake pathway.

Comparisons between WT and *PT8-Ov* suggest that there is a higher concentration of As in the latter, but that the differences between these plant lines were quite small compared to the experimental error. A small number of additional samples could have made a much stronger case for the observed trends. Near the edge of the root lower concentrations of As was recorded in *PT8-Ov* compared to WT, and lower colocalisation of As and S was seen compared to regions near the centre of the root. This suggests that despite faster uptake of As(V) and Pi by *PT8-Ov* As is rapidly translocated away from the epidermis, reduced to As(III) and bound to PCs in the stele.

Strong localisation of As and S to the pericycle was observed in *A. thaliana*. In WT these elements were almost entirely localised to only the pericycle cells closest to the xylem pole. Mutants defective in PC transporters ABCC1 and ABCC2, *abcc1-2*, also had high As concentrations in these cells but additionally had high As in the rest of the pericycle cells. It is possible that As is detoxified by chelation with PCs in all of the pericycle cells and transported to the xylem pole for xylem loading but that in *abcc1-2* this transport is disrupted and the As-PC complexes accumulate in pericycle cells away from the xylem pole. A PC-synthase deficient mutant, *cad1-3*, was very sensitive to As, and both a significantly lower correlation and a higher ratio of $^{75}As^{-}$ to $^{32}S^{-}$ signals from across all of the areas measured. Throughout the cortex of *cad1-3* mutants As was measured in higher concentrations than WT.

This information provides a better understanding of the mechanisms of As uptake and

detoxification. A good understanding of the interactions between Si, P and As pathways could be used to help develop As mitigation stategies such as breeding low accumulating cultivars that are still able to uptake sufficient Si and P, or cultivars that are detoxify and store As in the roots without translocation to the straw and grain.

Further work

The difficulty making quantitative comparisons between samples could be overcome slightly by using larger sample sizes. While this thesis has provided useful information about function of several genes in relation to the detoxification of As, additional studies on this topic would be useful to provide corroborative evidence to strengthen or challenge the observations I have presented and the conclusions that I have drawn from them.

An important challenge I found during this research is the difficulty to reliably identify biological structures within the samples. There was some ambiguity over the type of cells being measured and their function, a more precise knowledge of which would be very useful to better determine the function of the genes studied. Compartmentalisation of elements to specific regions within cells was demonstrated, but again it was not possible to determine the subcellular features observed. It may be possible to further this work by marking specific cells or features within the cells (such as the vacuole) using immunostaining with fluorescent protein markers and comparing the NanoSIMS data to fluorescent light micrographs of the same region. This method has been demonstrated successfully in cultured cells by Lau *et al.* [209] using the same instrument. Alternatively immunostaining with isotopes or nanoparticles could produce protein markers that are directly measurable with SIMS. This

has very recently been tested using fluorinated nanobodies and is able "to target proteins with subcellular resolution" [210]. These techniques could be combined to provide strong evidence of the localisation of heavy metals to specific cells or organelles and how these associations change under different conditions.

Bibliography

[1] E. Astolfi et al. "Relation between arsenic in drinking water and skin cancer". In: *Biological Trace Element Research* 3.2 (June 1981), pp. 133–143. ISSN: 0163-4984. DOI: 10.1007/BF02990453.

[2] World Health Organisation. *Guidelines for Drinking-water quality*. 3rd ed. 2003, pp. 306–308.

[3] Tina Levine et al. *Special Report on Ingested Inorganic Arsenic: Skin Cancer; Nutritional Essentiality*. Tech. rep. July. 1988.

[4] C H Tay. "Cutaneous manifestations of arsenic poisoning due to certain Chinese herbal medicine." In: *The Australasian journal of dermatology* 15.3 (Dec. 1974), pp. 121–31. ISSN: 0004-8380.

[5] O Neubauer. "Arsenical cancer; a review." In: *British journal of cancer* 1.2 (June 1947), pp. 192–251. ISSN: 0007-0920.

[6] C J Chen et al. "Cancer potential in liver, lung, bladder and kidney due to ingested inorganic arsenic in drinking water." In: *British journal of cancer* 66.5 (Nov. 1992), pp. 888–92. ISSN: 0007-0920.

[7] DG Kinniburgh and PL Smedley. "Arsenic contamination of groundwater in Bangladesh". In: *BGS Technical Report WC/00/19.* I (2001).

[8] M. Argos et al. "Arsenic exposure from drinking water, and all-cause and chronic-disease mortalities in Bangladesh (HEALS): a prospective cohort study". In: *The Lancet* 376.9737 (2010), pp. 252–258.

[9] A H Smith et al. "Cancer risks from arsenic in drinking water." In: *Environmental health perspectives* 97.6 (July 1992), pp. 259–67. ISSN: 0091-6765.

[10] M M Wu et al. "Dose-response relation between arsenic concentration in well water and mortality from cancers and vascular diseases." In: *American journal of epidemiology* 130.6 (Dec. 1989), pp. 1123–32. ISSN: 0002-9262.

[11] M. Vahter and E. Marafante. "Effects of low dietary intake of methionine, choline or proteins on the biotransformation of arsenite in the rabbit". In: *Toxicology letters* 37.1 (1987), pp. 41–46.

[12] P Mushak and A F Crocetti. "Risk and revisionism in arsenic cancer risk assessment." In: *Environmental health perspectives* 103.7-8 (1995), pp. 684–9. ISSN: 0091-6765.

[13] Michael F Hughes et al. "Arsenic Exposure and Toxicology: A Historical Perspective." In: *Toxicological sciences : an official journal of the Society of Toxicology* 123.2 (July 2011), pp. 305–332. ISSN: 1096-0929. DOI: 10.1093/toxsci/kfr184.

[14] T Loftas et al. *Dimensions of need. An atlas of food and agriculture*. Food and Agriculture organization of the United Nations, 1995.

[15] M M Dey, M N I Miah, and B A A Mustsfi. "Rice Production Constraints in Bangladesh: Implications for Further Research Priorities". In: *Rice research in Asia: Progress and priorities* (1996), p. 179. ISSN: 0851989977.

[16] S M Ullah. "Arsenic contamination of groundwater and irrigated soils of Bangladesh". In: *Abstracts: international conference on arsenic pollution of ground water in Bangladesh: causes, effects and remedies*. Vol. 8. 1998, p. 12.

[17] M.A. Ali et al. "Fate of arsenic extracted with groundwater". In: *Fate of Arsenic in the Environment* (2003), pp. 7–20.

[18] M B Alam and M A Sattar. "Assessment of arsenic contamination in soils and waters in some areas of Bangladesh". en. In: *Water Science & Technology* 42.7-8 (Oct. 2000), pp. 185–192.

[19] Andrew A. Meharg and Md Mazibur Rahman. "Arsenic contamination of Bangladesh paddy field soils: implications for rice contribution to arsenic consumption." In: *Environmental science and technology* 37.2 (Jan. 2003), pp. 229–234. ISSN: 0013-936X.

[20] M J Abedin, J Cotter-Howells, and A A Meharg. "Arsenic uptake and accumulation in rice (Oryza sativa L.) irrigated with contaminated water". In: *Plant and Soil* 240.2 (2002), pp. 311–319.

[21] Paul N Williams et al. "Arsenic limits trace mineral nutrition (selenium, zinc, and nickel) in Bangladesh rice grain." In: *Environmental science & technology* 43.21 (Nov. 2009), pp. 8430–6. ISSN: 0013-936X. DOI: 10.1021/es901825t.

[22] A S Prasad. "Discovery and importance of zinc in human nutrition." In: *Federation proceedings* 43.13 (Oct. 1984), pp. 2829–2834.

[23] Margaret P Rayman. "The importance of selenium to human health". In: *The Lancet* 356.9225 (July 2000), pp. 233–241. ISSN: 0140-6736.

[24] M Anke et al. "Nickel–an essential element." In: *IARC scientific publications* 53 (1984), p. 339. ISSN: 0300-5038.

[25] P N Williams et al. "Variation in arsenic speciation and concentration in paddy rice related to dietary exposure". In: *Environmental science & technology* 39.15 (2005), pp. 5531–5540.

[26] William R. Cullen and Kenneth J. Reimer. "Arsenic speciation in the environment". In: *Chemical Reviews* 89.4 (June 1989), pp. 713–764. ISSN: 0009-2665. DOI: 10.1021/cr00094a002.

[27] A. Gomez-Caminero et al. "Environmental Health Criteria 224 Arsenic and Arsenic Compounds". In: *World Health* 13 (2011).

[28] Paul Andrewes et al. "Do arsenosugars pose a risk to human health? The comparative toxicities of a trivalent and pentavalent arsenosugar." In: *Environmental science & technology* 38.15 (Aug. 2004), pp. 4140–8. ISSN: 0013-936X.

[29] B A Fowler. "Toxicology of environmental arsenic". In: *Adv. Mod. Toxicol* 2 (1977), p. 79.

[30] Shannon Eckstein. *Where we work Chars and Bay of Bengal Friendship NGO Bangaldesh*. Accessed: 2020-09-08. 2018. URL: https://friendship.ngo/about-us/where-we-work/ (visited on 04/09/2018).

[31] Yu Chen et al. "A prospective study of blood selenium levels and the risk of arsenic-related premalignant skin lesions." In: *Cancer epidemiology, biomarkers & prevention : a publication of the American Association for Cancer Research, cosponsored by the American Society of Preventive Oncology* 16.2 (Feb. 2007), pp. 207–13. ISSN: 1055-9965. DOI: 10.1158/1055-9965.EPI-06-0581.

[32] Julian E Spallholz, L Mallory Boylan, and M M Rhaman. "Environmental hypothesis: is poor dietary selenium intake an underlying factor for arsenicosis and cancer in Bangladesh and West Bengal, India?" In: *The Science of the total environment* 323.1-3 (May 2004), pp. 21–32. ISSN: 0048-9697. DOI: 10.1016/j.scitotenv.2003.09.034.

[33] Zhi Huang et al. "Low selenium status affects arsenic metabolites in an arsenic exposed population with skin lesions." In: *Clinica chimica acta; international journal of clinical chemistry* 387.1-2 (Jan. 2008), pp. 139–44. ISSN: 0009-8981. DOI: 10.1016/j.cca.2007.09.027.

[34] Wendy J Verret et al. "A Randomized, Double-Blind Placebo-Controlled Trial Evaluating the Effects of Vitamin E and Selenium on Arsenic-Induced Skin Lesions in Bangladesh". In: *Journal of Occupational and Environmental Medicine* 47.10 (2005). ISSN: 1076-2752.

[35] X. Y. Xu et al. "Growing rice aerobically markedly decreases arsenic accumulation". In: *Environmental science & technology* 42.15 (May 2008), pp. 5574–5579. ISSN: 0013-936X.

[36] Y Odanaka et al. "Absorption, translocation and metabolism of the arsenical fungicides, iron methanearsonate and ammonium iron methanearsonate, in rice plants". In: *J. Pesticide Sci* 12 (1987), pp. 199–208.

[37] L R Johnson and A E Hiltbold. "Arsenic Content of Soil and Crops Following Use of Methanearsonate Herbicides". In: *Soil Sci. Soc. Am. J* 33.2 (1969), pp. 279–282.

[38] Hinrich L Bohn. "Arsenic Eh-pH diagram and comparisons to the soil chemistry of phosphorus". In: *Soil Science* 121.2 (1976), pp. 125–127.

[39] M. Sadiq, T.H. Zaidi, and A.A. Mian. "Environmental behavior of arsenic in soils: Theoretical". In: *Water, Air, & Soil Pollution* 20.4 (1983), pp. 369–377.

[40] Jen-How Huang, Kan-Nian Hu, and Berryinne Decker. "Organic arsenic in the soil environment: speciation, occurrence, transformation, and adsorption behavior". In: *Water, Air, & Soil Pollution* 219.1-4 (2011), pp. 401–415.

[41] Gautam Samanta et al. "Flow Injection Hydride Generation Atomic Absorption Spectrometry for Determination of Arsenic in Water and Biological Samples from Arsenic-Affected Districts of West Bengal, India, and Bangladesh". In: *Microchemical Journal* 62.1 (May 1999), pp. 174–191. ISSN: 0026265X. DOI: 10.1006/mchj.1999.1713.

[42] P.H. Masscheleyn, R.D. Delaune, and W.H. Patrick Jr. "Effect of redox potential and pH on arsenic speciation and solubility in a contaminated soil". In: *Environmental Science & Technology* 25.8 (1991), pp. 1414–1419.

[43] A R Marin, P H Masscheleyn, and W H Patrick. "Soil redox-pH stability of arsenic species and its influence on arsenic uptake by rice". In: *Plant and Soil* 152.2 (May 1993), pp. 245–253. ISSN: 0032-079X. DOI: 10.1007/BF00029094.

[44] Zhilong Gong et al. "Unstable trivalent arsenic metabolites, monomethylarsonous acid and dimethylarsinous acid". In: *Journal of Analytical Atomic Spectrometry* 16.12 (Dec. 2001), pp. 1409–1413. ISSN: 02679477. DOI: 10.1039/b105834g.

[45] A R Marin, P H Masscheleyn, and W H Patrick. "The influence of chemical form and concentration of arsenic on rice growth and tissue arsenic concentration". In: *Plant and Soil* 139.2 (Jan. 1992), pp. 175–183. ISSN: 0032-079X. DOI: 10.1007/BF00009308.

[46] Andrew a. Meharg and Louise Jardine. "Arsenite transport into paddy rice (Oryza sativa) roots". In: *New Phytologist* 157.1 (Jan. 2003), pp. 39–44. ISSN: 0028-646X. DOI: 10.1046/j.1469-8137.2003.00655.x.

[47] R Wysocki et al. "The glycerol channel Fps1p mediates the uptake of arsenite and antimonite in Saccharomyces cerevisiae." In: *Molecular microbiology* 40.6 (June 2001), pp. 1391–401. ISSN: 0950-382X.

[48] L Li et al. "Molecular cloning of a novel water channel from rice: its products expression in Xenopus oocytes and involvement in chilling tolerance." In: *Plant science : an international journal of experimental plant biology* 154.1 (May 2000), pp. 43–51. ISSN: 1873-2259.

[49] Steve J. Hill and Andy S. Fisher. "Atomic Absorption, Methods and Instrumentation". In: *Encyclopedia of Spectroscopy and Spectrometry (Third Edition)*. Ed. by John C. Lindon, George E. Tranter, and David W. Koppenaal. Third Edition. Oxford: Academic Press, 2017, pp. 37–43. ISBN: 978-0-12-803224-4. DOI: https://doi.org/10.1016/B978-0-12-803224-4.00099-6.

[50] W. Guo et al. "Effect of silicate on the growth and arsenate uptake by rice (Oryza sativa L.) seedlings in solution culture". In: *Plant and Soil* 272.1-2 (May 2005), pp. 173–181. ISSN: 0032-079X. DOI: 10.1007/s11104-004-4732-0.

[51] Henry B F Dixon. "The Biochemical Action of Arsonic Acids Especially As Phosphate Analogues". In: *Advances in Inorganic Chemistry* 44 (1996). Ed. by A G Sykes B T - Advances in Inorganic Chemistry, pp. 191–227.

[52] C J Asher and P F Reay. "Arsenic Uptake by Barley Seedlings". In: *Functional Plant Biology* 6.4 (Jan. 1979), pp. 459–466.

[53] M J Abedin, J Feldmann, and Andrew A. Meharg. "Uptake kinetics of arsenic species in rice plants". In: *Plant Physiology* 128.3 (2002), p. 1120. DOI: 10.1104/pp.010733.0.01.

[54] LHP Jones and KA Handreck. "Silica in soils, plants, and animals". In: *Advances in agronomy* 19.2 (1967), pp. 107–149.

[55] Nicolas Théodore de Saussure. *Recherches chimiques sur la vegetation*. Nyon, 1804.

[56] HF Clements. “Interaction of factors affecting yield”. In: *Annual Review of Plant Physiology* 653 (1964), pp. 409–442.

[57] GH Snyder, DB Jones, and GJ Gascho. “Silicon fertilization of rice on Everglades Histosols”. In: *Soil Sci. Soc. Am. J* 50 (1986), pp. 1259–1263.

[58] LE Datnoff and CW Deren. “Silicon fertilization for disease management of rice in Florida”. In: *Crop Protection* 16.6 (1997), pp. 525–531.

[59] D Neumann and U zur Nieden. “Silicon and heavy metal tolerance of higher plants.” In: *Phytochemistry* 56.7 (Apr. 2001), pp. 685–92. ISSN: 0031-9422.

[60] S Yoshida. “Chemical aspects of the role of silicon in physiology of the rice plant”. In: *Bull. nat. Inst. agric. Sci., Japan, Ser. B (15)* (1965), pp. 1–58.

[61] KB Krauskopf. “The geochemistry of silica in sedimentary environments”. In: *Silica in sediments: Society of Economic* (1959), pp. 4–19.

[62] A Frey Wyssling. “Uber die Ausscheidung der Kieselsaure in der Pflanze”. In: *Ber. dt. bot. Ges* 48 (1930), pp. 179–183.

[63] LHP Jones and KA Handreck. “Studies of silica in the oat plant”. In: *Plant and Soil* 23.1 (1965), pp. 79–96.

[64] E Grosse-Brauckmann. “Adsorption of silicic acid by plants after fertilizing with calcium carbonate.” In: *Zeitschrift fur Pflanzenernahrung, Dungung und Bodenkund* 62 (1953), pp. 19–23.

[65] K Imaizumi and S Yoshida. “Edaphological studies on silicon supplying power of paddy soils”. In: *Bulletin of the National Institute of Agricultural Sciences* 8 (1958), pp. 261–304.

[66] M Matsubayashi. *Theory and practice of growing rice*. Fuji, 1963, p. 502.

[67] John A Raven. “The transport and function of silicon in plants”. In: (1983), pp. 179–207.

[68] Jian Feng Ma et al. “Role of Root Hairs and Lateral Roots in Silicon Uptake by Rice”. In: *Society* 127.December (2001), pp. 1773–1780. DOI: 10.1104/pp.010271.This.

[69] A Okuda and E Takahashi. “Studies on the physiological role of silicon in crop plant. Part 8 Some examination on the specific behavior of low land rice in silicon uptake”. In: *Japanese Journal of Soil Science and Manure* 33 (1962), pp. 217–221.

[70] M Hildebrand, K Dahlin, and BE Volcani. “Characterization of a silicon transporter gene family in Cylindrotheca fusiformis: sequences, expression analysis, and identification of homologs in other diatoms”. In: *Molecular and General Genetics ...* 260.5 (1998), pp. 480–486.

[71] Jian Feng Ma et al. “A rice mutant defective in Si uptake”. In: *Plant physiology* 130.December (2002), pp. 2111–2117. DOI: 10.1104/pp.010348.1.

[72] Jian Feng Ma et al. “A silicon transporter in rice.” In: *Nature* 440.7084 (Mar. 2006), pp. 688–91. ISSN: 1476-4687. DOI: 10.1038/nature04590.

[73] Jian Feng Ma et al. “An efflux transporter of silicon in rice.” In: *Nature* 448.7150 (July 2007), pp. 209–12. ISSN: 1476-4687. DOI: 10.1038/nature05964.

[74] Jian Feng Ma et al. “Transporters of arsenite in rice and their role in arsenic accumulation in rice grain.” In: *Proceedings of the National Academy of Sciences of the United States of America* 105.29 (July 2008), pp. 9931–5. ISSN: 1091-6490. DOI: 10.1073/pnas.0802361105.

[75] Junko Sakurai et al. “Identification of 33 rice aquaporin genes and analysis of their expression and function.” In: *Plant & cell physiology* 46.9 (Sept. 2005), pp. 1568–77. ISSN: 0032-0781. DOI: 10.1093/pcp/pci172.

[76] A A Meharg and M R Macnair. “Suppression of the High Affinity Phosphate Uptake System : A Mechanism of Arsenate Tolerance in Holcus lanatus L .” In: *Journal of experimental botany* 43.4 (1992), pp. 519–524.

[77] AA Meharg and MR Macnair. “Relationship between plant phosphorus status and the kinetics of arsenate influx in clones of deschampsia cespitosa (L.) beauv. that differ in their tolerance to”. In: *Plant and Soil* 162.1 (1994), pp. 99–106.

[78] Michio Tsutsumi. “Comparative toxicity of arsenite and arsenate to rice seedling under various levels of phosphate supply”. In: *Soil Sci. Plant Nutr.* 29.1 (1983), pp. 63–69.

[79] Md Joinal Abedin et al. “Arsenic accumulation and metabolism in rice (Oryza sativa L.)” In: *Environmental science & technology* 36.5 (2002), pp. 962–968.

[80] Zhongchang Wu et al. “Investigating the contribution of the phosphate transport pathway to arsenic accumulation in rice.” In: *Plant physiology* 157.1 (Sept. 2011), pp. 498–508. ISSN: 1532-2548. DOI: 10.1104/pp.111.178921.

[81] Hongfang Jia et al. “The phosphate transporter gene OsPht1; 8 is involved in phosphate homeostasis in rice”. In: *Plant Physiology* 156.3 (2011), pp. 1164–1175.

[82] Peitong Wang et al. “The role of OsPT8 in arsenate uptake and varietal difference in arsenate tolerance in rice”. In: *Journal of Experimental Botany* 67.21 (Sept. 2016), pp. 6051–6059. ISSN: 0022-0957. DOI: 10.1093/jxb/erw362. eprint: https://academic.oup.com/jxb/article-pdf/67/21/6051/17142824/erw362.pdf.

[83] W Armstrong. “Oxygen Diffusion from the Roots of Some British Bog Plants”. In: *Nature* 204.4960 (Nov. 1964), pp. 801–802. ISSN: 0028-0836. DOI: 10.1038/204801b0.

[84] Andrew A Meharg. “Arsenic in rice–understanding a new disaster for South-East Asia.” In: *Trends in plant science* 9.9 (Sept. 2004), pp. 415–7. ISSN: 1360-1385. DOI: 10.1016/j.tplants.2004.07.002.

[85] G. J. D. Kirk and Le Van Du. “Changes in rice root architecture, porosity, and oxygen and proton release under phosphorus deficiency”. In: *New Phytologist* 135.2 (Feb. 1997), pp. 191–200. ISSN: 0028-646X. DOI: 10.1046/j.1469-8137.1997.00640.x.

[86] W-J Liu et al. “Do phosphorus nutrition and iron plaque alter arsenate (As) uptake by rice seedlings in hydroponic culture?” In: *New Phytologist* 162.2 (May 2004), pp. 481–488. ISSN: 0028-646X. DOI: 10.1111/j.1469-8137.2004.01035.x.

[87] C M Hansel et al. “Characterization of Fe plaque and associated metals on the roots of mine-waste impacted aquatic plants.” In: *Environmental science & technology* 35.19 (Oct. 2001), pp. 3863–8. ISSN: 0013-936X.

[88] Nicole Keon Blute et al. “Arsenic sequestration by ferric iron plaque on cattail roots.” In: *Environmental science & technology* 38.22 (Nov. 2004), pp. 6074–7. ISSN: 0013-936X.

[89] Angelia L Seyfferth et al. “Arsenic localization, speciation, and co-occurrence with iron on rice (Oryza sativa L.) roots having variable Fe coatings.” In: *Environmental science & technology* 44.21 (Nov. 2010), pp. 8108–13. ISSN: 1520-5851. DOI: 10.1021/es101139z.

[90] N Belzile and A Tessier. “Interactions between arsenic and iron oxyhydroxides in lacustrine sediments”. In: *Geochimica et Cosmochimica Acta* 54.1 (1990), pp. 103–109.

[91] Xiaoguang Meng et al. “Combined effects of anions on arsenic removal by iron hydroxides.” In: *Toxicology letters* 133.1 (July 2002), pp. 103–11. ISSN: 0378-4274.

[92] E Smith, R Naidu, and A M Alston. “Chemistry of inorganic arsenic in soils: II. Effect of phosphorus, sodium, and calcium on arsenic sorption”. In: *Journal of Environmental Quality* 31.2 (2002), pp. 557–563. ISSN: 0047-2425.

[93] JR Davenport and FJ Peryea. “Phosphate fertilizers influence leaching of lead and arsenic in a soil contaminated with lead arsenate”. In: *Water, Air, & Soil Pollution* 9001 (1991), pp. 101–110.

[94] Frank J Peryea. “Phosphate-Induced Release of Arsenic from Soils Contaminated with Lead Arsenate”. In: *Soil Science Society of America Journal* 55.5 (1991), pp. 1301–1306.

[95] S B Ha et al. “Phytochelatin synthase genes from Arabidopsis and the yeast Schizosaccharomyces pombe.” In: *The Plant cell* 11.6 (June 1999), pp. 1153–64. ISSN: 1040-4651.

[96] Henrik V Scheller et al. “Phytochelatin synthesis and glutathione levels in response to heavy metals in tomato cells”. In: *Plant Physiology* 85.4 (1987), pp. 1031–1035.

[97] T Maitani et al. “The composition of metals bound to class III metallothionein (phytochelatin and its desglycyl peptide) induced by various metals in root cultures of Rubia tinctorum”. In: *Plant Physiology* 110.4 (1996), pp. 1145–1150. ISSN: 0032-0889.

[98] M E Schmöger, M Oven, and E Grill. “Detoxification of arsenic by phytochelatins in plants.” In: *Plant physiology* 122.3 (Mar. 2000), pp. 793–801. ISSN: 0032-0889.

[99] Om Parkash Dhankher et al. “Hyperaccumulation of arsenic in the shoots of Arabidopsis silenced for arsenate reductase (ACR2).” In: *Proceedings of the National Academy of Sciences of the United States of America* 103.14 (Apr. 2006), pp. 5413–8. ISSN: 0027-8424. DOI: 10.1073/pnas.0509770102.

[100] Garima Dixit et al. "Reduced arsenic accumulation in rice (Oryza sativa L.) shoot involves sulfur mediated improved thiol metabolism, antioxidant system and altered arsenic transporters". In: *Plant Physiology and Biochemistry* 99 (2016), pp. 86–96.

[101] Won-Yong Song et al. "A rice ABC transporter, OsABCC1, reduces arsenic accumulation in the grain". In: *Proceedings of the National Academy of Sciences of the United States of America* 111.44 (Oct. 2014). DOI: 10.1073/pnas.141491068111.

[102] Naoki Yamaji et al. "Orchestration of three transporters and distinct vascular structures in node for intervascular transfer of silicon in rice". In: *Proceedings of the National Academy of Sciences* 112.36 (2015), pp. 11401–11406. ISSN: 0027-8424. DOI: 10.1073/pnas.1508987112. eprint: https://www.pnas.org/content/112/36/11401.full.pdf.

[103] F J Zhao et al. "Arsenic uptake and metabolism in plants." In: *The New phytologist* 181.4 (Mar. 2009), pp. 777–94. ISSN: 1469-8137. DOI: 10.1111/j.1469-8137.2008.02716.x.

[104] Prasanna Kumarathilaka et al. "Arsenic speciation dynamics in paddy rice soil-water environment: sources, physico-chemical, and biological factors-a review". In: *Water research* 140 (2018), pp. 403–414.

[105] Prasanna Kumarathilaka et al. "Mitigation of arsenic accumulation in rice: An agronomical, physico-chemical, and biological approach–A critical review". In: *Critical Reviews in Environmental Science and Technology* 50.1 (2020), pp. 31–71.

[106] Gui-Lan Duan et al. "A CDC25 homologue from rice functions as an arsenate reductase." In: *The New phytologist* 174.2 (Jan. 2007), pp. 311–21. ISSN: 0028-646X. DOI: 10.1111/j.1469-8137.2007.02009.x.

[107] Petra M Bleeker et al. "Enhanced arsenate reduction by a CDC25-like tyrosine phosphatase explains increased phytochelatin accumulation in arsenate-tolerant Holcus lanatus." In: *The Plant journal : for cell and molecular biology* 45.6 (Mar. 2006), pp. 917–29. ISSN: 0960-7412. DOI: 10.1111/j.1365-313X.2005.02651.x.

[108] A M Glauert and P R Lewis. *Biological specimen preparation for transmission electron microscopy*. Princeton University Press Princeton, NJ, USA: 1998. ISBN: 0691007497.

[109] M Isaacson, D Johnson, and A V Crewe. "Electron beam excitation and damage of biological molecules; its implications for specimen damage in electron microscopy". In: *Radiation Research* 55.2 (1973), pp. 205–224. ISSN: 0033-7587.

[110] R E Thach and S S Thach. "Damage to biological samples caused by the electron beam during electron microscopy." In: *Biophysical journal* 11.2 (Feb. 1971), pp. 204–10. ISSN: 0006-3495. DOI: 10.1016/S0006-3495(71)86208-2.

[111] M. Goode and M. Hayat. "Principles and Techniques of Scanning Electron Microscopy". In: *Transactions of the American Microscopical Society* 90 (Apr. 1971), p. 255. DOI: 10.2307/3225035.

[112] Katie L Moore et al. "High-resolution secondary ion mass spectrometry reveals the contrasting subcellular distribution of arsenic and silicon in rice roots." In: *Plant physiology* 156.2 (June 2011), pp. 913–24. ISSN: 1532-2548. DOI: 10.1104/pp.111.173088.

[113] S E Kirk, J N Skepper, and A M Donald. "Application of environmental scanning electron microscopy to determine biological surface structure". In: *Journal of Microscopy* 233.2 (2009), pp. 205–224. ISSN: 1365-2818.

[114] Joseph I Goldstein et al. *Scanning electron microscopy and X-ray microanalysis*. Springer, 2017.

[115] Enzo Lombi et al. "Arsenic distribution and speciation in the fronds of the hyperaccumulator Pteris vittata". In: *New Phytologist* 156.2 (Nov. 2002), pp. 195–203. ISSN: 0028-646X. DOI: 10.1046/j.1469-8137.2002.00512.x.

[116] K Stetzenbach. *Fingerprinting of ground water by ICP-MS. Progress report, April 1, 1994–June 30, 1994*. Tech. rep. 1994.

[117] R Chiappini, JM Taillade, and S Brébion. "Development of a high-sensitivity inductively coupled plasma mass spectrometer for actinide measurement in the femtogram range". In: *J. Anal. At. Spectrom.* 11.July (1996), pp. 497–503.

[118] Annette L. Nolan, Enzo Lombi, and Mike J. McLaughlin. "Metal Bioaccumulation and Toxicity in Soils Why Bother with Speciation?" In: *ChemInform* 34.28 (July 2003), pp. 77–91. ISSN: 0931-7597. DOI: 10.1002/chin.200328295.

[119] E Lombi et al. "Speciation and distribution of arsenic and localization of nutrients in rice grains." In: *The New phytologist* 184.1 (Jan. 2009), pp. 193–201. ISSN: 1469-8137. DOI: 10.1111/j.1469-8137.2009.02912.x.

[120] P. Quevauviller et al. "Evaluation of a sequential extraction procedure for the determination of extractable trace metal contents in sediments". In: *Fresenius' Journal of Analytical Chemistry* 349.12 (1994), pp. 808–814. ISSN: 0937-0633. DOI: 10.1007/BF00323110.

[121] P Quevauviller. "Operationally defined extraction procedures for soil and sediment analysis I. Standardization". In: *TrAC Trends in Analytical Chemistry* 17.5 (May 1998), pp. 289–298. ISSN: 01659936. DOI: 10.1016/S0165-9936(97)00119-2.

[122] József Hlavay et al. "Determination of trace elements bound to soils and sediment fractions". In: *Pure Appl. Chem* 76.2 (2004), pp. 415–442.

[123] S.D. Young et al. "Characterizing the availability of metals in contaminated soils. I. The solid phase: sequential extraction and isotopic dilution". In: *Soil Use and Management* 21.1 (Dec. 2005), pp. 450–458. ISSN: 02660032. DOI: 10.1079/SUM2005348.

[124] Richard E Russo et al. "Laser ablation in analytical chemistry-a review." In: *Talanta* 57.3 (May 2002), pp. 425–51. ISSN: 1873-3573.

[125] K Niemax. "Laser ablation–reflections on a very complex technique for solid sampling." In: *Fresenius' journal of analytical chemistry* 370.4 (June 2001), pp. 332–40. ISSN: 0937-0633.

[126] O. Yavuz Ataman. "Vapor generation and atom traps: Atomic absorption spectrometry at the ng/L level". In: *Spectrochimica Acta Part B: Atomic Spectroscopy* 63.8 (Aug. 2008), pp. 825–834. ISSN: 05848547. DOI: 10.1016/j.sab.2008.03.013.

[127] Applied Speciation and Consulting LLC. *Hydride Generation vs . IC-ICP-MS for Selenium Speciation Analysis A side-by-side comparison*. Tech. rep. Iv.

[128] S Maity et al. "Evaluation and standardisation of a simple HG-AAS method for rapid speciation of As(III) and As(V) in some contaminated groundwater samples of West Bengal, India." In: *Chemosphere* 54.8 (Feb. 2004), pp. 1199–206. ISSN: 0045-6535. DOI: 10.1016/j.chemosphere.2003.09.035.

[129] R. Kirkham et al. "The Maia Spectroscopy Detector System: Engineering for Integrated Pulse Capture, Low-Latency Scanning and Real-Time Processing". In: 240.May (2010), pp. 240–243. DOI: 10.1063/1.3463181.

[130] Hidekazu Mimura et al. "Efficient focusing of hard x rays to 25 nm by a total reflection mirror". In: *Applied Physics Letters* 90.5 (2007), p. 051903. ISSN: 00036951. DOI: 10.1063/1.2436469.

[131] H. Kang et al. "Nanometer Linear Focusing of Hard X Rays by a Multilayer Laue Lens". In: *Physical Review Letters* 96.12 (Mar. 2006), pp. 1–4. ISSN: 0031-9007. DOI: 10.1103/PhysRevLett.96.127401.

[132] Enzo Lombi et al. "Fast x-ray fluorescence microtomography of hydrated biological samples." In: *PloS one* 6.6 (Jan. 2011), e20626. ISSN: 1932-6203. DOI: 10.1371/journal.pone.0020626.

[133] E Lombi et al. "Trends in hard X-ray fluorescence mapping: environmental applications in the age of fast detectors." In: *Analytical and bioanalytical chemistry* 400.6 (June 2011), pp. 1637–44. ISSN: 1618-2650. DOI: 10.1007/s00216-011-4829-2.

[134] Peter M Kopittke et al. "In situ distribution and speciation of toxic copper, nickel, and zinc in hydrated roots of cowpea." In: *Plant physiology* 156.2 (June 2011), pp. 663–73. ISSN: 1532-2548. DOI: 10.1104/pp.111.173716.

[135] Oliver Betz et al. "Imaging applications of synchrotron X-ray phase-contrast microtomography in biological morphology and biomaterials science. I. General aspects of the technique and its advantages in the analysis of millimetre-sized arthropod structure." In: *Journal of microscopy* 227.Pt 1 (July 2007), pp. 51–71. ISSN: 0022-2720. DOI: 10.1111/j.1365-2818.2007.01785.x.

[136] P. Cloetens et al. "Observation of microstructure and damage in materials by phase sensitive radiography and tomography". In: *Journal of Applied Physics* 81.9 (1997), p. 5878. ISSN: 00218979. DOI: 10.1063/1.364374.

[137] Heiko Wende. "Recent advances in x-ray absorption spectroscopy". In: *Reports on Progress in Physics* 67.12 (Dec. 2004), pp. 2105–2181. ISSN: 0034-4885. DOI: 10.1088/0034-4885/67/12/R01.

[138] Andrew A Meharg et al. “Speciation and localization of arsenic in white and brown rice grains.” In: *Environmental science & technology* 42.4 (Feb. 2008), pp. 1051–7. ISSN: 0013-936X.

[139] Katie L Moore et al. “Elemental imaging at the nanoscale: NanoSIMS and complementary techniques for element localisation in plants”. In: *Analytical and bioanalytical chemistry* (). DOI: DOI10.1007/s00216-011-5484-3.

[140] Enzo Lombi, Kirk G. Scheckel, and Ivan M. Kempson. “In situ analysis of metal(loid)s in plants: State of the art and artefacts”. In: *Environmental and Experimental Botany* 72.1 (Aug. 2011), pp. 3–17. ISSN: 00988472. DOI: 10.1016/j.envexpbot.2010.04.005.

[141] F. L. Arnot and J. C. Milligan. “A New Process of Negative Ion Formation”. In: *Proceedings of the Royal Society A: Mathematical, Physical and Engineering Sciences* 156.889 (Sept. 1936), pp. 538–560. ISSN: 1364-5021. DOI: 10.1098/rspa.1936.0166.

[142] R. H. Sloane and R. Press. “The Formation of Negative Ions by Positive-Ion Impact on Surfaces”. In: *Proceedings of the Royal Society A: Mathematical, Physical and Engineering Sciences* 168.933 (Oct. 1938), pp. 284–301. ISSN: 1364-5021. DOI: 10.1098/rspa.1938.0174.

[143] Frank Keywell. “A Mechanism for Sputtering in the High Vacuum Based upon the Theory of Neutron Cooling”. In: *Physical Review* 87.1 (1952), pp. 160–161.

[144] N Bohr. *Kgl. Danske Videnskab. Selskab, Mat-Fys. Medd. 18 (1948) 8. JA Brinkman: Radiation Damage in Solid, edited by DS Billington*. 1962.

[145] E Fermi. “Nuclear physics”. In: *(a course given by Enrico Fermi at the University of Chicago; notes compiled by J. Orear, AH Rosenfeld, and RA Schluter, revised edition) (The University of Chicago Press, Chicago, Illinois, 1950)*.

[146] Frank Keywell. “Measurements and CollisionRadiation Damage Theory of High-Vacuum Sputtering”. In: *Physical Review* 97.6 (1955), pp. 1611–1619.

[147] JA Davies et al. “The range of alkali metal ions of kiloelectron volt energies in aluminum”. In: *Canadian Journal of Chemistry* 38.9 (1960), pp. 1535–1546.

[148] O Almén and G Bruce. “Collection and sputtering experiments with noble gas ions”. In: *Nuclear Instruments and Methods* 11 (1961), pp. 257–278.

[149] Alfred Benninghoven, FG Rudenauer, and Helmut W Werner. “Secondary ion mass spectrometry: basic concepts, instrumental aspects, applications and trends”. In: (1987).

[150] F. L. Arnot and C. Beckett. “A New Process of Negative-Ion Formation. IV”. In: *Proceedings of the Royal Society A: Mathematical, Physical and Engineering Sciences* 168.932 (Oct. 1938), pp. 103–122. ISSN: 1364-5021. DOI: 10.1098/rspa.1938.0163.

[151] C A Andersen. “Progress in analytic methods for the ion microprobe mass analyzer”. In: *International Journal of Mass Spectrometry and Ion Physics* 2.1 (1969), pp. 61–74.

[152] C A Andersen. "Analytic methods for the ion microprobe mass analyzer. Part II." In: *International Journal of Mass Spectrometry and Ion Physics* 3.6 (1970), pp. 413–428.

[153] K Wittmaack. "Secondary ion yield variations due to cesium implantation in silicon". In: *Surface Science* 126.1-3 (1983), pp. 573–580.

[154] P Williams and RK Lewis. "Evaluation of a cesium primary ion source on an ion microprobe mass spectrometer". In: *Analytical ...* 49.9 (1977), pp. 1399–1403.

[155] H. A. Storms, K. F. Brown, and J. D. Stein. "Evaluation of a Cesium Positive Ion Source for Secondary Ion Mass Spectrometry". In: *Analytical Chemistry* 49.13 (1977), pp. 2023–2030.

[156] C A Andersen and J R Hinthorne. "Ion microprobe mass analyzer". In: *Science* 175.4024 (1972), pp. 853–860. ISSN: 0036-8075.

[157] G O Ramseyer and G H Morrison. "Relative sensitivity factors of elements in quantitative secondary ion mass spectrometric analysis of biological reference materials." In: *Analytical chemistry* 55.12 (Oct. 1983), pp. 1963–70. ISSN: 0003-2700.

[158] Helmut Liebl. "Ion Microprobe Mass Analyzer". In: *Journal of Applied Physics* 38.13 (1967), pp. 5277–5283. ISSN: 00218979. DOI: 10.1063/1.1709314.

[159] A O Nier and D J Schlutter. "Highperformance doublefocusing mass spectrometer". In: *Review of scientific instruments* 56.2 (1985), pp. 214–219. ISSN: 0034-6748.

[160] J Mattauch and R Herzog. "Über einen neuen Massenspektrographen". In: *Zeitschrift für Physik A Hadrons and Nuclei* 89.11 (1934), pp. 786–795. ISSN: 0939-7922.

[161] Anke Herrmann et al. "Nano-scale secondary ion mass spectrometry A new analytical tool in biogeochemistry and soil ecology: A review article". In: *Soil Biology and Biochemistry* 39 (Aug. 2007), pp. 1835–1850. DOI: 10.1016/j.soilbio.2007.03.011.

[162] A Benninghoven. "Secondary ion mass spectrometry of organic compounds". In: *TrAC Trends in Analytical Chemistry* 1.13 (1982), pp. 311–314.

[163] A Benninghoven. "Organic secondary ion mass spectrometry (SIMS) and its relation to Fast Atom Bombardment (FAB)". In: *International Journal of Mass Spectrometry and Ion ...* 46 (1983), pp. 459–462.

[164] C R M Grovenor et al. "Specimen preparation for NanoSIMS analysis of biological materials". In: *Applied Surface Science* 252.19 (2006), pp. 6917–6924.

[165] Enzo Lombi and Jean Susini. "Synchrotron-based techniques for plant and soil science: opportunities, challenges and future perspectives". In: *Plant and Soil* 320.1-2 (Jan. 2009), pp. 1–35. ISSN: 0032-079X. DOI: 10.1007/s11104-008-9876-x.

[166] Darrell G Schulze and Paul M Bertsch. "Synchrotron X-Ray Techniques in Soil, Plant, and Environmental Research". In: *Advances in Agronomy*. Advances in Agronomy 55 (1995). Ed. by Donald L Sparks, pp. 1–66. ISSN: 0065-2113. DOI: 10.1016/S0065-2113(08)60537-4.

[167] Katie L Moore et al. "NanoSIMS analysis of arsenic and selenium in cereal grain." In: *The New phytologist* 185.2 (Jan. 2010), pp. 434–45. ISSN: 1469-8137. DOI: 10.1111/j.1469-8137.2009.03071.x.

[168] Won-Yong Song et al. "Arsenic tolerance in Arabidopsis is mediated by two ABCC-type phytochelatin transporters." In: *Proceedings of the National Academy of Sciences of the United States of America* 107.49 (Dec. 2010), pp. 21187–92. ISSN: 1091-6490. DOI: 10.1073/pnas.1013964107.

[169] Olena K. Vatamaniuk et al. "AtPCS1, a phytochelatin synthase from Arabidopsis: Isolation and in vitro reconstitution". In: *Proceedings of the National Academy of Sciences* 96.12 (1999), pp. 7110–7115. ISSN: 0027-8424. DOI: 10.1073/pnas.96.12.7110. eprint: https://www.pnas.org/content/96/12/7110.full.pdf.

[170] R. Howden et al. "Cadmium-Sensitive, cad1 Mutants of Arabidopsis thaliana Are Phytochelatin Deficient". In: *Plant Physiology* 107.4 (1995), pp. 1059–1066. ISSN: 0032-0889. DOI: 10.1104/pp.107.4.1059. eprint: http://www.plantphysiol.org/content/107/4/1059.full.pdf.

[171] D. STUDER et al. "Vitrification of articular cartilage by high-pressure freezing". In: *Journal of Microscopy* 179.3 (1995), pp. 321–322. DOI: 10.1111/j.1365-2818.1995.tb03648.x. eprint: https://onlinelibrary.wiley.com/doi/pdf/10.1111/j.1365-2818.1995.tb03648.x.

[172] G Slodzian et al. "A thermal ionization source for a Cs+ ion probe". In: *Tiré à part-Office national d'études et de recherches aerospatiales* (1991).

[173] Emrys A. Jones, Nicholas P. Lockyer, and John C. Vickerman. "Depth Profiling Brain Tissue Sections with a 40 keV C60+ Primary Ion Beam". In: *Analytical Chemistry* 80.6 (2008). PMID: 18278949, pp. 2125–2132. DOI: 10.1021/ac702127q. eprint: https://doi.org/10.1021/ac702127q.

[174] C. W. Magee and R. E. Honig. "Depth profiling by SIMSdepth resolution, dynamic range and sensitivity". In: *Surface and Interface Analysis* 4.2 (1982), pp. 35–41. DOI: 10.1002/sia.740040202. eprint: https://onlinelibrary.wiley.com/doi/pdf/10.1002/sia.740040202.

[175] Nicole Grignon et al. "14N and 15N imaging by SIMS microscopy in soybean leaves". In: *Biology of the Cell* 74 (1992), pp. 143–146. ISSN: 0248-4900. DOI: https://doi.org/10.1016/0248-4900(92)90020-2.

[176] KE Smart et al. "NanoSIMS and EPMA analysis of nickel localisation in leaves of the hyperaccumulator plant Alyssum lesbiacum". In: *International Journal of Mass Spectrometry* 260.2-3 (2007), pp. 107–114.

[177] Shunsuke Miyashima et al. "Non-cell-autonomous microRNA165 acts in a dose-dependent manner to regulate multiple differentiation status in the Arabidopsis root". In: *Development* 138.11 (2011), pp. 2303–2313. ISSN: 0950-1991. DOI: 10.1242/dev.060491. eprint: https://dev.biologists.org/content/138/11/2303.full.pdf.

[178] Jed P Sparks et al. “Subcellular localization of silicon and germanium in grass root and leaf tissues by SIMS: evidence for differential and active transport”. In: *Biogeochemistry* 104.1-3 (2011), pp. 237–249.

[179] Katie L Moore et al. “High resolution SIMS analysis of arsenic in rice”. In: *Surface and interface analysis* 45.1 (2013), pp. 309–311.

[180] Julia Rebouillat et al. “Molecular genetics of rice root development”. In: *Rice* 2.1 (2009), p. 15.

[181] Harika Gupta. “Characteristics of Monocotyledonous Roots”. In: ().

[182] Fazal Ur Rehman Shah et al. “Heavy metal toxicity in plants”. In: *Plant adaptation and phytoremediation*. Springer, 2010, pp. 71–97.

[183] Lynn M Ramsay and Geoffrey M Gadd. “Mutants of *Saccharomyces cerevisiae* defective in vacuolar function confirm a role for the vacuole in toxic metal ion detoxification”. In: *FEMS Microbiology Letters* 152.February (1997), pp. 293–298.

[184] Xuexi Yang et al. “Evidence of vacuolar compartmentalization of arsenic in the hyperaccumulator Pteris vittata”. In: *Chinese Science Bulletin* 54.22 (Nov. 2009), pp. 4229–4233. DOI: 10.1007/s11434-009-0675-4.

[185] Stephan Clemens. “Evolution and function of phytochelatin synthases”. In: *Journal of Plant Physiology* 163.3 (Feb. 2006), pp. 319–332. ISSN: 0176-1617. DOI: 10.1016/J.JPLPH.2005.11.010.

[186] Erwin Grill, Ernst-L Winnacker, and Meinhart H Zenk. “Phytochelatins: the principal heavy-metal complexing peptides of higher plants”. In: *Science* 230.4726 (1985), pp. 674–676.

[187] R.G. Wilson. “SIMS quantification in Si, GaAs, and diamond - an update”. In: *International Journal of Mass Spectrometry and Ion Processes* 143 (1995), pp. 43–49. ISSN: 0168-1176. DOI: https://doi.org/10.1016/0168-1176(94)04136-U.

[188] Naoki Yamaji, Namiki Mitani, and Jian Feng Ma. “Functional analysis of a novel silicon transporter Lsi3 in rice”. In: *Plant and Cell Physiology Supplement* 2010 (2010), pp. 0156–0156. DOI: 10.14841/jspp.2010.0.0156.0.

[189] Ricardo F H Giehl and Nicolaus von Wirén. “Root nutrient foraging.” In: *Plant physiology* 166.2 (Oct. 2014), pp. 509–17. ISSN: 1532-2548. DOI: 10.1104/pp.114.245225.

[190] Catherine Bellini, Daniel I. Pacurar, and Irene Perrone. “Adventitious Roots and Lateral Roots: Similarities and Differences”. In: *Annual Review of Plant Biology* 65.1 (Apr. 2014), pp. 639–666. ISSN: 1543-5008. DOI: 10.1146/annurev-arplant-050213-035645.

[191] Benjamin Péret, Antoine Larrieu, and Malcolm Bennett. “Lateral root emergence: A difficult birth”. In: *Journal of experimental botany* 60 (Aug. 2009), pp. 3637–43. DOI: 10.1093/jxb/erp232.

[192] MC Drew et al. “Root function, development, growth and mineral nutrition.” In: *The rhizosphere.* (1990), pp. 35–57.

[193] BS Satapathy et al. "Evaluation of rice (Oryza sativa) under double transplanting in rainfed lowland rice ecosystem of Asom". In: *Indian Journal of Agronomy* 60.2 (2015), pp. 245–248.

[194] Fang Liu et al. "Comprehensive Sequence and Whole-Life-Cycle Expression Profile Analysis of the Phosphate Transporter Gene Family in Rice". In: *Molecular Plant* 4.6 (2011), pp. 1105–1122. ISSN: 1674-2052. DOI: https://doi.org/10.1093/mp/ssr058.

[195] Mayumi Tabuchi, Tomomi Abiko, and Tomoyuki Yamaya. "Assimilation of ammonium ions and reutilization of nitrogen in rice (Oryza sativa L.)" In: *Journal of experimental botany* 58.9 (2007), pp. 2319–2327.

[196] Kosala Ranathunge, Ernst Steudle, and Renee Lafitte. "Control of water uptake by rice (Oryza sativa L.): role of the outer part of the root". In: *Planta* 217.2 (2003), pp. 193–205.

[197] Chien Hui Syu et al. "Arsenic sequestration in iron plaque and its effect on As uptake by rice plants grown in paddy soils with high contents of As, iron oxides, and organic matter". In: *Soil Science and Plant Nutrition* 59.3 (2013), pp. 463–471. ISSN: 00380768. DOI: 10.1080/00380768.2013.784950.

[198] Yanshan Chen et al. "Arsenic transport in rice and biological solutions to reduce arsenic risk from rice". In: *Frontiers in plant science* 8 (2017), p. 268.

[199] Laurent Nussaume et al. "Phosphate import in plants: focus on the PHT1 transporters". In: *Frontiers in plant science* 2 (2011), p. 83.

[200] Erwin Grill, Ernst-L Winnacker, and Meinhart H Zenk. "Phytochelatins, a class of heavy-metal-binding peptides from plants, are functionally analogous to metallothioneins". In: *Proceedings of the National Academy of Sciences* 84.2 (1987), pp. 439–443.

[201] Erwin Grill et al. "Phytochelatins, the heavy-metal-binding peptides of plants, are synthesized from glutathione by a specific γ-glutamylcysteine dipeptidyl transpeptidase (phytochelatin synthase)". In: *Proceedings of the National Academy of Sciences* 86.18 (1989), pp. 6838–6842.

[202] Daisei Ueno et al. "Gene limiting cadmium accumulation in rice". In: *Proceedings of the national academy of sciences* 107.38 (2010), pp. 16500–16505.

[203] Fenglin Deng et al. "Engineering rice with lower grain arsenic". In: *Plant biotechnology journal* 16.10 (2018), pp. 1691–1699.

[204] Ralph Blum et al. "Cytosolic action of phytochelatin synthase". In: *Plant Physiology* 153.1 (2010), pp. 159–169.

[205] Jalean J. Petricka, Cara M. Winter, and Philip N. Benfey. "Control of Arabidopsis Root Development". In: *Annual Review of Plant Biology* 63.1 (2012). PMID: 22404466, pp. 563–590. DOI: 10.1146/annurev-arplant-042811-105501. eprint: https://doi.org/10.1146/annurev-arplant-042811-105501.

[206] Ernest M Gifford and Adriance Sherwood Foster. *Morphology and evolution of vascular plants*. Tech. rep. WH Freeman New York, 1989.

[207] Markus Geisler et al. "Arabidopsis immunophilin-like TWD1 functionally interacts with vacuolar ABC transporters". In: *Molecular biology of the cell* 15.7 (2004), pp. 3393–3405.

[208] Jiyoung Park et al. "The phytochelatin transporters AtABCC1 and AtABCC2 mediate tolerance to cadmium and mercury". In: *The Plant Journal* 69.2 (2012), pp. 278–288.

[209] KH Lau et al. "Development of a new bimodal imaging methodology: a combination of fluorescence microscopy and high-resolution secondary ion mass spectrometry". In: *Journal of microscopy* 240.1 (2010), pp. 21–31.

[210] Selda Kabatas et al. "Fluorinated nanobodies for targeted molecular imaging of biological samples using nanoscale secondary ion mass spectrometry". In: *J. Anal. At. Spectrom.* 34 (6 2019), pp. 1083–1087. DOI: 10.1039/C9JA00117D.

Appendix A

Oryza Sativa G2 detector counts

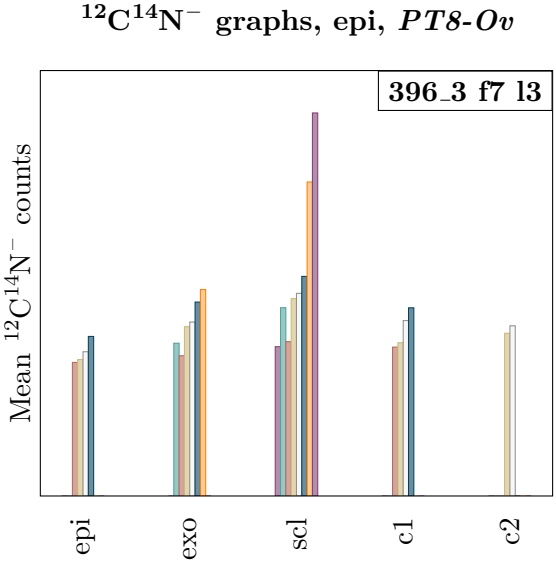

Figure A.1: Normalised mean $^{12}C^{14}N^-$ counts from the epidermal region, *PT8-Ov*. All y-axis limits are from 0 to 2.5

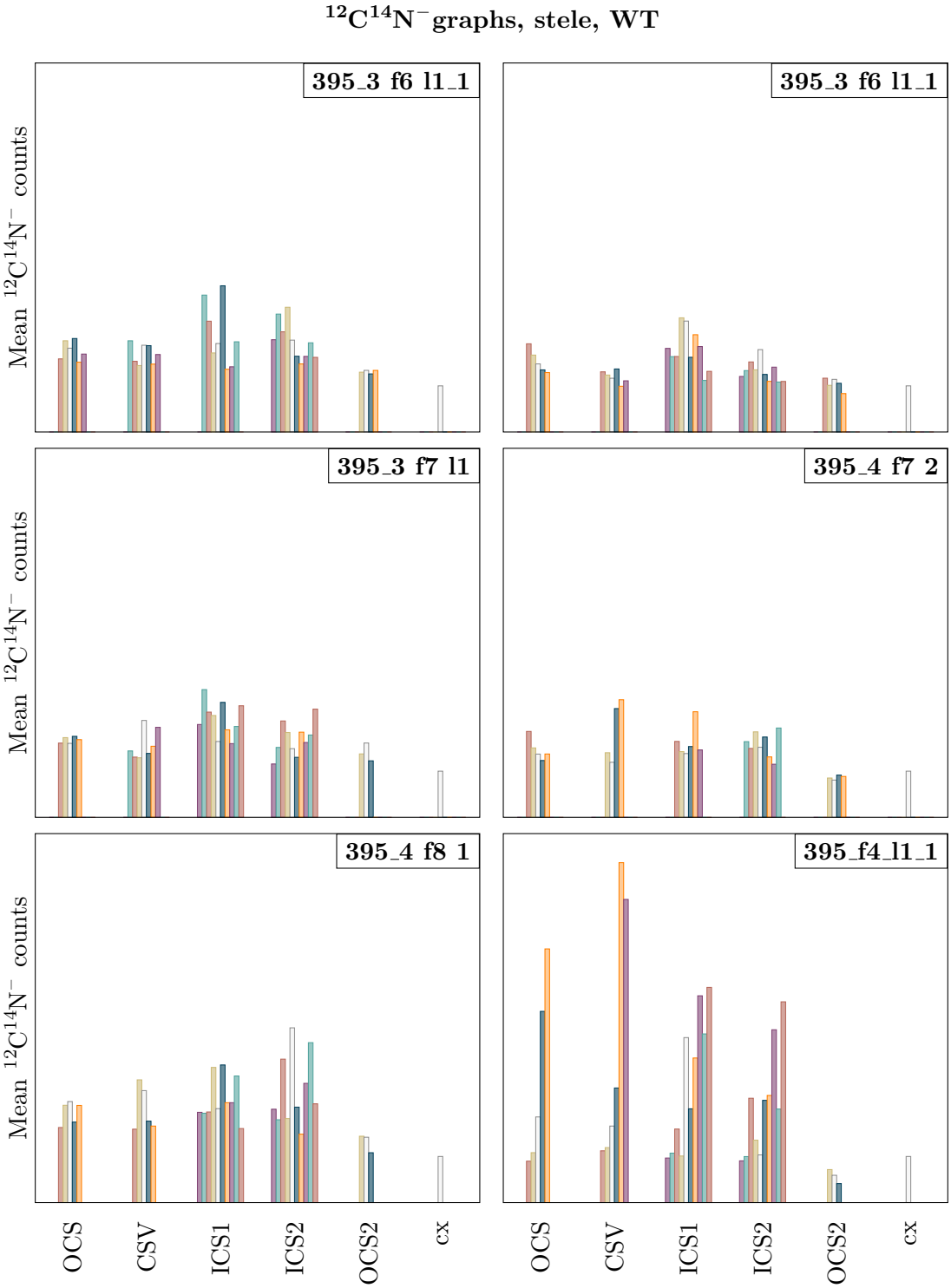

Figure A.2: Normalised mean $^{12}C^{14}N^-$ counts from the stele, WT. All y-axis limits are from 0 to 8.

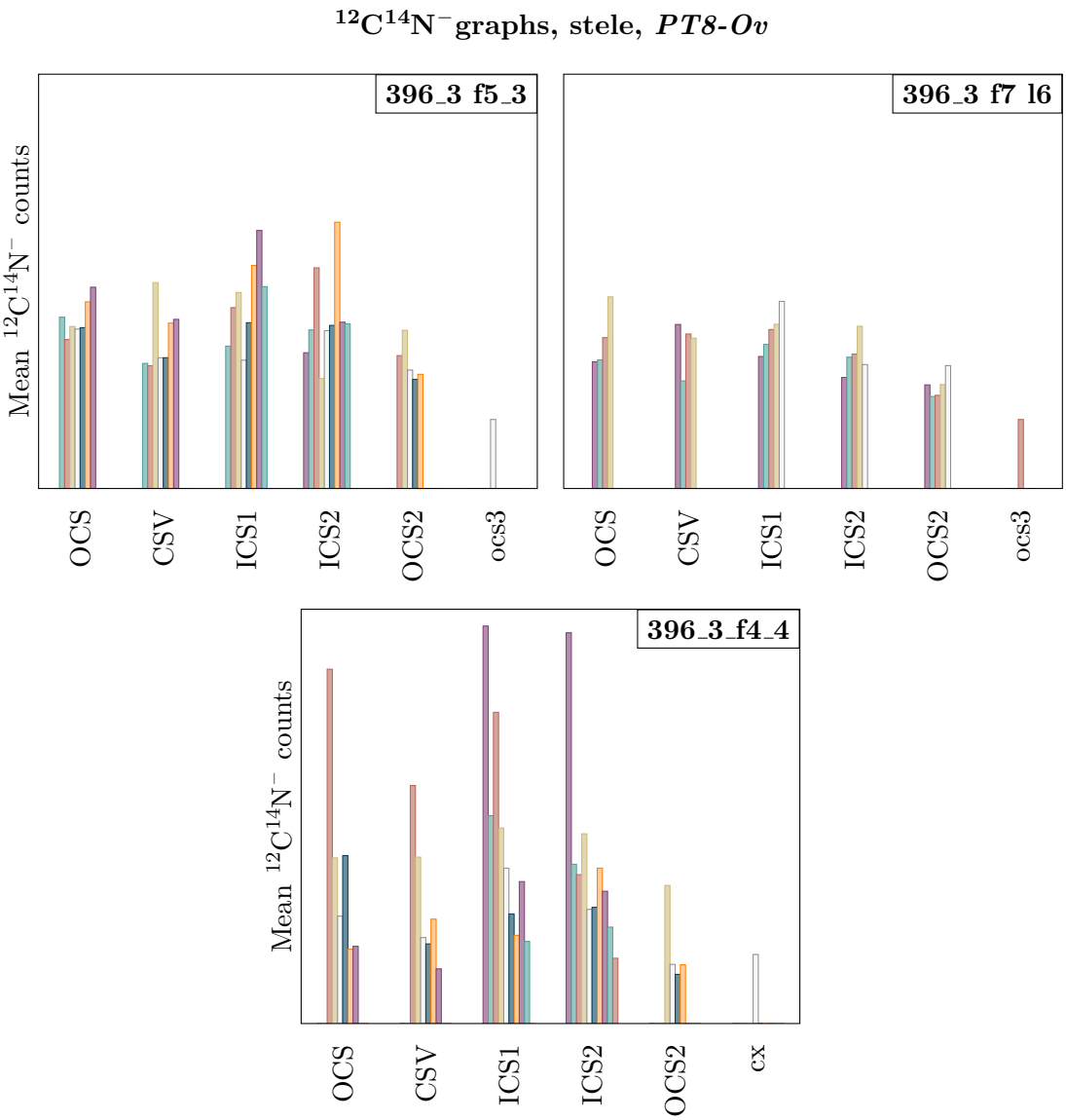

Figure A.3: Normalised mean $^{12}C^{14}N^-$ counts from the stele, *PT8-Ov*. All y-axis limits are from 0 to 6.

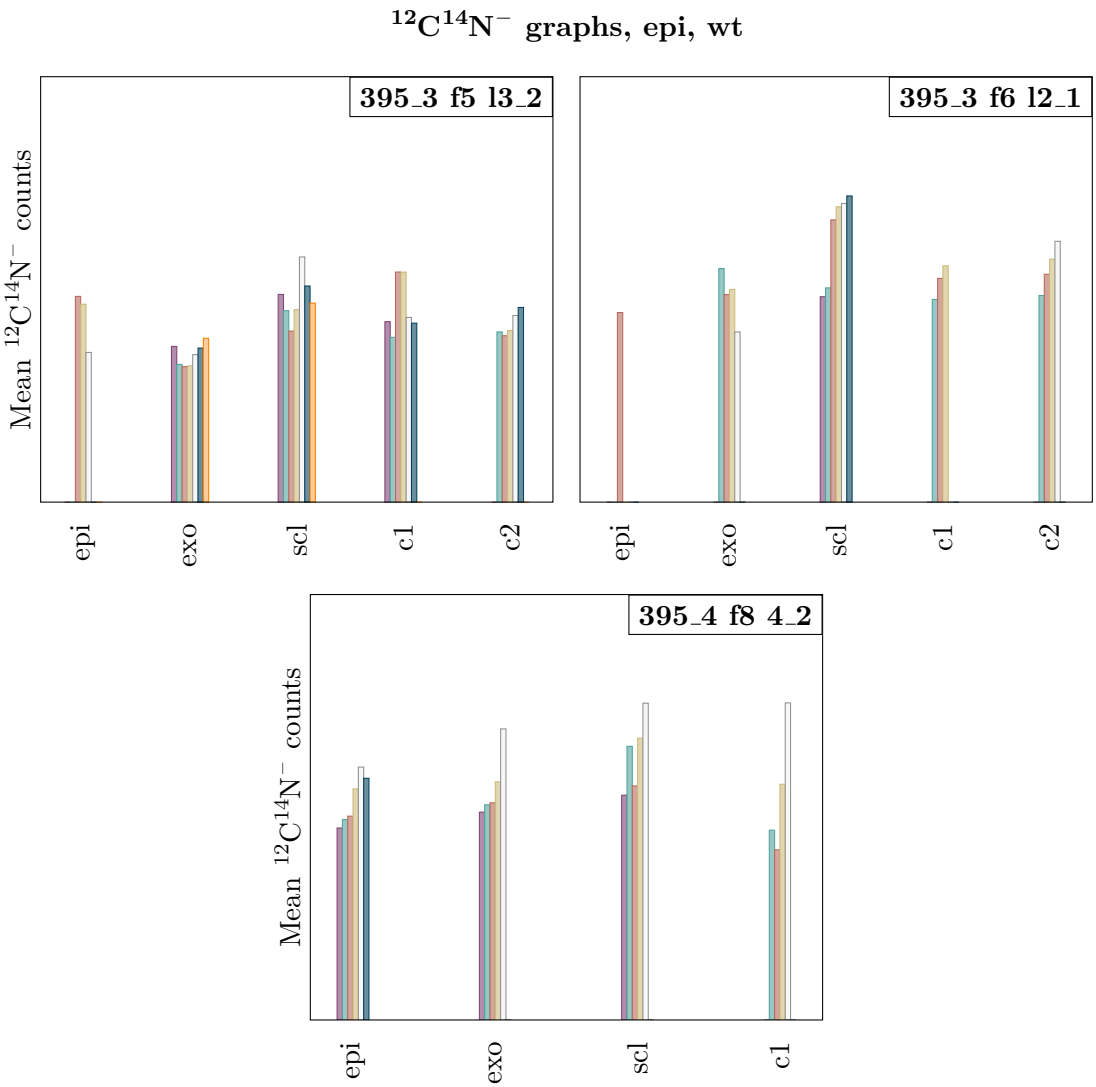

Figure A.4: Normalised mean $^{12}C^{14}N^-$counts from the epidermal region, WT. All y-axis limits are from 0 to 2.5.

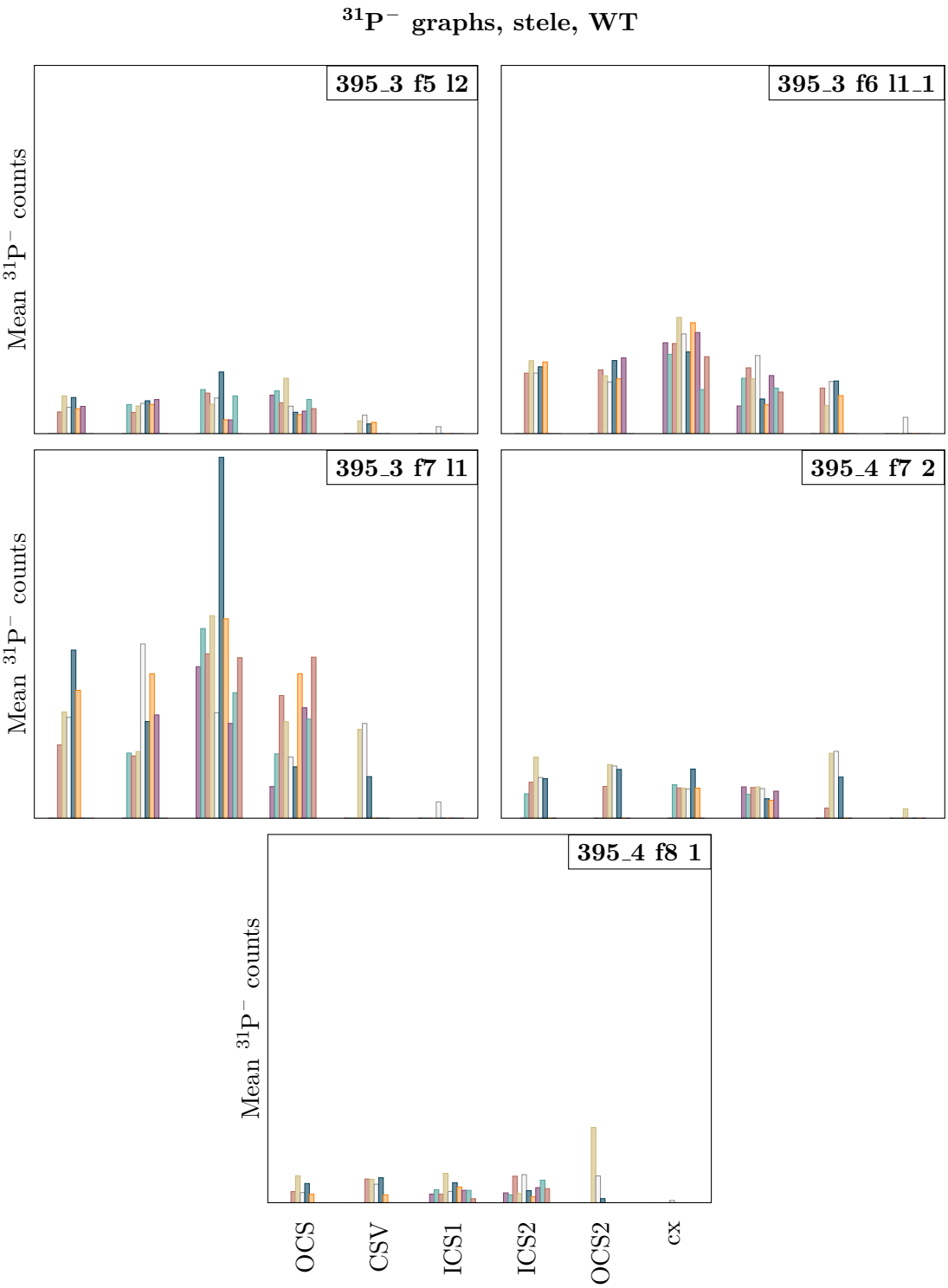

Figure A.5: $^{31}P^-$ signals from the stele, WT. ymax=0.0043

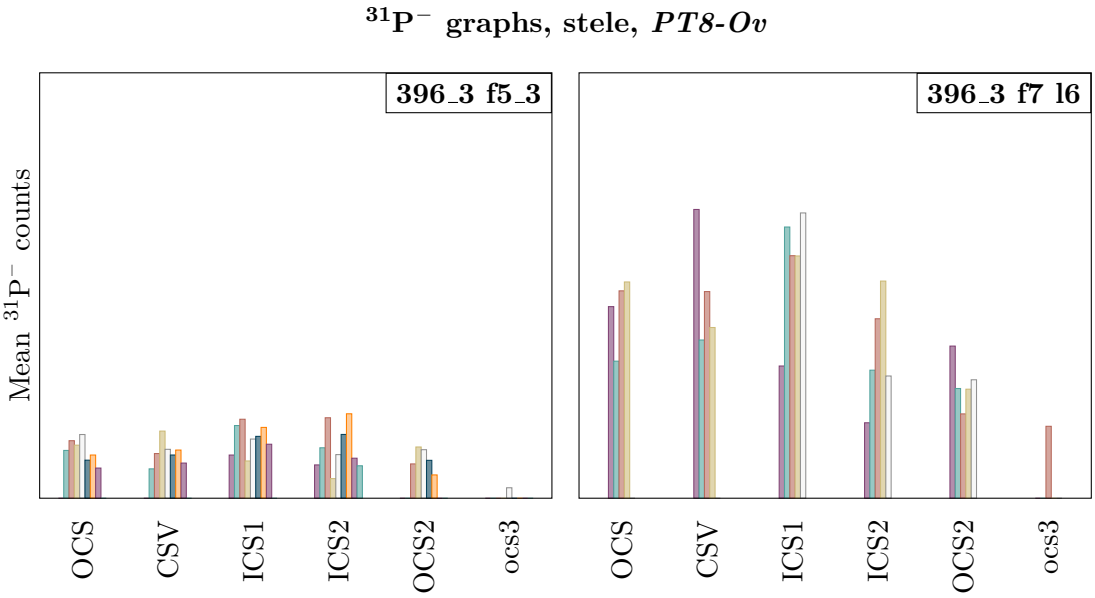

Figure A.6: $^{31}P^-$ signals from the stele, *PT8-Ov*. ymax=0.0043

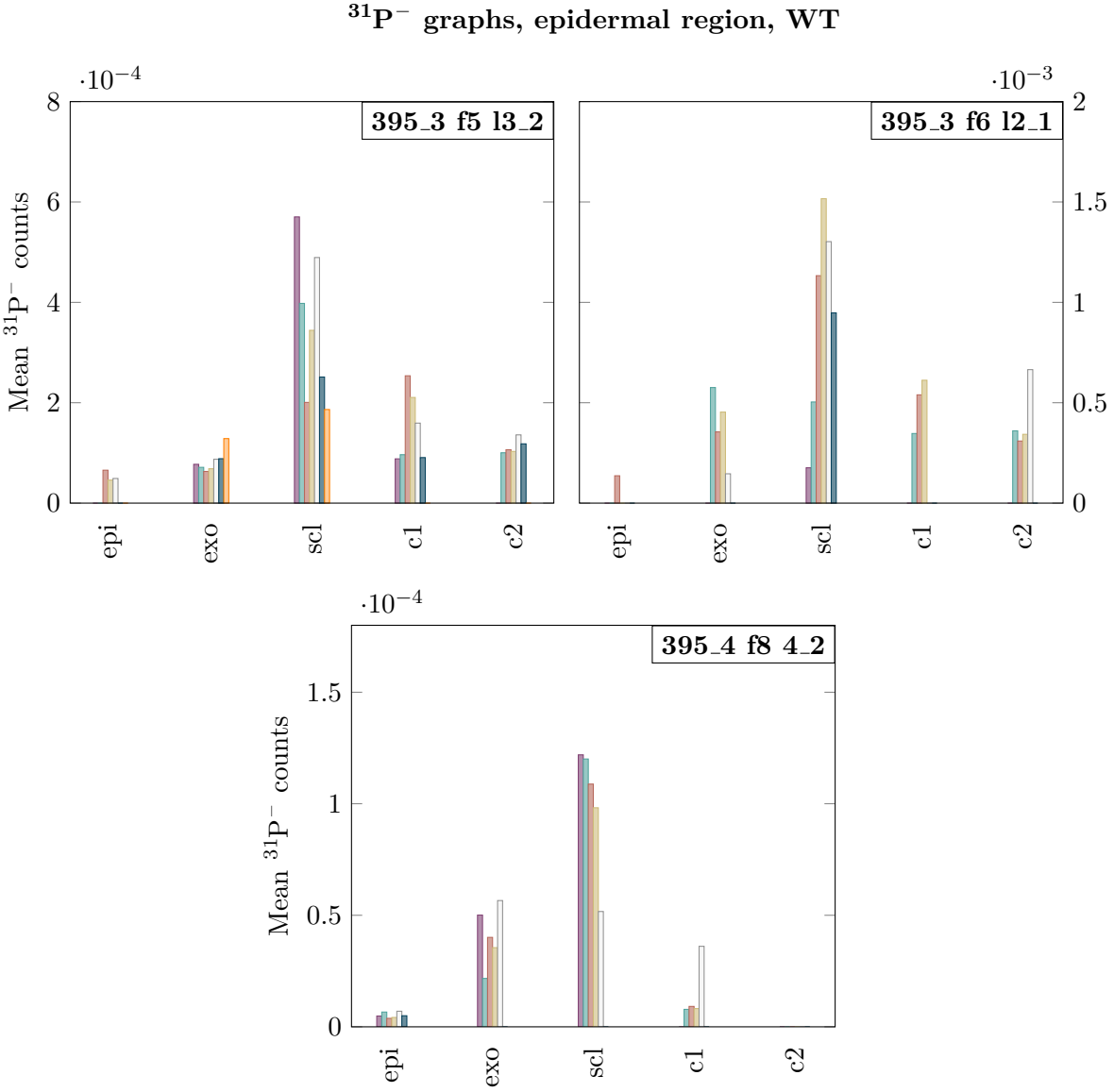

Figure A.7: $^{31}P^-$ signals from the epidermal region, WT.

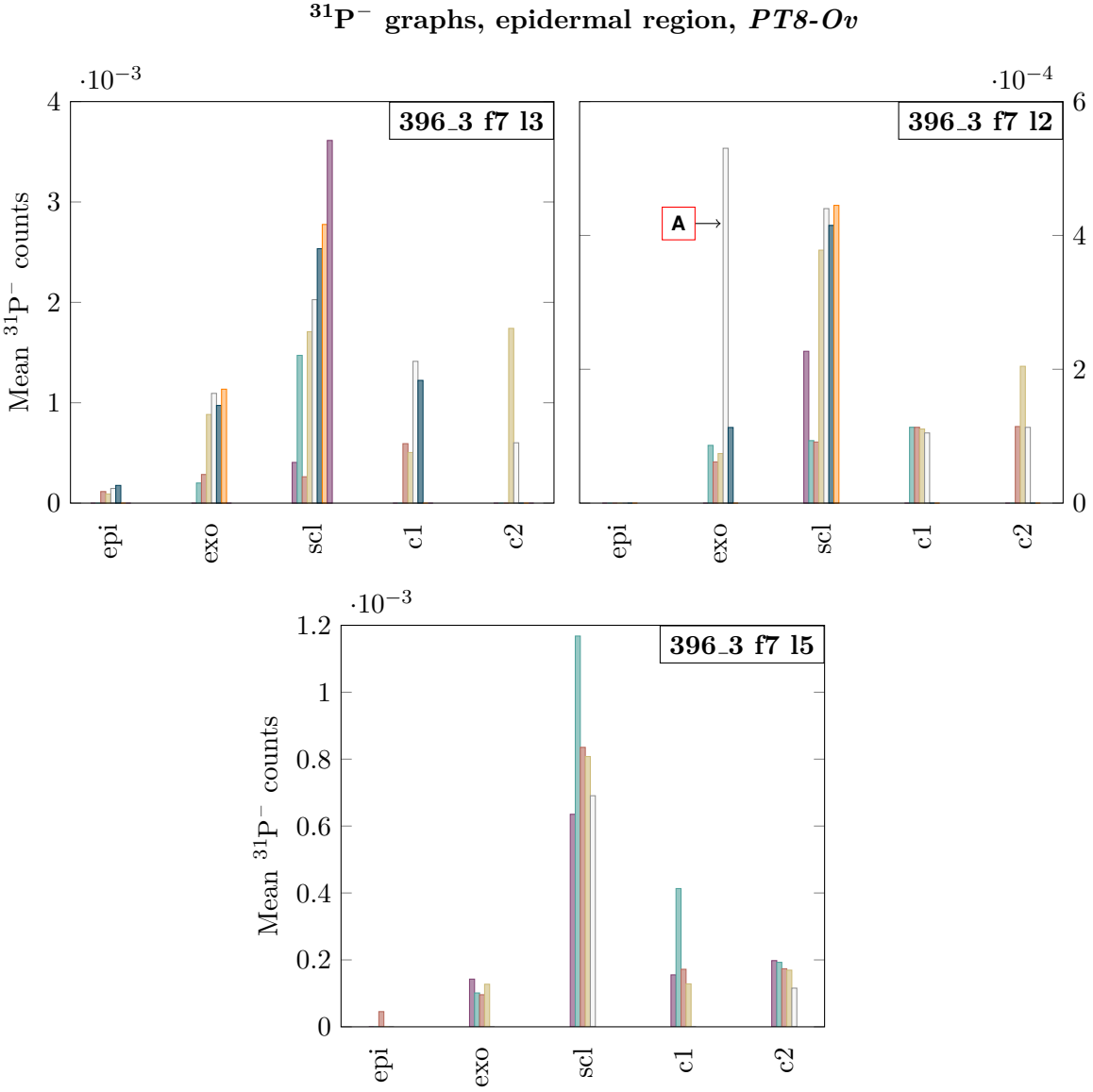

Figure A.8: $^{31}P^-$ signals from the epidermal region, *PT8-Ov*.

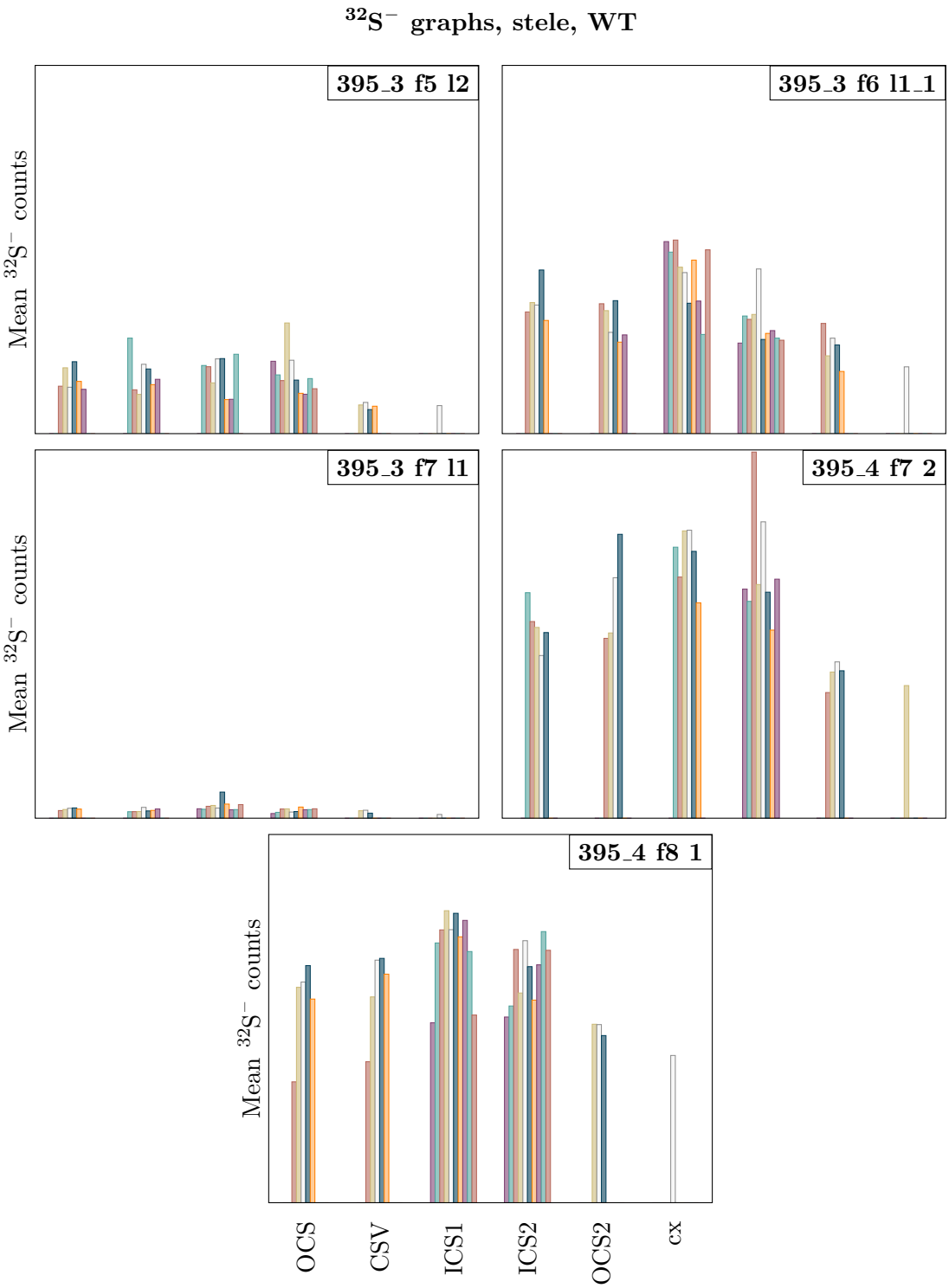

Figure A.9: $^{32}S^-$ signals from the stele, WT. ymax=0.045

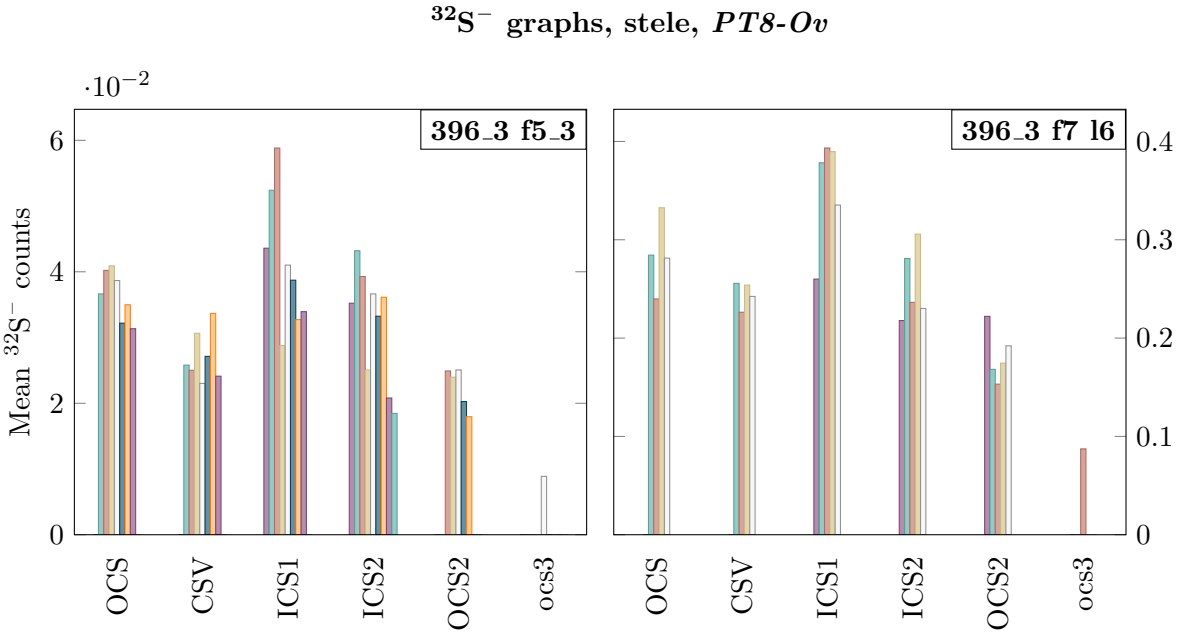

Figure A.10: $^{32}S^-$ signals from the stele, *PT8-Ov*. ymax=0.0043

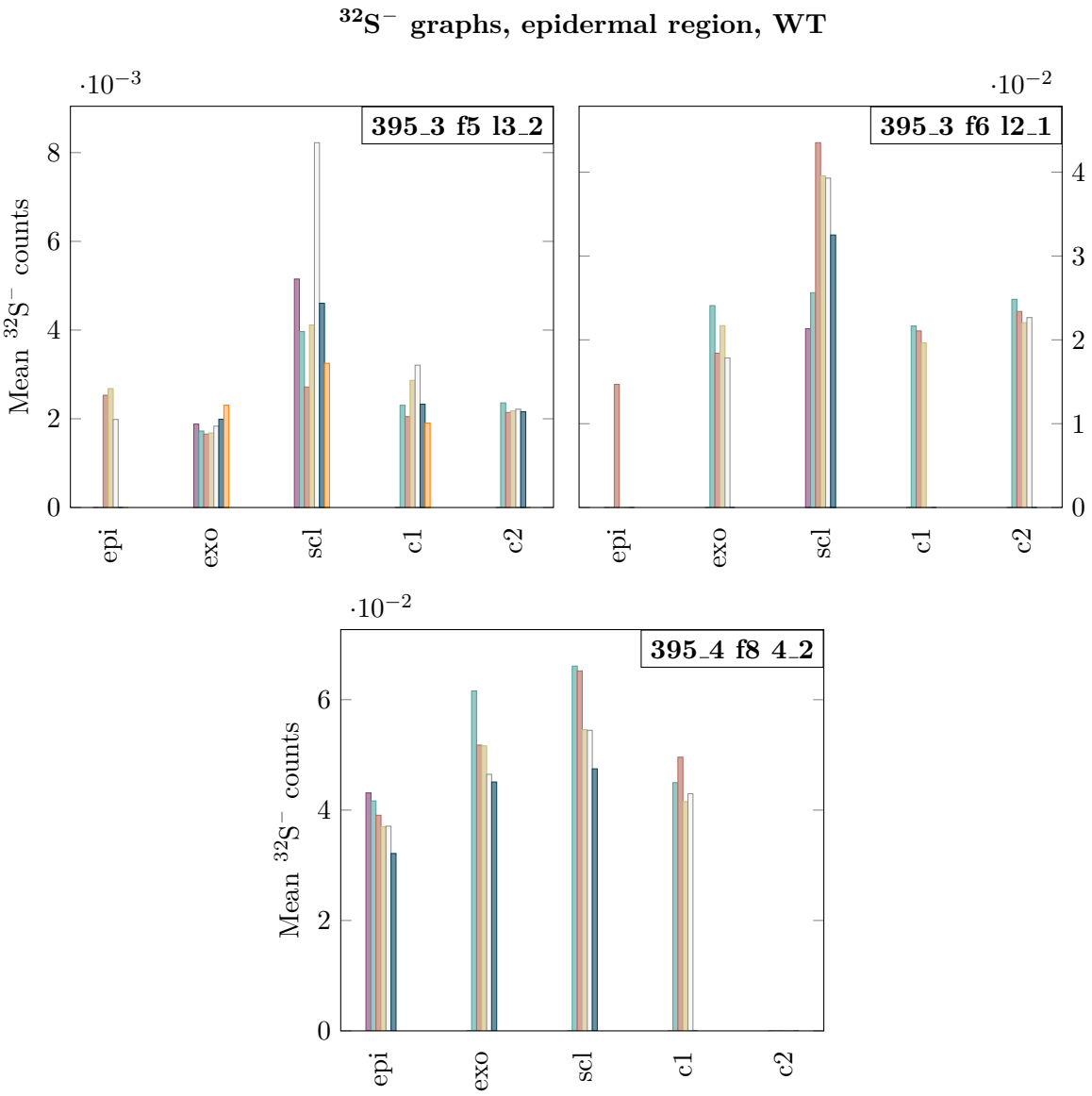

Figure A.11: $^{32}S^-$ signals from the epidermal region, WT.

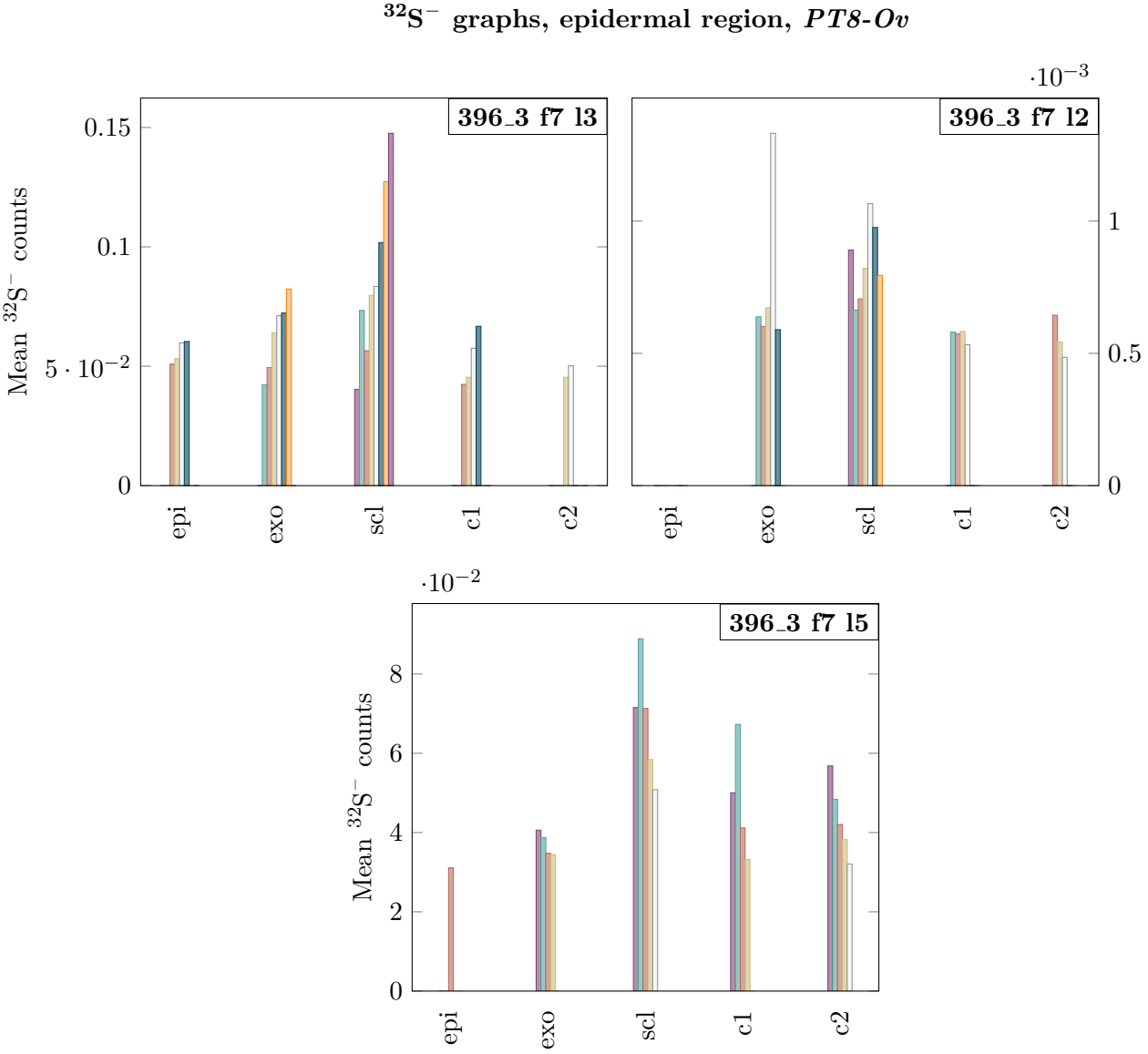

Figure A.12: $^{32}S^-$ signals from the epidermal region, *PT8-Ov*.

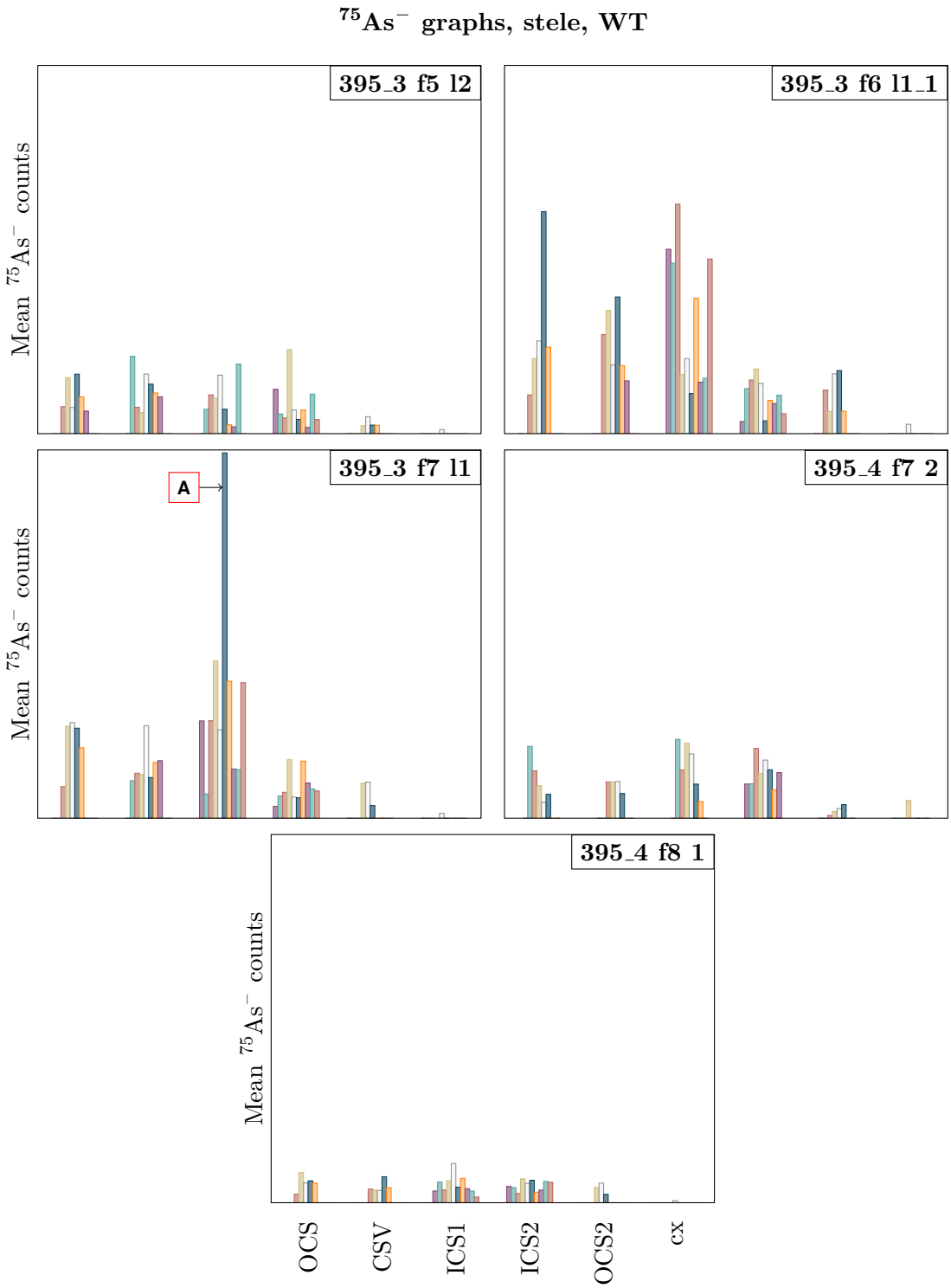

Figure A.13: ^{75}As$^-$ signals from the stele, WT. ymax=0.00032

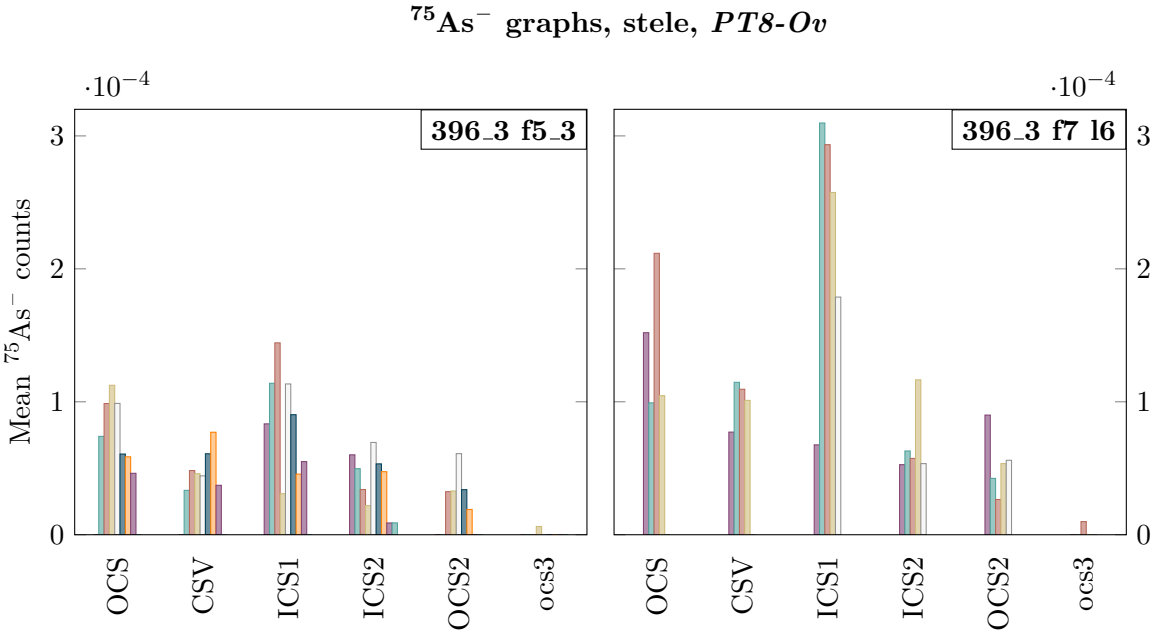

Figure A.14: ^{75}As$^-$ signals from the stele, *PT8-Ov*. ymax=3.2E-4

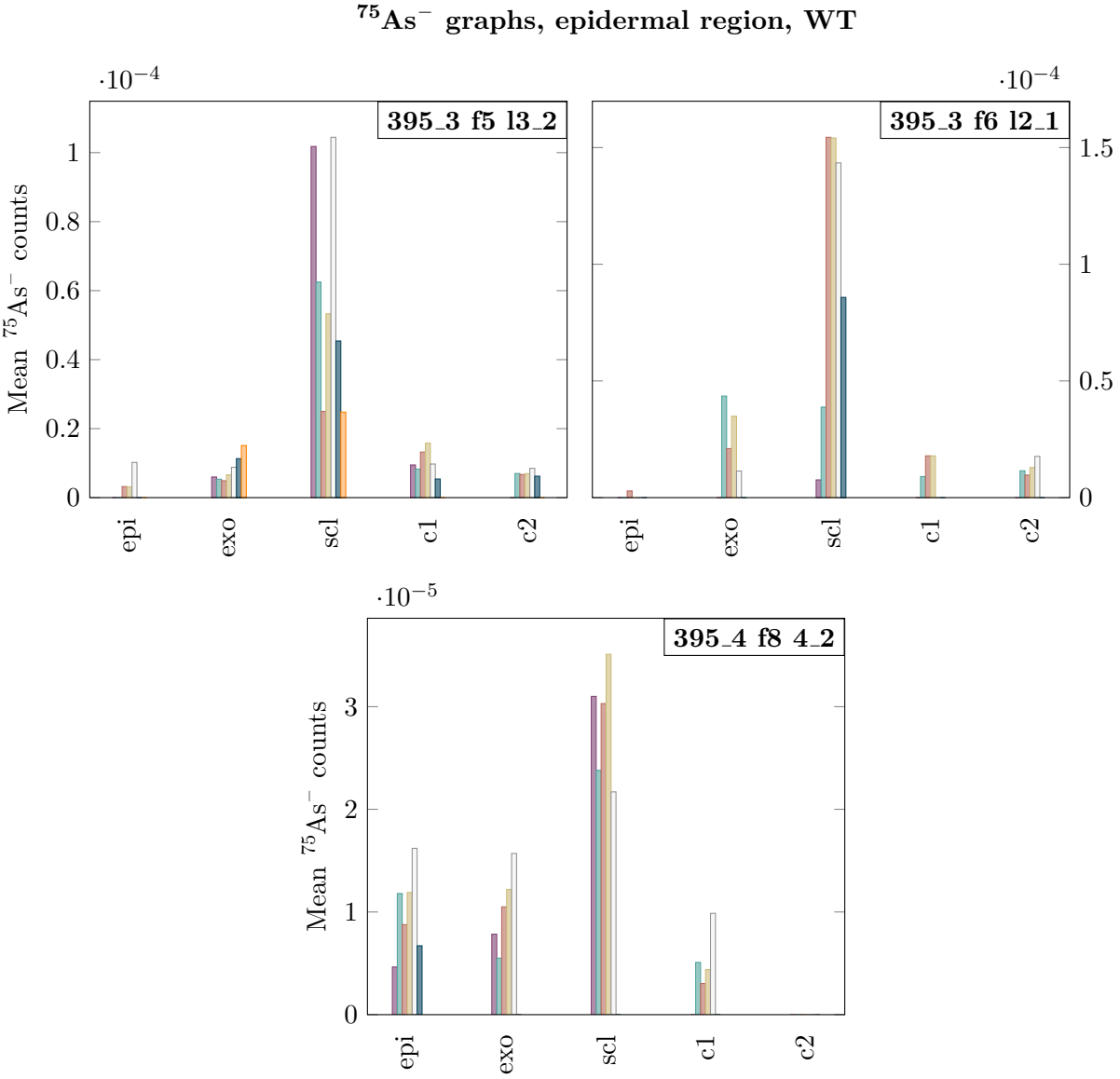

Figure A.15: $^{75}As^-$ signals from the epidermal region, WT.

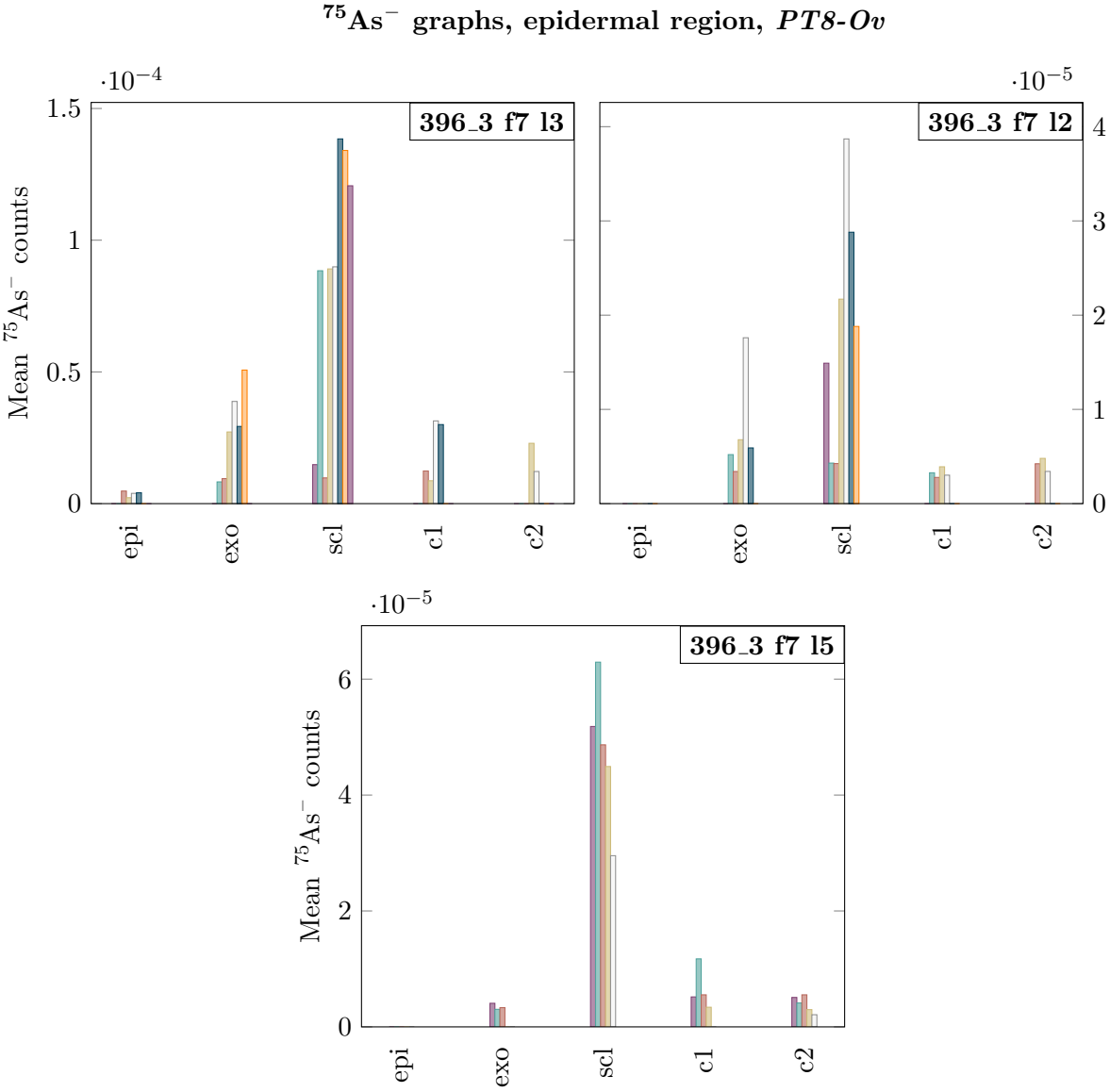

Figure A.16: $^{75}As^-$ signals from the epidermal region, *PT8-Ov*.

Appendix B

Oryza Sativa G2 sulphur arsenic ratios

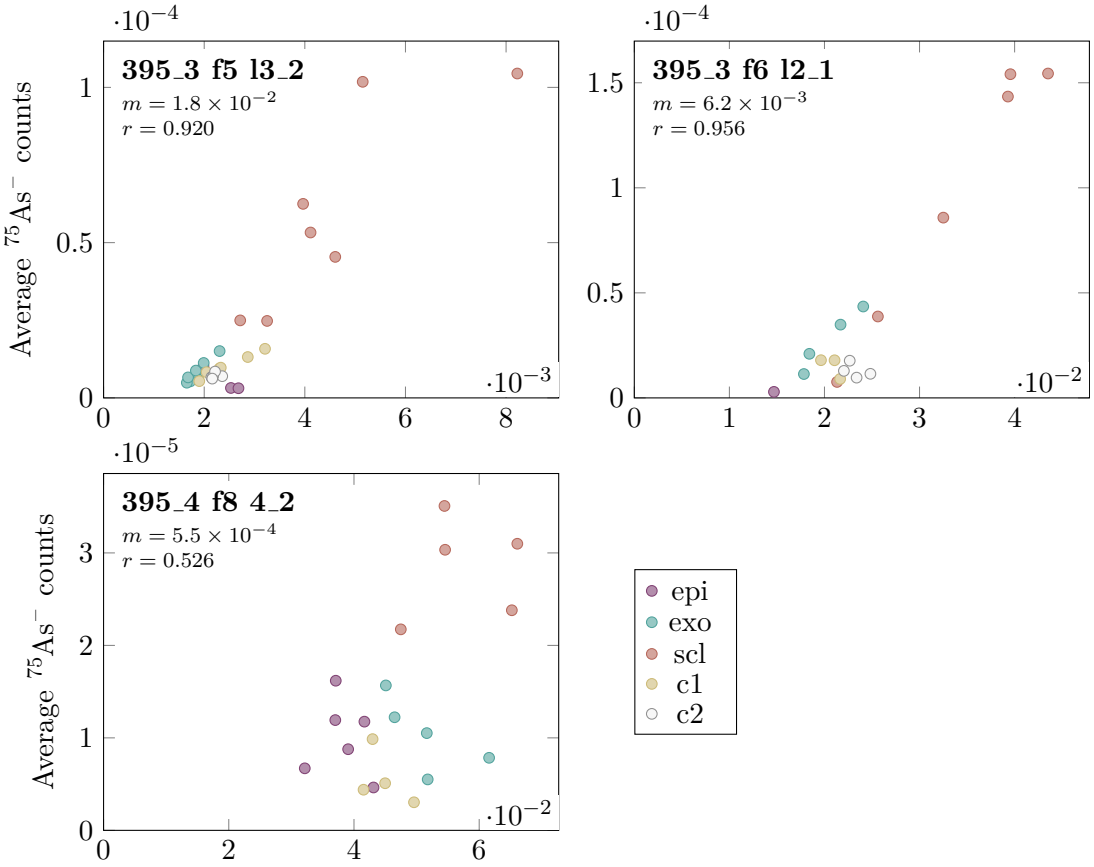

Figure B.1: Scatter graphs of average $^{75}As^-$ counts against average $^{32}S^-$ counts for WT sections, data recorded near the epidermis. (m) linear regression gradient given to two significant figures, (r) Pearson product-moment correlation coefficient give to three significant figures.

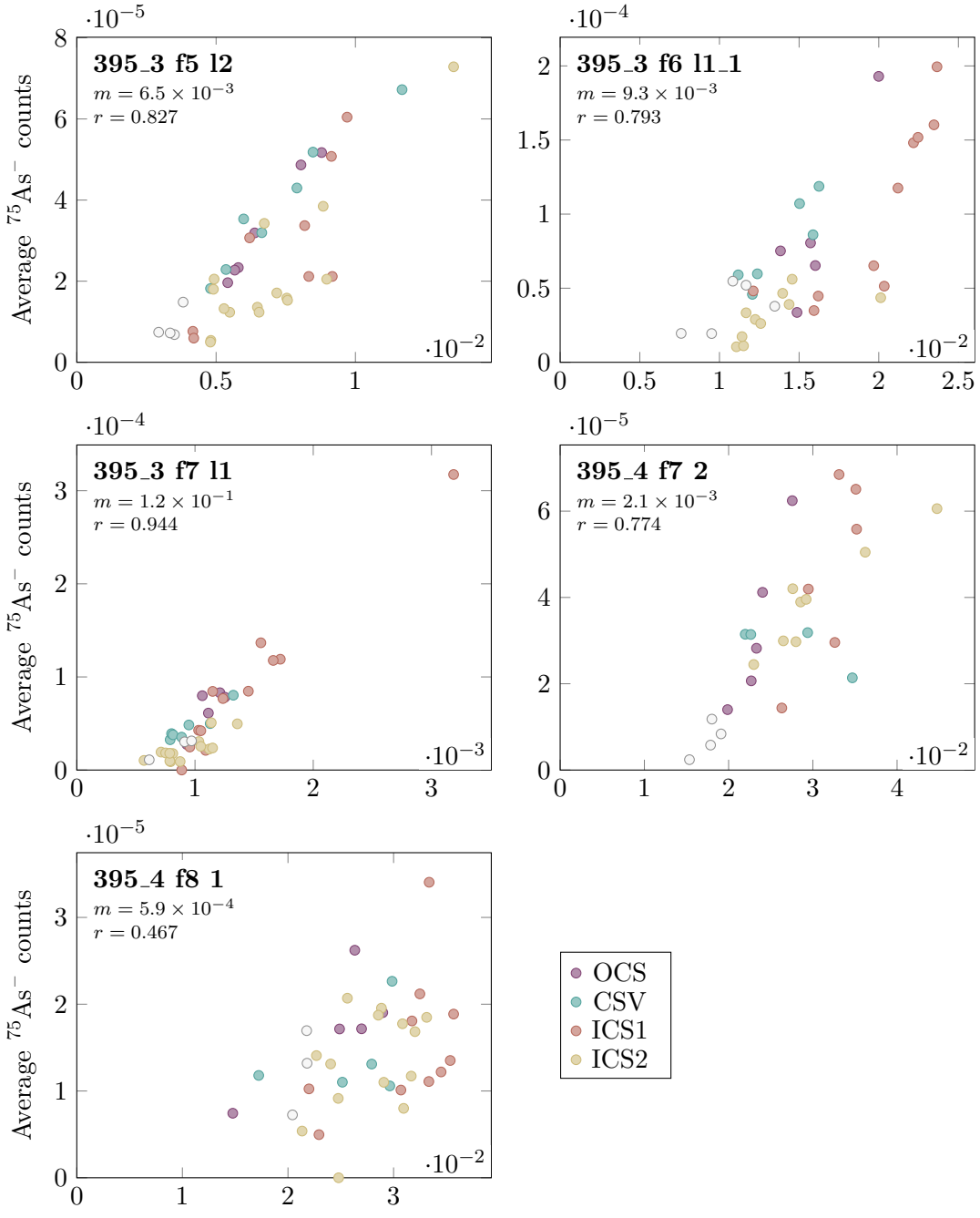

Figure B.2: Scatter graphs of average $^{75}As^-$ counts against average $^{32}S^-$ counts for WT sections, data recorded near the stele. (m) linear regression gradient given to two significant figures, (r) Pearson product-moment correlation coefficient give to three significant figures.

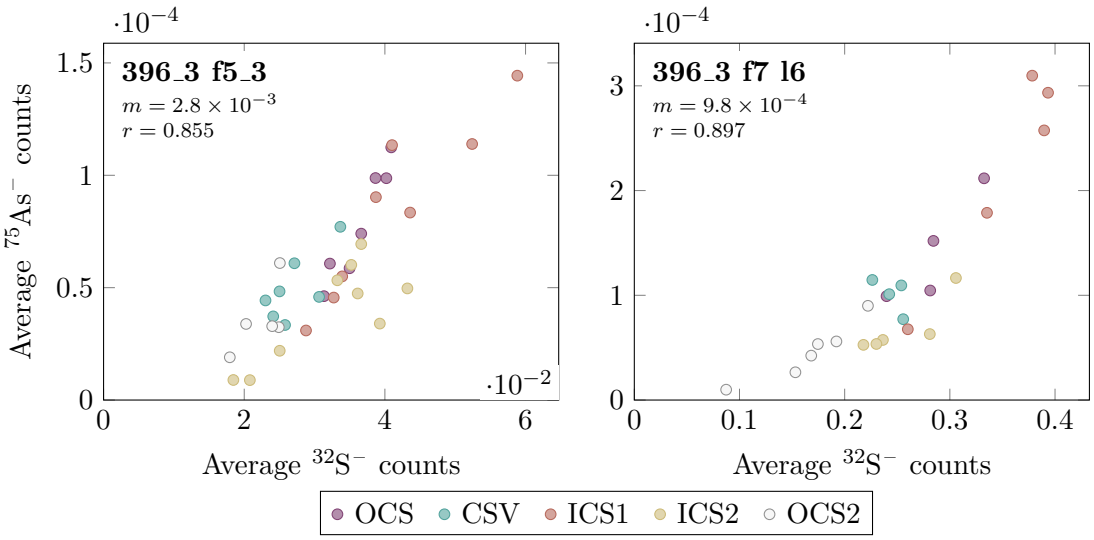

Figure B.3: Scatter graphs of average $^{75}As^-$ counts against average $^{32}S^-$ counts for *pt8* sections, data recorded near the stele. (m) linear regression gradient given to two significant figures, (r) Pearson product-moment correlation coefficient give to three significant figures.

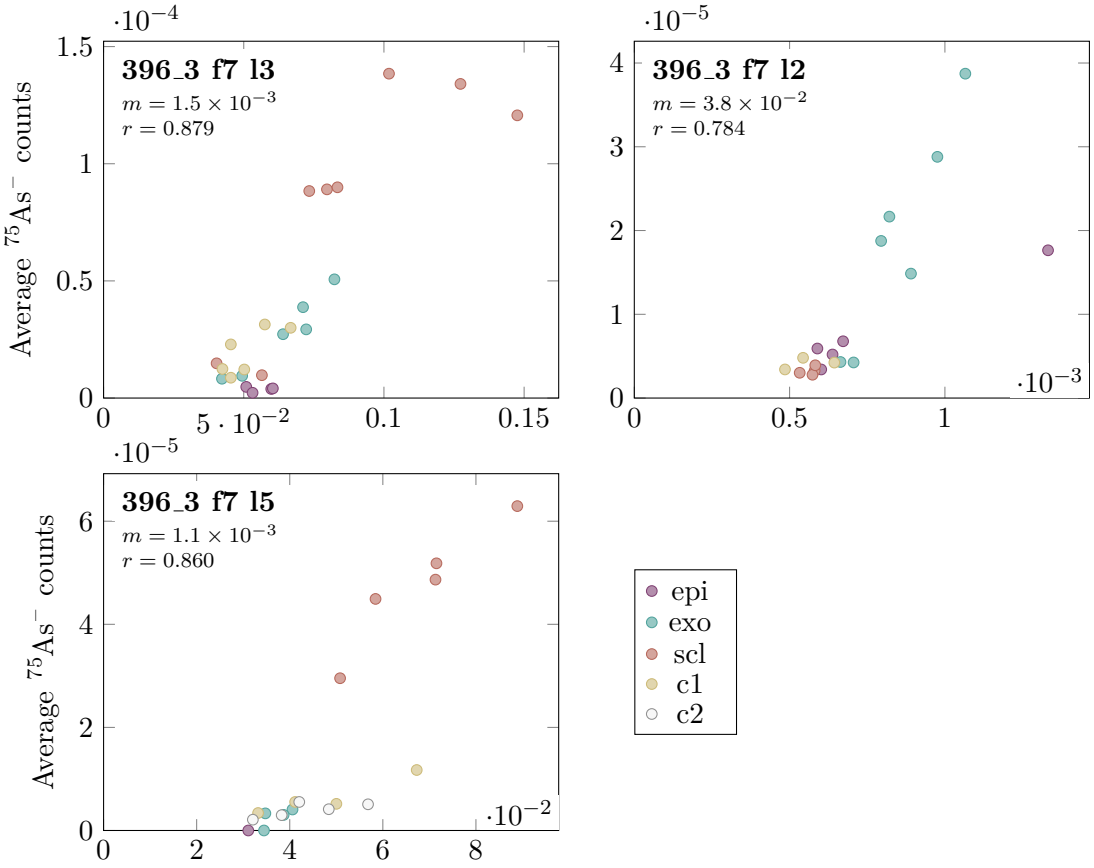

Figure B.4: Scatter graphs of average $^{75}As^-$ counts against average $^{32}S^-$ counts for WT sections, data recorded near the epidermis. (m) linear regression gradient given to two significant figures, (r) Pearson product-moment correlation coefficient give to three significant figures.

Appendix C

Arabidopsis ROI arsenic counts

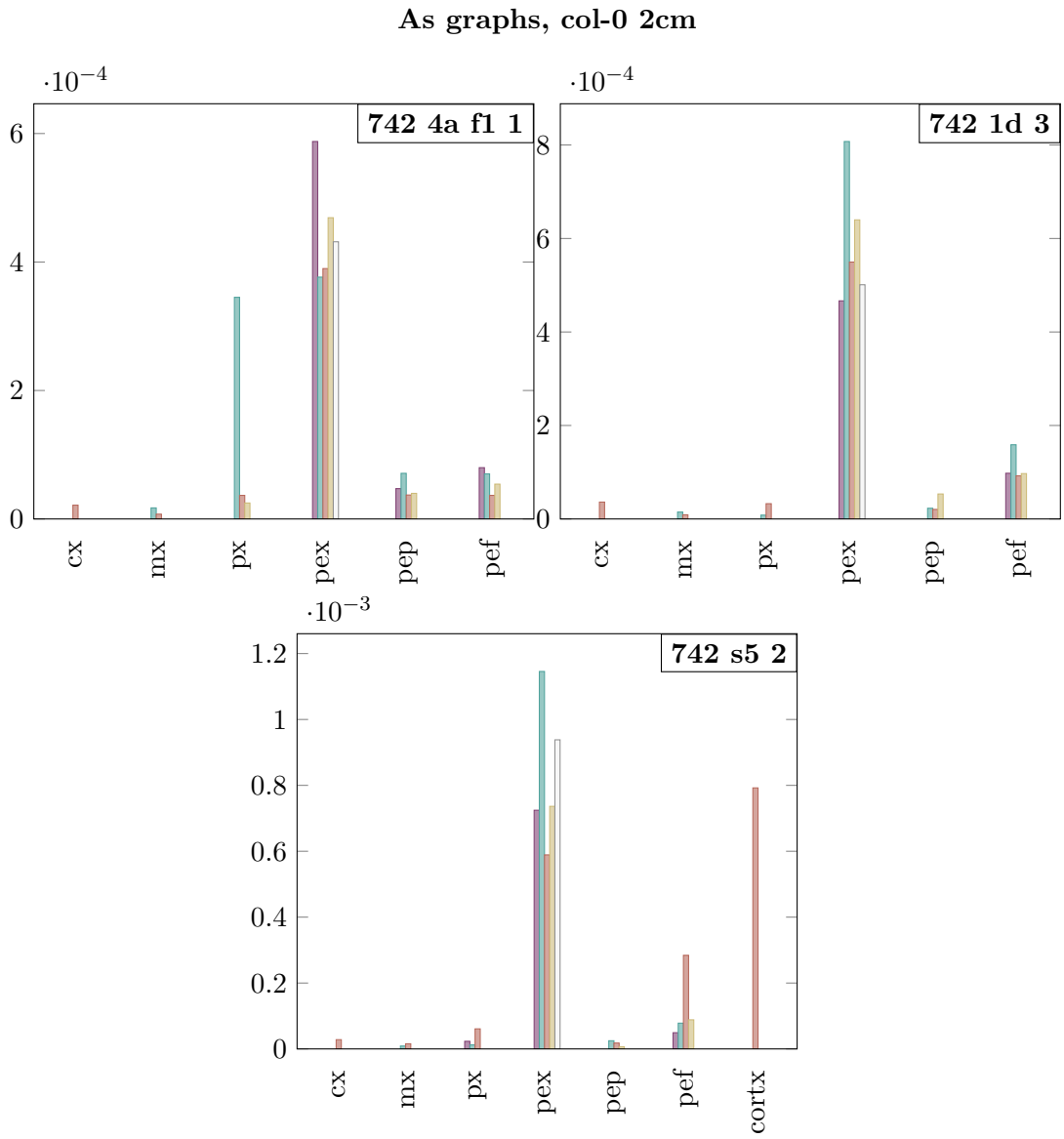

Figure C.1: As signals from the col-0 2cm

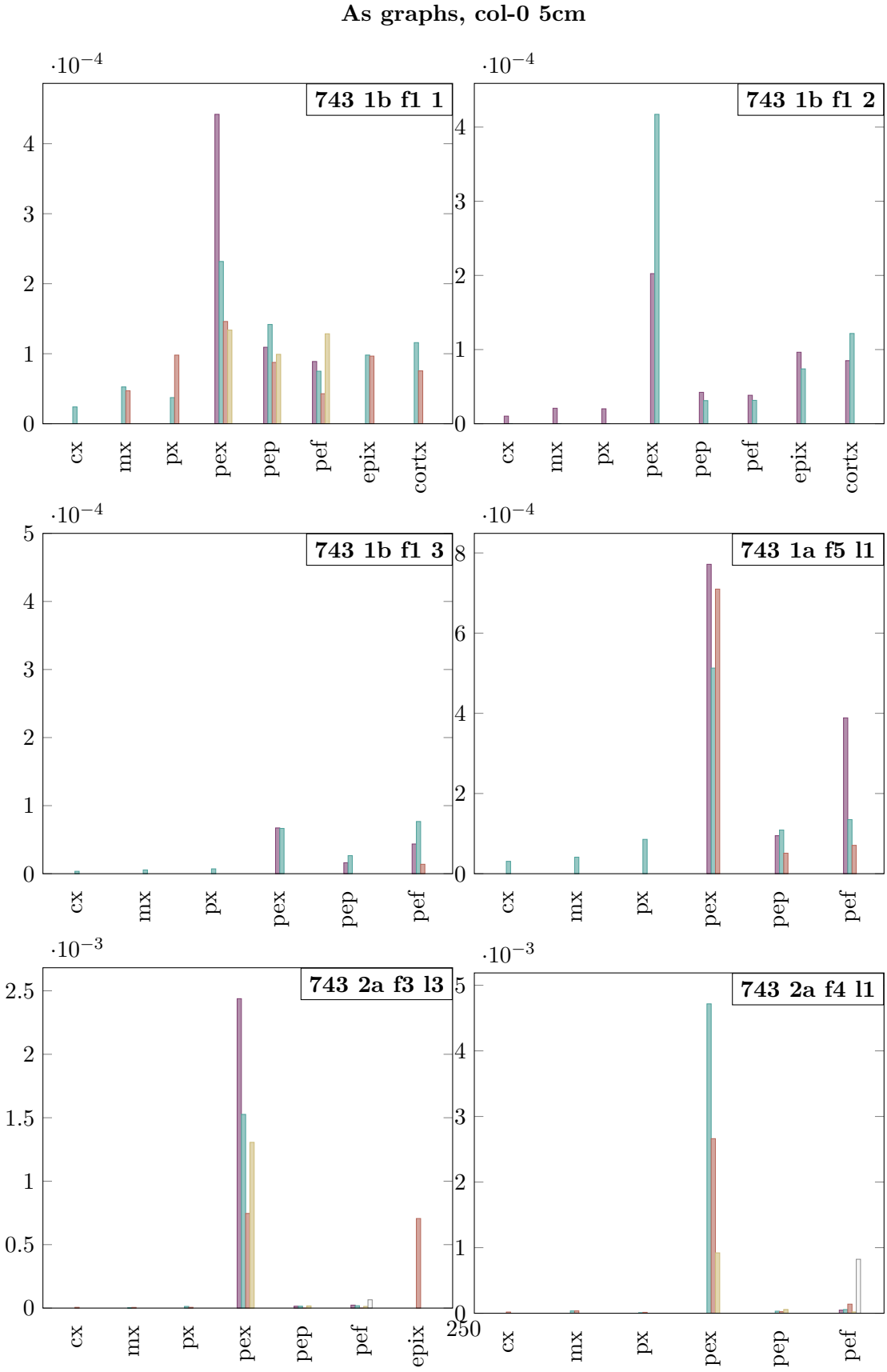

Figure C.2: As signals from col-0 5cm

As graphs, col-0 5cm (continued)

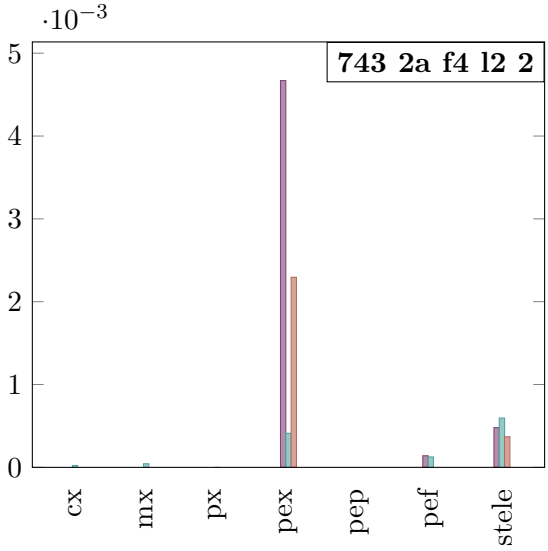

Figure C.3: As signals from col-0 5cm

As graphs *cad1-3*

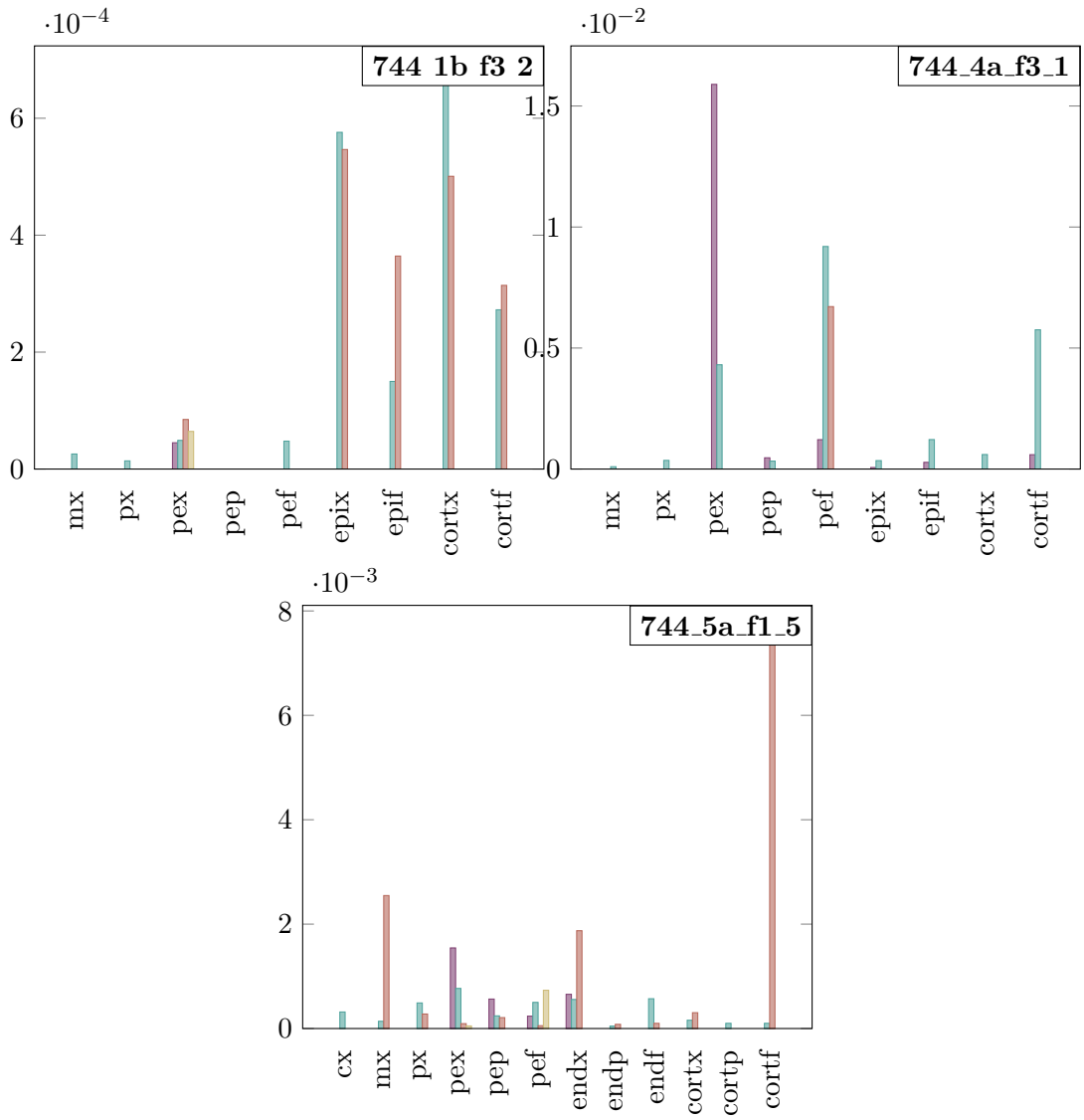

Figure C.4: As signals from the cad1-3 2cm

As graphs, *abcc1-2*

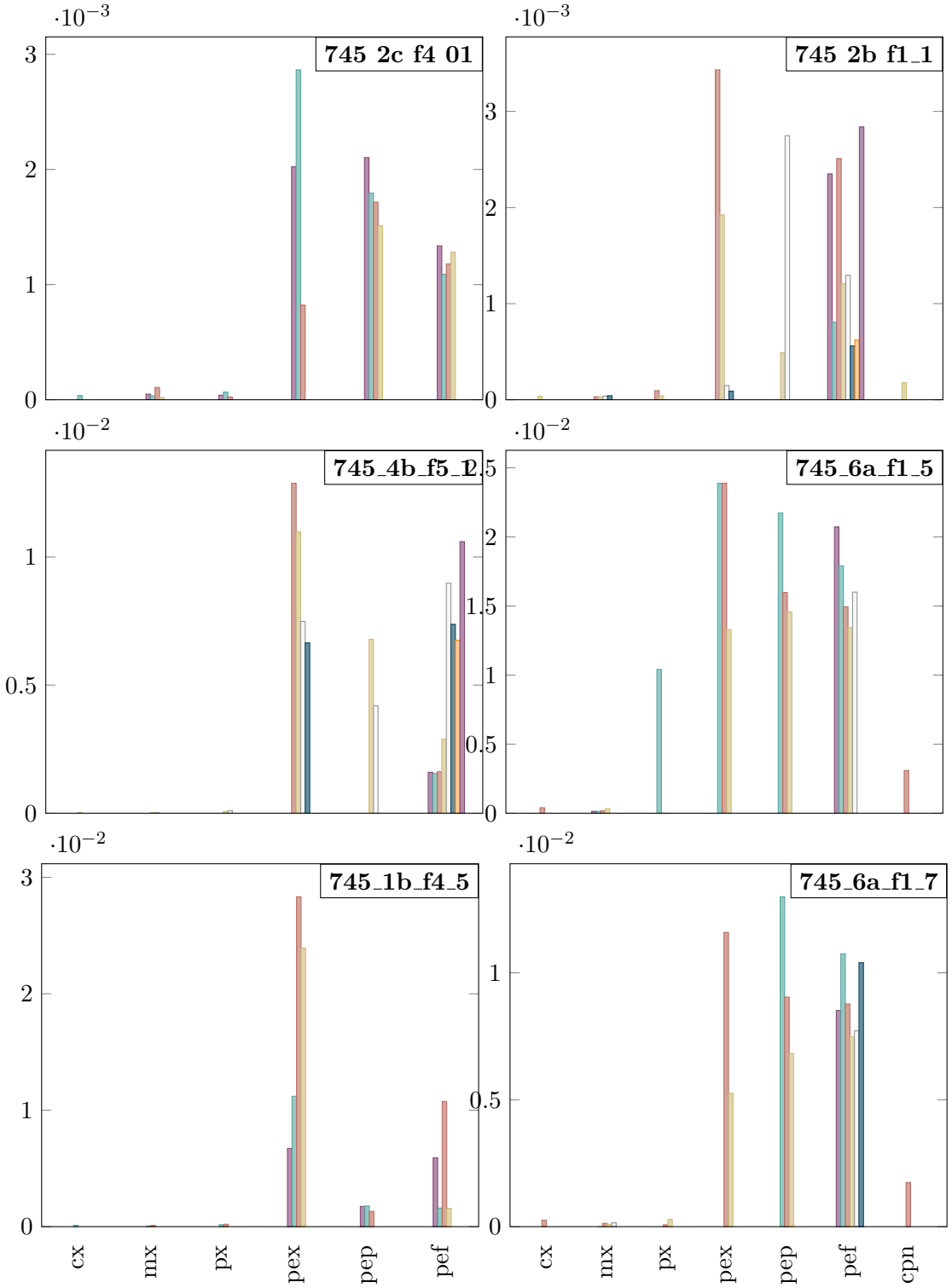

Figure C.5: As signals from *abcc1-2*

As graphs *abcc1-2* (continued)

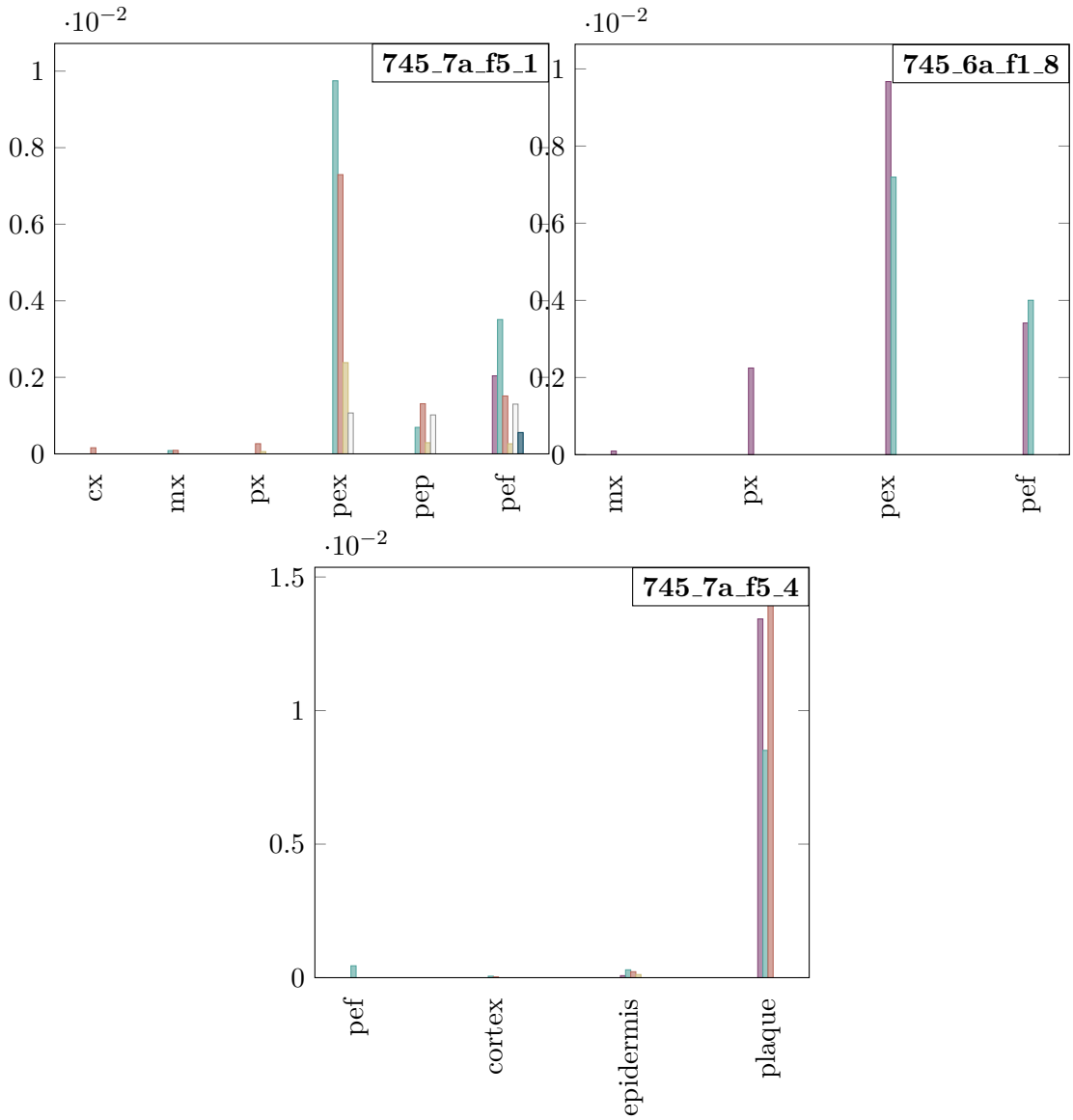

Figure C.6: As signals from the abbc1-2 2cm

Appendix D

c program source code

```
    // write detector names to file
    printf("Writing to file\n");

    for (int d = 0; d < detectors; d++)
    {
        fprintf(outptr,"%s, ",detnames[d]);
        if (d == detectors - 1)
        {
            fprintf(outptr,"\n");
        }
    }


    // write sum of blocks to file
    uint64_t currentblock;
    // iterate over rows of blocks
    for (int l = 0; l < BlocksHigh; l++)
    {
        // iterate over blocks within the rows
        for (int k = 0; k < BlocksWide; k++)
        {

            // iterate over the detectors
            for (int d = 0; d < detectors; d++)
            {
                // set sum of pixels in the currentblock to 0
                currentblock = 0;

                // iterate over rows and columns within block
                for (int j = 0; j < BlockHeight; j++)
                {
                    for (int i = 0; i < BlockWidth; i++)
                    {
                        currentblock += image[0][d][j + (BlockHeight * l)]
                        [i + (BlockWidth * k)];
                    }
                }
                fprintf(outptr,"%li, ",currentblock);

                if (d == detectors - 1)
```

```
41                  {
42                      fprintf(outptr,"\n");
43                  }
44              }
45          }
46      }
```

Lines 1-11 output the names of the detectors to the filestream. Lines 17-21 considers the NanoSIMS data as a grid of equal sized blocks, and iterates over the blocks. Line 24 iterates over the detectors. Lines 27-34 iterates over the pixels in each block and sums them. Line 37 outputs the result of this sum to a filestream and lines 39-41 adds a new line character every time a the result of the sum of the same block has been conducted for each of the detectors.

Appendix E

Arabidopsis sulphur arsenic ratios

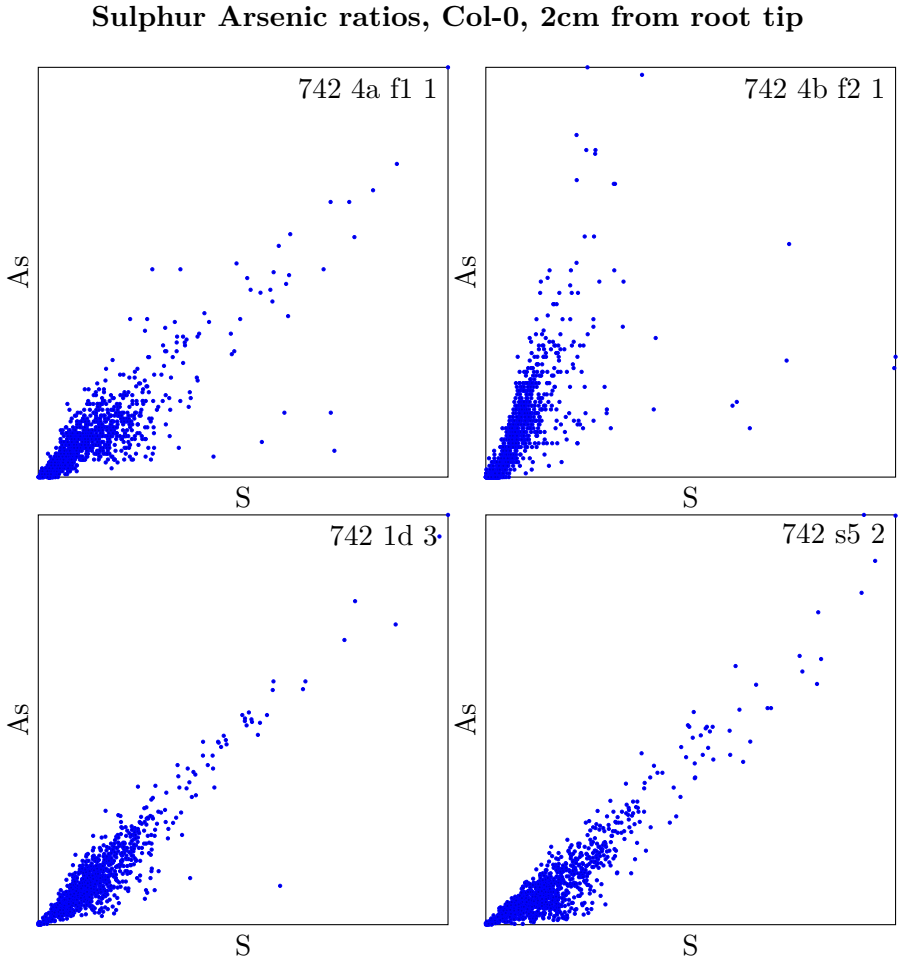

Figure E.1: $^{75}As^{-}$ $^{32}S^{-}$ detector ratios

Sulphur Arsenic ratios, Col-0, 5cm from root tip

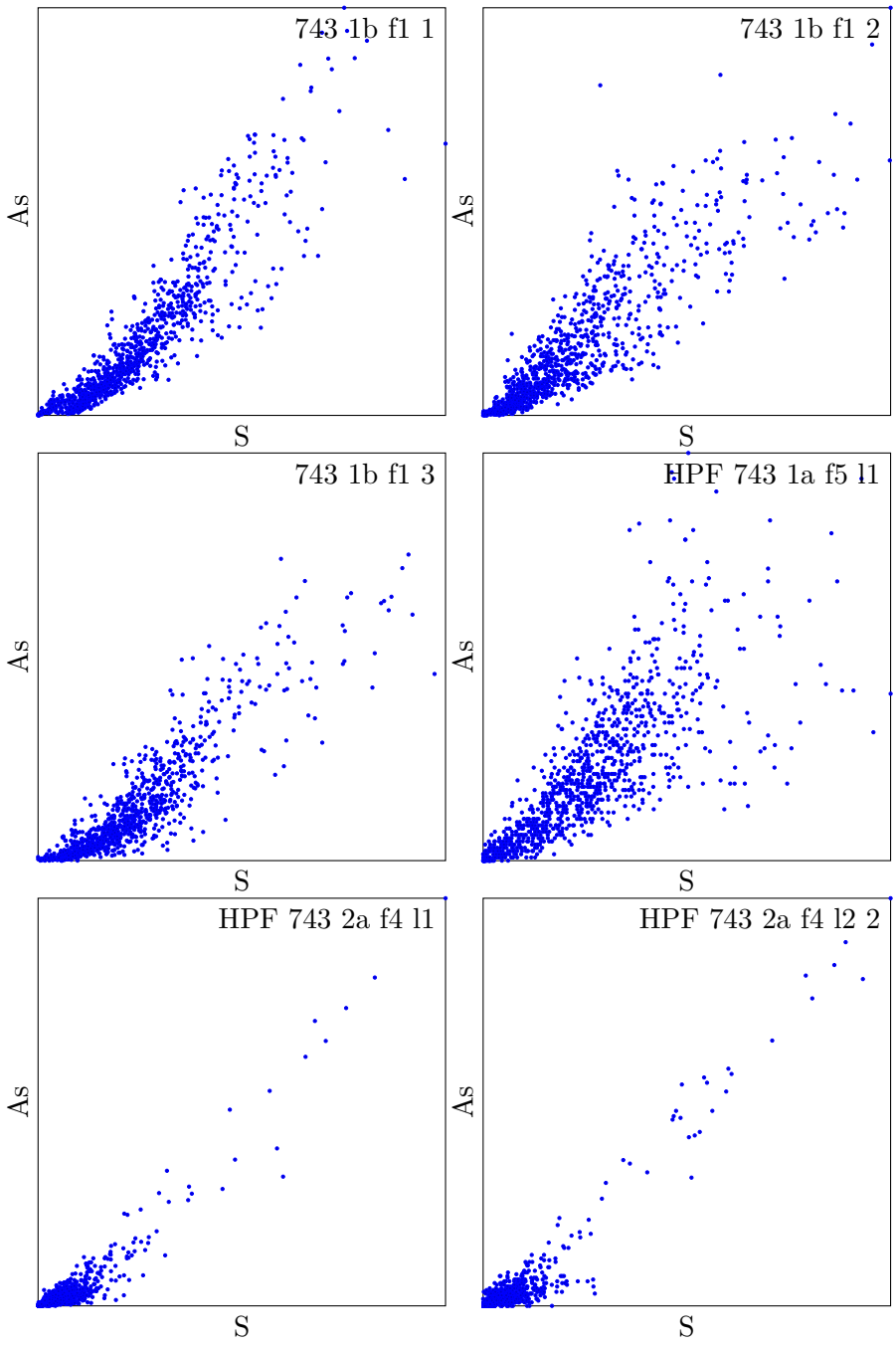

Figure E.2: $^{75}As^{-}$ $^{32}S^{-}$ detector ratios

Sulphur Arsenic ratios, *cad1-3*, 2cm from root tip

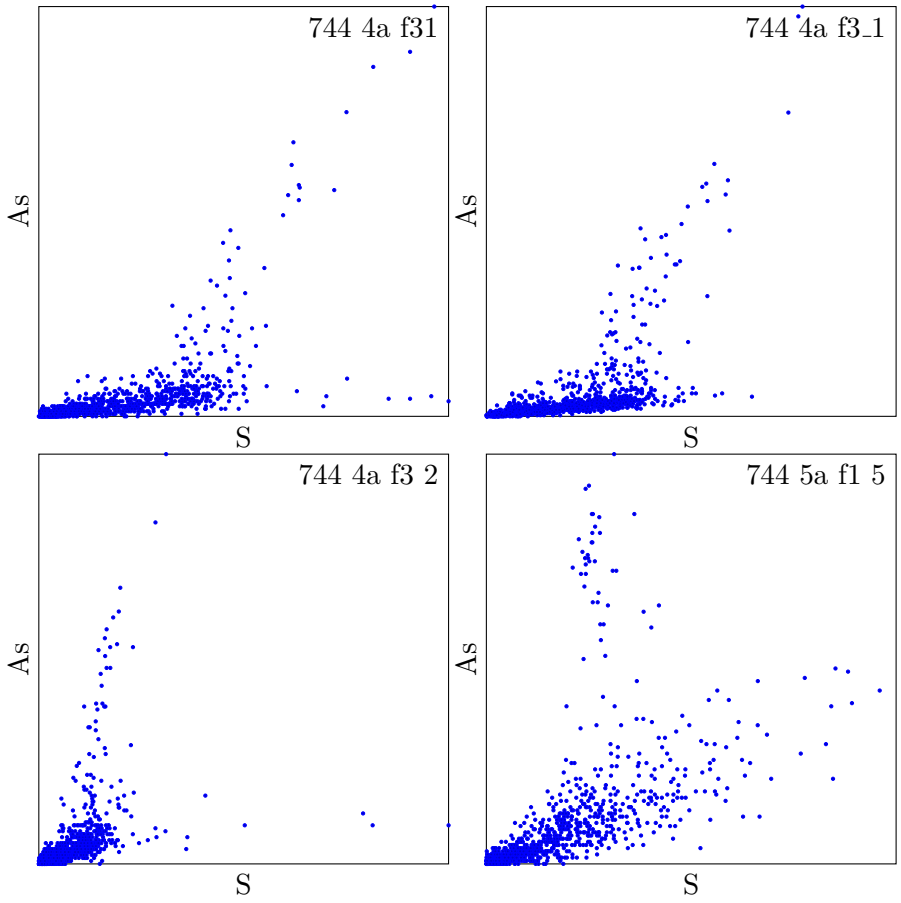

Figure E.3: $^{75}As^{-}$ $^{32}S^{-}$ detector ratios

Sulphur Arsenic ratios, *abcc1-2*, 2cm from root tip

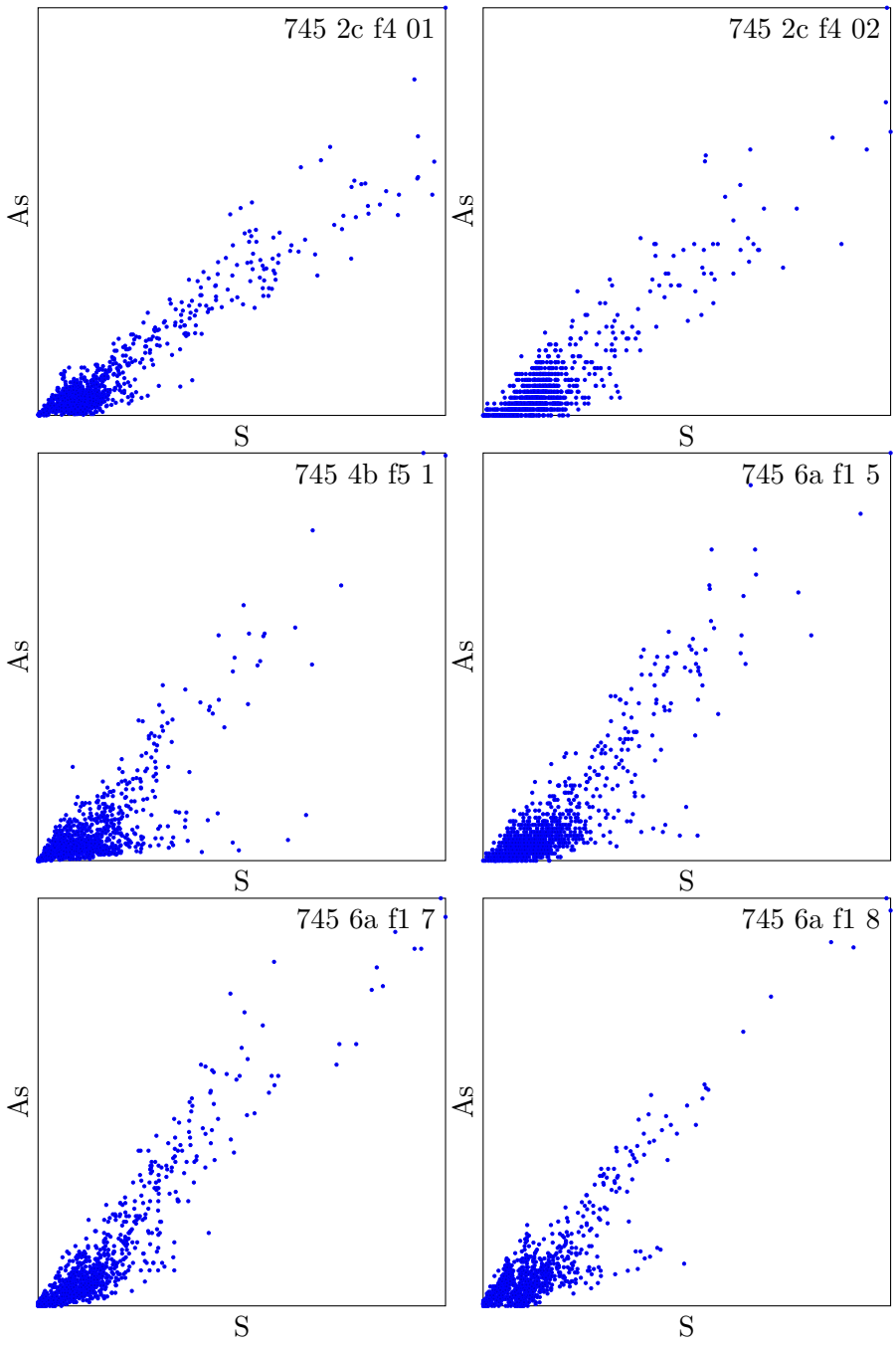

Figure E.4: $^{75}As^{-}$ $^{32}S^{-}$ detector ratios

Appendix F

Arabidopsis mass 32 HMR scan

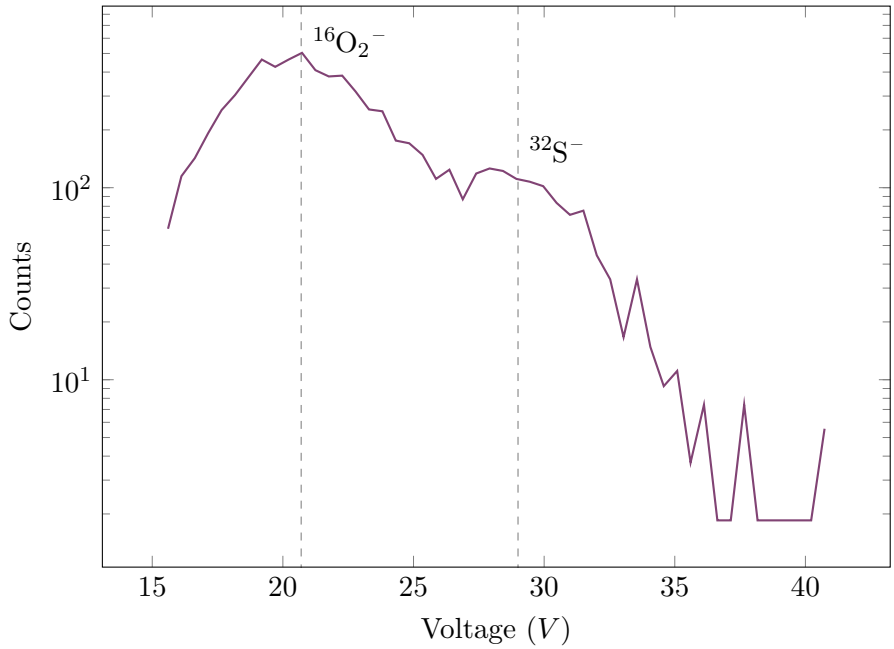

Figure F.1: HMR scan of Detector 2 tuned to mass 32, showing mass interference of $^{16}O_2{}^-$ (31.998 u) and $^{32}S^-$ (31.972 u). Detector 5 tuned to $^{75}As^-$.